β-DECAY TOTAL ABSORPTION SPECTROSCOPY AROUND A = 100-110 RELEVANT TO NUCLEAR STRUCTURE AND THE ASTROPHYSICAL R PROCESS

By

Alexander Connor Dombos

A DISSERTATION

Submitted to
Michigan State University
in partial fulfillment of the requirements
for the degree of

Physics — Doctor of Philosophy

2018

ABSTRACT

β-DECAY TOTAL ABSORPTION SPECTROSCOPY AROUND A = 100-110
RELEVANT TO NUCLEAR STRUCTURE AND THE ASTROPHYSICAL R PROCESS

By

Alexander Connor Dombos

This dissertation details the initiation of a new experimental program to study β decay that is now in use at the National Superconducting Cyclotron Laboratory and will be an integral part of the science conducted at the Facility for Rare Isotope Beams. This experimental program studies the β-decay properties of nuclides relevant to the astrophysical r process with the total absorption spectroscopy technique. Descriptions of r-process nucleosynthesis, an overview of β decay and γ decay, the experimental setups, and analysis procedures are included in this dissertation.

This dissertation contains the commissioning experiments of this experimental program. These commissioning experiments were performed at the Coupled Cyclotron Facility at the National Superconducting Cyclotron Laboratory and combined charged-particle detection using silicon detectors and γ-ray detection using a segmented total absorption spectrometer called the Summing NaI(Tl) (SuN) detector.

The commissioning experiment with a thermalized beam examined the β decay of ^{76}Ga. The extracted β-decay half-life agrees with previously published values. However, the extracted β-decay feeding intensity distribution disagrees with the existing decay scheme at the National Nuclear Data Center. The extracted distribution provided experimental data in the A = 76 mass chain. This experimental data can constrain nuclear structure models that calculate nuclear matrix elements for neutrinoless double-β decay.

The commissioning experiment with a fast beam studied neutron-rich nuclides in the

A = 100-110 mass region. This experiment was the first-ever application of the total absorption spectroscopy technique with a fast beam produced via projectile fragmentation. β-decay half-lives were extracted for ^{99}Y, ^{101}Zr, ^{102}Zr, ^{102m}Nb, ^{103}Nb, ^{104m}Nb, and ^{109}Tc. Overall, the extracted half-lives agree with previously published values. Additionally, the β-decay feeding intensity distributions and B(GT) distributions were extracted for ^{101}Zr, ^{102}Zr, and ^{109}Tc. The extracted distributions were compared to QRPA calculations, which are commonly used to provide β-decay properties in r-process reaction network calculations. In these comparisons, none of the QRPA calculations were able to reproduce the extracted distributions. The extracted distributions were compared to another set of QRPA calculations in an attempt to learn about the shape of the ground state of the parent nucleus. For ^{101}Zr and ^{102}Zr, calculations assuming a pure shape configuration (oblate or prolate) were not able to reproduce the extracted distributions. These results may indicate that some type of mixture between oblate and prolate is necessary to reproduce the extracted distributions. For ^{109}Tc, a comparison of the extracted distribution with QRPA calculations suggests a dominant oblate configuration.

ACKNOWLEDGMENTS

Thanks firstly to Artemis, my advisor, for listening to my ideas with excitement and respect, and treating me as a fellow explorer in the field of nuclear astrophysics. Her office door has always been open and she has graciously allowed me to ask questions (too many to count) at any time. Her openness has created an environment in which I have thrived. Thank you, Artemis!

I am incredibly grateful to everyone who I interacted with through using the SuN detector. This includes research physicists (Jorge), SuN postdoctoral researchers (Anna, Farheen, Mallory, Stephanie), SuN graduate students (Steve, Debra, Alicia, Caley), other graduate students (Wei Jia, Becky, Adriana), and undergraduate students (Jason, Antonius, Maya). In addition to being a wonderful friend, Steve deserves special recognition for his mentorship during my early years as a graduate student.

Thanks also to Professors Sean Liddick, Morten Hjorth-Jensen, Edward Brown, and Norman Birge for their advice, questions, and offering their valuable time to serve on my guidance committee. I would also like to thank the beam physicists, cyclotron operators, design group, electrical engineers, machinists, and others who made possible the experiments comprising this dissertation.

The expertise of the β group, especially Sean Liddick and Chris, has been invaluable. I am additionally grateful to Matthew Mumpower for being my national laboratory mentor through the Nuclear Science and Security Consortium. Matthew, thank you for teaching me how to run r-process reaction network calculations at Los Alamos National Laboratory during the summer of 2017 and for taking me on some truly memorable hikes! Thank you to members of my cohort at the NSCL, especially Chris, Eric, and Sam, for working on

coursework together and helping me gain the necessary programming skills to succeed in this graduate program. I would also like to thank Arthur Cole, who I worked with as an undergraduate for his continued guidance and friendship.

I am so thankful for the love and support of my parents, brother, grandparents, aunts and uncles, and neighbors. Finally, I want to thank my wife, Kelsey, for the love and support she has given me throughout this process while also completing her own doctoral degree in Neuroscience. There has been quite a large synaptic cleft between our neurons these past six years, but soon we will be reunited. I can't wait to begin our life together and use our hippocampi to make new memories!

TABLE OF CONTENTS

LIST OF TABLES

LIST OF FIGURES

Chapter 1

Introduction

1.1 Nuclides

The atomic nucleus is composed of nucleons (protons and neutrons). A nuclide is defined by a unique combination of proton number (or atomic number, Z) and neutron number (N). The notation for a nuclide is ${}^{\mathrm{A}}_{\mathrm{Z}}\mathrm{X}_{\mathrm{N}}$ where A is the mass number (number of nucleons), Z is the atomic number, X is the chemical symbol for the element (defined by the atomic number), and N is the neutron number. Isotopes are nuclides that contain the same atomic number but different neutron numbers, isotones are nuclides that contain the same neutron number but different atomic numbers, and isobars are nuclides that contain the same mass number.

Figure 1.1 shows the chart of the nuclides, which is a common graphic representation to display unstable and stable nuclides. Out of the more than 7000 nuclides that are predicted to exist, only a little more than 3000 have actually been observed. Of those nuclides that have been observed, less than 300 are stable. The rest are unstable and will decay by various processes until reaching a stable nuclide. The stable nuclides form the valley of stability.

In atoms, completely filled shells of electrons correspond to enhanced stability. Completely filled electronic shells correspond to the noble gases, where the first ionization energy (the energy required to remove an electron from the atom) is a local maximum. Immediately following (meaning, increasing Z by 1) a noble-gas element, there is a relatively large

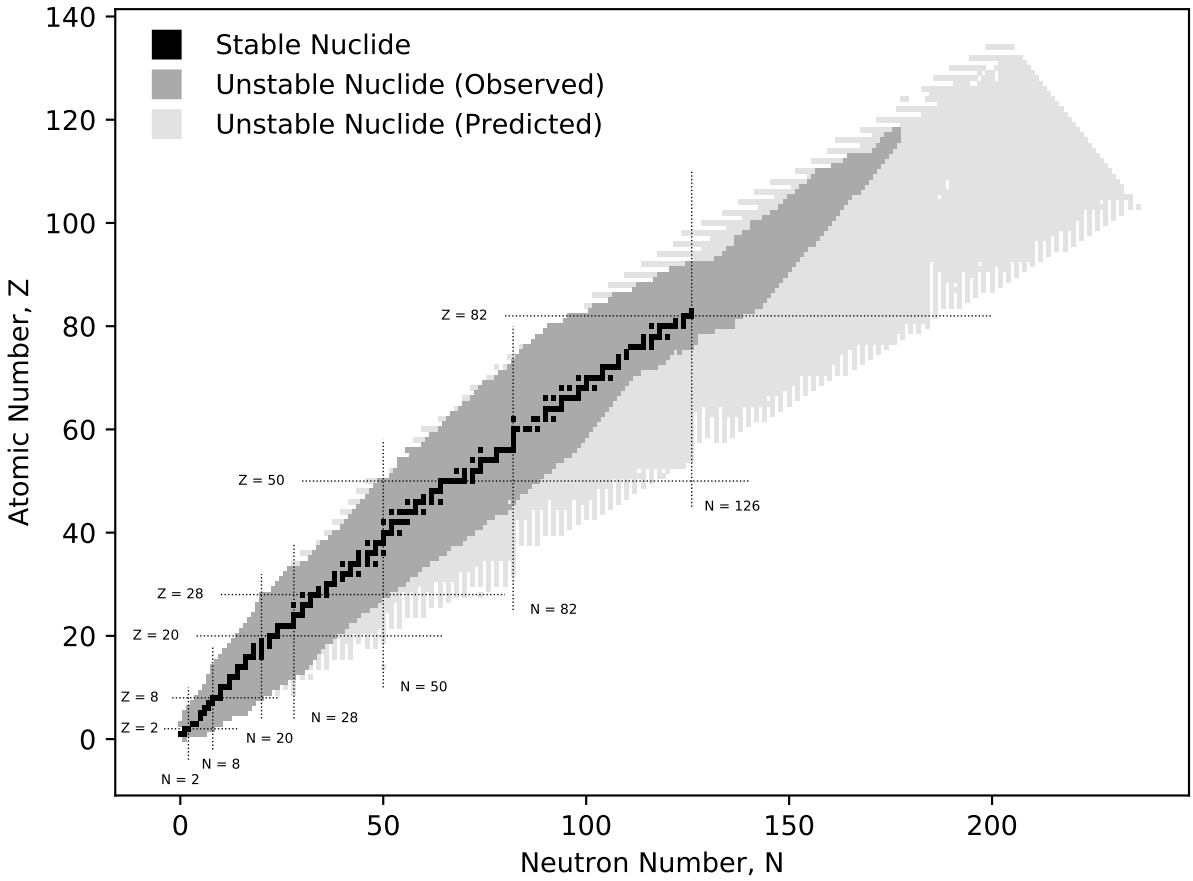

Figure 1.1: Chart of the nuclides. Each shaded cell is an individual nuclide, defined by a unique combination of atomic number (Z) and neutron number (N). The stable nuclides are black, the unstable nuclides that are experimentally known to exist are dark gray, and the unstable nuclides that are predicted to exist according to the FRDM (2012) [3] mass model are light gray. An unstable nuclide is predicted to exist if both the one-proton separation energy (the energy required to remove a proton from the nucleus) and one-neutron separation energy (the energy required to remove a neutron from the nucleus) are greater than zero. In other words, an unstable nuclide is predicted to exist if the spontaneous emission of nucleons is energetically forbidden. The black, dotted lines indicate magic numbers that correspond to closed shells of nucleons.

decrease in the first ionization energy. A similar phenomenon is also observed for nucleons. Nucleons fill single-particle states, and groups of single-particle states with similar energies form shells. Separate shells exist for protons and neutrons. Completely filled shells correspond to enhanced stability. Immediately following a completely filled shell (a closed shell), there is a relatively large decrease in the amount of energy required to remove a nucleon from the nucleus. For example, at a neutron closed shell, the one-neutron separation energy (the energy required to remove a neutron from the nucleus) is a local maximum. Immediately following the neutron closed shell, there is a relatively large decrease in the one-neutron separation energy. Similarly, the neutron capture cross section (the probability for the nucleus and a neutron outside of the nucleus to merge together) at a neutron closed shell is relatively small.

The nuclear shell model [26, 27, 28, 29, 30, 31] describes the configuration of single-particle states for nucleons and successfully predicts where closed shells occur for protons and neutrons. Closed shells for protons and neutrons occur at "magic numbers" and are labeled in the chart of the nuclides in Fig. 1.1. The magic numbers for protons and neutrons are 2, 8, 20, 28, 50, and 82. There is an additional magic number for neutrons at N = 126. These magic numbers can change and evolve far from stability.

1.2 Abundances

One goal within the field of nuclear astrophysics is to explain the origin of the nuclides in the solar system. A necessary first step in achieving that goal is making a detailed inventory of the nuclides that exist in the solar system. One example of an inventory that scientists use is an abundance distribution (or abundance pattern). The solar system abundance pattern

displays the amount of each element or isobar in the solar system.

The amounts (or abundances) of the elements in the solar system are typically obtained from two independent and complementary sources [32]. One source for elemental abundances is absorption spectroscopy of the Sun's photosphere. In this case, the presence of an absorption line in the absorption spectrum indicates the presence of an element (different elements have different absorption lines), and the magnitude of the absorption line leads to inference of the abundance (for example, a relatively large magnitude indicates a relatively large abundance). Because the Sun accounts for almost all of the mass in the solar system, the abundance pattern of the Sun is considered to be representative for the entire solar system. In addition, the current abundances from absorption spectroscopy are believed to reflect the abundances at the formation of the solar system [32]. Another source for elemental abundances is mass spectrometry of meteorites called CI chondrites (the "C" stands for "carbonaceous" and "I" indicates the geological type locality). Out of the different types of meteorites, CI chondrites have been modified the least by chemical and physical processes since the formation of the solar system [32]. Only five CI chondrites have been identified [4]. The elemental abundances obtained from CI chondrites are generally more accurate than those obtained from absorption spectroscopy [32, 4]. Nevertheless, the abundances obtained from both sources are generally in good agreement. For example, the abundances of 56 elements can be obtained from both sources. Out of the common 56 elemental abundances, the relative abundances of 41 elements from both sources agree within 15% [4].

For each element, a recommended abundance is chosen from one of the two sources, an average value of both sources, or a theoretical value [4]. Once the elemental abundances have been obtained, isotopic abundances of the solar system are obtained using isotopic compositions as found on Earth (see Sec. 2.5 of Ref. [4]). For example, Ref. [33] contains these

isotopic compositions. Finally, one way of expressing abundances is with the cosmochemical scale, which normalizes silicon to 10^6 atoms (see, for example, Fig. 1.2).

1.3 Nucleosynthesis

Nucleosynthesis refers to all the different processes that produce nuclides. Many nucleosynthesis processes were first outlined in 1957 by Burbidge, Burbidge, Fowler, and Hoyle (referred to as the B^2FH paper) [34]. While the nucleosynthesis processes described in the B^2FH paper have been revised since 1957, this seminal work provides a foundation for the current theory of nucleosynthesis.

The top panel of Fig. 1.2 shows the solar system abundance pattern. All features in the abundance pattern can be explained with different nucleosynthesis processes. Big Bang nucleosynthesis produced mostly hydrogen and helium, and small amounts of ^{2}H, ^{3}He, and ^{7}Li. Nuclear fusion inside of stars is mostly responsible for the production of nuclides with $12 \leq A \leq 56$. Material undergoing nuclear statistical equilibrium and then cooling (as happens in type Ia supernovae and core-collapse supernovae) is mostly responsible for the production of nuclides within the iron peak ($50 \lesssim A \lesssim 62$). The nucleosynthesis processes that produce heavier nuclides will be discussed in the following section.

1.3.1 Nucleosynthesis Beyond the Iron Peak

Beyond the iron peak, the Coulomb barrier is insurmountably large and fusion is endothermic. Nucleosynthesis beyond the iron peak instead proceeds with a γ-induced process and two neutron-induced processes. These three processes do not have a Coulomb barrier because γ rays and neutrons are electrically neutral. Historically, these three processes have received

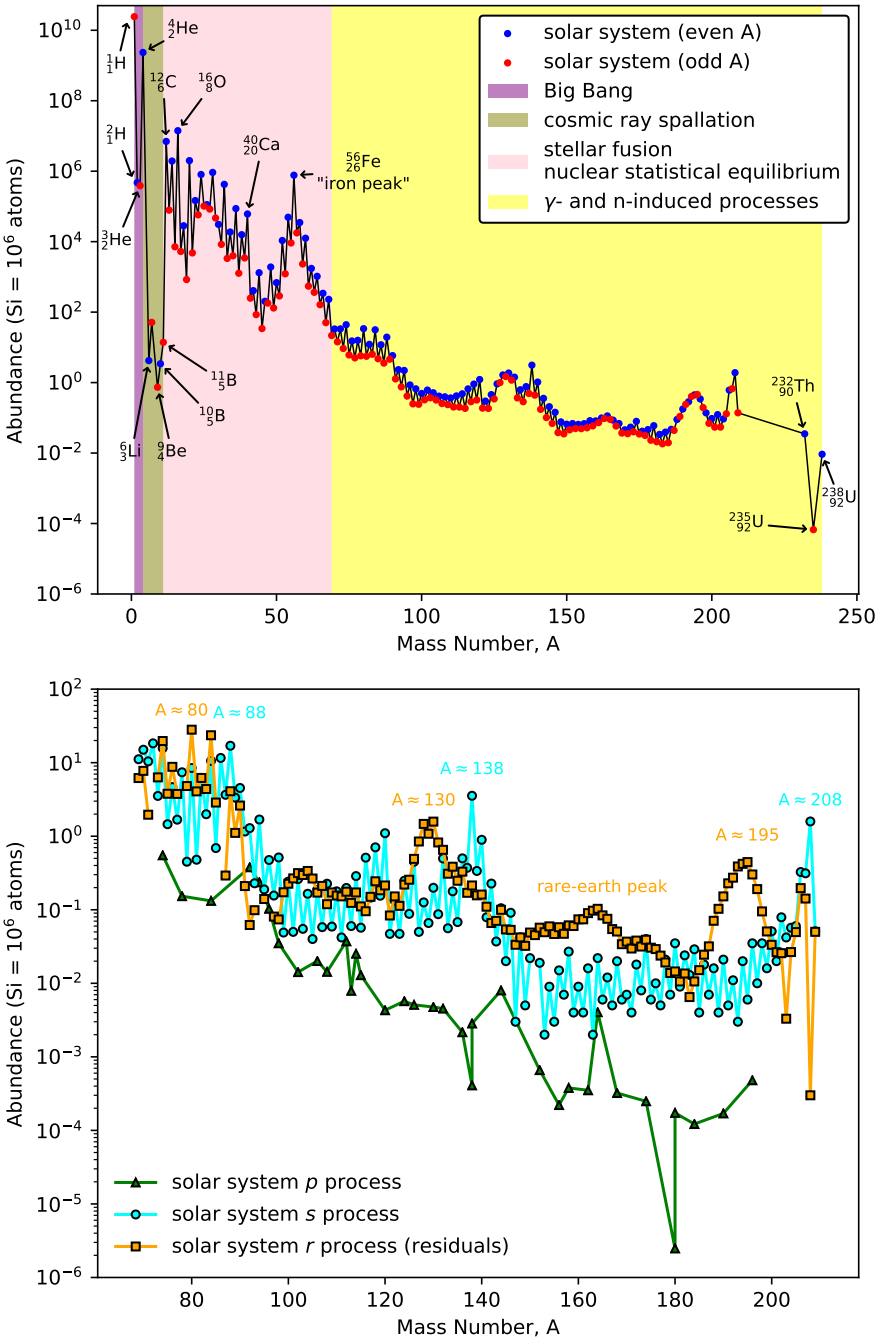

Figure 1.2: Abundances of nuclides in the solar system and the processes responsible for their production. The top panel shows the decomposition of the abundances by both parity of mass number and production mechanism. In the top panel, various nuclides are labeled. The bottom panel shows the decomposition of the abundances beyond the iron peak into the individual abundance patterns of the p process, s process, and r process. In the bottom panel, different features arising from nuclear structure are labeled in the abundance patterns of the s process and r process. Both panels use the cosmochemical scale, which normalizes silicon to 10^6 atoms. The abundance data is from Ref. [4] (solar system), Ref. [5] (p process), Ref. [6] (s process), and Ref. [7] (r process).

the most attention because they are most likely the dominating nucleosynthesis processes beyond the iron peak. However, there may be additional processes. The γ-induced process is the p process [5], and the two neutron-induced processes are the slow neutron-capture process (s process) [35, 36] and rapid neutron-capture process (r process) [7]. The solar system abundance patterns of these three processes are shown in the bottom panel of Fig. 1.2. A schematic illustration of the operation of these three processes in the chart of the nuclides is shown in Fig. 1.3. Regarding possible additional processes, some authors have proposed, for example, the intermediate neutron-capture process (i process) [37].

The p process is responsible for producing the 35 neutron-deficient stable nuclides that cannot be produced by the s process or r process. During the p process, photodisintegration reactions occur on existing seed nuclei. The photodisintegration reactions include (γ, p), (γ, n), and (γ, α) reactions. Because these γ-induced reactions are integral to the p process, some authors instead use the term γ process instead of p process. The seed nuclei are produced in the s process and/or r process.

As shown in Fig. 1.3, two of the 35 nuclides that can only be produced in the p process are ^{78}Kr and ^{84}Sr. In this case, ^{78}Kr is produced by a series of (γ, n) reactions on the seed nucleus ^{80}Kr. Similarly, ^{84}Sr is produced by a series of (γ, n) reactions on the seed nucleus ^{86}Sr. The schematic illustration in Fig. 1.3 neglects the possibility of ^{78}Kr and ^{84}Sr being produced in a more complex series of photodisintegration reactions and β^+ decay.

As shown in the bottom panel of Fig. 1.2, the contribution from the p process to the solar system abundance pattern is much less than the contribution from the s process or r process. However, the p process is an active area of research because uncertainties exist in the astrophysical site as well as the nuclear physics input. Concerning the nuclear physics, uncertainties exist in the cross sections (the probability for a reaction to occur) for the

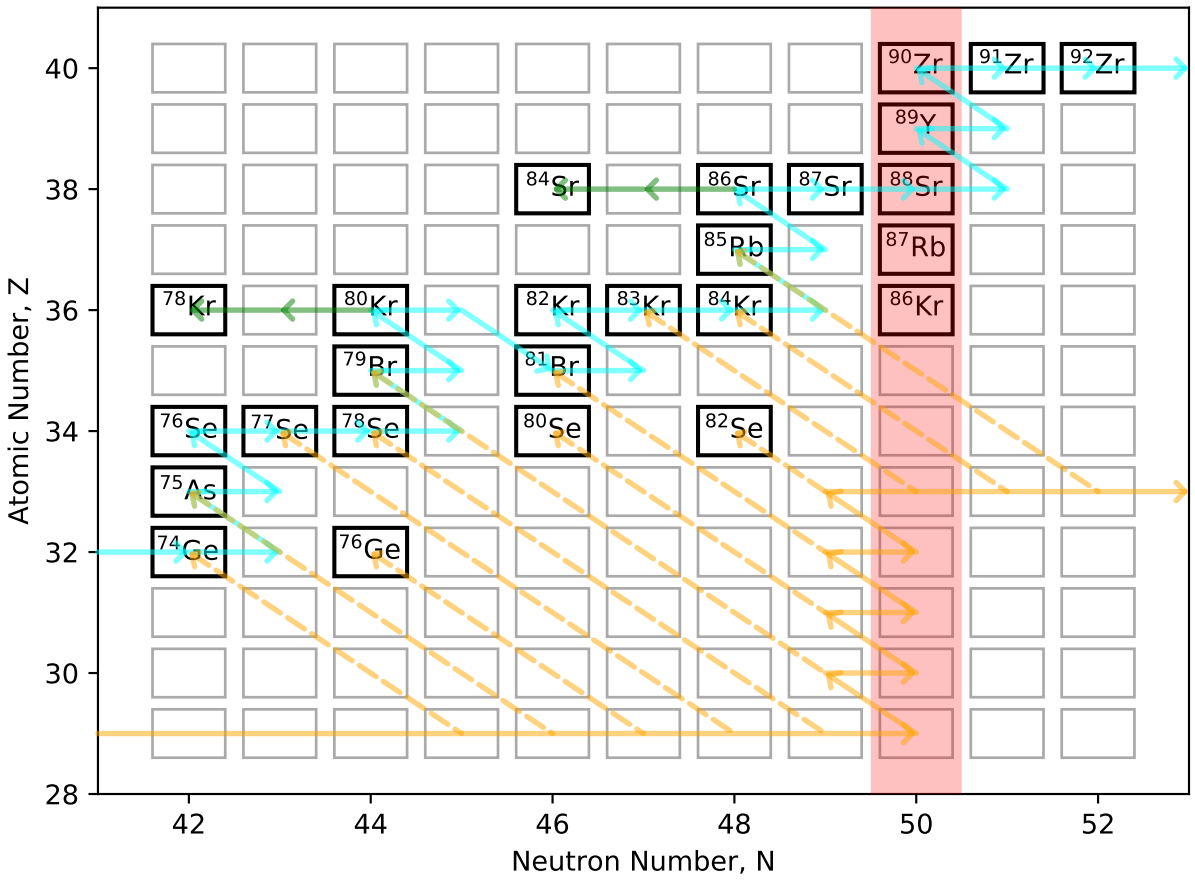

Figure 1.3: Schematic illustration of the operation of the p process (green arrows), s process (cyan arrows), and r process (orange arrows) for a region of the chart of the nuclides. The r process shows the operation during the neutron flux (orange, solid arrows) and decay back to the valley of stability after the neutron flux (orange, dashed arrows). The neutron closed shell at the magic number N = 50 is indicated with the red, shaded region. A cell that is labeled and outlined in black indicates a stable nuclide. A cell that is not labeled and outlined in gray indicates an unstable nuclide. This illustration ignores the possibility of "branching points" in the s process.

photodisintegration reactions. Researchers are currently trying to reduce these uncertainties by measuring cross sections for relevant (p,γ) and (α,γ) capture reactions [38, 39, 40, 41, 42, 43, 44]. From the capture-reaction measurements, the cross sections for the inverse reactions (the photodisintegration reactions) are obtained using the reciprocity theorem (also known as detailed balance).

The bottom panel of Fig. 1.2 shows that the s process and r process contribute approximately equally to the solar system abundance pattern. Because the p-process contribution to the solar system abundance pattern is relatively small, the s process and r process each contribute approximately half to the total abundance of stable nuclides beyond the iron peak. However, these two neutron-induced processes occur in different astrophysical environments and on different timescales.

The s process occurs in asymptotic giant branch (AGB) stars. This type of star is formed in a late phase of stellar evolution for low-mass stars. During this phase, neutrons are primarily produced from two sources. One source is the $^{13}\mathrm{C}(\alpha,n)^{16}\mathrm{O}$ reaction, which results in a neutron density between 10^6 and 10^8 neutrons/cm^3 [36]. The other source is the $^{22}\mathrm{Ne}(\alpha,n)^{25}\mathrm{Mg}$ reaction, which results in a neutron density up to 10^{10} neutrons/cm^3 [36]. The s process occurs on the order of thousands of years and is divided into a "weak" component (producing nuclides with $\mathrm{A} \lesssim 90$), a "main" component (producing nuclides with $90 \lesssim \mathrm{A} \lesssim 205$), and a "strong" component (producing nuclides with $\mathrm{A} \gtrsim 205$). These three components differ in the average number of neutrons captured per seed nucleus.

In the s process, the timescale for neutron capture τ_n is generally much longer than the timescale for β^- decay τ_β. That is, $\tau_n \gg \tau_\beta$. In other words, an unstable nuclide produced from neutron capture will undergo β^- decay before capturing another neutron. In this sense, neutron capture is "slow" compared to β^- decay, hence the name slow neutron-

capture process. A representative path for the s process is shown in Fig. 1.3. Some nuclides, such as ^{82}Kr, can only be produced in the s process. These nuclides are shielded from the r process by stable nuclides. For ^{82}Kr, the stable nuclide ^{82}Se acts as a shield from the r process (see Fig. 1.3). The path of the s process proceeds close to the valley of stability, and is never more than one unit away from stability. As mentioned in Sec. 1.1, magic numbers of nucleons correspond to enhanced stability. At the magic number N = 50 in Fig. 1.3, the neutron capture cross section is relatively small. This means the probability of capturing a neutron is relatively small at N = 50. As a consequence, the abundance accumulates at magic numbers such as N = 50, resulting in peaks in the solar system abundance pattern. The neutron magic numbers at N = 50, 82, and 126 produce local maxima in the solar system abundance pattern that are attributed to the s process at A $\approx$ 88, $\approx$ 138, and $\approx$ 208, respectively (Fig. 1.2).

Unlike the s process, in the r process the timescale for neutron capture τ_n is much shorter than the timescale for β^- decay τ_β. That is, $\tau_n \ll \tau_\beta$. In other words, an unstable nuclide may capture many neutrons before undergoing β^- decay. In this sense, neutron capture is "rapid" compared to β^- decay, hence the name rapid neutron-capture process. Rapid neutron capture requires a relatively large neutron density, with typical values ranging from 10^{24} to 10^{28} neutrons/cm^3. A representative path for the r process is shown in Fig. 1.3. The path of the r process proceeds far from the valley of stability and involves many neutron-rich nuclides. Creating heavy, unstable nuclides with neutron capture during the r process occurs on the order of seconds. When there are no more neutrons to be captured, the unstable nuclides produced during the r process will undergo β^- decay back to the valley of stability. An example of a nuclide that can only be produced in the r process is ^{76}Ge (see Fig. 1.3).

As happens in the s process, the matter accumulates at neutron magic numbers during the r process. However, the reason for the accumulation in the two processes is different. In the environment in which the r process takes place, there are high-energy γ rays that can cause photodisintegration reactions. When a nuclide at N = 50 captures a neutron, a photodisintegration reaction has a very large probability to occur, bringing the nuclide back to the neutron magic number. This is because the photodisintegration cross section immediately after a neutron magic number is relatively large. As a result, the nuclides at neutron magic numbers act as "waiting points," in that the r process must wait for β^- decay in order to continue onto the next isotopic chain. At a given neutron magic number, the r process encounters a larger range of atomic numbers at smaller mass numbers compared to the s process (for example, see Fig. 1.3). This results in local maxima in the solar system abundance pattern that are broader and at smaller mass numbers compared to the s process. The neutron magic numbers at N = 50, 82, and 126 produce local maxima in the solar system abundance pattern that are attributed to the r process at A $\approx$ 80, $\approx$ 130, and $\approx$ 195, respectively (Fig. 1.2). Another structure that appears in the solar system abundance pattern that is attributed to the r process is the "rare-earth peak" at A $\approx$ 160 [45]. The formation of this structure is sensitive to physics at the late stages of the r process when nuclides undergo β^- decay back to the valley of stability.

Because the s process occurs close to the valley of stability, the relevant neutron capture cross sections can be experimentally measured. The nuclear physics for the s process is therefore generally well understood and theoretical models can successfully reproduce the s-process solar system abundance pattern. Given this success, the r-process contribution to the solar system abundance pattern is obtained by subtracting the s-process contribution from the solar system abundance pattern [46]. Due to this subtraction, the r-process solar

system abundance pattern is actually a "residual" abundance pattern.

1.4 r process

Of all the nucleosynthesis processes described in Sec. 1.3, this dissertation focuses on the r process. The r process is one of the nucleosynthesis processes described in the B^2FH paper [34]. In the six decades that have passed since this pioneering work was published, theoretical models are unable to reproduce the r-process solar system abundance pattern (bottom panel of Fig. 1.2). This inability is due to uncertainties in the astrophysical environment and the nuclear physics properties of nuclides relevant to the r process.

1.4.1 Astronomical Observations

Astronomical observations of old stars in certain parts of the Milky Way Galaxy provide important information about the r process. One way to classify stars is by their composition. Specifically, stars may be classified by their metal content (or "metallicity"). In this case, a metal is any element heavier than hydrogen and helium. The first stars formed approximately 100 million years after the Big Bang [47]. These stars formed out of the hydrogen and helium from the Big Bang, were massive, quickly underwent stellar evolution, and exploded as supernovae [48]. The lifetime for these hypothetical "Population III" stars was only a few million years. When these stars exploded as supernovae, they enriched the interstellar medium with metals. Forming out of the enriched interstellar medium were "Population II" stars. Compared to Population III stars, Population II stars are less massive and have longer lifetimes (greater than 10 billion years) [48]. Due to their long lifetimes, some of these stars can still be observed this current day. Finally, there are "Population I" stars,

such as the Sun, which formed out of the interstellar medium further enriched by multiple nucleosynthesis events from Population II stars. Population I stars therefore have a higher metal content than Population II stars. In general, metallicity correlates with the age of a star. The older the star, the lower the metallicity for that star. The younger the star, the higher the metallicity for that star. Furthermore, stars are found in different parts of the Milky Way Galaxy, which is organized into a flat disk, a spherical bulge at the center, and a surrounding spherical halo.

The halo of the Milky Way Galaxy contains Population II stars. These stars are called metal-poor halo stars [6, 48, 49, 47, 50]. They are metal-poor because they contain less than 1% of the Sun's iron abundance. A small subset of these metal-poor halo stars show an enrichment or enhancement in the abundances of neutron-capture elements ($Z > 30$) relative to non-neutron-capture elements ($Z < 30$). For example, approximately 3-5% show a strong enhancement of r-process elements (known as r-II stars) and approximately 14% show a mild enhancement of r-process elements (known as r-I stars) [51]. Figure 1.4 shows the elemental abundances for ten metal-poor halo stars (specifically, r-I and r-II stars) compared to the r-process solar system abundance pattern. For $56 \leq Z < 83$, the relative abundance patterns for these r-I and r-II stars agree with each other and contain the same relative abundances as the r-process solar system abundance pattern. That is, the r-process solar system abundance pattern can be scaled to match the abundance patterns for the r-I and r-II stars. More examples of this phenomenon for r-I stars may be found in Ref. [52]. This similarity is remarkable given that these stars have different formation histories. Recall that the Sun is relatively young and formed out of the interstellar medium that was enriched by many nucleosynthesis events. Meanwhile, the r-I and r-II stars are relatively old, scattered throughout the halo, and formed out of the interstellar medium that was enriched by only

one or two nucleosynthesis events. The similarity in the abundance patterns suggests that the r process is a "universal" process and produces a "universal" abundance pattern (for $56 \leq Z < 83$). In other words, regardless of when and where the r process occurs, the r process operates in a consistent manner and always produces the same elements in the same relative amounts (for $56 \leq Z < 83$).

While the relative elemental abundances for r-I and r-II stars agree with each other and the r-process solar system abundance pattern for $56 \leq Z < 83$, there is more scatter for the lighter neutron-capture elements ($Z < 49$). Possible explanations for this scatter include observational uncertainties, multiple sites or components for the r process [53, 54], or additional nucleosynthesis processes [55, 56]. Regarding the possibility of multiple sites or components for the r process, a "weak r process" would produce nuclides with $A \lesssim 130$ (corresponding to the lighter neutron-capture elements) and a "main r process" would produce nuclides with $A \gtrsim 130$ (corresponding to the heavier neutron-capture elements) [6]. This dissertation focuses on the mass region relevant to the weak r process.

The r-I and r-II stars provide other important information about the r process. One detail is that because r-I and r-II stars are relatively old, the r process was happening early in the history of the universe in order to enrich the interstellar medium out of which those stars formed. None of the enrichment in r-I and r-II stars could have been from the s process because not enough time had passed to reach the AGB phase necessary for s process nucleosynthesis. Another detail is that because only approximately 3-5% of metal-poor halo stars are r-II stars, the r process is a relatively rare process.

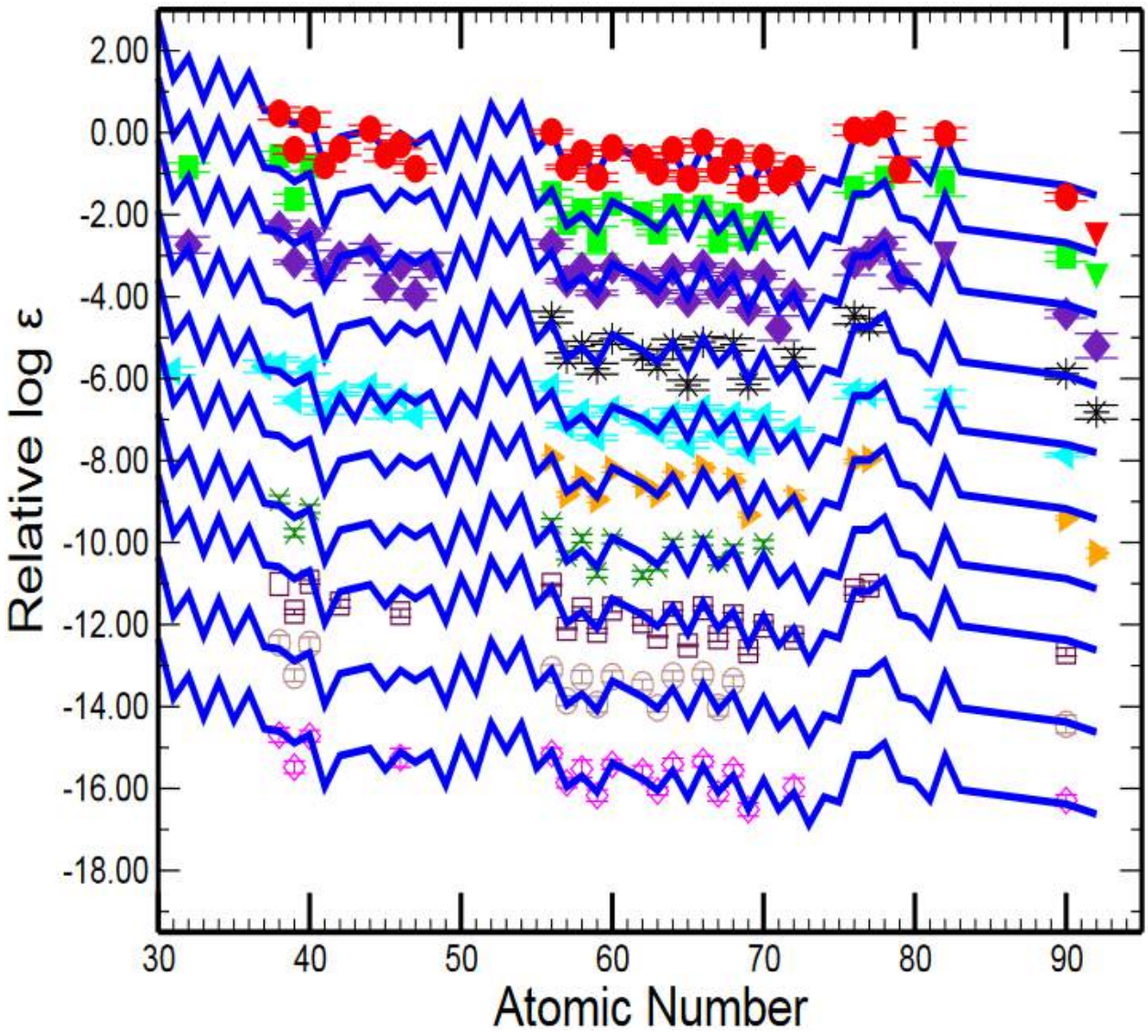

Figure 1.4: Elemental abundances in ten metal-poor halo stars (specifically, r-I and r-II stars). Markers of the same type and color correspond to the same r-I or r-II star. The solid blue lines are the r-process solar system abundance pattern. The only difference between the blue lines is a scaling factor. The scaling factor is obtained by normalizing the europium abundance in the r-process solar system abundance pattern to that in the r-I or r-II star. Europium is chosen due to being an r-process element. Figure adapted from Ref. [8].

1.4.2 Astrophysical Sites

The r process requires a neutron-rich environment. Of the many sites that have been proposed for the site of the r process, two sites have received the most attention. These two sites are core-collapse supernovae and the compact-object mergers [57].

1.4.2.1 Core-collapse Supernovae

A core-collapse supernova occurs when the iron core of a massive star undergoes gravitational collapse. The remnant from this event is a proto-neutron star, which cools by releasing a large amount of energy in the form of neutrinos. The neutrinos deposit energy on the surface of the proto-neutron star, which drives material off the surface of the proto-neutron star. This outflow of neutrinos and material from the surface of the proto-neutron star is called the neutrino-driven wind [58, 59]. The material driven from the surface is initially in the form of free nucleons. As the material expands and cools, some nucleons combine into α particles, which in turn combine to form seed nuclei for eventual neutron capture reactions. As the material further expands and cools, the seed nuclei rapidly capture neutrons from the large abundance of free neutrons, forming r-process nuclides.

The neutrino-driven wind from a core-collapse supernova initially was favored as the site of the r process. One reason for being favored concerns the observations of metal-poor halo stars described in Sec. 1.4.1. The massive Population III stars quickly underwent stellar evolution, and some would have become core-collapse supernovae. If the r process occurred in the neutrino-driven winds from these core-collapse supernovae, then the interstellar medium would have quickly been enriched with r-process elements. This would explain the abundances that are observed in r-I and r-II stars. However, recent simulations of neutrino-driven winds have had difficulty in producing the most neutron-rich nuclides associated with the r

process [60]. These simulations have shown that the conditions do not appear to be sufficiently neutron-rich to produce nuclides associated with the third peak at A $\approx$ 195 (see Fig. 1.2). Instead, these simulations only produce nuclides with A $\lesssim$ 130 (associated with the lighter neutron-capture elements). Therefore, the neutrino-driven winds from core-collapse supernovae could be a site for the weak r process mentioned in Sec. 1.4.1.

1.4.2.2 Compact-object Mergers

A compact object may be either a neutron star or a black hole. While the merging of a neutron star (NS) and black hole could be a potential site of the r process [61], this section will only consider the merging of two neutron stars (hereafter referred to as a NS-NS merger) [62]. Figure 1.5 shows a NS-NS merger. As the two neutron stars approach each other, they become deformed from gravity and neutron-rich material is ejected from the merging system. Gravitational waves are also generated. The ejected material is called dynamical ejecta [63]. One origin of dynamical ejecta is the tidal tails, as shown in Fig. 1.5. As the name implies, the tidal tails form as a result of tidal forces. Another origin of dynamical ejecta is the contact interface of the two neutron stars. In any case, the dynamical ejecta is flung out into space, and, similar to the case described for core-collapse supernovae in Sec. 1.4.2.1, the ejecta expands and cools, and seed nuclei are formed which can then rapidly capture neutrons [64].

The dynamical ejecta is very neutron-rich. Therefore, simulations of the r process in NS-NS mergers can easily produce nuclides associated with the third peak at A $\approx$ 195 (see Fig. 1.2). In addition, simulations show even heavier nuclides are produced. These heavier nuclides are susceptible to fission (spontaneous fission, neutron-induced fission, and β-delayed fission). When these nuclides fission, the resulting fragments can themselves capture neutrons

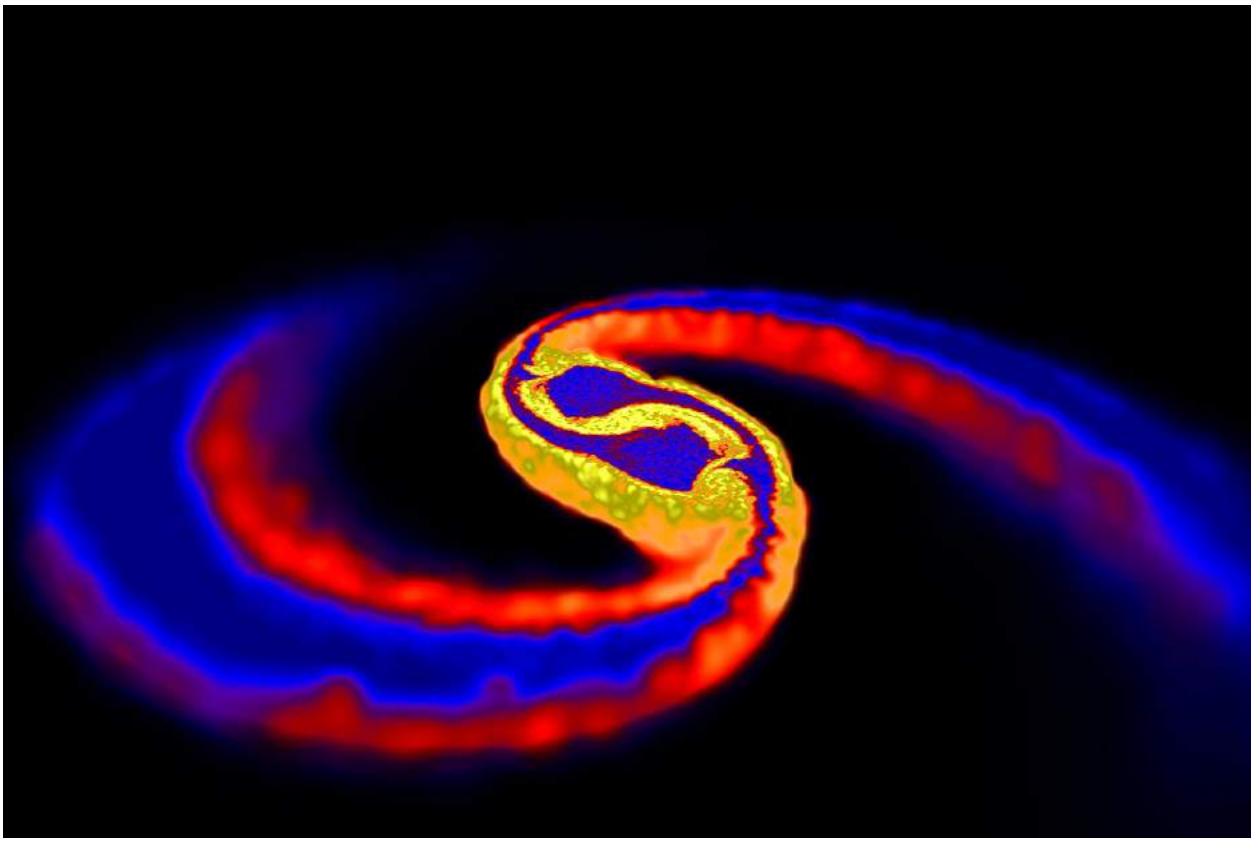

Figure 1.5: Snapshot of a simulation of a NS-NS merger. The color indicates the magnitude of the magnetic field (the lighter the color, the larger the magnitude of the magnetic field). The two neutron stars are in the center, surrounded by dynamical ejecta in the tidal tails. Figure adapted from Refs. [9, 10].

and eventually become susceptible to fission. This repeating cycle of fission and neutron capture is called "fission recycling" or "fission cycling." Simulations show that if fission cycling occurs, the r-process abundance pattern is "robust." That is, the abundance pattern is insensitive to variations in properties of the merging system [65].

Initially, NS-NS mergers were not favored as the dominant site of the r process [66]. This was due to the presumably long time (approximately 100-1000 million years [66, 67]) to merge (or coalesce). Within this amount of time, the interstellar medium would not have been enriched with r-process elements to explain the abundances that are observed in r-I and r-II stars. However, recent studies have shown that even with long times to merge, NS-NS mergers can explain these observed abundances [68, 69]. Furthermore, a recent discovery made while studying ultra-faint dwarf galaxies provides evidence [70], and a recent discovery of a kilonova confirms [71] that NS-NS mergers are a site of the r process. These two recent discoveries are discussed below.

The first recent discovery concerns ancient and ultra-faint dwarf galaxies, which orbit the Milky Way Galaxy. Reticulum II [70] is an ancient and ultra-faint dwarf galaxy, and the tenth such galaxy for which elemental abundances were obtained. While all the stars in the other nine galaxies do not show any enrichment in neutron-capture elements, seven of the nine stars in Reticulum II are r-II stars. These seven stars have abundances that follow the universal r-process abundance pattern [70]. These observations suggest that a rare and prolific r-process event was responsible for the enrichment observed in Reticulum II. The event was rare in that only one of ten of these galaxies have any form of enrichment. The event was prolific in that a large yield of r-process elements was produced in order for seven of the nine stars to be r-II stars. The rate and yield for this r-process event are incompatible with core-collapse supernovae as the site of the r process, but compatible with a NS-NS

merger [70]. Compared to NS-NS mergers, core-collapse supernovae are more frequent and produce smaller amounts of r-process elements. Therefore, if core-collapse supernovae were the dominant site of the r process, one would expect the amount of r-process enrichment to be the same in all ten ultra-faint dwarf galaxies.

The second recent discovery concerns the observation of a kilonova. The r process produces many unstable neutron-rich nuclides far from the valley of stability, which will eventually undergo β^- decay back to the valley of stability. As the nuclides undergo β^- decay, energy will be released in different forms of radiation, such as electrons and γ rays. This radiation will deposit energy in the surrounding material, which will affect the black-body radiation from the surrounding material. The black-body radiation that is powered by the radioactive decay of nuclides created in the r process is called a kilonova [72]. A kilonova is therefore the electromagnetic counterpart to the emission of gravitational waves from the merging of two neutron stars. Recently, a kilonova was observed by various observatories [71] in coincidence with the detection of gravitational waves from the merging of two neutron stars [73]. The gravitational waves were detected by the LIGO-Virgo detector network. This event confirmed that NS-NS mergers are a site of the r process.

One observable from a kilonova is the light curve. The light curve displays the luminosity of the kilonova as a function of time. Any observed light curve will be affected by the possible presence of lanthanides ($57 \leq \mathrm{Z} \leq 71$) and actinides ($89 \leq \mathrm{Z} \leq 103$) [74]. This is because lanthanides and actinides have a complex atomic structure, which creates a large number of absorption lines. The large number of absorption lines increases the opacity of the material, which increases the time for photons to diffuse out of the material and be observed. If the material contains lanthanides and actinides, the observed light curve will be relatively dim and peak at red wavelengths on the timescale of weeks. If the material does not contain

lanthanides and actinides, the observed light curve will be relatively bright and peak at blue wavelengths on the timescale of days. In the recent kilonova observation, both components were observed in the light curve [75]. The blue component was associated with dynamical ejecta from the collision interface, which is hot and less neutron-rich. The red component was associated with dynamical ejecta from the tidal tails, which is cold and very neutron-rich. The red component was also associated with a wind from an accretion disk that formed around the remnant from the merger.

1.4.3 Nuclear Physics

Understanding whether NS-NS mergers are the only site, the dominant site, or one of multiple sites of the r process will require reducing the uncertainty in the nuclear physics. In this case, nuclear physics refers to all the nuclear physics properties of nuclides that participate in the r process. The nuclear physics properties include masses, fission properties, neutron capture cross sections, and β-decay properties. One way of assessing the uncertainty in the nuclear physics is with a reaction network calculation.

Figure 1.6 shows the result of a reaction network calculation for the r process. The reaction network is called PRISM (Portable Routines for Integrated nucleoSynthesis Modeling) [11, 12]. The input to a reaction network is the astrophysical environment and the nuclear physics. The astrophysical environment determines important quantities such as the temperature and density as a function of time, which in turn affect the rate at which different nuclear processes occur during the r process. The astrophysical environment used in the reaction network calculation that produced Fig. 1.6 is a NS-NS merger. The nuclear physics also determines the rate at which different nuclear processes occur during the r process. At each time step in the reaction network calculation, the relative abundances of all the nuclides

are calculated, from which a relative abundance pattern can be created. The relative abundance pattern is then normalized and compared to the r-process solar system abundance pattern. If the astrophysical environment and nuclear physics are correct, the abundance pattern from the reaction network calculation should agree with the r-process solar system abundance pattern.

Unlike the illustration in Fig. 1.3, Fig. 1.6 shows the full path of the r process. Each quadrant in Fig. 1.6 corresponds to a different time step during the reaction network calculation. Each quadrant contains a top panel and bottom panel. The top panel compares the reaction network calculation abundance pattern with the r-process solar system abundance pattern. The bottom panel shows how the r process proceeds in the chart of the nuclides by showing the relative abundance of each nuclide. Each time step in Fig. 1.6 emphasizes the main stages of the r process that were described Sec. 1.3.1. In the upper left quadrant of Fig. 1.6, seed nuclei are exposed to an extreme flux of neutrons. In the upper right quadrant of Fig. 1.6, nuclei rapidly capture many neutrons before undergoing β^- decay, and therefore move far from the valley of stability. This quadrant shows the accumulation of abundance at the neutron magic numbers, as discussed in Sec. 1.3.1. Because the astrophysical environment used in this reaction network calculation is very neutron-rich, the path of the r process reaches the neutron drip line. The lower left quadrant of Fig. 1.6 shows that once the neutron flux ends, all the nuclei produced during the r process will undergo β^- decay back to the valley of stability. Note that the neutron flux is exhausted in less than one second (the time is labeled in each quadrant), as discussed in Sec. 1.3.1. During this stage, energy is released during β^- decay in different forms of radiation. This radiation powers the kilonova described in Sec. 1.4.2.2. Finally, the lower right quadrant of Fig. 1.6 shows that the nuclei will continue to undergo β^- decay until reaching a stable or relatively long-

lived nuclide. Overall, as time progresses, the temperature and density (which are labeled in each quadrant) decrease because the material is expanding and cooling as described in Sec. 1.4.2.2.

The last time step in the reaction network calculation is the lower right quadrant of Fig. 1.6. In the last time step, there are discrepancies between the abundance pattern from the reaction network calculation and the r-process solar system abundance pattern. A significant factor in the discrepancies is the uncertainty in the nuclear physics properties of nuclides that participate in the r process.

Different nuclear processes that can occur during the r process are shown in Fig. 1.7 in terms of the abundance weighted timescale [12]. The abundance weighted timescale is defined as

$$\tau_j = \left(\frac{\sum_i Y_i}{\sum_i Y_i \lambda_{ij}} \right), \tag{1.1}$$

where τ is the timescale, λ is the rate, Y is the abundance, i runs over all nuclides, and j is a specific reaction or decay channel. Inspecting the abundance weighted timescale as a function of time reveals which reaction and decay channels are most important at any given time during the r process. The smaller the abundance weighted timescale, the more important that particular process is at that specific time during the r process. For example, at the beginning of the r process, neutron-induced reactions are the dominating processes and therefore have the lowest abundance weighted timescales. Meanwhile, at the end of the r process, β^- decay is the dominant process and therefore has the lowest abundance weighted timescale.

Figures 1.6 and 1.7 illustrate the complexity of modeling the r process and trying to reproduce the abundance pattern observed in the solar system. Figure 1.6 shows the r

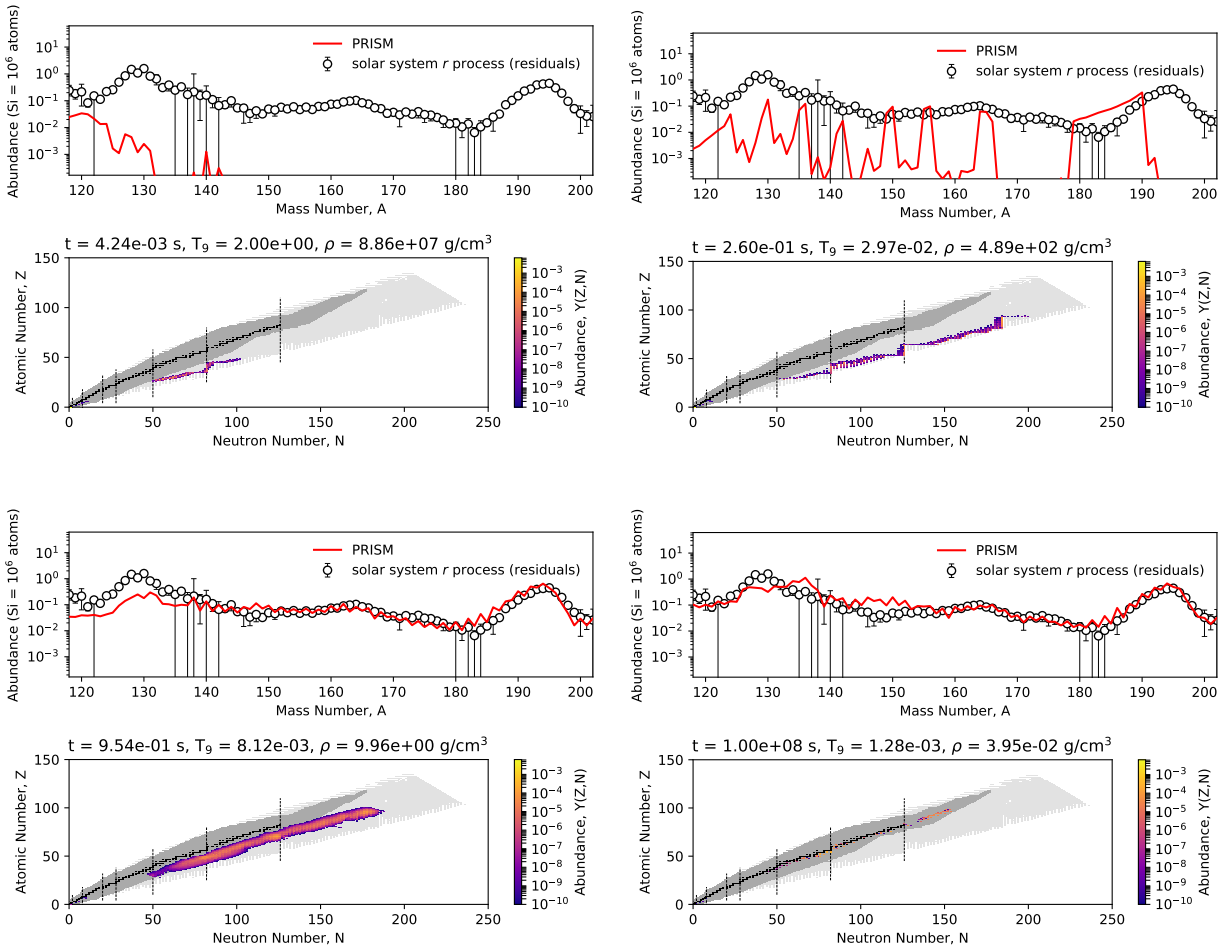

Figure 1.6: Abundance pattern and path of the r process at different times for a NS-NS merger. Each quadrant corresponds to a different time step in a reaction network calculation. The reaction network is called PRISM [11, 12]. Each quadrant contains a top panel and bottom panel. The top panels show the absolute abundance pattern of the r process for the solar system and from the reaction network calculation. The abundances are expressed in the cosmochemical scale, which normalizes silicon to 10^6 atoms. The bottom panels show the chart of the nuclides, with stable nuclides in black, unstable nuclides that are experimentally known to exist in dark gray, and unstable nuclides that are predicted to exist according to the FRDM (2012) [3] mass model in light gray. The neutron magic numbers (N = 2, 8, 20, 28, 50, 82, 126) are indicated with a black, dashed line. The relative abundances of nuclides produced from the PRISM calculation are shown with shaded cells. Each quadrant has a label for time in units of seconds (t), temperature in units of 10^9 K (T_9), and density in units of g/cm^3 (ρ).

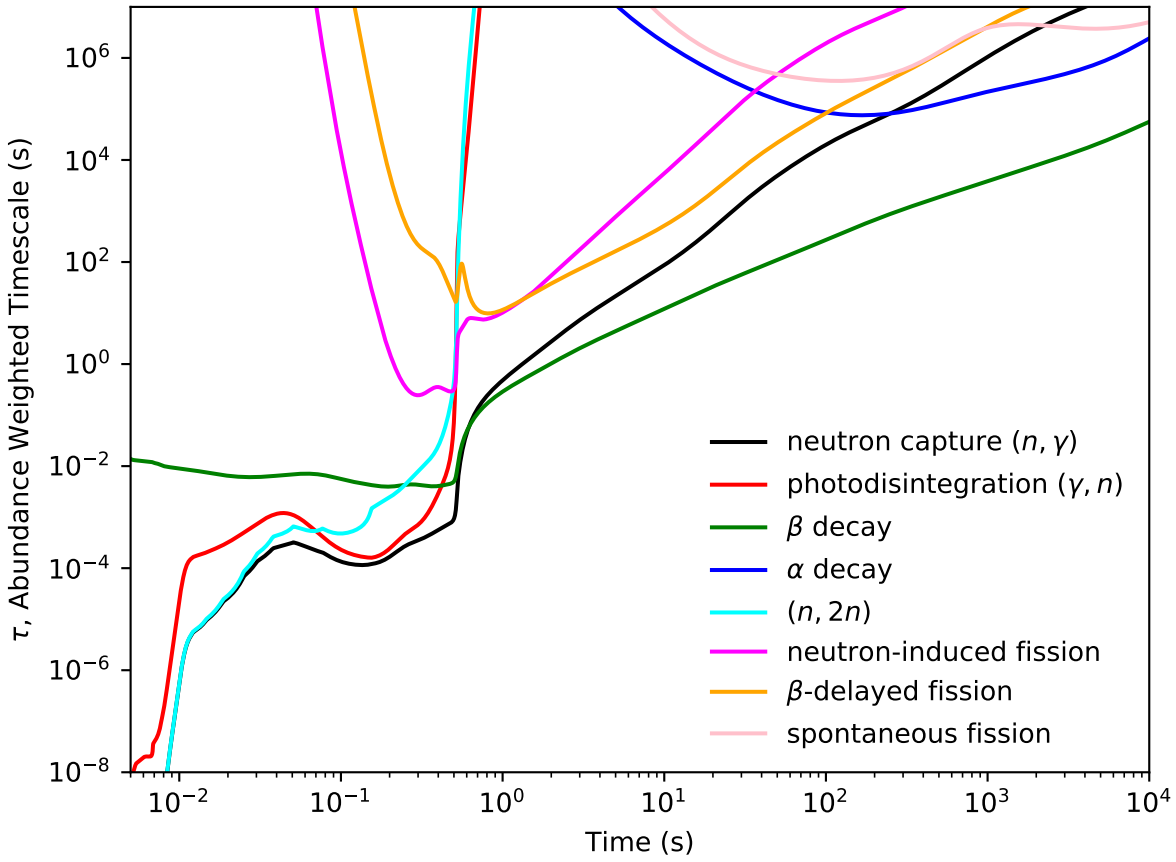

Figure 1.7: Abundance weighted timescales for important nuclear processes during the r process for a NS-NS merger.

process involves thousands of nuclides, many of which are far from the valley of stability and have not been experimentally studied. Figure 1.7 shows the reaction and decay channels that must be known for each nuclide. Experimentalists will never be able to measure all the relevant nuclear physics properties of all nuclides that participate in the r process. This situation creates a reliance on theoretical models to accurately calculate the nuclear physics properties where experimental data are nonexistent and experiments are currently unfeasible. Of all the important nuclear physics properties that play an important role in the r process, this dissertation focuses on experimental measurements related to β^- decay. These experimental measurements will constrain theoretical models and provide more confidence in their extrapolation far from the valley of stability.

1.5 β decay

1.5.1 β-decay Classification

β decay is governed by the weak interaction and refers to three processes:

$$\text{electron capture:}\ {}^{\mathrm{A}}_{\mathrm{Z}}\mathrm{X}_{\mathrm{N}} + e^- \rightarrow {}^{\mathrm{A}}_{\mathrm{Z-1}}\mathrm{Y}_{\mathrm{N+1}} + \nu_e \tag{1.2}$$

$$\beta^+ \text{ decay:}\ {}^{\mathrm{A}}_{\mathrm{Z}}\mathrm{X}_{\mathrm{N}} \rightarrow {}^{\mathrm{A}}_{\mathrm{Z-1}}\mathrm{Y}_{\mathrm{N+1}} + e^+ + \nu_e \tag{1.3}$$

$$\beta^- \text{ decay:}\ {}^{\mathrm{A}}_{\mathrm{Z}}\mathrm{X}_{\mathrm{N}} \rightarrow {}^{\mathrm{A}}_{\mathrm{Z+1}}\mathrm{Y}_{\mathrm{N-1}} + e^- + \bar{\nu}_e \tag{1.4}$$

where ${}^{\mathrm{A}}_{\mathrm{Z}}\mathrm{X}_{\mathrm{N}}$ is the notation for a nuclide described in Sec. 1.1, e^- is an electron, e^+ is a positron, ν_e is an electron neutrino, and $\bar{\nu}_e$ is an electron antineutrino. In β decay, a neutron is converted to a proton, or vice versa. All three processes conserve the number of nucleons (A remains constant), so β decay connects isobars. Conventionally, the original nuclide

$\left({}^{\mathrm{A}}_{\mathrm{Z}}\mathrm{X}_{\mathrm{N}}\right)$ is called the parent or mother, and the final nuclide $\left({}_{\mathrm{Z}-1}{}^{\mathrm{A}}\mathrm{Y}_{\mathrm{N}+1}\text{ or }{}_{\mathrm{Z}+1}{}^{\mathrm{A}}\mathrm{Y}_{\mathrm{N}-1}\right)$ is called the daughter.

For a given nuclide, there are multiple levels with different amounts of energy (one ground state and multiple excited states). Therefore, β decay can connect different levels in the parent with different levels in the daughter. These different connections are called β-decay transitions. For a given β-decay transition, energy is released and shared between the final products (the daughter and leptons) as kinetic energy. The amount of energy released is

$$\text{electron capture:}\quad Q + E_{x,p} - E_{x,d} = \left[m\left({}^{A}_{Z}X_N\right) - m\left({}_{Z-1}{}^{A}Y_{N+1}\right)\right]c^2 + E_{x,p} - E_{x,d} \tag{1.5}$$

$$\beta^+\text{ decay:}\quad Q + E_{x,p} - E_{x,d} = \left[m\left({}^{A}_{Z}X_N\right) - m\left({}_{Z-1}{}^{A}Y_{N+1}\right) - 2m_e\right]c^2 + E_{x,p} - E_{x,d} \tag{1.6}$$

$$\beta^-\text{ decay:}\quad Q + E_{x,p} - E_{x,d} = \left[m\left({}^{A}_{Z}X_N\right) - m\left({}_{Z+1}{}^{A}Y_{N-1}\right)\right]c^2 + E_{x,p} - E_{x,d} \tag{1.7}$$

where Q is the ground-state-to-ground-state Q value, $E_{x,p}$ is the energy of the level in the parent, $E_{x,d}$ is the energy of the level that is populated in the daughter, $m\left({}^{A}_{Z}X_N\right)$ is the atomic mass of a nuclide, m_e is the mass of the electron, and c is the speed of light. A β-decay transition can only occur if $Q + E_{x,p} - E_{x,d}$ is positive.

Electron capture occurs for neutron-deficient nuclei. In electron capture, a proton captures an electron from an atomic orbital. The proton is converted into a neutron and a monoenergetic neutrino is emitted. The electron that is captured is usually from one of the inner electronic shells. The vacancy from the captured electron is filled by an electron from an outer shell, resulting in the emission of X rays or Auger electrons.

β^+ decay also occurs for neutron-deficient nuclei. In β^+ decay, a proton is converted into a neutron, and a positron and neutrino are emitted. The three-body final state (daughter, positron, neutrino) of β^+ decay leads to a continuous distribution of positron (and neutrino)

kinetic energy that extends from zero up to $Q + E_{x,p} - E_{x,d}$. The kinetic energy of the recoiling daughter nucleus is negligible. Note that Eq. 1.6 implies that β^+ decay is only possible if $\left[m\left({}^{A}_{Z}X_N\right) - m\left({}^{A}_{Z-1}Y_{N+1}\right)\right]c^2 > 2m_e c^2$.

β^- decay occurs for neutron-rich nuclei and is therefore relevant to the r process and this dissertation. In β^- decay, a neutron is converted into a proton, and an electron and antineutrino are emitted. The three-body final state (daughter, electron, antineutrino) of β^- decay leads to a continuous distribution of electron (and antineutrino) kinetic energy that extends from zero up to $Q + E_{x,p} - E_{x,d}$. The kinetic energy of the recoiling daughter nucleus is negligible. This dissertation involves the study of only neutron-rich nuclei, and therefore any future reference to β decay will mean β^- decay.

The total angular momentum must be conserved in a β-decay transition

$$\vec{J}_p = \vec{J}_d + \vec{L}_\beta + \vec{S}_\beta \tag{1.8}$$

where $\vec{J}_p$ is the total angular momentum of the parent, $\vec{J}_d$ is the total angular momentum of the daughter, $\vec{L}_\beta$ is the orbital angular momentum of the leptons, and $\vec{S}_\beta$ is the intrinsic spin angular momentum of the leptons. The electron and antineutrino both have an intrinsic spin angular momentum of 1/2. For a given β-decay transition, this leads to two possible values for S_β. If the intrinsic spin angular momenta of the electron and antineutrino are antiparallel, then those spins couple to create $S_\beta = 0$. If this occurs, the transition is a Fermi transition. If the intrinsic spin angular momenta of the electron and antineutrino are parallel, then those spins couple to create $S_\beta = 1$. If this occurs, the transition is a Gamow-Teller transition. A β-decay transition is classified by the amount of orbital angular momentum carried off by the leptons. If $L_\beta = 0$, the transition is classified as an allowed

Table 1.1: Classifications of β-decay transitions. Adapted from Ref. [1].

Transition Type	L_β	$\Delta\pi$	ΔJ
Superallowed	0	No	0
Allowed	0	No	0, 1
First forbidden	1	Yes	0, 1, 2
Second forbidden	2	No	1, 2, 3
Third forbidden	3	Yes	2, 3, 4

transition. These transitions are most probable. Other transitions exist such as forbidden transitions. The word "forbidden" is a misnomer because these transitions do occur, but with a smaller probability compared to allowed transitions. The degree of being forbidden increases as L_β increases. Whether or not there is a change in parity between the initial level in the parent and the final level in the daughter is determined with $\Delta\pi = (-1)^{L_\beta}$. The selection rules for β-decay transitions are summarized in Table 1.1.

1.5.2 β-delayed γ-ray Emission

A β-decay transition may populate an excited state in the daughter nucleus. Emission of a γ ray may occur when the excited state decays to a lower-energy state. This is an example of β-delayed γ-ray emission.

γ-ray transitions connect an initial state to a final state in the same nucleus (in this case, the daughter). There may be multiple γ-ray transitions as the excited state decays to the ground state. With each γ-ray transition, the γ ray carries off an integer unit of angular momentum λ that can range from

$$|(J_i - J_f)| \leq \lambda \leq |(J_i + J_f)| \tag{1.9}$$

where J_i is the total angular momentum of the initial state, J_f is the total angular momentum

Table 1.2: Classifications of γ-ray transitions. Adapted from Ref. [1].

Name	Radiation Type	λ	$\Delta\pi$
Electric dipole	E1	1	Yes
Magnetic dipole	M1	1	No
Electric quadrupole	E2	2	No
Magnetic quadrupole	M2	2	Yes
Electric octupole	E3	3	Yes
Magnetic octupole	M3	3	No
Electric hexadecapole	E4	4	No
Magnetic hexadecapole	M4	4	Yes

of the final state, and λ is called the multipolarity. For a given γ-ray transition there can be a range of values for the multipolarity, but typically the lowest multipolarity is most probable. For a given multipolarity, whether or not there is a change in parity between the initial and final states determines the type (electric or magnetic) of the transition. The selection rules for γ-ray transitions are summarized in Table 1.2.

1.5.3 Internal Conversion

Internal conversion is a process that may also occur when an excited state decays to a lower-energy state in the same nucleus (in this case the daughter). During this process, the excited nucleus interacts electromagnetically with an electron from an atomic orbital, which causes the electron to be emitted. The vacancy from the emitted electron is filled by an electron from an outer shell, resulting in the emission of X rays or Auger electrons. The energy of the emitted electron is

$$E_{IC} = (E_i - E_f) - E_{BE} \tag{1.10}$$

where E_{IC} is the energy of the emitted electron (the internal conversion electron), E_i is the energy of the initial state, E_f is the energy of the final state, and E_{BE} is the binding energy of the internal conversion electron. Unlike β-decay electrons, which have a continuous

distribution of kinetic energies, conversion electrons are monoenergetic. Internal conversion is characterized by an internal conversion coefficient

$$\alpha = \frac{T_{IC}}{T_\gamma} \tag{1.11}$$

where α is the internal conversion coefficient, T_{IC} is the emission rate of the conversion electron, and T_γ is the emission rate of the γ ray. The internal conversion electron may be ejected from different atomic shells (for example, the K, L, or M shells), and the total internal conversion coefficient is defined as

$$\alpha_{\text{total}} = \alpha_{\text{K}} + \alpha_{\text{L}} + \alpha_{\text{M}} + ... \tag{1.12}$$

Internal conversion coefficients may be calculated using the BrIcc program [13, 14] provided by the National Nuclear Data Center. Approximate values for the internal conversion coefficients may be calculated with

$$\alpha(E\lambda) = \frac{Z^3}{n^3}\left(\frac{\lambda}{\lambda+1}\right)\left(\frac{e^2}{4\pi\epsilon_0\hbar c}\right)^4\left(\frac{2m_e c^2}{E}\right)^{\lambda+5/2} \tag{1.13}$$

$$\alpha(M\lambda) = \frac{Z^3}{n^3}\left(\frac{e^2}{4\pi\epsilon_0\hbar c}\right)^4\left(\frac{2m_e c^2}{E}\right)^{\lambda+3/2} \tag{1.14}$$

where Z is the atomic number of the nucleus, n is the principal quantum number of the electron that is ejected, λ is the multipolarity of the transition, e is the charge of the electron, ϵ_0 is the permittivity of free space, $\hbar$ is the reduced Planck constant, c is the speed of light, m_e is the mass of the electron, and E is the transition energy [1]. Equation 1.13 is used when

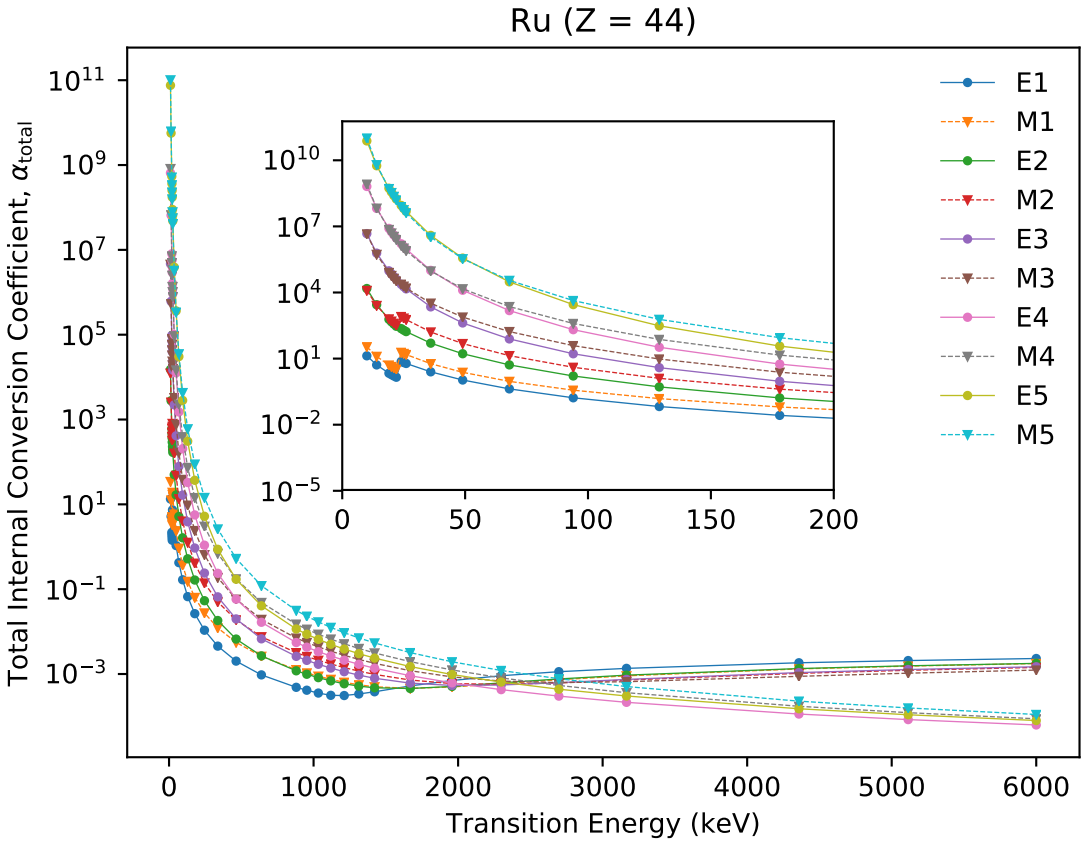

Figure 1.8: Total internal conversion coefficients for ruthenium (Z = 44) for a range of transition energies and multipolarities. The total internal conversion coefficients were obtained with the BrIcc program [13, 14] provided by the National Nuclear Data Center. The inset shows a zoomed-in view of the low transition energy region.

the transition type is electric, while Eq. 1.14 is used when the transition type is magnetic. Inspecting Eqs. 1.13 and 1.14 shows that internal conversion will be significant for heavier (large Z) nuclei, lower-energy transitions, and higher-multipolarity transitions. The latter two features can be seen in Fig. 1.8, which shows the total internal conversion coefficients for ruthenium (Z = 44) for a range of transition energies and multipolarities. For a given type and multipolarity, as the transition energy decreases, the total internal conversion coefficient increases. For a given type and transition energy, as the multipolarity increases, the total internal conversion coefficient increases.

1.5.4 β-delayed Neutron Emission

β-delayed neutron emission occurs when a neutron-rich parent nucleus undergoes β decay and populates a neutron-unbound excited state in the daughter nucleus. This is energetically possible whenever the ground-state-to-ground-state Q value for the β decay is greater than the one-neutron separation energy in the daughter. The daughter may then emit a neutron and populate a level in the one-neutron daughter ${}^{\mathrm{A-1}}_{\mathrm{Z}}\mathrm{Y}_{\mathrm{N-1}}$. This process is written as

$$ {}^{\mathrm{A}}_{\mathrm{Z}}\mathrm{X}_{\mathrm{N}} \rightarrow {}^{\mathrm{A-1}}_{\mathrm{Z}}\mathrm{Y}_{\mathrm{N-1}} + \mathrm{n} \tag{1.15} $$

The two-body final state leads to a monoenergetic neutron, but note that different levels populated in the one-neutron daughter will lead to different monoenergetic neutrons. Any excited level populated in the one-neutron daughter will decay by emitting radiation.

1.5.5 β-decay Scheme

Important information regarding the β decay of a nuclide is collected in a "decay scheme." A decay scheme displays information about the β-decaying state in the parent and the states populated in the daughter from β decay. An example of a decay scheme is shown in the left panels of Fig. 1.9. This decay scheme will illustrate some of the topics that have already been mentioned regarding β decay. This decay scheme shows the β decay of a parent with Z protons and A nucleons to a daughter with Z+1 protons and A nucleons. In this example, only the ground state of the parent undergoes β decay (and not an excited state, such as a β-decaying isomeric state). The ground state of the parent has an energy (E_x), spin (J), and parity (π). The subscript "p" in $(E_x, J^\pi)_\mathrm{p}$ refers to the parent. For the ground state, E_x is zero. The ground-state-to-ground-state Q value is shown with the red arrows. The

left panels differ in that each one shows a different β-decay transition from the parent to the daughter. These different transitions are labeled with the blue arrows. The different states in the daughter have subscripts i, j, k, l, and m. Each β-decay transition has a β-decay feeding intensity I_β. This is the probability of populating the state in the daughter during the β decay. As a probability distribution, the β-decay feeding intensity distribution is normalized to unity (1.0 or 100%).

The bottom left panel in Fig. 1.9 is an example of a ground-state-to-ground-state transition. All other panels on the left side show a β-decay transition that populates an excited state in the daughter. Any excited state will deexcite by emitting γ rays or internal conversion electrons. Decay schemes also show information about the deexcitation of excited states (such as branching ratios for γ-ray transitions between states), but that information is not shown in Fig. 1.9. The energy released in a given β-decay transition that is shared between the final products (daughter, electron, and antineutrino) as kinetic energy is shown with the green arrows. The green arrows represent the quantity $Q - E_x$ where Q is the ground-state-to-ground-state Q value (red arrows) and E_x is the energy of the populated state in the daughter. In other words, the green arrows represent the quantity given by Eq. 1.7 (where, as mentioned earlier, the initial energy of the parent is assumed to be zero). As already mentioned regarding Eq. 1.7, for a given β-decay transition the kinetic energy shared between the final products is

$$Q - E_x = \left[m\left({}^{A}_{Z}X_N\right) - m\left({}^{A}_{Z+1}Y_{N-1}\right) \right] c^2 = K_e + K_{\bar{\nu}_e} + K_d \tag{1.16}$$

$$\approx K_e + K_{\bar{\nu}_e} \tag{1.17}$$

where Q is the ground-state-to-ground-state Q value (red arrows), m is the atomic mass, c

is the speed of light, K_e is the kinetic energy of the electron, $K_{\bar{\nu}_e}$ is the kinetic energy of the antineutrino, and K_d is the kinetic energy of the daughter nucleus. Equation 1.16 ignores the mass of the antineutrino and the difference in electron binding energies of the parent and daughter, while Eq. 1.17 ignores the kinetic energy of the daughter nucleus K_d (the daughter nucleus is massive compared to the electron and antineutrino and therefore has a negligible kinetic energy). The quantity $Q - E_x$ (green arrows) is the maximum kinetic energy available to the electron or antineutrino.

As already mentioned, the three-body final state of β decay leads to a continuous distribution of electron (and antineutrino) kinetic energies. The continuous distribution of electron kinetic energies is obtained from Fermi's theory of β decay (for example, see Sec. 8.3 of Ref. [1]). For a given β-decay transition on the left panels of Fig. 1.9, the right panels show the continuous distribution of electron kinetic energies. The distribution of electron kinetic energies is given by

$$\frac{dN}{dK_e} = C\left(K_e^2 + 2K_e m_e c^2\right)^{\frac{1}{2}} \left((Q - E_x) - K_e\right)^2 \left(K_e + m_e c^2\right), \tag{1.18}$$

where $\frac{dN}{dK_e}$ is the number of electrons per kinetic energy, and C is a constant. The distribution of electron kinetic energies is shown with the black solid lines in the right panels of Fig. 1.9. As already mentioned, the distribution is continuous and extends from 0 to $Q - E_x$ (green arrows). These distributions are commonly called phase space distributions. Equation 1.18 neglects many effects in β decay, one being the Coulomb attraction of the positively charged daughter nucleus and negatively charged electron. This effect is accounted for with a Fermi function. Different expressions exist in the literature for the Fermi function (for example, Refs. [76, 77]) with all of them yielding approximately the same result (red, cyan, and blue

dotted lines in the right panels of Fig. 1.9). Multiplying the Fermi function and the phase space distribution yields the "corrected" electron kinetic energy distribution (red, cyan, and blue solid lines in the right panels of Fig. 1.9). In terms of physics, the Fermi function distorts the phase space distribution by shifting the electron kinetic energy distribution to smaller values. Each distribution has an average electron kinetic energy $\langle E \rangle$ (orange arrow in the right panels of Fig. 1.9). As an aside, these averages and the antineutrino kinetic energy spectra (not shown in the right panels of Fig. 1.9) are needed to calculate the decay heat [78, 79, 80, 81, 82, 83] and total antineutrino energy spectrum [84, 85, 86, 80, 81, 82, 83] from nuclear reactors.

As already mentioned, β^- decay is the decay mode that is relevant to this dissertation. However, for completeness, a decay scheme for β^+ decay is shown in the left panels of Fig. 1.10. For a given β-decay transition in the left panels of Fig. 1.10, the right panels show the continuous distribution of positron kinetic energies. The quantities labeled in Fig. 1.10 have already been defined in the explanation of Fig. 1.9. The energy released in a given β-decay transition that is shared between the final products (daughter, positron, and neutrino) as kinetic energy is $Q - E_x - 2m_e c^2$. The quantity $Q - E_x - 2m_e c^2$ is the maximum kinetic energy available to the positron or neutrino. The average of each distribution in the right panels refers to the average positron kinetic energy. In β^+ decay, the Fermi function takes into account the Coulomb repulsion of the positively charged daughter nucleus and positively charged positron. In terms of physics, the Fermi function distorts the phase space distribution by shifting the positron kinetic energy distribution to larger values.

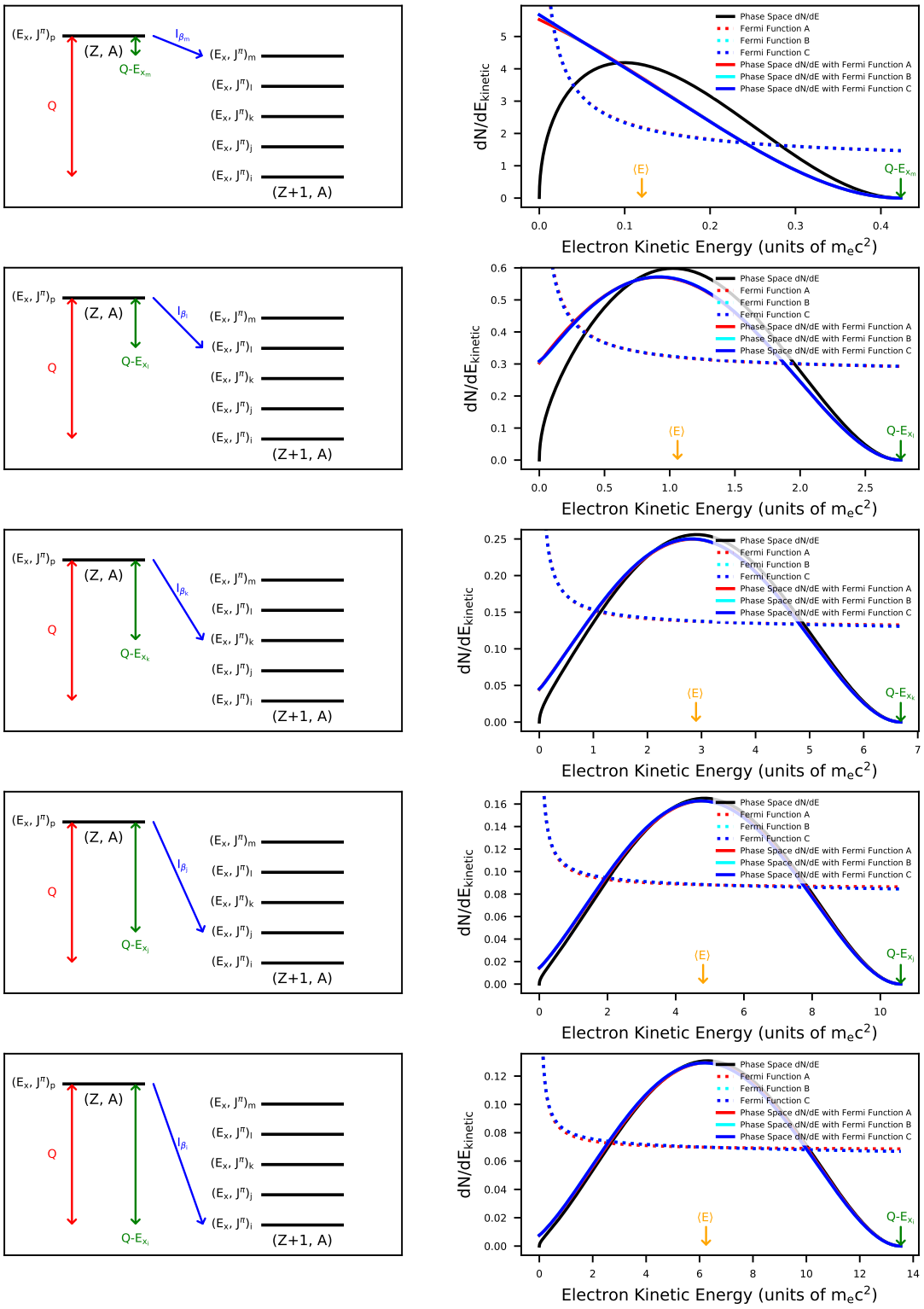

Figure 1.9: A simplified decay scheme for β^- decay, with different transitions, Fermi functions, and electron kinetic energy distributions. See main text for details. All functions and distributions are normalized to unity. In the right panels, the red, cyan, and blue lines (both dotted and solid) are on top of each other.

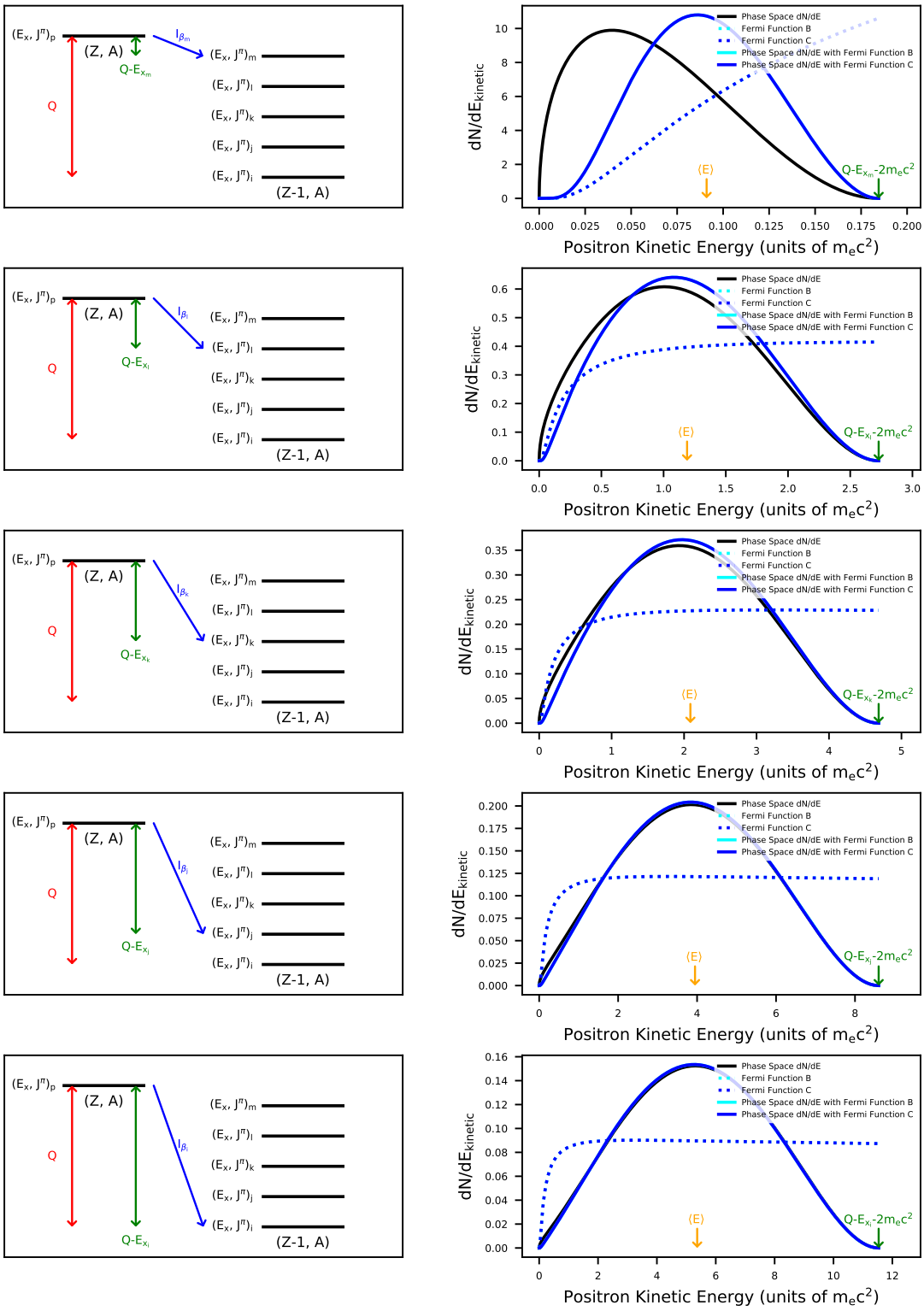

Figure 1.10: A simplified decay scheme for β^+ decay, with different transitions, Fermi functions, and positron kinetic energy distributions. See main text for details. All functions and distributions are normalized to unity. In the right panels, the cyan and blue lines (both dotted and solid) are on top of each other.

1.5.6 Half-life

A fundamental property of a β-decaying nuclide is the β-decay half-life. This is the time required for half of the nuclei in a sample to undergo β decay. The number of β-decaying nuclei at any time is given by

$$N(t) = N_0 e^{-\frac{\ln(2)}{T_{1/2}}t} = N_0 e^{-\lambda t} \tag{1.19}$$

where $N(t)$ is the number of β-decaying nuclei at time t, N_0 is the number of nuclei at time $t = 0$, $T_{1/2}$ is the β-decay half-life, and λ is the decay constant ($\lambda = \ln(2)/T_{1/2}$). If an unstable parent nucleus decays to an unstable daughter nucleus, the number of daughter nuclei at any time is given by

$$N_2(t) = N_{2,t=0} e^{-\lambda_2 t} + \frac{\lambda_1}{\lambda_2 - \lambda_1} N_{1,t=0} \left(e^{-\lambda_1 t} - e^{-\lambda_2 t} \right) \tag{1.20}$$

where $N_2(t)$ is the number of daughter nuclei at time t, $N_{1,t=0}$ is the number of parent nuclei at time $t = 0$, $N_{2,t=0}$ is the number of daughter nuclei at time $t = 0$, λ_1 is the decay constant of the parent, and λ_2 is the decay constant of the daughter.

The β-decay half-life is an important nuclear physics property that is needed for r process reaction network calculations (Sec. 1.4.3). In the r process, half-lives determine the timescale for producing the heaviest nuclides. This will in turn affect the abundance pattern from the reaction network calculation.

As mentioned in Sec. 1.4.3, experimentalists will never be able to measure the β-decay half-lives of all nuclides that participate in the r process. This situation creates a reliance on theoretical models to accurately calculate the β-decay half-lives where experimental data

are nonexistent and experiments are currently unfeasible. Theoretical models calculate the β-decay half-life according to the following equation [87, 88]

$$\frac{1}{T_{1/2}} = \frac{(g_A/g_V)^2}{K} \sum_{0<E_x<Q} f(Q - E_x) B(\mathrm{GT}, E_x) \tag{1.21}$$

where $f(Q - E_x)$ is the Fermi integral, $B(\mathrm{GT}, E_x)$ is the Gamow-Teller transition strength distribution, $K = 6143.6(17)$ s [89], and $g_A/g_V = -1.270(3)$ [90]. First, a theoretical model calculates the Gamow-Teller transition strength distribution. This distribution provides information about the probability of a transition occurring during β decay from the parent nucleus to one of the many possible states in the daughter nucleus. The Gamow-Teller transition strength is proportional to the square of the overlap of the initial and final state [91]

$$B(\mathrm{GT}) \propto |\langle \psi_f | \hat{O}_{\mathrm{GT}} | \psi_i \rangle|^2 \tag{1.22}$$

where ψ_i is the wave function of the initial state (the parent state), ψ_f is the wave function of the final state (one of the daughter states), and $\hat{O}_{\mathrm{GT}}$ is the Gamow-Teller operator. The Gamow-Teller transition strength must be calculated for each transition to all the daughter states. The Gamow-Teller transition strength is then weighted by the Fermi integral (also referred to as the integrated phase space factor). The Fermi integral can be numerically computed (see Fig. 1.11) and represents the number of ways the electron and antineutrino can share the available energy. According to Eq. 1.21, the β-decay half-life is related to the amount of $B(\mathrm{GT})$ (weighted by the Fermi integral) that is below the ground-state-to-ground-state Q value.

Theoretical models also calculate a related β-decay property that is important for r-process reaction network calculations. This quantity is the β-delayed neutron emission prob-

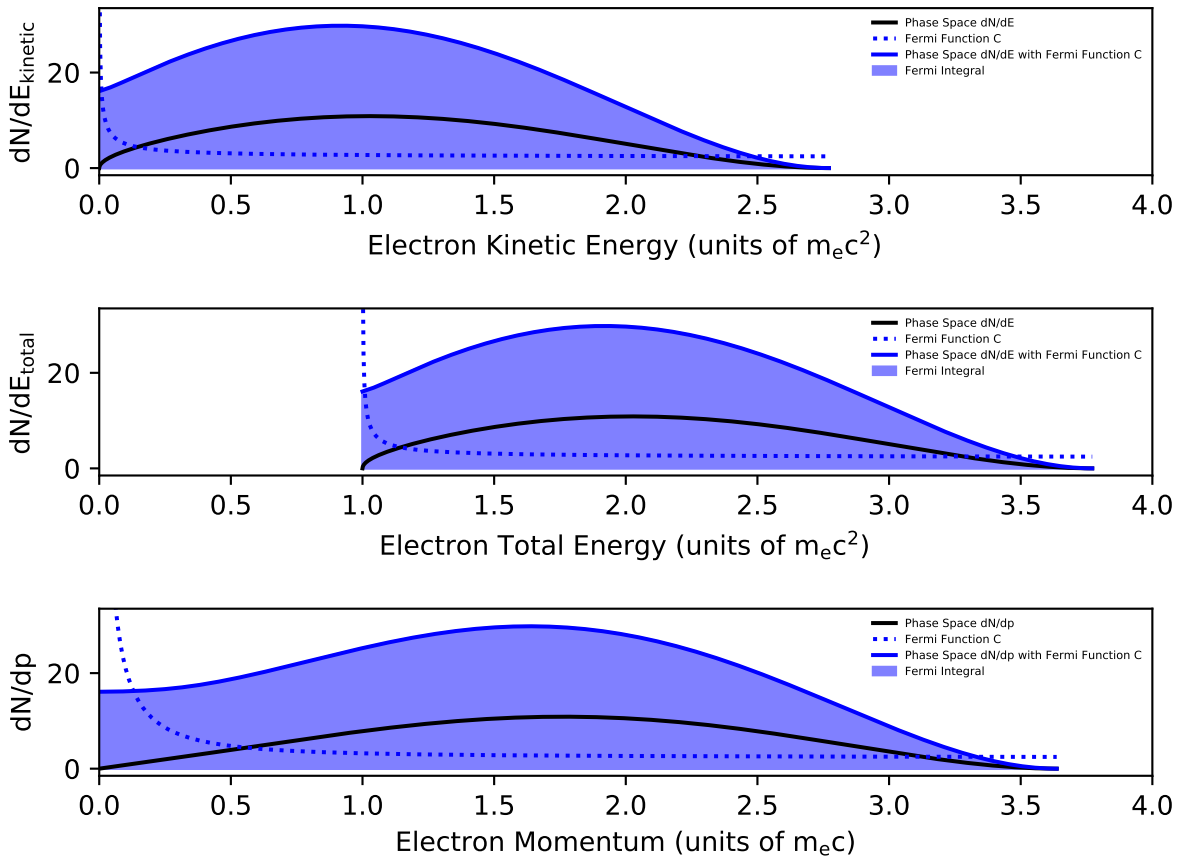

Figure 1.11: Definition of the Fermi integral for a single, representative β-decay transition in terms of electron kinetic energy (top panel), electron total energy (middle panel), and electron momentum (bottom panel). The Fermi integral is the area under the corrected phase space distribution. Unlike Fig. 1.9, the functions and distributions are not normalized to unity.

ability. This quantity is the probability of the parent to undergo β decay to the daughter and then the daughter to emit a neutron. Theoretical models calculate the β-delayed neutron emission probability according to the following equation [87, 88]

$$P_n = \frac{\sum\limits_{S_n<E_x<Q} f(Q-E_x)B(\mathrm{GT},E_x)}{\sum\limits_{0<E_x<Q} f(Q-E_x)B(\mathrm{GT},E_x)} \tag{1.23}$$

where P_n is the β-delayed neutron emission probability, and S_n is the one-neutron separation energy in the daughter nucleus. According to Eq. 1.23, the β-delayed neutron emission probability is related to the fraction of $B(\mathrm{GT})$ (weighted by the Fermi integral) that is above the one-neutron separation energy of the daughter nucleus.

Because theoretical models are relied upon to calculate β-decay properties (β-decay half-lives and β-delayed neutron emission probabilities) needed for r-process reaction network calculations, the calculated properties must be accurate in order for the predicted abundance pattern to have any meaningful comparison to the r-process solar system abundance pattern. Usually, the accuracy of a theoretical model is evaluated by comparing its predictions of $T_{1/2}$ and P_n with experimental measurements of those quantities. However, $T_{1/2}$ and P_n are "integral quantities" or "integral properties." That is, they are single numbers that are obtained from a summation in Eqs. 1.21 and 1.23. These single numbers do not provide information about the detailed structure of the $B(\mathrm{GT})$ distribution that is necessary to calculate $T_{1/2}$ and P_n. Furthermore, the summation in Eqs. 1.21 and 1.23 introduces the possibility of obtaining the same $T_{1/2}$ and P_n values from different $B(\mathrm{GT})$ distributions. For example, different nuclear structure models could predict the same $T_{1/2}$ for a nuclide using different $B(\mathrm{GT})$ distributions. This possibility casts uncertainty on which of the nuclear structure models is best for extrapolation to nuclides relevant to the r process. A more

sensitive comparison to the theoretical models would be the actual experimental $B(\mathrm{GT})$ distribution, because this is sensitive to the nuclear structure [91, 92] as seen in Eq. 1.22. The experimental $B(\mathrm{GT})$ distribution is defined as

$$B(\mathrm{GT}, E_x) = K \left(\frac{g_V}{g_A}\right)^2 \frac{I_\beta(E_x)}{f(Q_\beta - E_x)T_{1/2}}, \tag{1.24}$$

where I_β is the β-decay feeding intensity to a particular excitation energy. The units of $B(\mathrm{GT})$ using Eq. 1.24 are implicitly assumed to be $g_A^2/4\pi$. The quantities E_x, I_β, Q_β, and $T_{1/2}$ can be obtained with experimental measurements.

Figure 1.12 is an illustration that shows the relation between the β-decay feeding intensity distribution, the Fermi integral, and the $B(\mathrm{GT})$ distribution. Note that as the energy of the populated level in the daughter increases, $Q - E_x$ decreases. In terms of physics, there are fewer ways for the electron and antineutrino to share the available energy. As a consequence, the Fermi integral decreases (top portion of the middle panel of Fig. 1.12). The top portions of the three panels in Fig. 1.12 show that for large excitation energy, even if the β-decay feeding intensity is small, because the Fermi integral is also small, there can be a significant contribution to $B(\mathrm{GT})$. Therefore, extracting the β-decay feeding intensities, even if they are small, is very important for obtaining the experimental $B(\mathrm{GT})$ distribution.

1.6 Pandemonium Effect

Traditionally, the β-decay feeding intensity distribution has been measured with detectors designed for good energy resolution but which suffer from poor intrinsic detection efficiency. These detectors are usually constructed out of high-purity germanium. With high-resolution

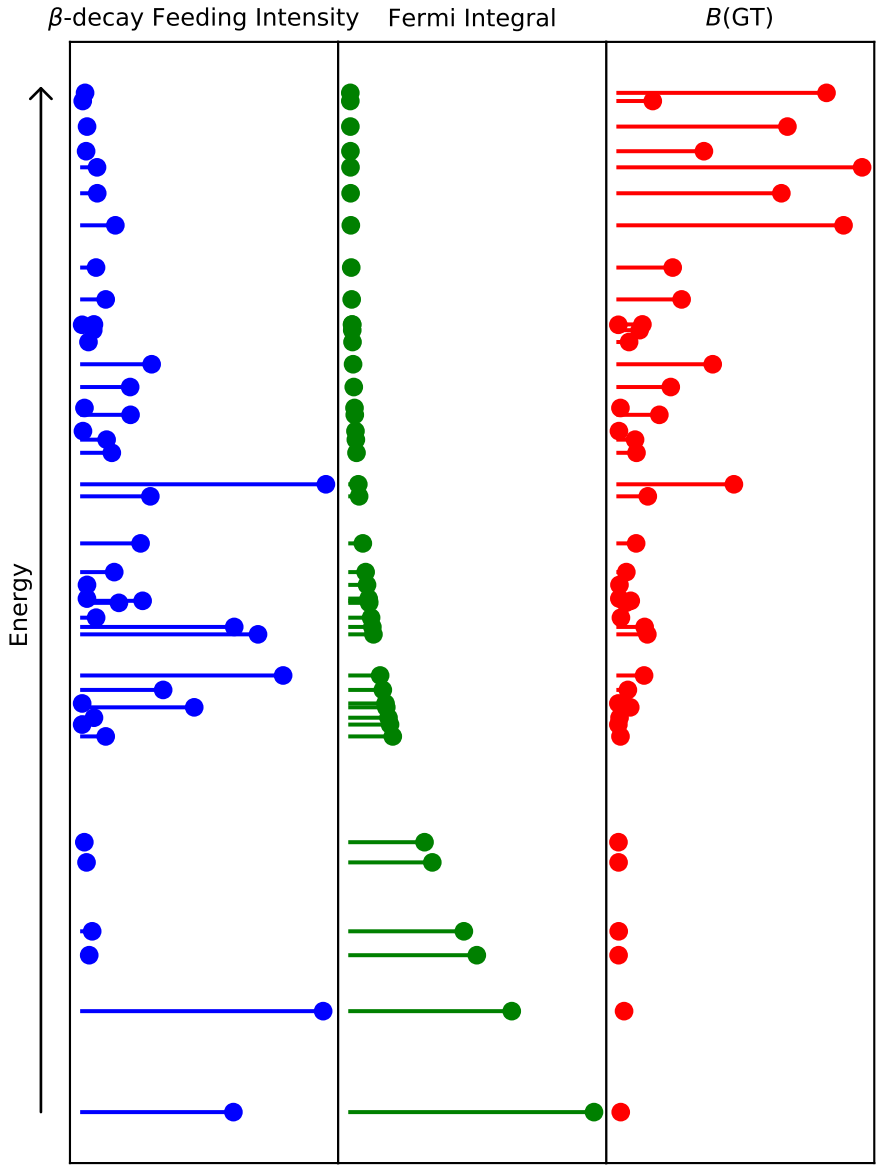

Figure 1.12: Representative comparison of β-decay feeding intensity, Fermi integral, and B(GT).

detectors, the analysis method to extract the β-decay feeding intensity distribution is a γ-ray intensity balance

$$I_\beta(E_x) = I_\gamma^{(out)}(E_x) - I_\gamma^{(in)}(E_x). \tag{1.25}$$

In this case, the β-decay feeding intensity to each level is determined by balancing the absolute γ-ray intensity (corrected for internal conversion and detector efficiency) recorded in and out of each level. However, problems arise when using this analysis method for a nuclide with a complex and fragmented β-decay scheme. Figure 1.13 shows an example of a complex and fragmented β-decay scheme with many β-decay transitions and γ-ray transitions. As the energy of states in the daughter increases, the spacing between states decreases. This leads to a quasi-continuum of states. The β-decay feeding intensity to states in the quasi-continuum may be very fragmented and consist of many β-decay transitions that have a small β-decay feeding intensity. In addition, the following γ-ray cascades to the ground state may be very fragmented as well. If low-intensity and/or high-energy γ rays populating a level are not recorded due to limited detection efficiency, then $I_\gamma^{(in)}(E_x)$ is artificially reduced and $I_\beta(E_x)$ is artificially enhanced. This problem is known in the literature as the Pandemonium effect [93]. Therefore, for a nuclide with a complex and fragmented β-decay scheme (which will generally occur for nuclides relevant to the r process), using a γ-ray intensity balance will bias the β-decay feeding intensity distribution to lower energies and miss part of the distribution at high excitation energy. Instead of using a γ-ray intensity balance with a high-resolution detector, different techniques and detectors have been developed to accurately extract the β-decay feeding intensity distribution.

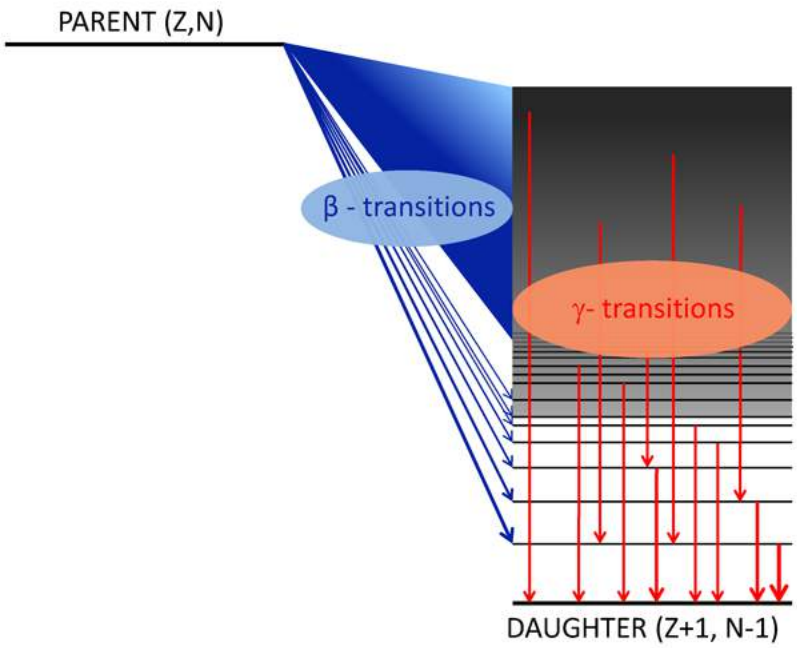

Figure 1.13: A complex and fragmented β-decay scheme with many β-decay transitions and γ-ray transitions. Figure adapted from Ref. [15].

1.7 Total Absorption Spectroscopy

The problem posed by the Pandemonium effect can be solved using the technique of total absorption spectroscopy (TAS) [91, 92]. This technique requires a detector (called a total absorption spectrometer) that is optimized for geometric and intrinsic detection efficiency. These detectors surround the radioactive source with ideally 4π solid angle coverage and are typically constructed with large scintillating crystals.

The TAS technique can be illustrated with the simple case of the β decay of ^{60}Co. Almost 100% of the β-decay feeding intensity is assigned to the level in the daughter ^{60}Ni at 2505 keV, which deexcites by emitting two sequential γ rays with energies of 1173 keV and 1332 keV [94]. In the TAS spectrum (top panel of Fig. 1.14), these two γ rays are summed together to create a "sum peak" at the energy of the excited state (2505 keV). Of course, no total absorption spectrometer has 100% summing efficiency, so there are instances

of "incomplete summation." For example, this can occur if only one of the two γ rays is detected, creating the two small peaks at 1173 keV and 1332 keV. Or, a γ ray Compton scatters and then escapes the sensitive volume of the detector.

If the total absorption spectrometer is segmented, then each segment can be treated as an independent detector that detects the individual γ rays. The histograms from each segment can be added together to create the sum-of-segments spectrum (middle panel of Fig. 1.14). The dominant feature of this spectrum is the double peak structure at the energies of 1173 keV and 1332 keV. If multiple γ rays enter the same segment in the same event, then "summation within a segment" has occurred. For the example of ^{60}Co, this results in a small peak at 2505 keV.

The segmentation also allows for the creation of a multiplicity spectrum (bottom panel of Fig. 1.14), which is the number of segments that detect energy in the event. A lower (higher) γ-ray multiplicity of the cascade corresponds to a lower (higher) number of segments that detect energy in the multiplicity spectrum. The multiplicity spectrum depends on the actual γ-ray multiplicity of the cascade and on the energy of the detected γ rays. For the example of ^{60}Co, the majority of the events are when the segmented total absorption spectrometer detects energy in two segments (bottom panel of Fig. 1.14).

One quantity of interest with a total absorption spectrometer is the full-energy summing efficiency. For a given excited state populated in β decay, this quantity is the probability to produce a count in the sum peak in the TAS spectrum. The full-energy summing efficiency depends on how the deexcitation of an excited state is partitioned in terms of number of γ rays and their individual energies. For example, consider an excited state populated in β decay at 2000 keV, which deexcites with two γ-ray cascades. The first γ-ray cascade consists of two γ rays that each have an energy of 1000 keV. The second γ-ray cascade consists

of five γ rays that each have an energy of 400 keV. The full-energy summing efficiency is different for these two γ-ray cascades. Another quantity of interest with a total absorption spectrometer is the total summing efficiency. For a given excited state populated in β decay, this quantity is the probability to produce a count anywhere in the TAS spectrum, not just in the sum peak.

Unlike a high-resolution detector, which detects individual γ rays, a total absorption spectrometer measures entire γ-ray cascades. The TAS spectrum is therefore sensitive to levels populated in β decay. The β-decay feeding intensity to a level is determined from the number of γ-ray cascades from that level.

1.8 Summing NaI(Tl) (SuN) detector

The Summing NaI(Tl), or SuN, detector (Fig. 1.15) [95] at the National Superconducting Cyclotron Laboratory (NSCL) was used for the experiments presented in this dissertation. SuN is a segmented total absorption spectrometer that is ideally suited to use the TAS technique. SuN is a right-circular cylindrical detector that is 16 inches in diameter, 16 inches in length, has a 1.8 inches diameter bore hole along the beam axis, and can separate into a top half and bottom half in order to fit around the beam line. Each half consists of four optically isolated segments, and each segment contains a large NaI(Tl) crystal that is read out by three photomultiplier tubes (PMTs). The NSCL Digital Data Acquisition System (DDAS) [96] is used to record signals in SuN. Together, the large summing efficiency and relatively good energy resolution for a scintillator (85(2)% full-energy summing efficiency and an average segment energy resolution of 6.1(2)% for the 661 keV γ ray from the β decay of ^{137}Cs) make SuN ideally suited for TAS experiments.

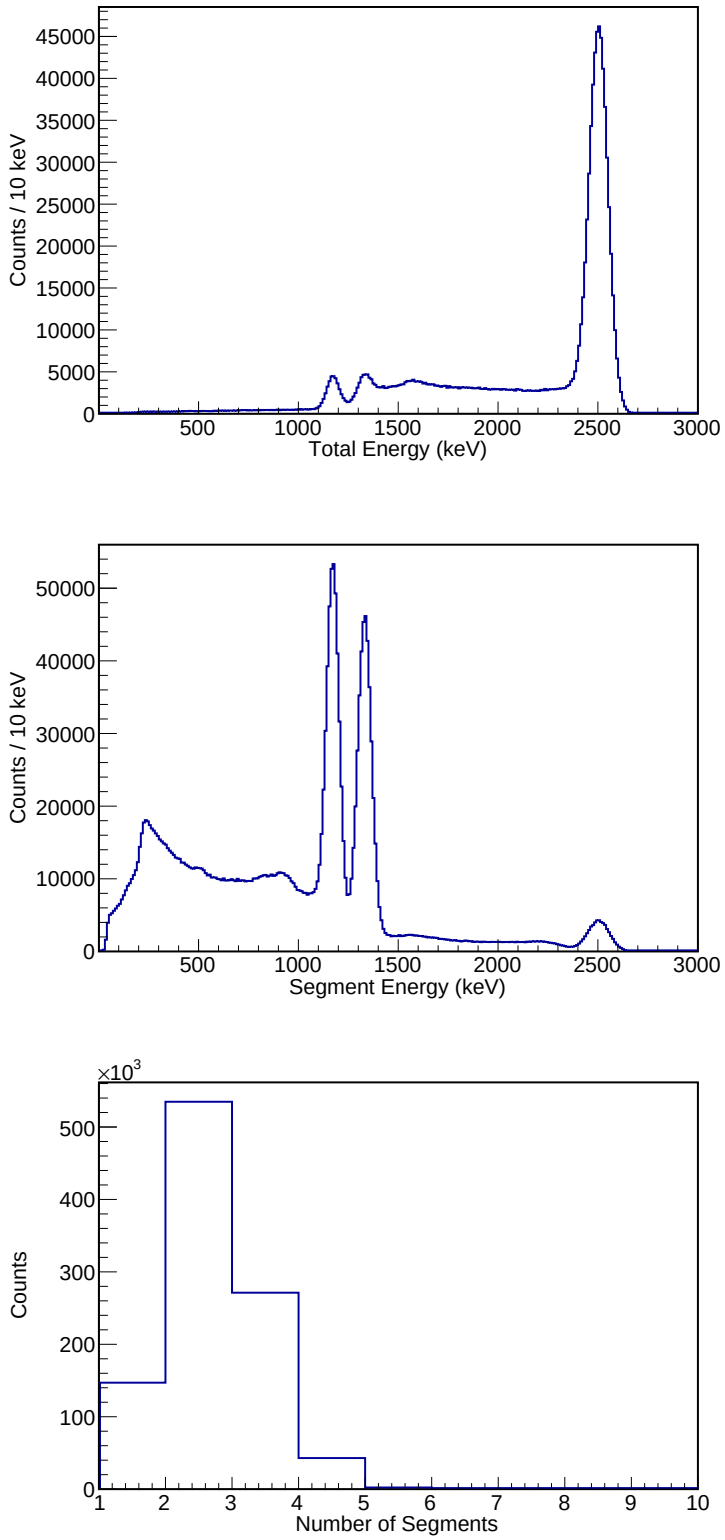

Figure 1.14: Example spectra obtained with a ^{60}Co source at the center of a segmented total absorption spectrometer. The spectra are the TAS spectrum (top panel), sum-of-segments spectrum (middle panel), and multiplicity spectrum (bottom panel).

The segmentation of SuN is powerful in that both the total energy deposition as well as the energy deposition in each segment is recorded for a given event. For β-decay experiments with SuN, this translates into knowing the level populated in the daughter nucleus and also the possible subsequent electromagnetic deexcitation of that level in the form of γ rays. Adding together the histograms from all eight segments produces the sum-of-segments spectrum in which individual γ rays can be identified, while adding together the energies of all eight segments on an event-by-event basis produces the TAS spectrum in which sum peaks that correspond to levels can be identified. In other words, the individual segments of SuN provide a way of performing low-resolution, discrete γ-ray spectroscopy, while the entire detector is used as a calorimeter to apply the TAS technique.

1.9 Dissertation Motivation

The A = 100-110 mass region is located between the first r-process peak at A $\approx$ 80 and the second r-process peak at A $\approx$ 130 (see Fig. 1.2). This mass region corresponds to lighter neutron-capture elements where there is more scatter in the abundance patterns of metal-poor halo stars (Sec. 1.4.1). This mass region corresponds to the weak r process (Sec. 1.4.1), whose site is under debate. Measurements of β-decay properties in this mass region will reduce the uncertainty in the nuclear physics needed to determine the site of the weak r process.

In addition, the A = 100-110 mass region is an intermediate mass region that can be studied at current experimental facilities, and nuclides in this region are expected to have an appreciable amount of low-lying Gamow-Teller transition strength [97] that can be extracted with β decay. Experimental B(GT) distributions in this mass region can be used to

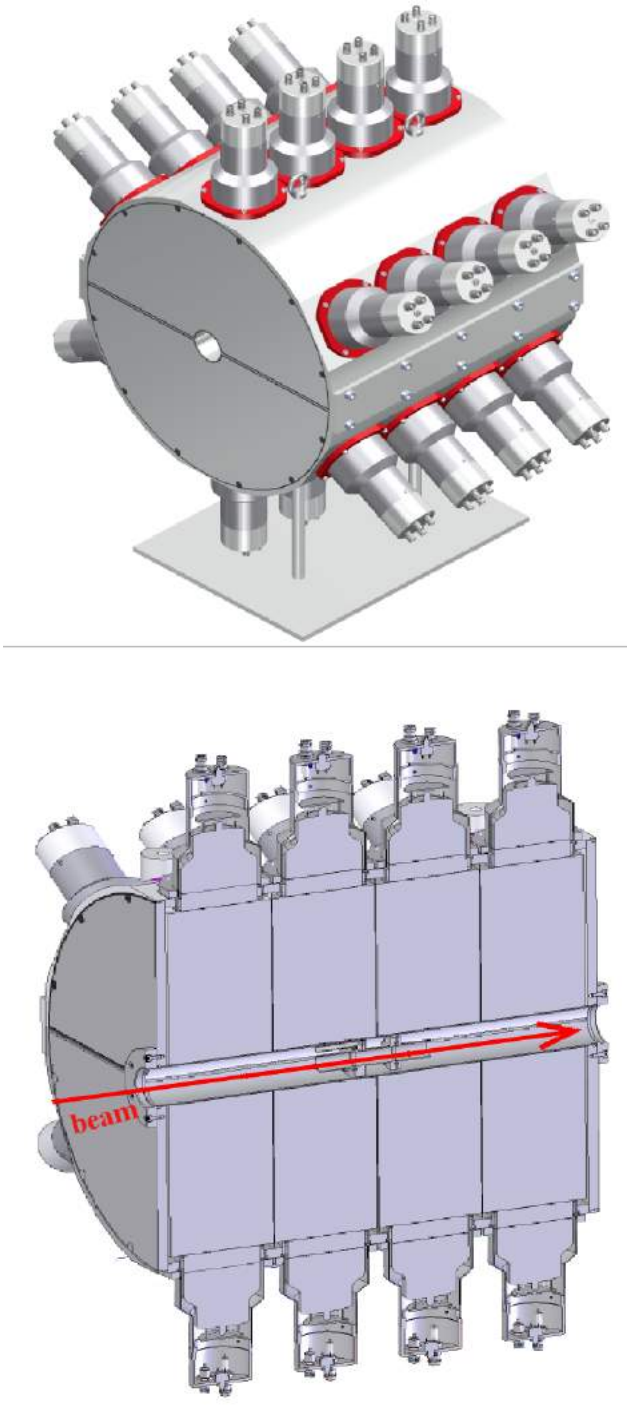

Figure 1.15: The Summing NaI(Tl) (SuN) detector.

compare to and constrain theoretical models commonly used to provide β-decay properties in r-process reaction network calculations. Constraining these theoretical models with experimental measurements will provide more confidence in their extrapolation far from the valley of stability where experimental data are nonexistent and experiments are currently unfeasible.

Finally, for nuclides in this mass region, a comparison of theoretical and experimental B(GT) distributions may be used to learn about the shape (spherical, oblate, or prolate) of the ground state of the parent. This idea was proposed by I. Hamamoto et al. for neutron-deficient nuclides in the $28 < Z < 66$ region [98, 99], explored further by P. Sarriguren et al. for neutron-deficient and neutron-rich nuclides [100, 101, 102, 103, 104, 105, 106, 107, 87, 88, 108, 109, 110], and experimentally studied by researchers primarily at the University of Valencia [111, 112, 79, 113, 114, 115, 82]. Certain nuclides in the A = 100-110 mass region have been shown to have different B(GT) distributions depending on the shape of the ground state of the parent [87, 88].

This dissertation contains the results of using the SuN detector and the TAS technique to extract β-decay feeding intensity distributions and B(GT) distributions for nuclides relevant to the r process. Chapter 2 describes the commissioning experiment for SuN at the NSCL with a thermalized beam. Chapter 3 describes the first-ever application of the TAS technique with a fast beam produced via projectile fragmentation. Chapter 4 provides a summary and outlook for this dissertation.

Chapter 2

β-decay Studies with Thermalized Beams

The experiment titled "Commissioning of the SuN detector" was performed on April 18, 2013 at the NSCL (experiment e13502). This experiment was the first application of SuN in any type of β-decay experiment. Prior to e13502, SuN had only been used at the Nuclear Science Laboratory at the University of Notre Dame to measure (p, γ) and (α, γ) reactions in regular and inverse kinematics for the p process [25]. Experiment e13502 served as the proof-of-principle experiment to demonstrate that SuN could successfully be used as a total absorption spectrometer in β-decay experiments, before being used in future experiments with exotic nuclei relevant to the r process. The data analysis from this experiment provided an opportunity to develop the tools and methods necessary to extract the β-decay feeding intensity distribution in all future experiments. As an aside, the data set from this experiment was used by other researchers to develop the so-called β-Oslo technique [116], which is used to experimentally constrain neutron capture reaction rates using β decay and the traditional reaction-based Oslo method [117, 118].

2.1 Motivation

2.1.1 Technical Motivation

The nuclide ^{76}Ga was chosen for the commissioning experiment for the following reasons:

1. The decay scheme of ^{76}Ga was supposedly well known and the level scheme of ^{76}Ge had been extensively studied in previous experiments.

2. The relatively large ground-state-to-ground-state Q value for β-decay (6916.2 keV [16]) allowed for the study of the β-decay feeding intensity distribution over a broad energy range.

3. The daughter ^{76}Ge is essentially stable, which precluded the possibility of contamination of experimental spectra from the radioactivity of future generations.

4. A beam of ^{76}Ga was available from the NSCL beam thermalization area (described in Sec. 2.2). This meant the beam delivered to the experimental end station would be free of beam contaminants (that is, a pure beam).

2.1.2 Physics Motivation: Neutrinoless Double-β Decay

The nuclide ^{76}Ga is part of the A = 76 isobaric chain, which is shown in Fig. 2.1. In this and other isobaric chains, nuclear masses and the pairing interaction conspire to create a scenario in which single-β decay is energetically forbidden while double-β decay is energetically allowed. If, in the latter process, two electrons and no neutrinos are emitted, this process is called neutrinoless double-β ($0\nu\beta\beta$) decay and denoted as ${}^{A}_{Z}X_{N} \rightarrow {}^{A}_{Z+2}Y_{N-2} + 2e^{-}$. An observation of $0\nu\beta\beta$ decay would demonstrate the violation of conservation of total lepton

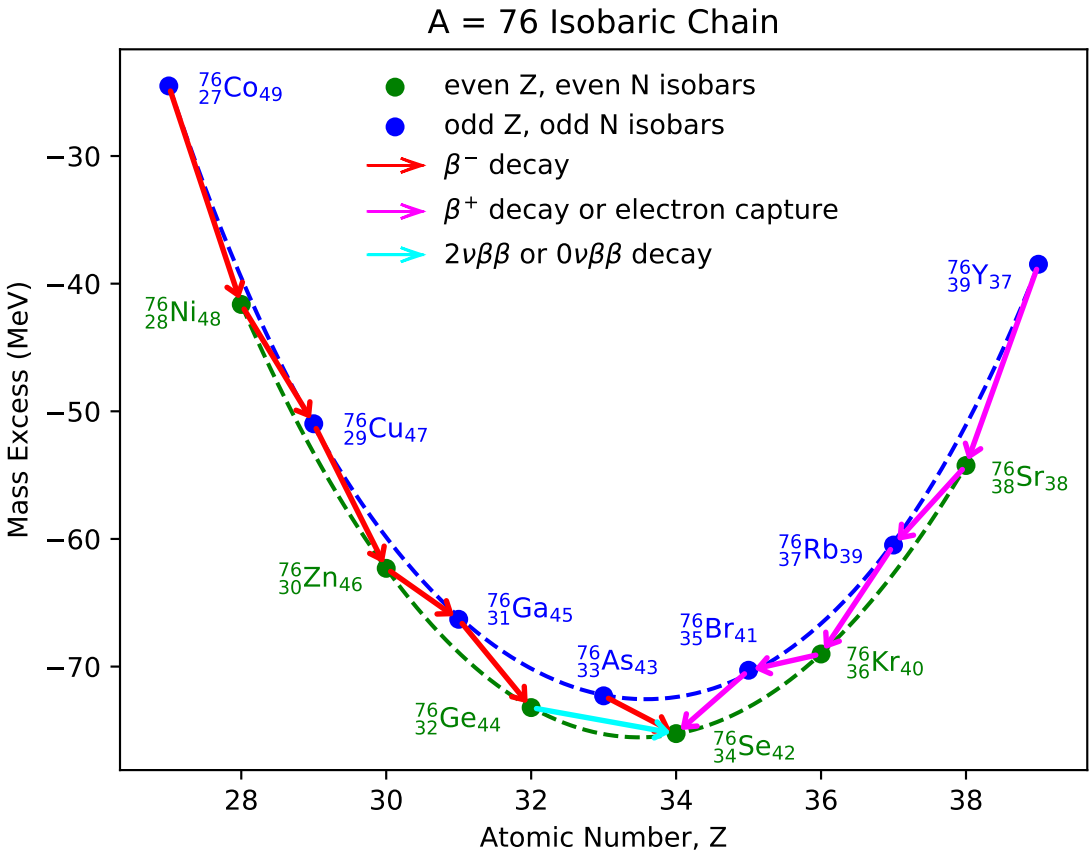

Figure 2.1: Isobaric chain for A = 76, which contains ^{76}Ga. Data for the mass excess is from Ref. [16]. The nuclide ^{76}Ge can undergo two-neutrino double-β ($2\nu\beta\beta$) decay, and is a candidate for neutrinoless double-β ($0\nu\beta\beta$) decay. The nuclide ^{76}Ga undergoes β decay to ^{76}Ge.

number and establish that neutrinos are Majorana particles as opposed to Dirac particles [119, 120].

The even-even nucleus ^{76}Ge is a promising $0\nu\beta\beta$-decay candidate for many experimental reasons. The $Q_{\beta\beta}$ value ($Q_{\beta\beta} = 2039.061 \pm 0.007$ keV) [121] of this nucleus places the region of interest above many, but not all, sources of background. In addition, this nucleus is easily compatible with the existing experimental technique of using high-purity germanium detectors, which increases the signal-to-noise ratio due to the excellent energy resolution provided by these types of detectors. While $0\nu\beta\beta$ decay has never been observed

in any nucleus, the search for this process remains steadfast. Highly sensitive experiments performed by multinational collaborations such as the Heidelberg-Moscow experiment [122], the International Germanium Experiment (IGEX) [123, 124], and the Germanium Detector Array (GERDA) phase I [125] have placed lower limits on the half-life of ^{76}Ge $0\nu\beta\beta$ decay. The next generation of experiments of GERDA phase II [126] and MAJORANA [127] are devoted to observing and measuring the half-life of $0\nu\beta\beta$ decay in ^{76}Ge, or, if no observation is made, placing a strong lower limit on the half-life.

Together with experimental efforts, theory has focused on calculating nuclear matrix elements necessary for $0\nu\beta\beta$ decay in ^{76}Ge [119]. The nuclear matrix elements are important because they are needed to calculate the decay rate for $0\nu\beta\beta$ decay, denoted as $(T^{0\nu}_{1/2})^{-1}$, assuming the theoretical description is given by light neutrino exchange, as [119]

$$(T^{0\nu}_{1/2})^{-1} = G_{0\nu}|M_{0\nu}|^2\langle m_{\beta\beta}\rangle^2, \tag{2.1}$$

where $G_{0\nu}$ is the phase space factor [128, 129, 130, 131], $M_{0\nu}$ is the nuclear matrix element, and $\langle m_{\beta\beta}\rangle$ is the effective mass of the neutrino. According to Eq. 2.1, the nuclear matrix elements can be used with current lower limits on the half-life to provide upper limits on $\langle m_{\beta\beta}\rangle$ or extract $\langle m_{\beta\beta}\rangle$ if the half-life is eventually measured.

The nuclear matrix elements have been calculated using different nuclear structure models, and for a given nucleus can be quite uncertain [132, 133]. Three models which have provided recent calculations relevant to ^{76}Ge are the shell model [134], quasiparticle random phase approximation (QRPA) [135], and the interacting boson model (IBM-2) [136]. These three models were recently compared to one another for the case of ^{76}Ge and deficiencies were found in all three models [137], a problem that is common to all $0\nu\beta\beta$-decay candidates.

The commissioning experiment described in this chapter provided new experimental data in the A = 76 mass chain that can be compared to some of the aforementioned theoretical calculations. The new experimental data was the β-decay feeding intensity distribution of ^{76}Ga as a function of excitation energy in the daughter nucleus ^{76}Ge, obtained with the TAS technique. Because the β-decay feeding intensity distribution is sensitive to the wave functions of the ground state of the parent and those of the populated daughter states, the measurement can be used to test the nuclear structure models which are used to calculate the nuclear matrix elements.

2.2 Experimental Details

The experiment was performed at the National Superconducting Cyclotron Laboratory (NSCL) at Michigan State University. The Coupled Cyclotron Facility produced a primary beam of $^{76}Ge^{32+}$ with an energy of 130 MeV/u which was impinged on a ^{9}Be production target that had a thickness of 399 mg/cm^2. Using a 184 mg/cm^2 Al wedge, the A1900 fragment separator [138] created a secondary beam with a momentum acceptance of 0.5% of approximately 73% of $^{76}Ga^{31+}$ (the nuclide of interest) and 27% of $^{74}Zn^{30+}$.

After the A1900 fragment separator, the secondary beam was sent to the NSCL beam thermalization area. The specific piece of equipment used from the NSCL beam thermalization area was the linear gas cell [139, 140] (also referred to as the Argonne gas catcher, having been constructed at Argonne National Laboratory) in the N4 vault. The linear gas cell (shown in Fig. 2.2) was 1.2 meters long, filled with helium gas at 92 torr, preceded by a solid degrader system, and followed by an extraction system. The solid degrader system consisted of a 1555 μm Al degrader and a 1045 μm silicon dioxide wedge to remove nearly

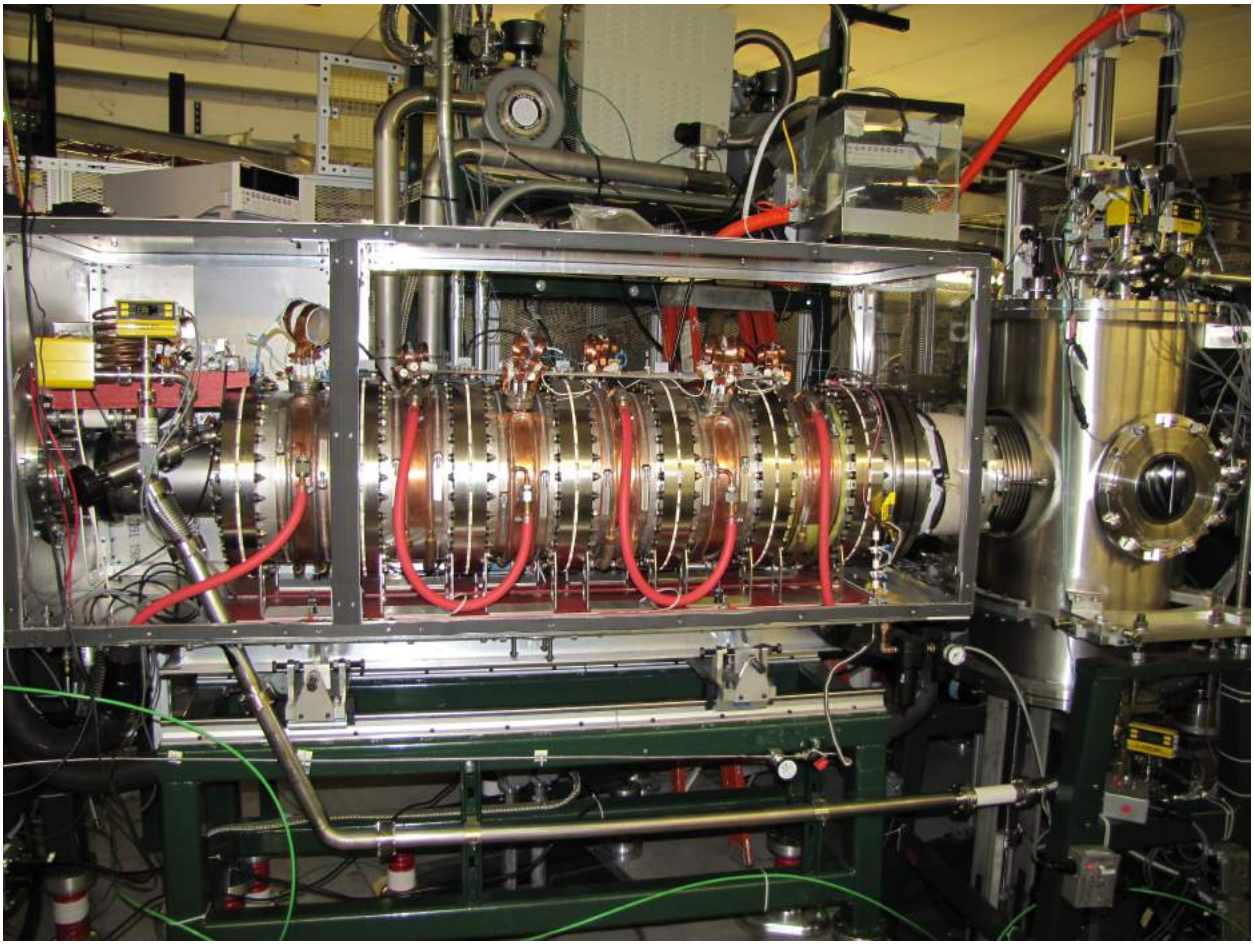

Figure 2.2: The linear gas cell in the N4 vault used for NSCL experiment e13502. The secondary beam from the A1900 fragment separator enters from the right side of the picture. Ions are thermalized though collisions with helium gas and then extracted on the left side of the picture.

all of the kinetic energy and spread in kinetic energy of the secondary beam before entering the linear gas cell, respectively. By changing the angle of the degrader, primarily $^{76}Ga^{31+}$ was stopped in the linear gas cell after passing through a thin Al window. The ions were thermalized through collisions with helium gas within the linear gas cell, and subsequently extracted using the extraction system. A scan of the activity as a function of mass of the ions extracted from the linear gas cell revealed the molecular ion $[^{76}Ga(H_2O)]^+$ to be the most common, and this was delivered to the experimental end station.

The experimental end station (shown in Fig. 2.3) consisted of the Summing NaI(Tl)

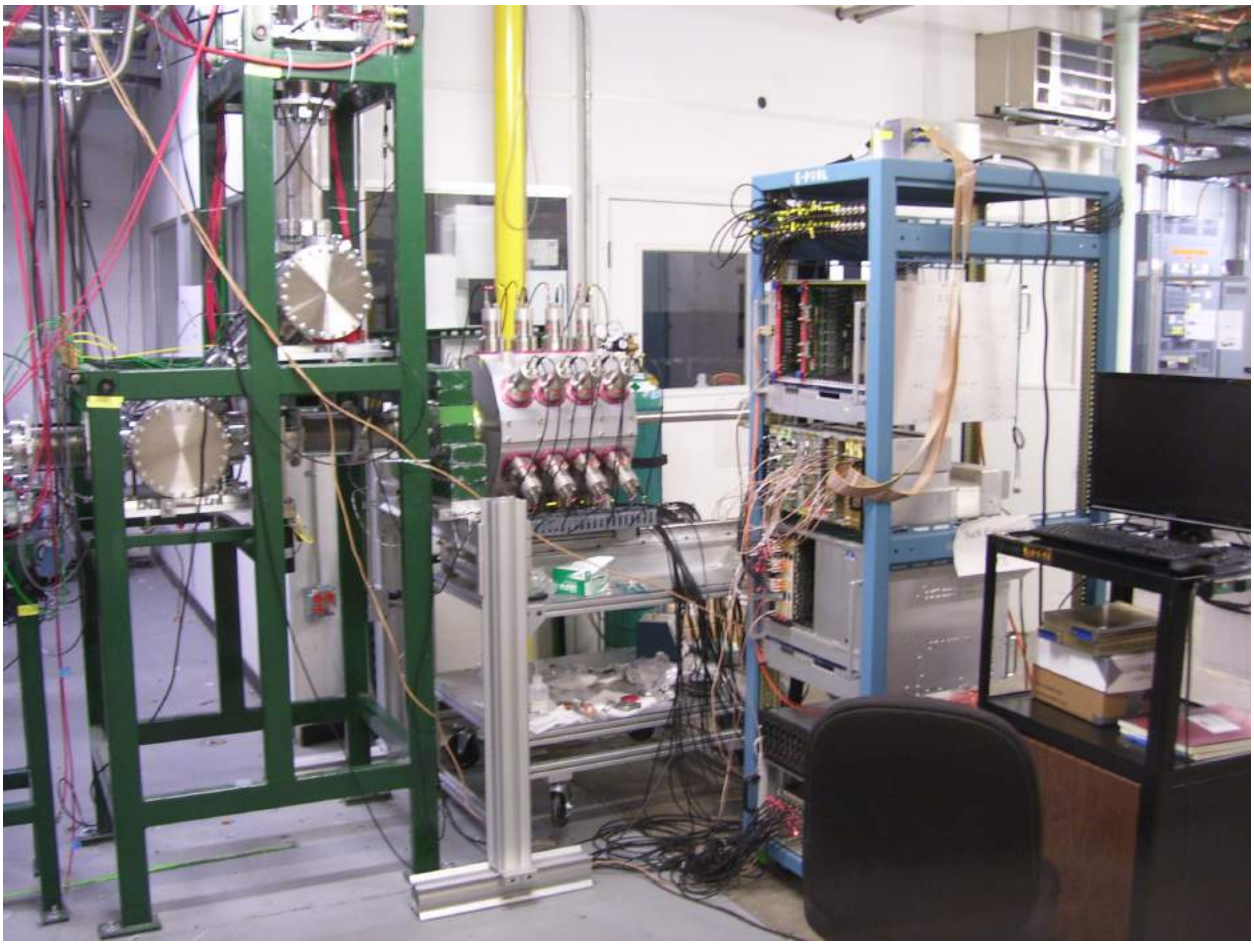

Figure 2.3: Experimental end station attached to the D Line for NSCL experiment e13502. The thermalized beam enters from the left side of the picture.

(SuN) detector [95] and a small silicon surface barrier detector installed inside the bore hole of SuN. The silicon surface barrier detector (shown in Fig. 2.4) was manufactured by ORTEC with model number B-019-200-1500 (active area of 200 mm^2 and depletion depth of 1500 μm). In front of the silicon surface barrier detector was a rectangular aluminum frame that was 0.5 mm thick which held a thin aluminum foil. The ^{76}Ga ions, which had an energy of approximately 40 keV and intensity of approximately 500 particles per second, were implanted into the aluminum target foil. The electrons from the β decay of ^{76}Ga were detected in the silicon surface barrier detector in coincidence with the β-delayed radiation in SuN.

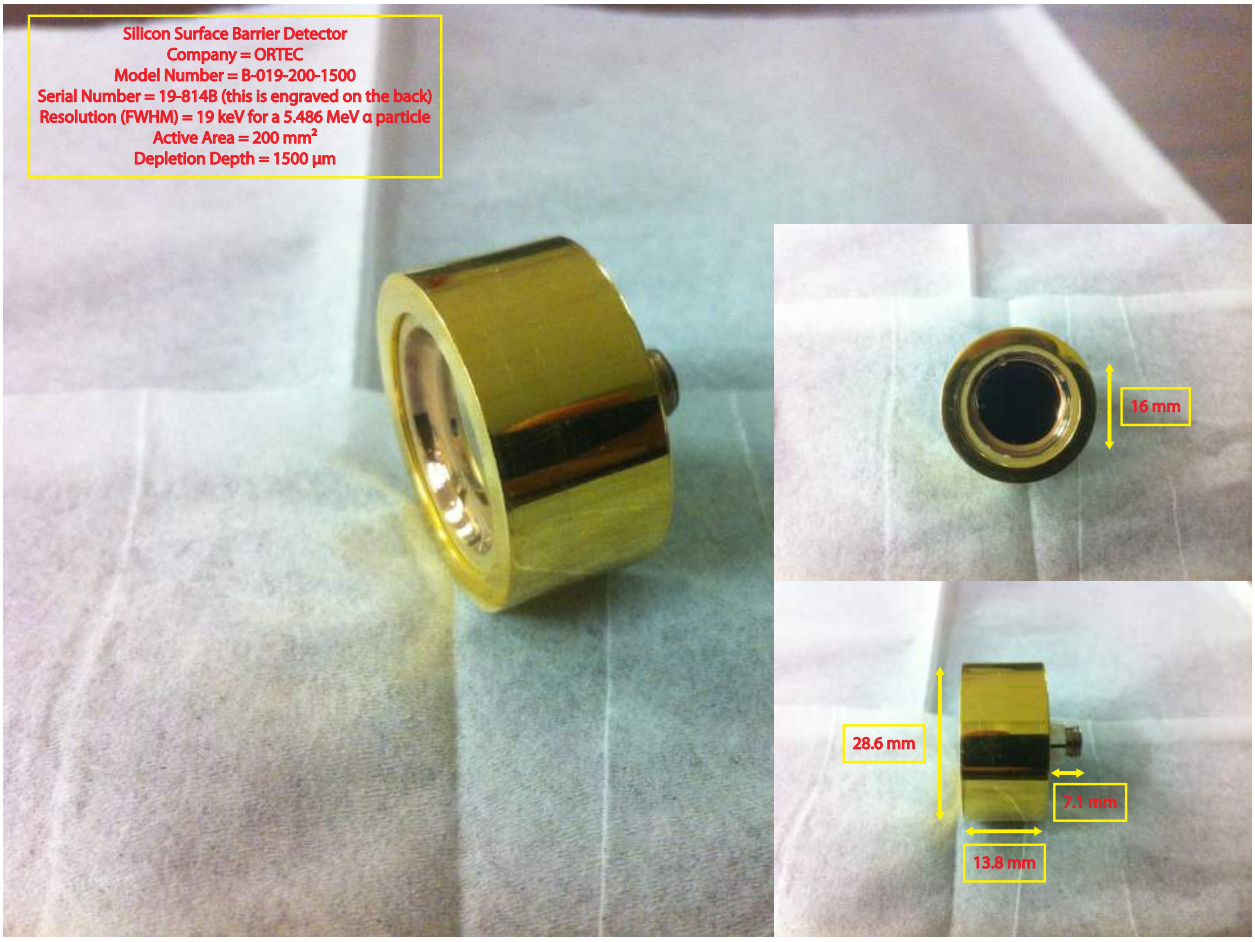

Figure 2.4: The silicon surface barrier detector installed inside the bore hole of SuN for NSCL experiment e13502.

2.3 Analysis

Before the start of the experiment, the PMTs of SuN were gain matched by adjusting the high voltage applied to each PMT. The high voltage was adjusted until the 1460.8 keV γ ray from the decay of ^{40}K that is present in room background appeared at approximately the same channel number for each PMT. Then the PMTs and segments of SuN were further gain matched and calibrated, respectively, in software with the following procedure. First, the PMTs were gain matched by applying a multiplication factor to the energy of each outer PMT so that the ^{40}K peak appeared at the same channel number as the corresponding peak in the central PMT within a given segment. Then the energy of all three PMTs for a given segment were added together to determine the energy deposition within that segment. An individualized quadratic calibration was then applied to each segment so that γ rays were located at the correct energy. For this analysis, the calibration used the 563, 1108, and 3952 keV γ rays, which are emitted following the β decay of ^{76}Ga. A ^{60}Co source was placed at the center of SuN with the intention of using the 1173 keV and 1332 keV γ rays to calibrate the segments. However, the activity of the source was found to be too high for an efficient detector such as SuN. The high activity altered the resolution and efficiency of those γ rays and the summed energy of those γ rays. Finally, the energy of all eight segments were added together to create the TAS spectrum (an energy threshold of 80 keV was applied to each segment before being added to the TAS spectrum). Due to the energy threshold applied to each segment, the TAS spectrum will naturally have an energy threshold of 80 keV as well. Because the location of a "sum peak" in the TAS spectrum has a dependence on the multiplicity of the γ ray decay cascade (due to the non-proportional light yield in a NaI(Tl) crystal [141]), a multiplicity-dependent correction factor was applied to the TAS spectrum.

Table 2.1: High voltages and multiplication factors used to gain match each PMT of SuN for NSCL experiment e13502. For a given PMT label, the letter indicates the top or bottom half of SuN ("B" for bottom and "T" for top), the first number indicates the segment of SuN, and the second number indicates the PMT within the segment. For example, the label T23 means PMT 3 of segment 2 of the top half of SuN.

PMT	High Voltage (V)	Gain Matching Multiplication Factor
B11	+840	0.99834
B12	+828	1.00000
B13	+825	0.99847
B21	+842	0.99560
B22	+870	1.00000
B23	+840	0.99490
B31	+894	1.02325
B32	+869	1.00000
B33	+847	0.99627
B41	+927	0.99026
B42	+944	1.00000
B43	+910	0.98896
T11	+736	0.98660
T12	+746	1.00000
T13	+772	1.00387
T21	+779	1.00143
T22	+779	1.00000
T23	+770	1.00544
T31	+798	1.02295
T32	+808	1.00000
T33	+811	1.02954
T41	+842	1.01592
T42	+838	1.00000
T43	+850	1.01931

The high voltages and multiplication factors used to gain match each PMT of SuN are listed in Table 2.1, and the segment calibrations are shown in Fig. 2.5.

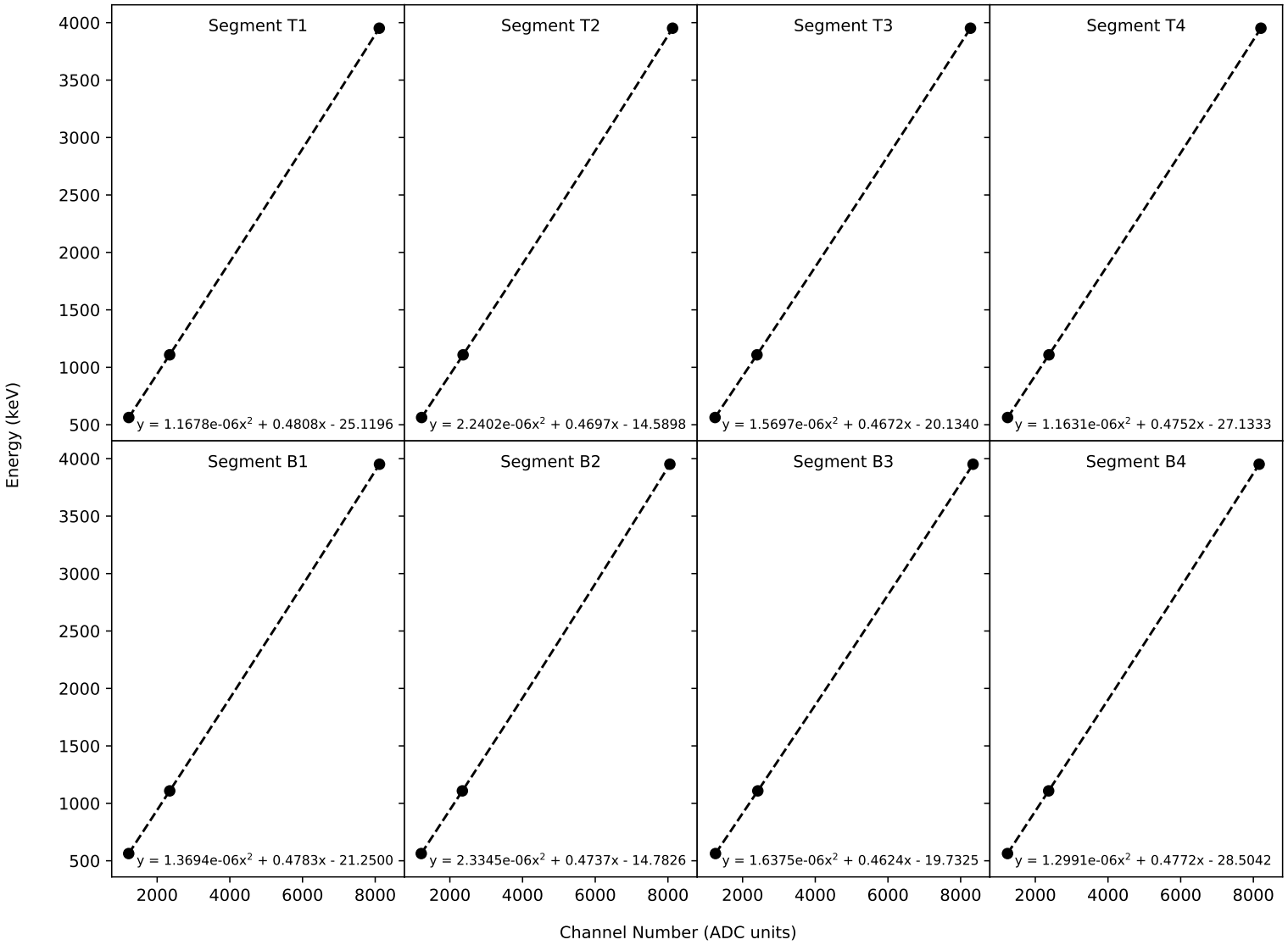

Figure 2.5: Calibrations for each segment of SuN for NSCL experiment e13502. For a given segment label, the letter indicates the top or bottom half of SuN ("B" for bottom and "T" for top), and the number indicates the segment number. For example, the label T2 means segment 2 of the top half of SuN.

There were no external trigger requirements to record data in the experiment. Comparing the TAS spectrum of normalized room background (blue, dotted line in Fig. 2.6) to the TAS spectrum of the β decay of ^{76}Ga in singles mode (green, dashed line in Fig. 2.6) reveals that the lower energies are dominated by room background. Subtracting the two spectra to create a TAS spectrum corresponding purely to the β decay of ^{76}Ga would create significant statistical fluctuations. Instead, the background radiation was removed by adding a coincidence requirement between a β-decay electron in the silicon surface barrier detector and β-delayed γ rays in SuN, producing a so-called β-gated TAS spectrum (black, solid line in Fig. 2.6). The TAS spectrum with the coincidence requirement shows significant suppression of the background radiation, no issues from beam-induced background, and clearly visible "sum peaks." For example, the first excited state in ^{76}Ge occurs at 563 keV, the second excited state occurs at 1108 keV, and some of the higher-energy excited states that have a relatively large β-decay feeding intensity occur at 2920, 3142, 3182, and 3952 keV.

The β-gated TAS spectrum was used to extract the β-decay feeding intensity distribution. The distribution was extracted with a combination of a folding procedure and χ^2 minimization. The folding procedure used the detector response functions of SuN, which were modeled with GEANT4 [142]. GEANT4 (GEometry ANd Tracking) is a software package that uses Monte Carlo methods to simulate how particles interact with matter. The interaction of γ rays and electrons with matter is built into the physics libraries of GEANT4. After SuN and the silicon surface barrier detector were constructed in GEANT4, the detector response functions were obtained by repeatedly sampling how β-decay electrons and γ-ray cascades interacted with the silicon surface barrier detector and SuN. The GEANT4 modeling of SuN has been verified by comparing experimental and simulated spectra for standard calibration sources such as ^{60}Co and ^{137}Cs [95], and resonances for the ^{27}Al(p,γ)^{28}Si reaction [95].

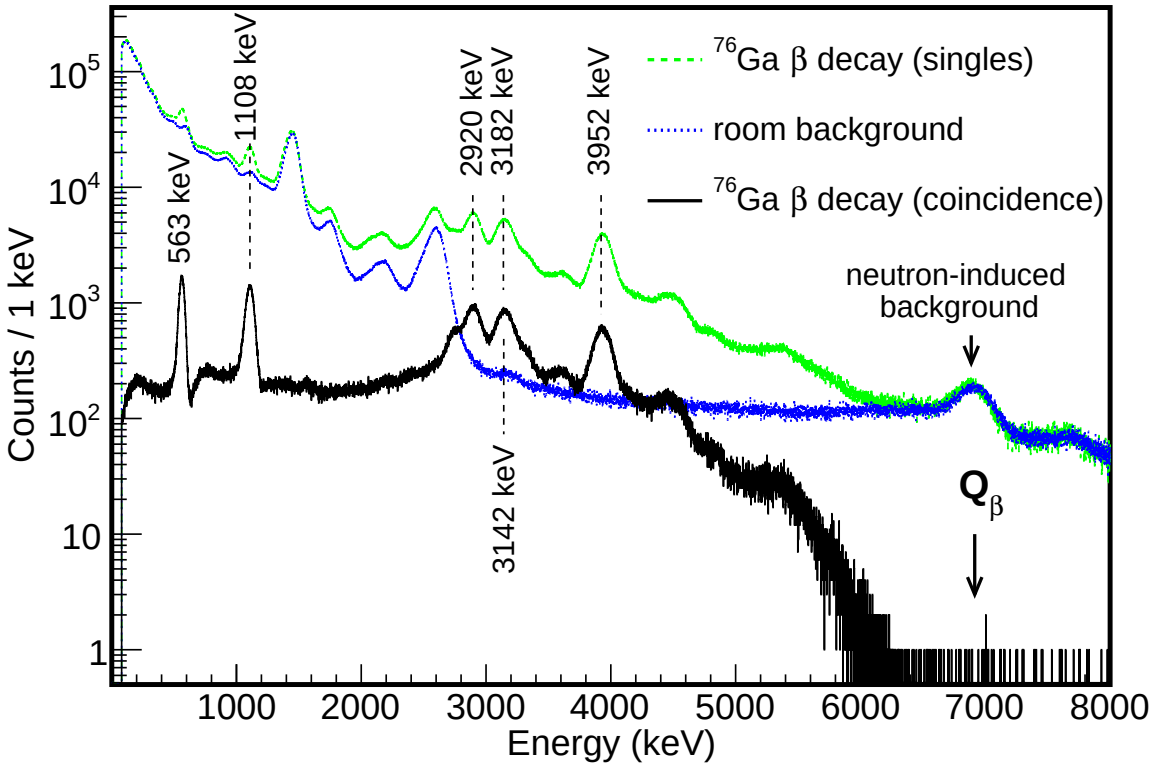

Figure 2.6: The TAS spectrum of SuN for the β decay of ^{76}Ga in singles (green, dashed line), normalized room background (blue, dotted line), and with a coincidence requirement with the silicon surface barrier detector (black, solid line). The energies of prominent sum peaks are labeled in the coincidence spectrum. There is also a label for the Q value for the β decay of ^{76}Ga at 6916.2(2.0) keV [17].

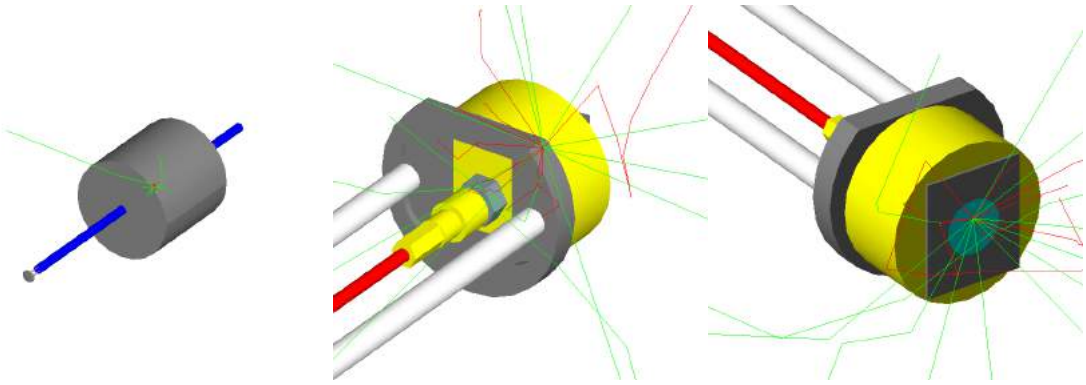

Figure 2.7: Visualization of the GEANT4 simulation for the SuN detector (left panel) and the silicon surface barrier detector attached to the target holder at the center of SuN (middle and right panels). The aluminum frame and aluminum foil are shown attached to the front of the silicon surface barrier detector. The sensitive volume of the silicon surface barrier detector (the silicon wafer) is not visible. The green lines are γ-ray tracks and the red lines are β-decay electron tracks.

The GEANT4 model of SuN and the silicon surface barrier detector was used to simulate each γ-ray cascade from the existing decay scheme for the β decay of ^{76}Ga [18] from the National Nuclear Data Center (NNDC). Each γ-ray cascade had a corresponding TAS spectrum, sum-of-segments spectrum, and multiplicity spectrum. These spectra were described in Sec. 1.7. The conditions imposed on the simulated spectra of these γ-ray cascades were identical to those imposed on the experimental spectra, such as the energy threshold applied to each SuN segment, as well as the same coincidence requirement with the silicon surface barrier detector by including β-decay electrons that have a kinetic energy distribution modified by a Fermi function [76]. The electron kinetic energy distribution and Fermi function were described in Sec. 1.5.5. A visualization of the GEANT4 simulation of SuN and the silicon surface barrier detector is shown in Fig. 2.7. An example of the energy deposition in the detectors from β-decay electrons is shown in Fig. 2.8.

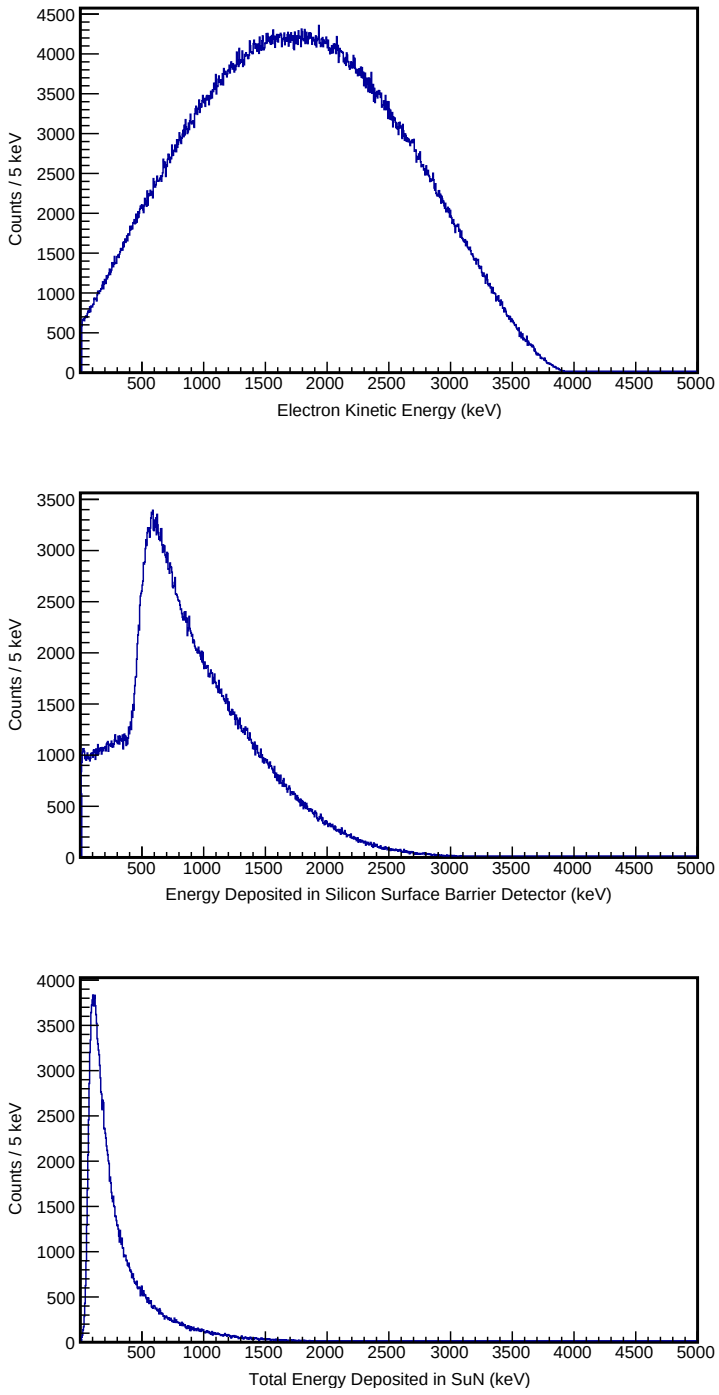

Figure 2.8: Example spectra from simulations showing the energy deposition in the detectors only from β-decay electrons. No γ rays were emitted in the simulation that created these spectra. The top panel shows the input electron kinetic energy distribution, the middle panel shows the energy deposited in the silicon surface barrier detector, and the bottom panel shows the total energy deposited in SuN. These spectra were obtained from a GEANT4 simulation of 2000000 events of electrons from a (Z, A) = (31, 76) nuclide. The maximum electron kinetic energy was 4000 keV. Electrons were isotropically emitted from the center of the aluminum foil (see Fig. 2.7).

The simulated spectra from all the γ-ray cascades were used to minimize the global χ^2:

$$\chi^2_{\text{global}} = \sum_i \sum_j \left(\frac{e_{ij} - s_{ij}}{\sqrt{e_{ij}}} \right)^2, \tag{2.2}$$

where the index i runs over all spectra included in the fit (typically the TAS spectrum, sum-of-segments spectrum, and multiplicity spectrum), the index j runs over all bins for each spectrum included in the fit, and e_{ij} and s_{ij} are the contents of spectrum i at bin j for experiment and simulation, respectively. The TAS spectrum, sum-of-segments spectrum, and multiplicity spectrum were fit simultaneously. Including these two latter spectra is important because the efficiency of SuN to produce a count in the TAS spectrum depends on the energy of the individual γ rays and multiplicity of the γ-ray cascade, information that is contained in the sum-of-segments spectrum and multiplicity spectrum, respectively. The quantity s_{ij} is affected by many different γ-ray cascades and therefore, for a given i, is defined as

$$s_{ij} = \sum_k p_k c_{jk}, \tag{2.3}$$

where the index k runs over all simulated γ-ray cascades, p_k is the probability for a particular γ-ray cascade, and c_{jk} is the content of bin j produced by γ-ray cascade k. The probabilities were continuously varied until χ^2_{global} was minimized. Note that the probabilities in Eq. 2.3 are the β-decay feeding intensity to a particular level multiplied by the probability for a specific γ-ray cascade from that level to the ground state. Because the probabilities of all γ-ray cascades from a level to the ground state must sum to unity, the sum of p_k for a given level is the β-decay feeding intensity to that level.

If the experimental spectra were not reproduced with the χ^2 minimization procedure using γ-ray cascades from the existing decay scheme, then so-called "pseudo levels" were

added to the existing decay scheme. A pseudo level is placed at a specific excitation energy in the existing decay scheme, and acts as a representative for all nearby levels within a bin size that depends on the energy resolution of SuN. Because knowing all the possible ways that a pseudo level can deexcite to the ground state is unknown, transitions to all levels in the existing decay scheme were included in the fitting process.

The aforementioned procedure was used here for the β decay of ^{76}Ga. Comparing the experimental and simulated spectra using the existing decay scheme reveals that even though ^{76}Ga is only one unit away from stability, the existing decay scheme is not well known (Fig. 2.9). Indeed, the existing decay scheme suffers from typical symptoms of the Pandemonium effect: in general, there is an overestimation of the β-decay feeding intensity at lower excitation energies, and an underestimation of the β-decay feeding intensity at higher excitation energies; in particular, the 1539 keV level that was previously observed in a high-resolution experiment to have a relatively large β-decay feeding intensity [20] is negligible in the present measurement.

In order to reproduce the experimental spectra, the β-decay feeding intensity to existing levels was adjusted. In addition, three pseudo levels were added to the existing decay scheme at 4600, 4950, and 5350 keV.

2.4 Results

2.4.1 Half-Life

The β-decay half-life of ^{76}Ga was measured by turning the beam off and measuring the implanted activity as a function of time. This allows one to create a decay curve, shown in Fig. 2.10, from which the half-life can be extracted. The decay curve is a histogram of

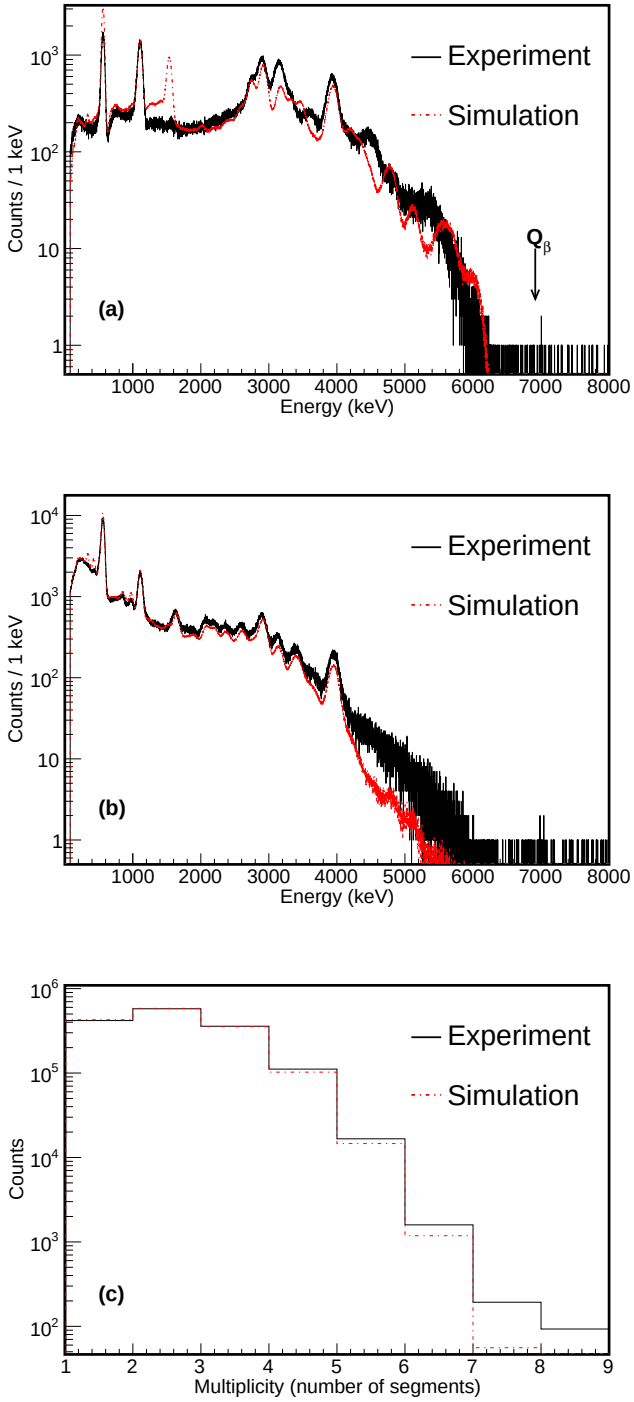

Figure 2.9: Comparison of experimental (black, solid line) and simulated (red, dashed-dotted line) spectra using the existing decay scheme [18] to illustrate the discrepancy with the measurements reported in the present work. The spectra are (a) the TAS spectrum, (b) sum-of-segments spectrum, and (c) multiplicity spectrum. All three spectra were created with an energy threshold of 80 keV applied to each SuN segment. There is a label for Q value in the TAS spectrum for the β decay of ^{76}Ga at 6916.2(2.0) keV [17].

time differences between the beginning of the run (beam off) and when a β-decay electron is registered in the silicon surface barrier detector. The decay curve between 0 and 300 s was fit using an exponential function. Only an exponential function was necessary because background and daughter contributions were absent. A half-life of 30.6(3) s was obtained for the β decay of ^{76}Ga, in reasonably good agreement with previous measurements. The half-life of ^{76}Ga has been measured four times in the past: Ref. [19] used fast neutron bombardment on natural Ge to produce ^{76}Ga via a (n,p) reaction, and obtained a half-life of 32(3) s; Ref. [20] used a (n,p) reaction on a GeO_2 target (enriched to 73.89% in ^{76}Ge) to produce ^{76}Ga, and obtained a half-life of 27.1(2) s; Ref. [21] produced ^{76}Ga from fission, and obtained a half-life of 29.8(4) s; Ref. [22] created ^{76}Ga with a (n,p) reaction on Ge metal (enriched to 92.82% in ^{76}Ge), and obtained a half-life of 32.6(6) s.

2.4.2 Total Absorption Spectroscopy

The TAS spectrum, sum-of-segments spectrum, and multiplicity spectrum were fit simultaneously in order to extract the β-decay feeding intensity distribution. Systematic uncertainties coming from the energy calibration and binning were taken into account and the final β-decay feeding intensity distribution in Table 2.2 is an average of all the fits with the aforementioned different fitting conditions of the energy calibration and binning. An example of one of those fitting conditions with a specific energy calibration and binning is shown in Fig. 2.11.

Three different sources of uncertainty contribute to the total uncertainty that is reported in Table 2.2. The first source of uncertainty comes from fitting with different conditions. For each excitation energy, the minimum, average, and maximum intensity of the different fitting conditions was calculated. The uncertainty is the difference between the average and the minimum/maximum intensity. The weighted average of the uncertainty from different

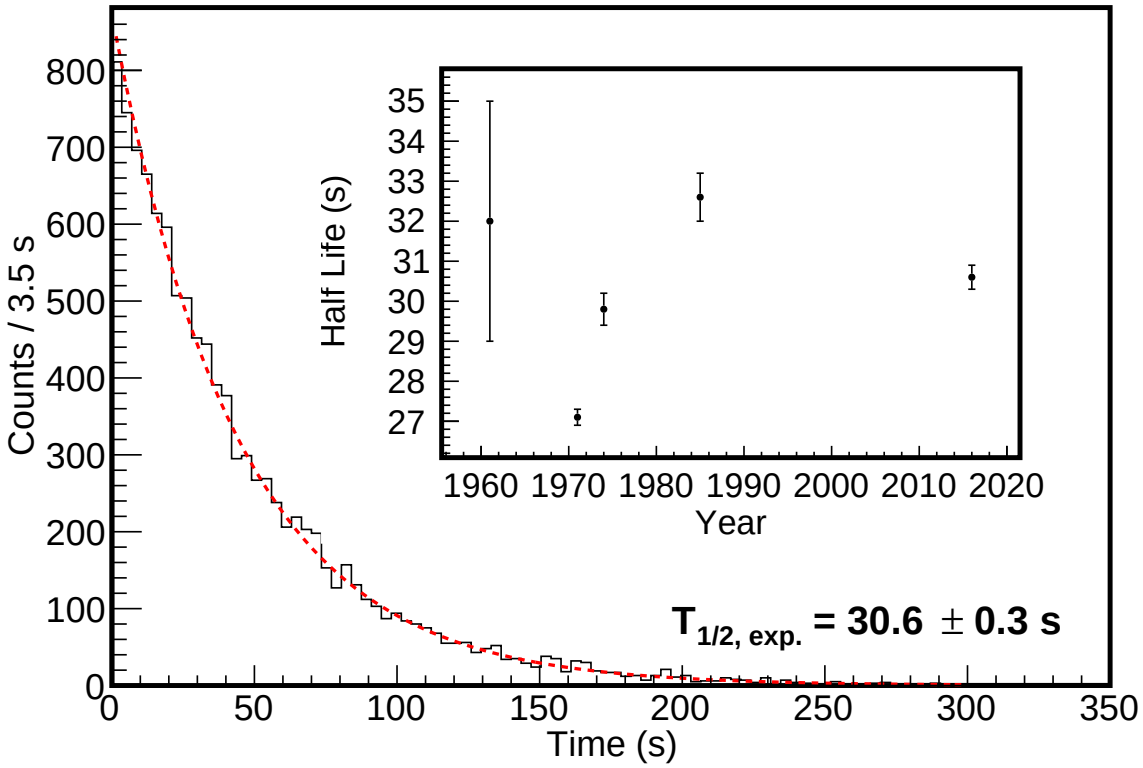

Figure 2.10: The experimental decay curve for the β decay of ^{76}Ga (black, solid line) and the exponential fit from 0 to 300 s (red, dashed line). The extracted half-life is 30.6(3) s. The inset shows the history of measurements of the half-life of ^{76}Ga. The measurement from 1961 is from Ref. [19], from 1971 is from Ref. [20], from 1974 is from Ref. [21], from 1985 is from Ref. [22], from 2016 is from the current work [23].

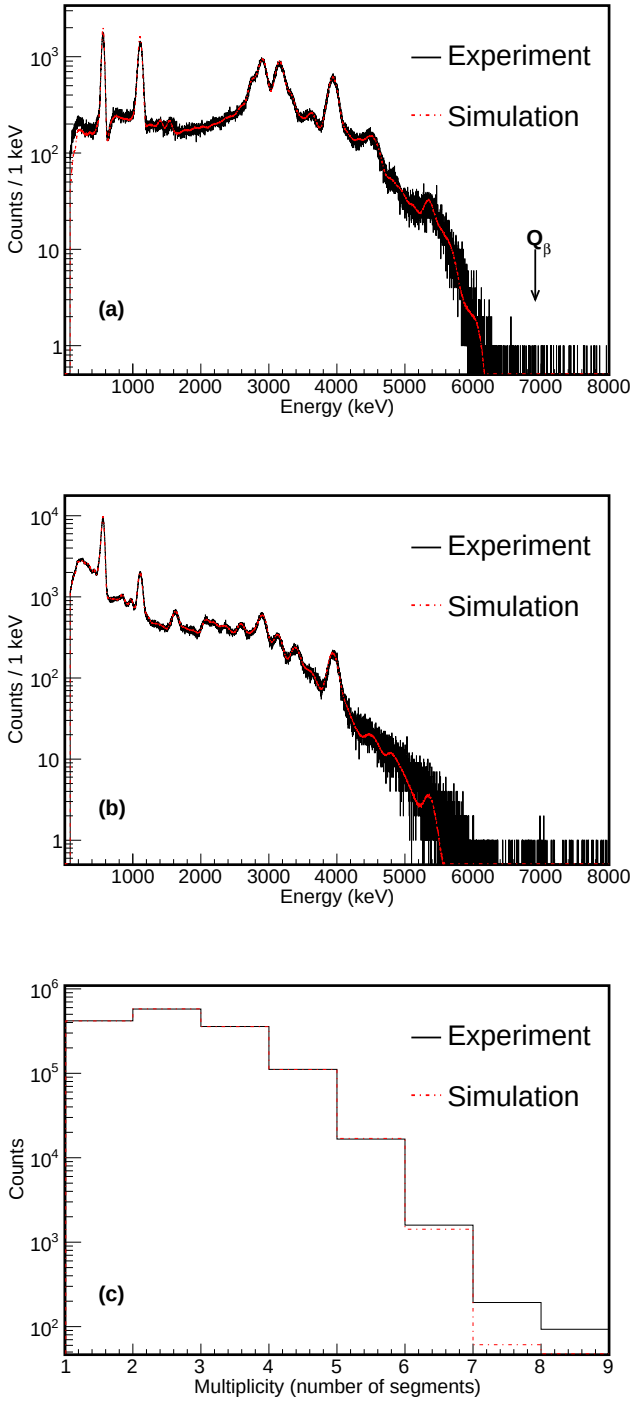

Figure 2.11: Comparison of experimental (black, solid line) and simulated (red, dashed-dotted line) spectra after fitting all three spectra simultaneously with the decay scheme modifications for (a) the TAS spectrum, (b) sum-of-segments spectrum, and (c) multiplicity spectrum. This is an example of one of the different fitting conditions with a specific energy calibration and binning. All three spectra were created with an energy threshold of 80 keV applied to each SuN segment. There is a label for Q value in the TAS spectrum for the β decay of ^{76}Ga at 6916.2(2.0) keV [17].

Table 2.2: The β-decay feeding intensity distribution of ^{76}Ga as a function of excitation energy in the daughter nucleus ^{76}Ge. Intensity values below 10^{-4} % are set to 0.

Energy (keV)	Intensity (%)	Error (–)	Error (+)	Energy (keV)	Intensity (%)	Error (–)	Error (+)
563	7.3	0.2	0.2	3887	3	1	1
1108	11.7	0.9	0.9	3952	12	1	1
1410	0.34	0.04	0.04	4122	1.4	0.2	0.2
1539	0.5	0.1	0.1	4193	1.2	0.2	0.2
1911	0.21	0.04	0.04	4239	0.04	0.04	0.05
2020	0.11	0.05	0.04	4327	2.4	0.4	0.3
2591	1.1	0.3	0.3	4364	0.1	0.1	0.3
2655	0			4477	2.3	0.3	0.3
2692	0.6	0.4	0.4	4600	3.4	0.6	0.6
2748	5.4	0.9	0.9	4720	0.31	0.07	0.06
2769	0			4784	0.54	0.09	0.09
2842	3.9	0.4	0.4	4813	0		
2920	9.8	0.9	0.9	4815	0.6	0.1	0.1
3142	9	1	1	4950	1.1	0.3	0.2
3182	7.4	0.9	0.9	5122	0.7	0.1	0.1
3232	0.7	0.2	0.2	5350	1.6	0.3	0.3
3312	1.8	0.2	0.2	5523	0.7	0.2	0.2
3323	2.9	0.3	0.3	5663	0.7	0.3	0.3
3335	0.2	0.2	0.2	5750	0.19	0.08	0.08
3409	0.24	0.04	0.04	5883	0.2	0.2	0.2
3478	1.6	0.2	0.2	6021	0.03	0.03	0.1
3633	2.8	0.4	0.4	6065	0.1	0.1	0.1

fitting conditions was 6%. The second source of uncertainty comes from the statistics of the TAS spectrum. The inherent statistical uncertainty in the number of counts per bin in the TAS spectrum is directly related to the uncertainty in the extracted β-decay feeding intensity distribution. The weighted average of the uncertainty from statistics was also 6%. The third source of uncertainty is from the efficiency of SuN. The efficiency of SuN depends on the multiplicity of the γ decay cascade and on the energy of the individual γ rays. The procedure described in Ref. [95] was used to estimate the uncertainty in the efficiency. The weighted average of the uncertainty from summing efficiency was 9%.

2.4.3 Theory

The ground state and β-decay properties of ^{76}Ga were calculated with the shell model. The calculations were performed with the NuShellX@MSU code [143]. The $jj44$ model space was used, which has an inert core of ^{56}Ni and active nucleons in the $0f_{5/2}$, $1p_{1/2}$, $1p_{3/2}$, and $0g_{9/2}$ single-particle orbitals for both protons and neutrons. Two Hamiltonians were used: the JUN45 Hamiltonian [144] and the jj44b Hamiltonian [145].

The NNDC [18] lists (2^+, 3^+) for the spin and parity of the ground state of ^{76}Ga, while a measurement of the magnetic moment [146] prefers a 2^- assignment when compared to shell-model calculations. With the JUN45 Hamiltonian there are 11 states below 300 keV in ^{76}Ga with spins (1-5)$^-$ and 2^+. Due to the uncertainty in the energy of the states, determining the spin and parity of the ground state in this situation is not possible with these Hamiltonians. Thus, the theoretical β decay for 2^+, 3^+, and 2^- were considered and compared with experiment. Shown in Fig. 2.12 is the cumulative β-decay feeding intensity of ^{76}Ga as a function of excitation energy in the daughter nucleus ^{76}Ge. Fig. 2.12 contains the measurement from the present work, along with theoretical calculations using

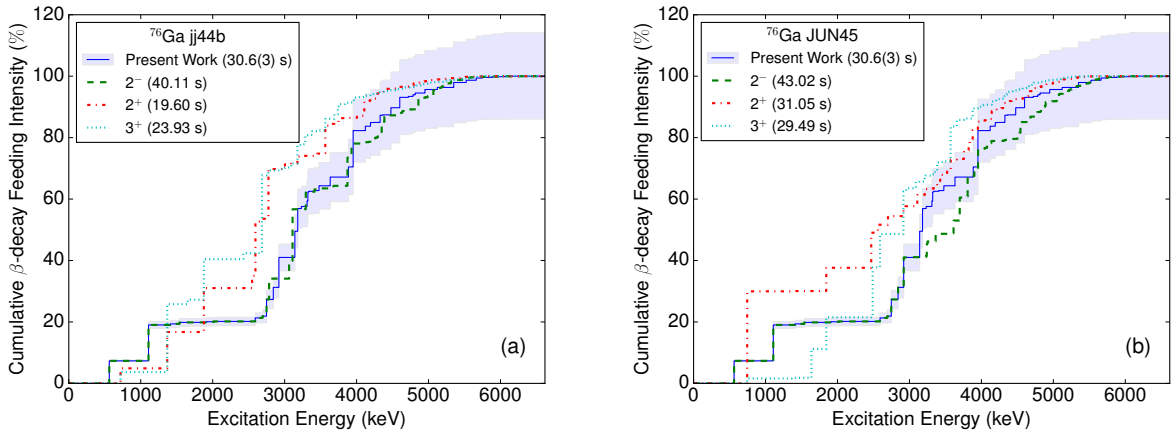

Figure 2.12: Cumulative β-decay feeding intensity of ^{76}Ga as a function of excitation energy in the daughter nucleus ^{76}Ge for the present work (blue, solid line, with uncertainty in light-blue shading) and calculations with different Hamiltonians and different assumptions of the spin and parity of the ground state of ^{76}Ga. Panel (a) contains calculations using the jj44b Hamiltonian and panel (b) contains calculations using the JUN45 Hamiltonian. The half-life from the present work and theoretical calculations are in parentheses. For the present work, the blue, solid line is the cumulative average intensity, and the lower/upper bound of the light-blue uncertainty band is the cumulative minimum/maximum intensity. See text for an explanation of why the 2$^-$ calculation and the present work are identical at relatively low excitation energy.

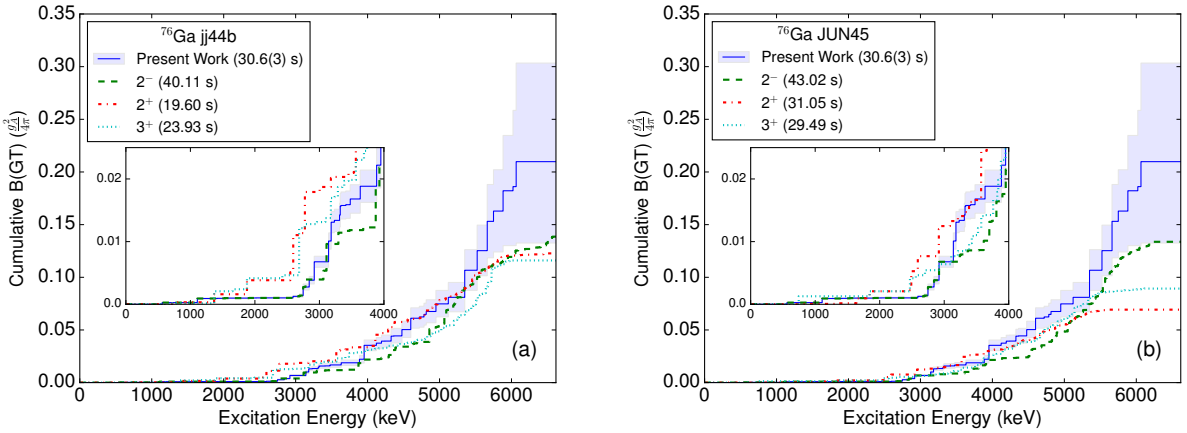

Figure 2.13: Same as Fig. 2.12, but for cumulative B(GT). The inset shows a zoomed-in view of the low excitation energy region.

the two Hamiltonians and different assumptions of the spin and parity of the ground state of ^{76}Ga. Calculating the first-forbidden (FF) β-decay transitions in the $jj44$ model space is not practical because most of the FF one-body transitions lie outside the model space (only the $0f_{5/2}$ to $0g_{9/2}$ is inside). The results for the two Hamiltonians in Fig. 2.12 generally agree with each other but differ on the detailed spectra for the daughter nucleus ^{76}Ge. Based on a comparison of experimental β^--decay half-lives with those calculated with these Hamiltonians in the $jj44$ model space a quenching factor of $g_A = 0.4g_{A_0}$ is required [147]. This quenching factor of $g_A = 0.4g_{A_0}$ was applied to both Hamiltonians. This is a larger quenching than the typical value of $g_A \approx 0.7g_{A_0}$ found for the sd and pf model spaces. The larger quenching is related to the fact that a large fraction of the β^- giant Gamow-Teller resonance lies outside the $jj44$ model space. The larger quenching approximately takes into account the coupling between the low-lying GT transitions to the missing part of the GT giant resonance.

The β-decay feeding intensity distribution was converted to a Gamow-Teller transition strength, B(GT), distribution according to Eq. 1.24. In Eq. 1.24, the β-decay feeding intensity distribution from the present work was used for I_β, the half-life from the present work was used for $T_{1/2}$, and the Q_β value was taken from the 2012 Atomic Mass Evaluation [17]. The Fermi integrals were calculated numerically as explained in Ref. [148]. A comparison of the present work to shell model calculations is shown in Fig. 2.13.

With these Hamiltonians, the states with negative parity in ^{76}Ge lie above 2.5 MeV. If the ground state of ^{76}Ga has positive parity, then the β-decay to states in ^{76}Ge below 2.5 MeV is GT. With a quenching factor of $g_A = 0.4g_{A_0}$ there is good agreement with the experimental half-life especially for the JUN45 interaction (see Figs. 2.12 and 2.13). When the ground state of ^{76}Ga has negative parity, all of the transitions to the low-lying positive

parity states in ^{76}Ge are FF. In this case the experimental values of the β-decay feeding intensity and Gamow-Teller transition strength were used in place of a theoretical estimate up to a threshold of 2.8 MeV for the jj44b interaction and a threshold of 3 MeV for the JUN45 interaction. With this method the half-life for the 2^- decay obtained with the jj44b Hamiltonian agrees with experiment, bearing in mind that there may also be FF transitions above the thresholds. Combining the results of this work and that in Ref. [146], the jj44b Hamiltonian is somewhat preferred and the ground state of ^{76}Ga is likely 2^-.

2.5 Conclusions

In an effort to provide experimental data that can be compared to theoretical models that are used to calculate nuclear matrix elements relevant to the neutrinoless double-β decay of ^{76}Ge, the β decay of ^{76}Ga was studied for the first time using the technique of total absorption spectroscopy with the SuN detector at the National Superconducting Cyclotron Laboratory. The measurement revises current values for the β-decay feeding intensity distribution found in the existing decay scheme at the National Nuclear Data Center because the existing decay scheme appears to have suffered from the Pandemonium effect. Regarding the theoretical calculations, the jj44b Hamiltonian does better than JUN45 for this particular decay for the assumed spin and parity of the ground state of ^{76}Ga. This is evident by the comparison to the β-decay feeding intensity distribution (Fig. 2.12), where jj44b can reproduce the data in the whole energy region. However, there are many nearly degenerate spin and parities predicted for ^{76}Ga and the experimental value for the ground state is not definite. The overall success of these two Hamiltonians will depend on their comparison to a wide range of data, which goes beyond the scope of this chapter.

Chapter 3

β-decay Studies with Fast Beams

The experiment titled "Probing the r-process path with total absorption spectroscopy" was performed from November 26, 2014, through December 4, 2014 at the NSCL (experiment e12001). Having performed the proof-of-principle experiment with a thermalized beam described in Ch. 2, the goal of this second β-decay experiment with SuN was to study the β-decay properties of neutron-rich nuclides relevant to the r process. These nuclides were studied with a fast beam, and this experiment was the first-ever application of the TAS technique with a fast beam produced via projectile fragmentation. β-decay experiments using fast beams require the use of more complex experimental setups and analysis procedures, compared to those using thermalized beams. β-decay half-lives were extracted for the nuclides ^{99}Y, ^{101}Zr, ^{102}Zr, ^{102m}Nb, ^{103}Nb, ^{104m}Nb, and ^{109}Tc. Additionally, the β-decay feeding intensity distributions and B(GT) distributions were extracted for ^{101}Zr, ^{102}Zr, and ^{109}Tc.

3.1 Experimental End Station

The Coupled Cyclotron Facility (Fig. 3.1) at the NSCL produced a primary beam of ^{124}Sn^{45+} with an energy of 120 MeV/u, which impinged upon a ^{9}Be production target with a thickness of 403 mg/cm^2. The resulting ions from the fragmentation reaction were filtered with the A1900 fragment separator [138], using a 60 mg/cm^2 aluminum wedge, to produce a secondary

cocktail beam that consisted of neutron-rich nuclides with atomic numbers ranging from 39 to 43 and mass numbers ranging from 100 to 110. Due to the use of the full momentum acceptance (5%) of the separator, a thin (30 mg/cm^2), plastic (BC-400), position-sensitive scintillator at the intermediate dispersive image was used to provide information about the momentum (and time of flight) of an ion. The scintillator was referred to as the "Image 2" or "I2" scintillator. After the A1900 fragment separator, the ions were delivered to the experimental end station in the S2 vault. The experimental end station, ordered along the beam line, consisted of two silicon PIN detectors, an implantation station, and the Summing NaI(Tl) (SuN) detector. The implantation station consisted of a double-sided silicon-strip detector (DSSD) and a silicon surface barrier detector. Signals from all of the detectors in the end station were recorded with the NSCL Digital Data Acquisition System (DDAS) [96]. The experimental end station in the S2 vault is shown in Fig. 3.2, and an overview of the electronics setup is shown in Fig. 3.3.

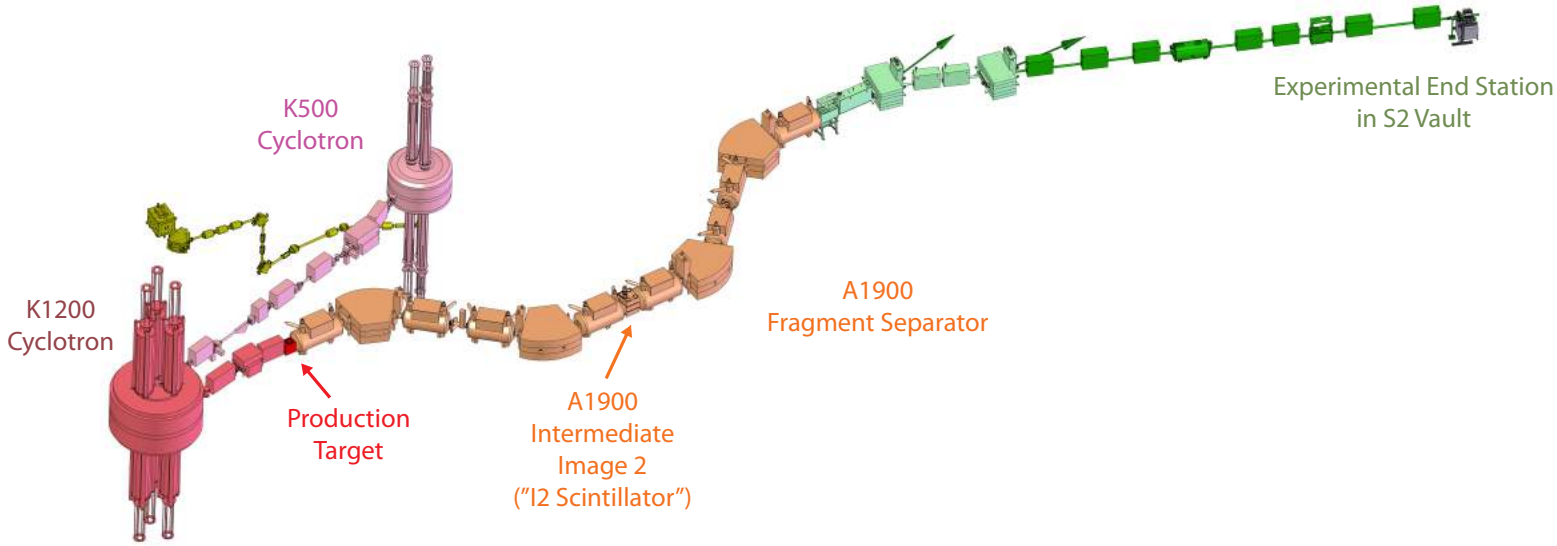

Figure 3.1: Schematic layout of the Coupled Cyclotron Facility at the NSCL. Shown are the K500 cyclotron, K1200 cyclotron, A1900 fragment separator, and the experimental end station in the S2 vault. More details can be seen in Fig. A.1.

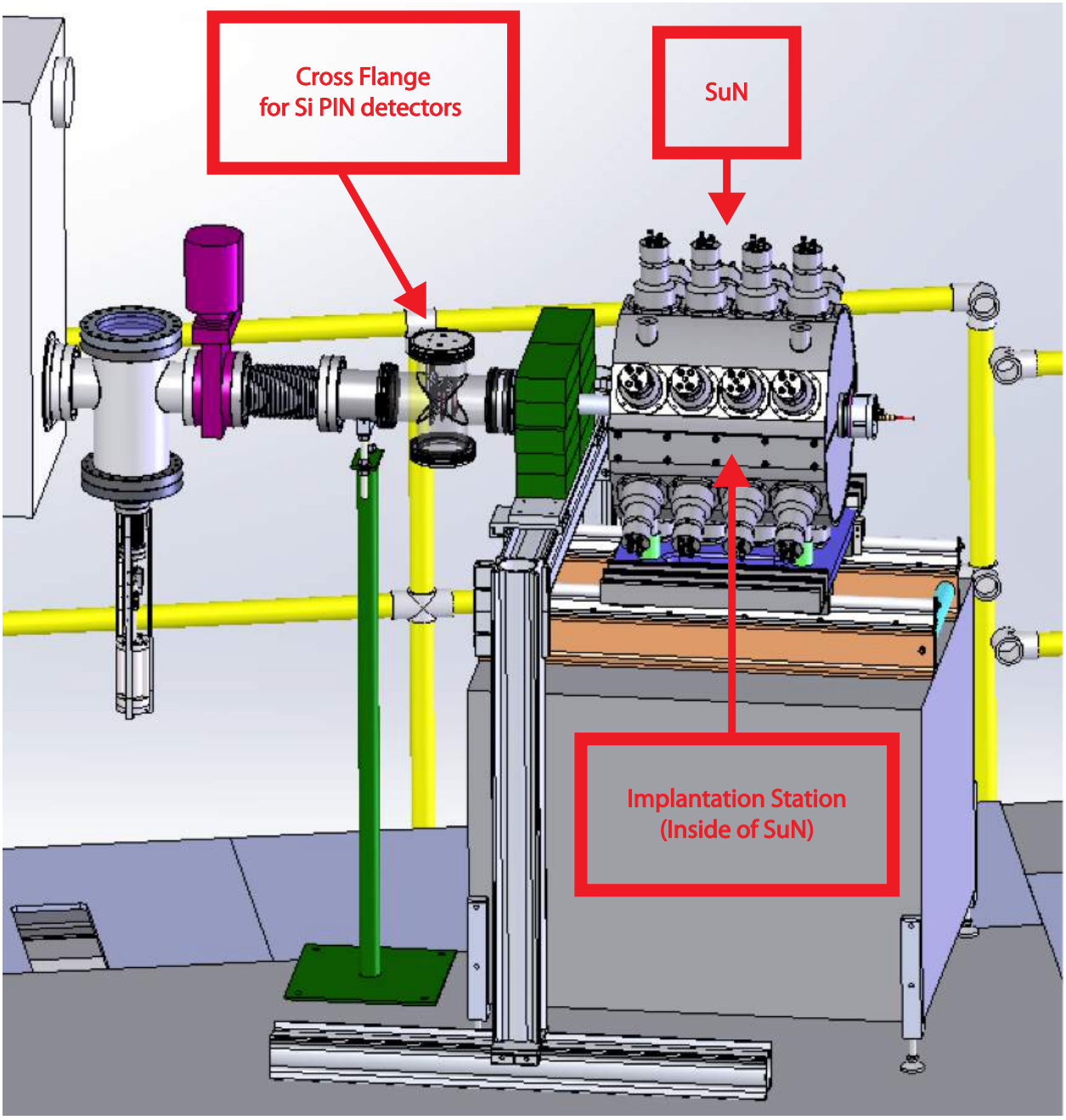

Figure 3.2: Experimental end station in the S2 vault for NSCL experiment e12001. The secondary beam from the A1900 fragment separator enters from the left side of the picture. More details can be seen in Fig. A.2.

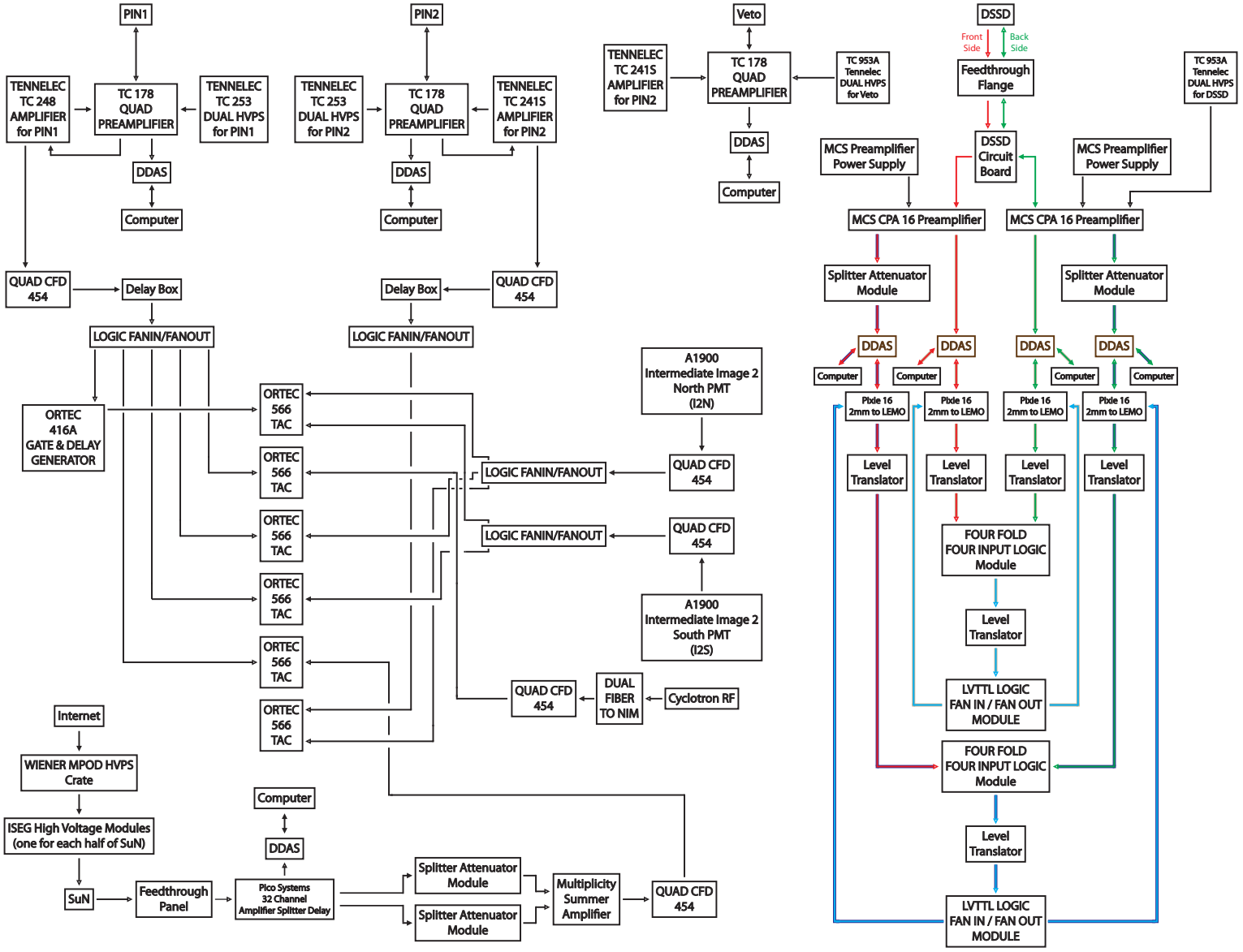

Figure 3.3: Overview of the electronics setup for NSCL experiment e12001. All detectors are shown along with trigger conditions. More details can be seen in Fig. A.3.

3.1.1 Silicon PIN Detectors

The two silicon PIN detectors (Fig. 3.4) were installed in the cross flange upstream from SuN and provided information about the energy loss and time of flight of an ion. These two detectors were designated PIN1 and PIN2. PIN1 and PIN2, which had thicknesses of 488 μm and 503 μm, respectively, were rotated 40° to create effective thicknesses of approximately 637 μm and 657 μm, respectively. The angle of rotation was chosen so that, after energy deposition in the PIN detectors, the ions of interest would stop, or implant, at the center of the DSSD.

PIN1 was biased with +50 V (leakage current of 1.2 μA) and PIN2 was biased with +32 V (leakage current of 0.72 μA). Signals from PIN1 and PIN2 were passed to a feedthrough flange to reach the outside of the beam line and were then sent into preamplifiers (Tennelec TC 178 Quad Preamplifiers). The output of each preamplifier was sent through a passive splitter in order to extract energy and timing information necessary for particle identification. For energy, one signal from the splitter went directly into DDAS. For timing, one signal from the splitter went to an amplifier (Tennelec TC 248 Amplifier for PIN1 and Tennelec TC 241S Amplifier for PIN2). Signals from the amplifiers were processed in constant fraction discriminators (Canberra Quad CFD 454), and used as the "start" input for multiple time-to-amplitude converters (Ortec 566 TACs). The timing signals were used in multiple TACs with the use of logic fan-in / fan-out modules.

The preamplifiers had gain settings of 0.1 GeV, 1 GeV, and 10 GeV, and the gain setting was chosen based on the amount of energy deposition in the PIN detectors by the secondary beam. The segment of the A1900 fragment separator immediately before the experimental setup in the S2 vault was segment 6. Using the magnetic rigidity of segment 6, $(B\rho)_6$ =

3.2097 Tm, the energy deposition of the ions of interest in the PIN detectors according to LISE++ was approximately 1.6-1.9 GeV for PIN1 and approximately 2.1-2.5 GeV for PIN2. Consequently, the preamplifier channels for both PIN detectors had gain settings of 10 GeV.

Both PIN detectors were tested with an ^{241}Am source before the start of the experiment using the 0.1 GeV gain setting. The goal of these tests was to try to improve the energy resolution of the PIN detectors and therefore improve particle identification. These tests included adjusting the energy filter parameters in DDAS, applying different biasing voltages, and testing different channels of the preamplifiers. The optimized energy resolution of both PIN detectors after these tests was approximately 4% at $E_\alpha = 5486$ keV. PIN1 had a slightly better energy resolution and was chosen as the first PIN detector in the path of the secondary beam. The results from these tests obtained with the 0.1 GeV gain setting were assumed to also apply for the 10 GeV gain setting used for the experiment.

3.1.2 Implantation Station

The implantation station (Fig. 3.5) was installed in the center of the borehole of SuN. The DSSD was positioned at the geometric center of SuN, and was used to detect high-energy ion implantations and subsequent low-energy β-decay electrons, which were spatially and temporally correlated to one another [149]. The correlation procedure is described in Sec. 3.2.2. Simultaneous detection of implantations (depositing energy on the order of GeV in the DSSD) and β-decay electrons (depositing energy on the order of keV and MeV in the DSSD) was achieved with dual-gain preamplifiers (specifically, Multi Channel Systems 16-channel preamplier CPA 16). The low-gain stage (0.09 V/pC) was used for detecting implantations, while the high-gain stage (1.63 V/pC) was used for detecting β-decay electrons. Manufactured by Micron Semiconductor Ltd. [150], the DSSD was designed

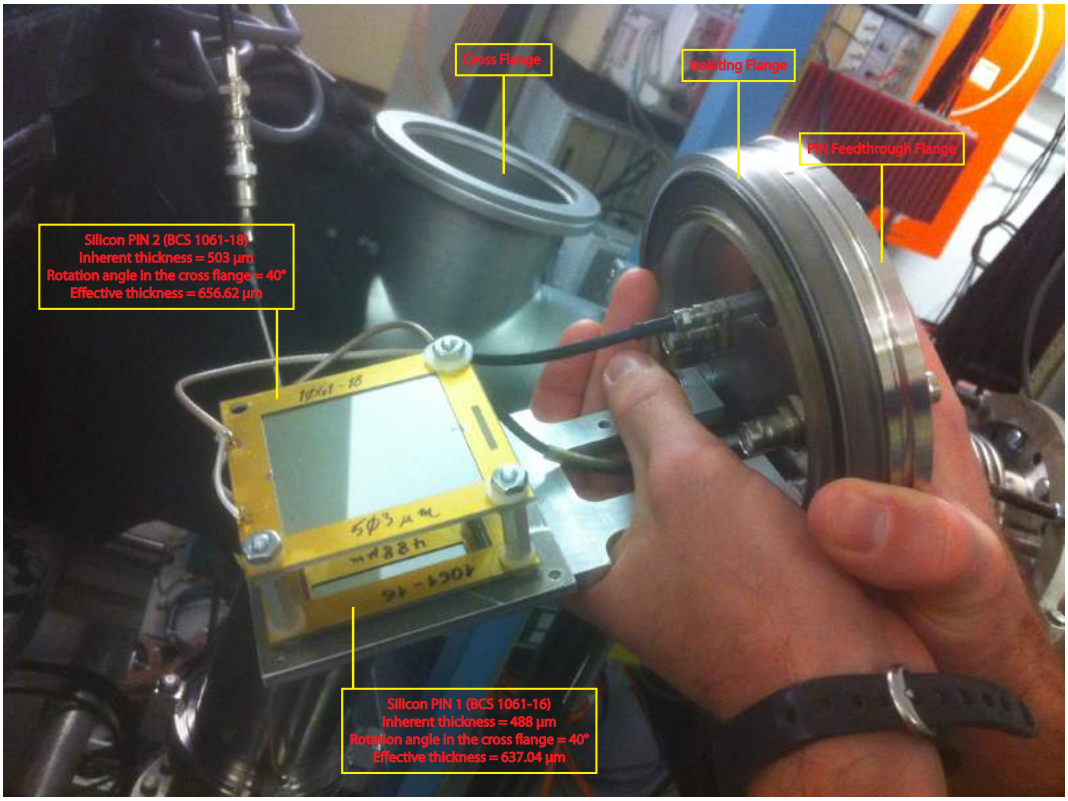

Figure 3.4: The two silicon PIN detectors used for NSCL experiment e12001. These were installed in the cross flange (labeled in the picture) with a specific rotation angle.

to fit inside the borehole of SuN using the BB8 design. The silicon chip of the DSSD had a thickness of 1030 μm, dimensions of 21.8 mm by 21.8 mm, and an active area of 20.0 mm by 20.0 mm. There were 16 horizontal strips on the front side and 16 vertical strips on the back side, effectively creating 256 pixels. The 16 strips on a side were numbered 0 through 15. All strips had a pitch of 1250 μm. Roughly 25 mm downstream from the DSSD was a silicon surface barrier detector that acted as a veto detector to detect any ions (particularly light, charged particles) that did not stop in the DSSD. The veto detector was manufactured by ORTEC with model number BU-014-300-500 (active area of 300 mm^2 and depletion depth of 500 μm).

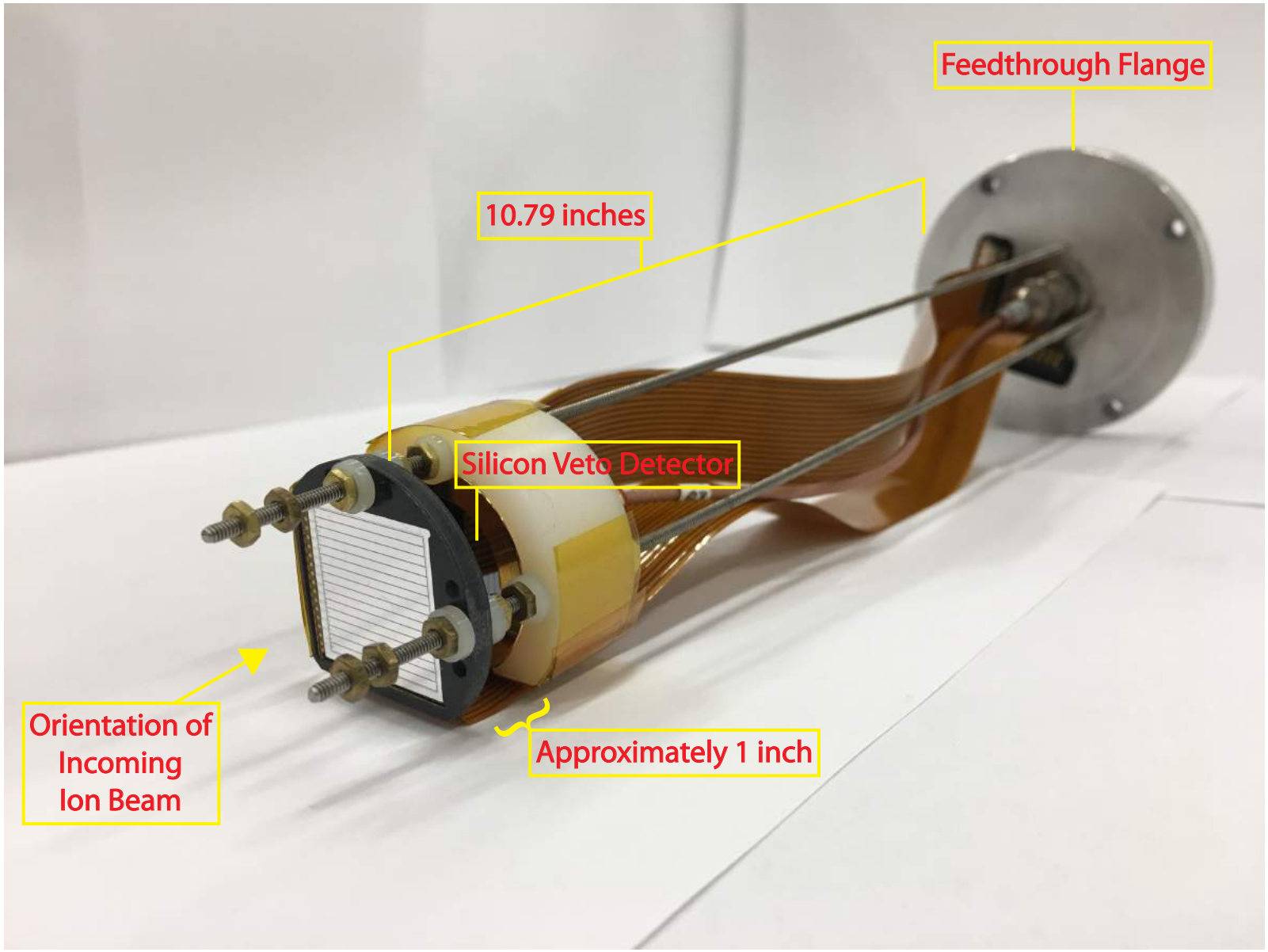

Figure 3.5: The implantation station used for NSCL experiment e12001. Shown are the double-sided silicon-strip detector (DSSD) and the silicon surface barrier detector (veto). More details can be seen in Fig. A.5.

Two nearly identical implantation stations, labeled "1" and "2", were constructed before the start of the experiment. Having a second, spare implantation station was beneficial in case one failed or was damaged during the experiment. The only difference between them was the high voltage applied to the detectors, as indicated on the manufacturer specification sheets. Implantation station "2" was used for NSCL experiment e12001. In this implantation station, the back side of the DSSD was biased with +90 V (leakage current of 0.17 μA), and the veto detector was biased with +50 V (leakage current of 0.18 μA). In implantation station "1", the back side of the DSSD was biased with +110 V (leakage current of 0.56 μA), and the veto detector was biased with +60 V (leakage current of 0.15 μA). For both implantation stations, the high voltage input for the preamplifier for the front side of the DSSD was terminated with a 50 Ω resistor.

As mentioned earlier, the implantation station was carefully designed and constructed to fit inside the small borehole of SuN. The implantation station was suspended by two stainless steel threaded rods, which connected into the feedthrough flange. A nylon holder supported the veto detector. To ensure the DSSD was at the geometric center of SuN, two distances were maintained. One was that the distance between the edge of the feedthrough flange and the back of the DSSD was 10.79 inches (see Fig. 3.5). The other was that the distance between the edge of the backup ring and the edge of the centering ring was 0.125 inches (see Fig. 3.2). The DSSD and veto detector were held in place with plastic washers and brass hex nuts. Kapton tape secured the cables from the DSSD to the holder for the veto detector. Kapton tape also protected the cables as they slid against the inside of SuN's beam pipe when the implantation station was inserted or removed.

The DSSD was read out with two cables (one directly attached to the front side and one directly attached to the back side). Each cable carried 18 signals: 16 signals for the

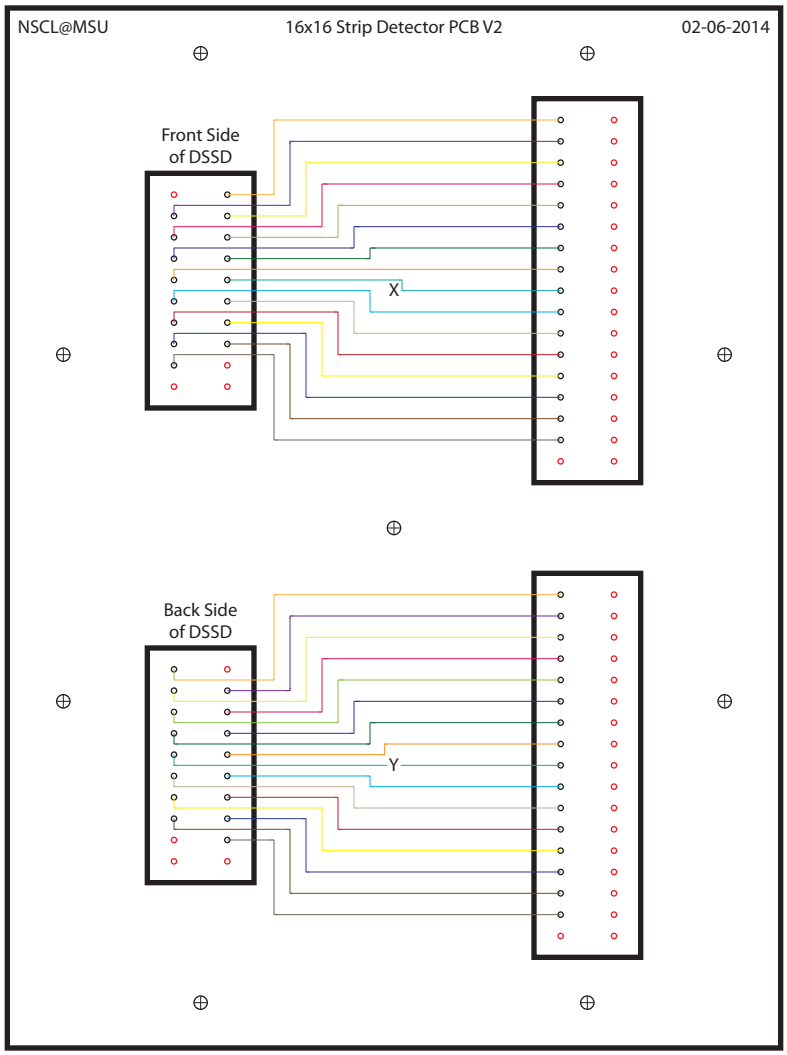

Figure 3.6: Diagram of the circuit board that was an intermediate stage between the DSSD and the dual-gain preamplifiers. More details can be seen in Fig. A.6.

individual strips, 1 signal for the frame, and 1 signal for the guard ring. Each cable was passed to the feedthrough flange to reach the circuit board (Fig. 3.6) outside of SuN. The circuit board was necessary to properly group the signals together and match the input specifications of the dual-gain preamplifiers.

Using the capabilities of DDAS, traces were recorded for the low-gain stage of the DSSD. They were recorded with a delay of 2.5 μs and a length of 6 μs. Observing traces during the experiment showed that the signals were being clipped (left panel of Fig. 3.7). That

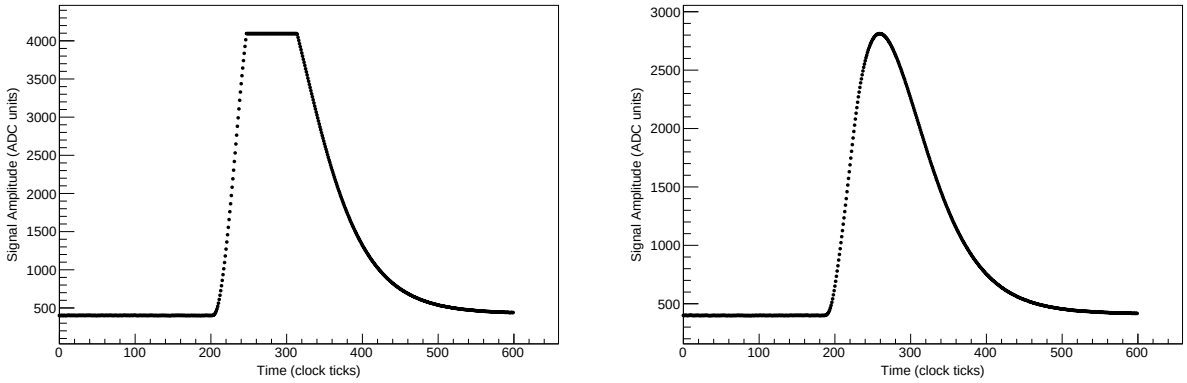

Figure 3.7: Traces recorded for strips of the low-gain stage of the DSSD. Left panel: A clipped signal for strip number 4 on the front side. Right panel: A non-clipped signal for strip number 7 on the front side. One clock tick equals 10 nanoseconds.

is, the energy deposited in the DSSD from ions saturated the analog-to-digital converters (ADCs) of DDAS. One problem with clipped signals is obtaining an accurate determination of the energy deposition in the DSSD. This problem was solved during the experiment with a splitter/attenuator module. Signals were split for each strip of the low-gain stage, with one output terminated with a 50 Ω resistor so that the amplitude of the signal was attenuated. This prevented the signal from being clipped (right panel of Fig. 3.7).

3.1.2.1 DSSD triggering conditions

An external trigger, which was a "front-back coincidence" and configured in hardware, was required to record signals in the DSSD. For a given side of the DSSD, an OR signal was generated whenever a strip produced a signal above threshold. Whenever an OR from the front side and an OR from the back side overlapped in time, an AND signal was created and used as a validation window for recording the raw signals that originally produced the OR signals. The external trigger reduced the recording of random noise, which enabled the lowering of trigger thresholds and therefore increased the detection efficiency of low-energy

β-decay electrons.

The electronics setup for the external trigger is shown in detail in Fig. 3.3 (also Figs. A.3 and A.4), and the main points will be discussed here. Different signals and timing parameters were used to create the external trigger, which was required for both the low-gain and high-gain stages of the DSSD. Only the high-gain stage could be tested with radioactive sources, and the timing parameters for the high-gain stage were assumed to also work for the low-gain stage and were confirmed with beam. The external trigger required a "breakout module" or "breakout box" (identified as "Pixie 16 2mm to LEMO" in Figs. 3.3, A.3, and A.4), which was used to provide input to and view output from a DDAS module. Because each side of the DSSD had 16 strips and each DDAS module contained 16 channels, each combination of gain stage and side of the DSSD had a corresponding DDAS module. For example, there was a DDAS module dedicated to the high-gain stage and front side of the DSSD. Individual strips had raw signals (yellow and purple signals in the top panel of Fig. 3.8). If the energy deposition in a strip was above the trigger threshold, the DDAS module produced a channel trigger associated with that strip (blue and green signals in the top panel of Fig. 3.8). The channel trigger could be viewed with "o0" of the breakout module, and the delay of each channel trigger (white and red arrows in the top panel of Fig. 3.8) could be adjusted. Each DDAS module also had a 16-channel OR, which was produced when the energy deposition in any of the 16 strips was above the trigger threshold (yellow and blue signals in the middle panel of Fig. 3.8). The OR could be viewed with "o6" of the breakout module, and the width of each OR (red and white arrows in the middle panel of Fig. 3.8) could be adjusted. The delay of each OR was adjusted so that the OR signals from each side of the DSSD overlapped in time. The OR from each side was sent into a logic module (Four Fold Four Input Logic Module) to create an AND signal (purple signal in the middle panel of Fig. 3.8). The AND

signal was created when the two OR signals overlapped in time (in other words, a front-back coincidence). The AND signal was eventually sent as input to the DDAS module ("i4" of the breakout module) and interpreted by the DDAS module as an external trigger (viewed with "o3" of the breakout module). An example of a successful front-back coincidence is shown in the bottom panel of Fig. 3.8. In this case, the channel triggers (yellow and purple signals in the bottom panel of Fig. 3.8) were successfully delayed to fall inside the external trigger (blue and green signals in the bottom panel of Fig. 3.8). When that occurred, a validated trigger (viewed with "o2" of the breakout module) was created whose presence allowed the system to acquire data.

3.1.2.2 DSSD Calibrations and Thresholds

The strips of the high-gain stage of the DSSD were calibrated with radioactive sources of ^{228}Th, ^{241}Am, and ^{249}Cf. The thresholds for the strips in the high-gain stage ranged from 150 keV to 200 keV. The strips of the DSSD in the low-gain stage were gain matched with secondary beam. The strips of the DSSD in the low-gain stage could have also been gain matched with primary beam, which was delivered to the experimental end station.

3.1.3 Summing NaI(Tl) (SuN) Detector

Surrounding the implantation station was the SuN detector (Fig. 3.9) to detect β-delayed radiation and employ the TAS technique.

3.1.3.1 Gain Matching and Calibration

The same procedure described in Sec. 2.3 was used to gain match the PMTs of SuN. The high voltages and multiplication factors used to gain match each PMT of SuN are listed in

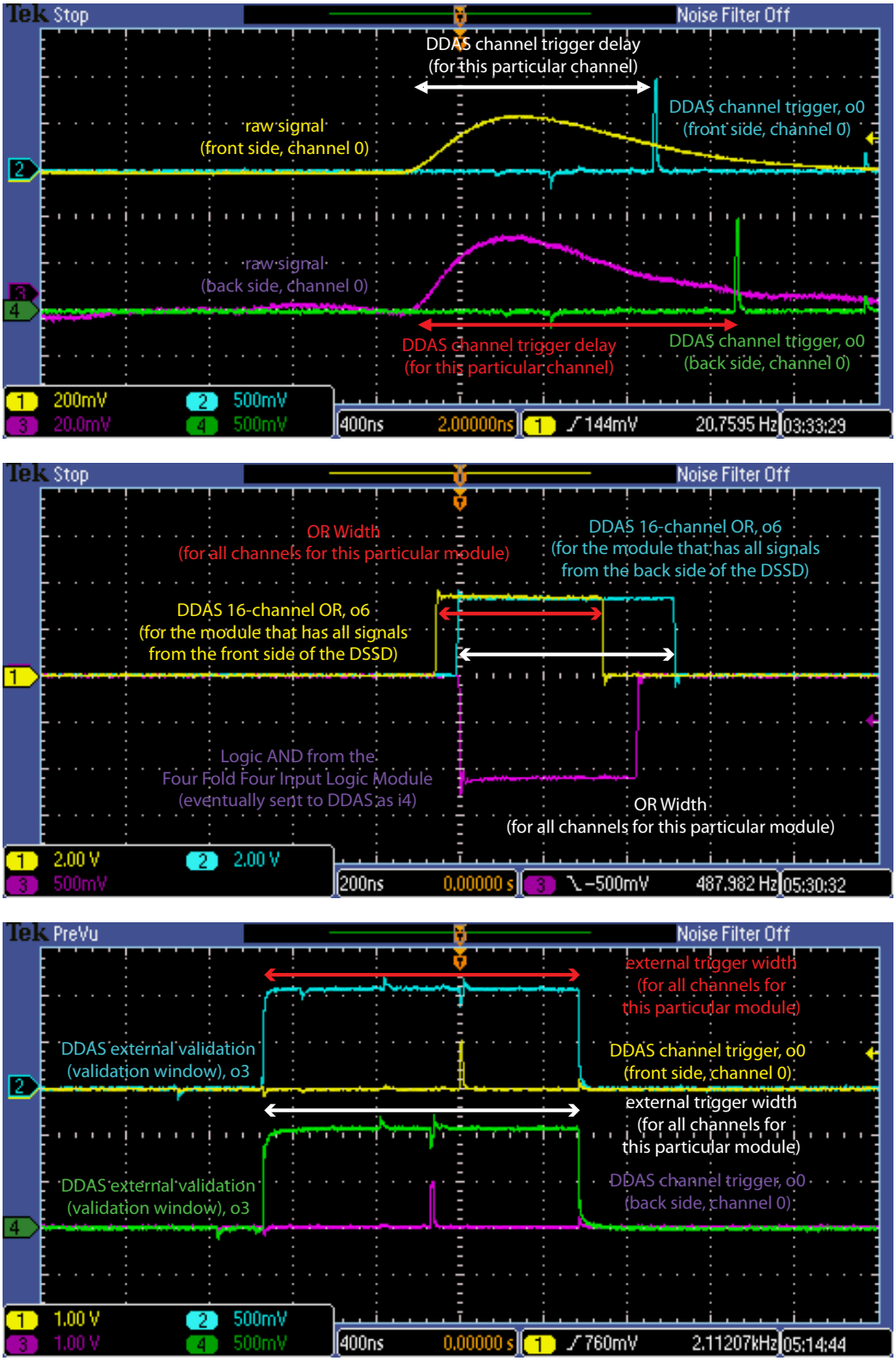

Figure 3.8: DSSD strip and logic signals used to create the front-back coincidence external trigger. The annotations describe either signals of the same color or a timing parameter. See main text for details.

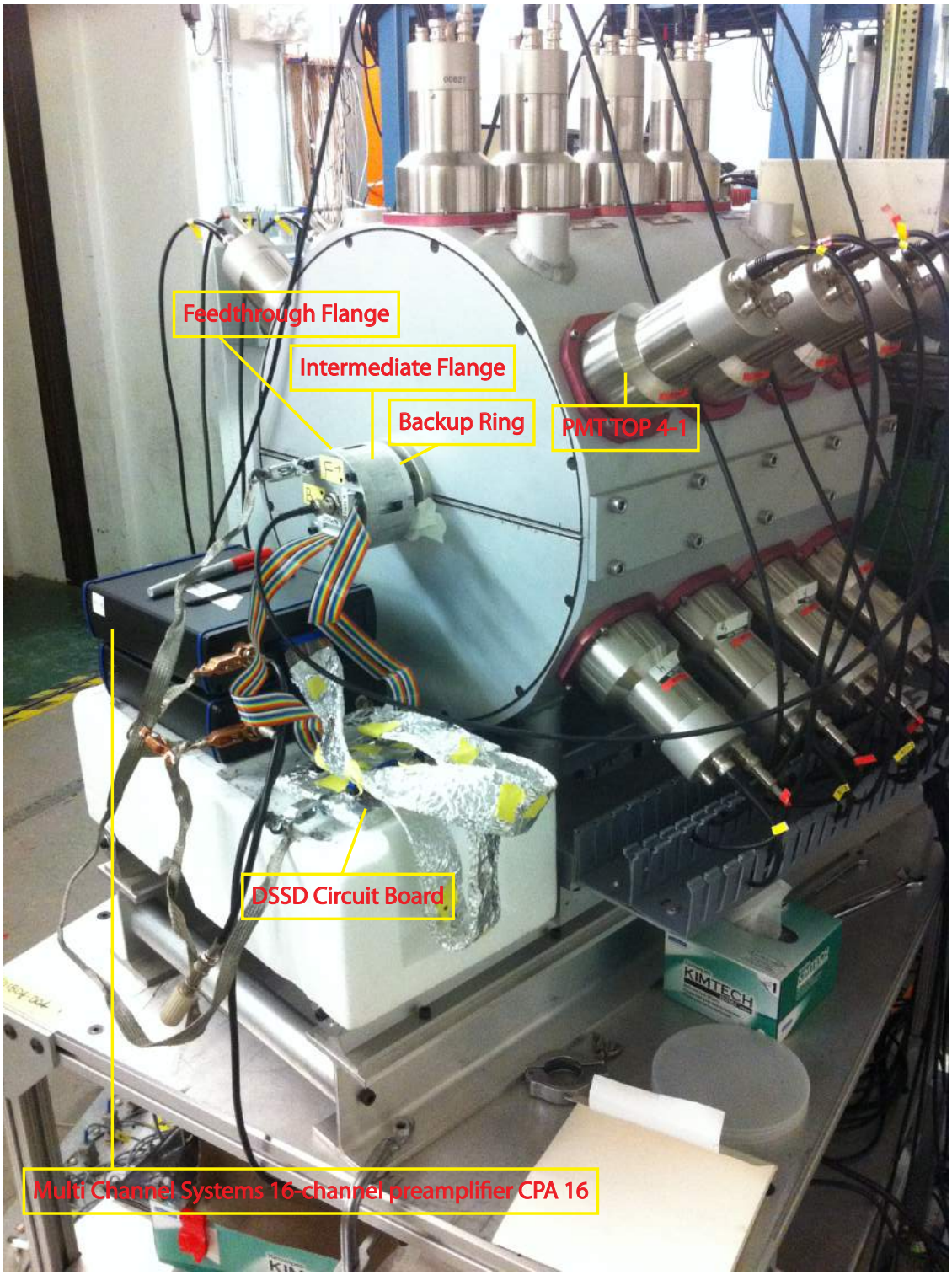

Figure 3.9: The SuN detector during NSCL experiment e12001. Also shown are cables for the implantation station inside of SuN, and the circuit board and dual-gain preamplifiers for the DSSD. More details can be seen in Fig. A.7.

Table 3.1: High voltages and multiplication factors used to gain match each PMT of SuN for NSCL experiment e12001. For a given PMT label, the letter indicates the top or bottom half of SuN ("B" for bottom and "T" for top), the first number indicates the segment of SuN, and the second number indicates the PMT within the segment. For example, the label T23 means PMT 3 of segment 2 of the top half of SuN.

PMT	High Voltage (V)	Gain Matching Multiplication Factor
B11	+839	1.00302
B12	+823	1.00000
B13	+824	1.00471
B21	+837	0.98604
B22	+869	1.00000
B23	+831	0.98516
B31	+895	1.01071
B32	+858	1.00000
B33	+835	1.01021
B41	+915	0.99010
B42	+936	1.00000
B43	+899	0.99156
T11	+732	1.00636
T12	+744	1.00000
T13	+782	1.01613
T21	+779	0.98897
T22	+774	1.00000
T23	+769	0.98874
T31	+798	0.98781
T32	+806	1.00000
T33	+817	0.98880
T41	+842	1.00502
T42	+829	1.00000
T43	+852	1.00746

Table 3.1.

The segments of SuN were calibrated with the same procedure described in Sec. 2.3. An effort was made to use as many radioactive sources as possible and to cover as broad of an energy range as possible. The sources used in the calibration are shown in Table 3.2. The segment calibrations are shown in Fig. 3.10 and the residual plots are shown in Fig. 3.11. In Figs. 3.10 and 3.11, note that some of the lower-energy γ rays were not detected in the outer segments of SuN.

Table 3.2: Standard radioactive sources used to calibrate the segments of SuN.

Source	Decay	γ-ray Energy (keV)
^{241}Am	$^{241}\text{Am} \rightarrow {}^{237}\text{Np}$	59.5
^{228}Th	$^{212}\text{Pb} \rightarrow {}^{212}\text{Bi}$	238.6
^{249}Cf	$^{249}\text{Cf} \rightarrow {}^{245}\text{Cm}$	388.2
^{228}Th	$^{208}\text{Tl} \rightarrow {}^{208}\text{Pb}$	583.2
^{137}Cs	$^{137}\text{Cs} \rightarrow {}^{137}\text{Ba}$	661.7
^{60}Co	$^{60}\text{Co} \rightarrow {}^{60}\text{Ni}$	1173.2
^{60}Co	$^{60}\text{Co} \rightarrow {}^{60}\text{Ni}$	1332.5
^{228}Th	$^{208}\text{Tl} \rightarrow {}^{208}\text{Pb}$	2614.5

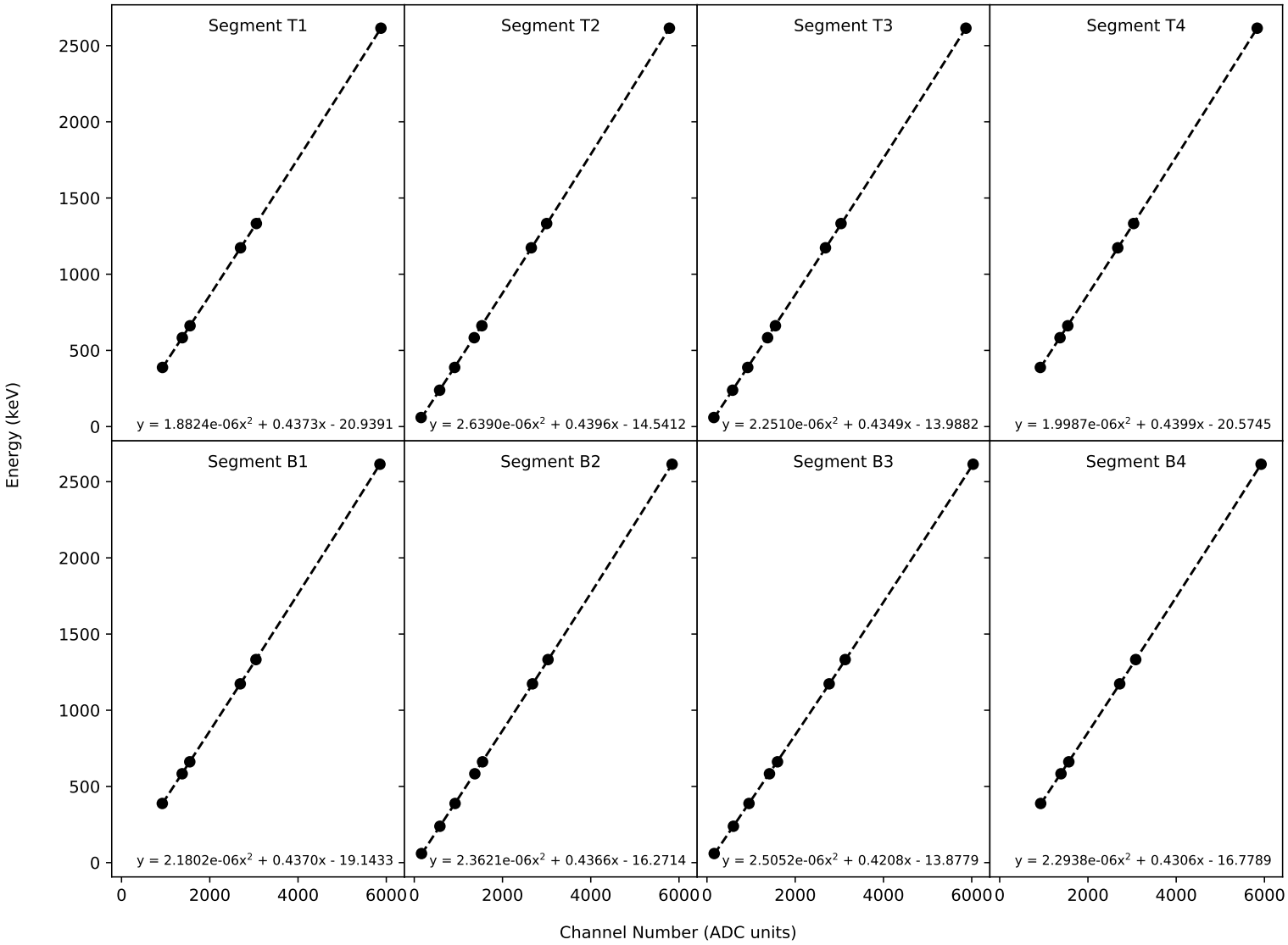

Figure 3.10: Calibrations for each segment of SuN for NSCL experiment e12001. For a given segment label, the letter indicates the top or bottom half of SuN ("B" for bottom and "T" for top), and the number indicates the segment number. For example, the label T2 means segment 2 of the top half of SuN.

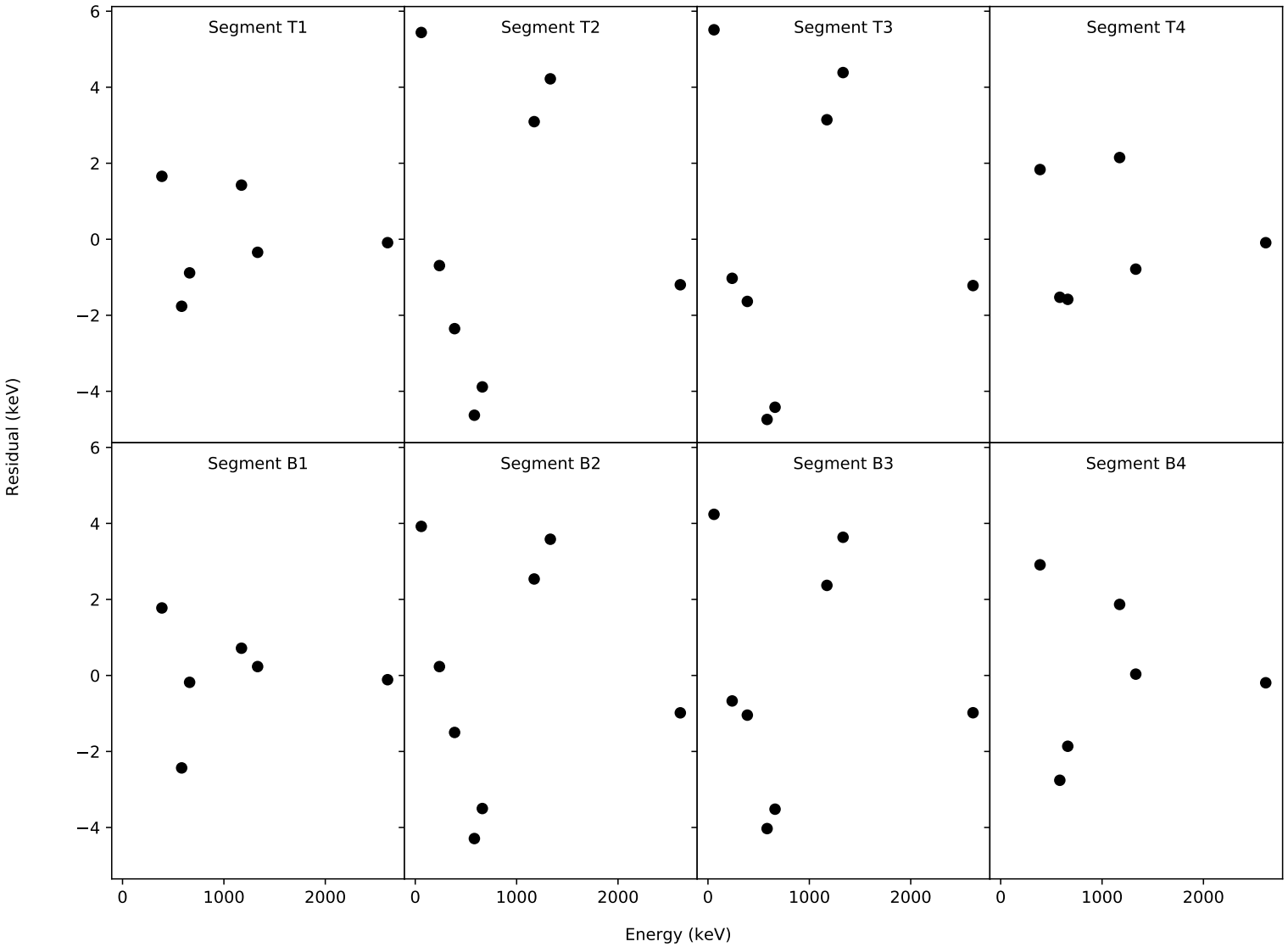

Figure 3.11: Residual plots for the SuN segment calibrations for NSCL experiment e12001. For a given segment label, the letter indicates the top or bottom half of SuN ("B" for bottom and "T" for top), and the number indicates the segment number. For example, the label T2 means segment 2 of the top half of SuN.

3.1.3.2 Thresholds

The existing decay schemes of the nuclides studied in NSCL experiment e12001 contained many low-energy γ rays (less than 100 keV). To increase the detection efficiency of these low-energy γ rays, the trigger thresholds for all of SuN's PMTs were lowered before the start of the experiment. The trigger thresholds were lowered until the 59.5 keV γ ray from the α decay of ^{241}Am was visible, while at the same time not triggering on electronic noise. [1]

In NSCL experiment e13502 described in Ch. 2, a sharp threshold of 80 keV was applied to each SuN segment (Sec. 2.3). The sharp threshold was necessary to achieve the same detection efficiency for SuN in experiment and simulation. A sharp threshold at 80 keV was possible because the decay scheme of ^{76}Ga did not contain low-energy γ rays below 80 keV. In NSCL experiment e12001, a sharp threshold was not applied to each SuN segment. Instead, a gradual threshold was implemented in the GEANT4 simulation (see Sec. 3.2.3.1). The gradual threshold in simulation mimicked the application of the DDAS trigger filter threshold in experiment.

3.2 Analysis

3.2.1 Particle Identification

Particle identification was achieved with measurements of energy loss, time of flight, and momentum for each ion. Energy loss was obtained with the two silicon PIN detectors (Sec. 3.1.1). According to the Bethe formula, energy loss is proportional to q^2/v^2, where q is the

[1] A triple PMT coincidence was configured for SuN in later experiments, starting with NSCL experiment e14041. That is, all three PMTs had to collect scintillation light within a certain time window for the signals to be recorded. This allowed the trigger thresholds to be lowered further while still maintaining a reasonable counting rate for each PMT.

charge state and v is the velocity of a nucleus. If a nucleus is fully stripped of electrons, the charge state q is equal to the atomic number. Charge-state contamination will affect the particle identification process if a nucleus is not fully stripped of electrons, and is discussed below. Therefore, for a given velocity, energy loss measurements provided elemental identification in the experiment. To separate isotopes within a given element, a mass measurement was required. The mass measurement was obtained with the time of flight through the A1900 fragment separator to the experimental end station, because these quantities are related:

$$t = \frac{L}{v} = \frac{L}{c}\sqrt{1 + \left(\frac{mc}{B\rho q}\right)^2} = \frac{L}{c}\sqrt{1 + \left(\frac{Auc}{B\rho q}\right)^2}, \tag{3.1}$$

where t is the time of flight, L is the flight path the nucleus travels, v is the velocity, c is the speed of light, m is the mass, A is the mass number, u is the atomic mass unit, $B\rho$ is the magnetic rigidity, and q is the charge state. If a nucleus is fully stripped of electrons, the charge state q is equal to the atomic number. The magnet settings and slits of the A1900 fragment separator establish a magnetic rigidity. Therefore, for a given element (specifying q in Eq. 3.1), the time of flight determined the mass and provided isotopic identification. Measurements of time of flight were obtained with different combinations of timing signals and TACs. As mentioned in Sec. 3.1.1, the two silicon PIN detectors provided the "start" input for the TACs. The "stop" input for the TACs was provided by either the radio frequency (RF) signal from the cyclotrons, a signal from the SuN detector, or a signal from the I2 scintillator. The signal from SuN was the sum of the signals from the eight central PMTs. The I2 scintillator had a PMT on either end, called "I2 North" or "I2N" and "I2 South" or "I2S". Signals from I2N and I2S provided the "stop" input for the TACs.

A particle identification spectrum with energy loss from PIN1 and time of flight between

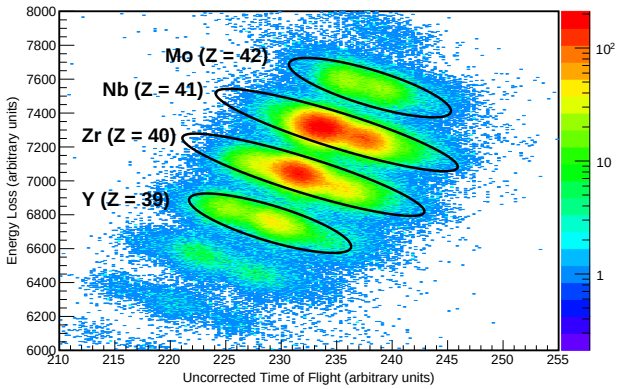

Figure 3.12: Particle identification spectrum for ions implanted in the DSSD for experiment e12001. The energy loss is from PIN1 and the time of flight is between PIN1 and I2N. This spectrum has uncorrected time of flight on the x-axis. Therefore only individual elements can be identified, not isotopes of a given element.

PIN1 and I2N is shown in Fig. 3.12. In this plot, only individual elements can be identified, not isotopes for a given element. Further improvements described in Sec. 3.2.1.1 were made to the particle identification spectrum to identify isotopes for a given element.

3.2.1.1 Momentum Correction to the Time of Flight

Due to the low production rates of the nuclides of interest, the full momentum acceptance (5%) of the A1900 fragment separator was used to transport as many nuclides as possible to the experimental end station. For a given nuclide, this leads to a distribution in $B\rho$ and L in Eq. 3.1, and therefore a distribution in the time of flight. This is the reason isotopes cannot be identified in Fig. 3.12. The particle identification spectrum was improved by examining the association between time of flight and position (proportional to momentum) at the I2 scintillator. Position at the I2 scintillator was determined with a TAC that had the "start" input from I2S and the "stop" input from I2N. The time difference between I2S and I2N was related to the position of an ion passing through the I2 scintillator.

Figure 3.13 shows an example of removing the association between time of flight and

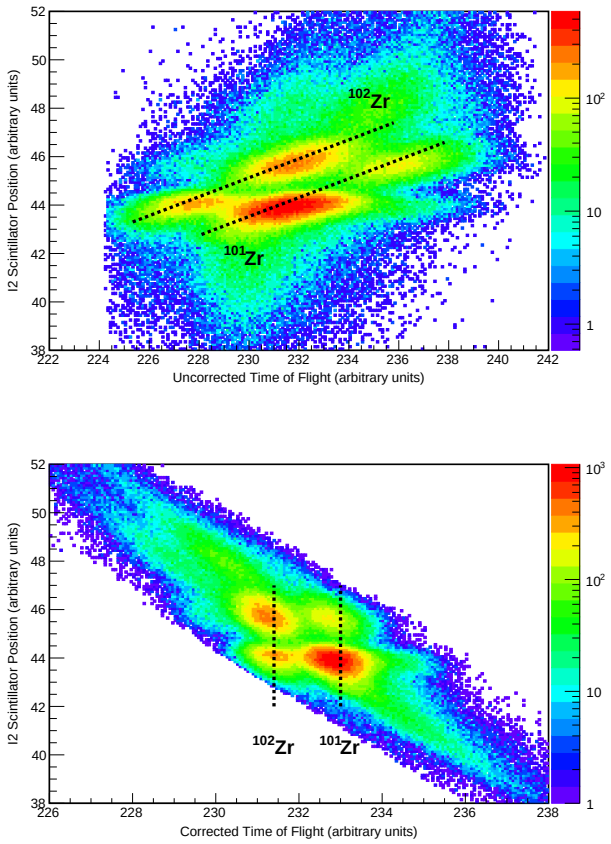

Figure 3.13: Top panel: Position at the I2 scintillator vs. time of flight between PIN1 and I2N for Zr isotopes implanted in the DSSD. Each band is a separate isotope of Zr. This spectrum has uncorrected time of flight on the x-axis. Bottom panel: Same as the top panel except the x-axis is corrected time of flight. In this panel, an isotope has the same time of flight regardless of position at the I2 scintillator. The horizontal gap in intensity around the value of 45 that is present in both panels is due to the I2 scintillator being damaged during NSCL experiment e12001.

position at the I2 scintillator for Zr isotopes implanted in the DSSD. Each band is a separate isotope of Zr. The top panel uses uncorrected time of flight, which has an association between time of flight and position at the I2 scintillator. The bottom panel uses corrected time of flight, which has this association removed. The corrected time of flight, which is proportional to the mass-to-charge ratio (A/q) of an ion, was obtained with a coordinate system rotation for only the x-axis.

The particle identification spectrum, using corrected time of flight, is shown in Fig.

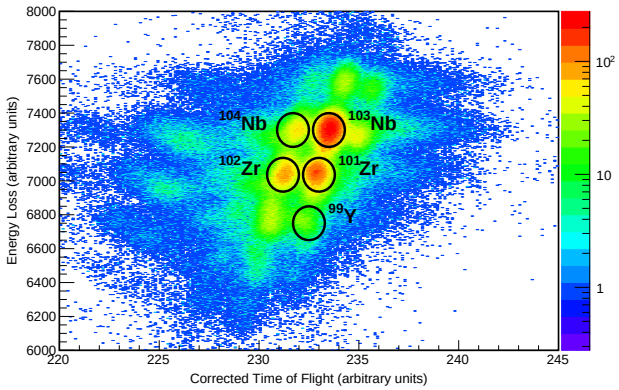

Figure 3.14: Particle identification spectrum for ions implanted in the DSSD during experiment e12001. The energy loss is from PIN1 and the time of flight is between PIN1 and I2N. This spectrum has corrected time of flight on the x-axis.

3.14. Individual nuclides were identified using isomeric transitions, β-decay half-lives, and correlated β-delayed γ rays. An example of an isomeric transition is shown in Fig. 3.15. The isomeric transition is from hydrogen-like $^{99}_{40}\mathrm{Zr}^{39+}$, which was a charge-state contaminant of the fully stripped ion of interest $^{102}_{40}\mathrm{Zr}^{40+}$. The nuclide ^{99}Zr has an excited state at 252 keV with a lifetime of 293 ns [24]. The excited state deexcites by emitting two γ rays with energies of 130 keV and 122 keV. The individual γ rays and summed energy were detected in the TAS spectrum and sum-of-segments spectrum for ions implanted into the DSSD using the particle identification gate for ^{102}Zr.

3.2.1.2 Charge States

The relatively heavy nuclides delivered to the experimental end station meant that not all ions were fully stripped of electrons, resulting in charge-state contamination in the particle identification spectrum. Because the corrected time of flight is proportional to the mass-to-charge ratio (A/q) of an ion, certain ions with approximately the same A/q will appear in the same area in the particle identification spectrum. For example, hydrogen-like $^{98}_{40}\mathrm{Zr}^{39+}$ had

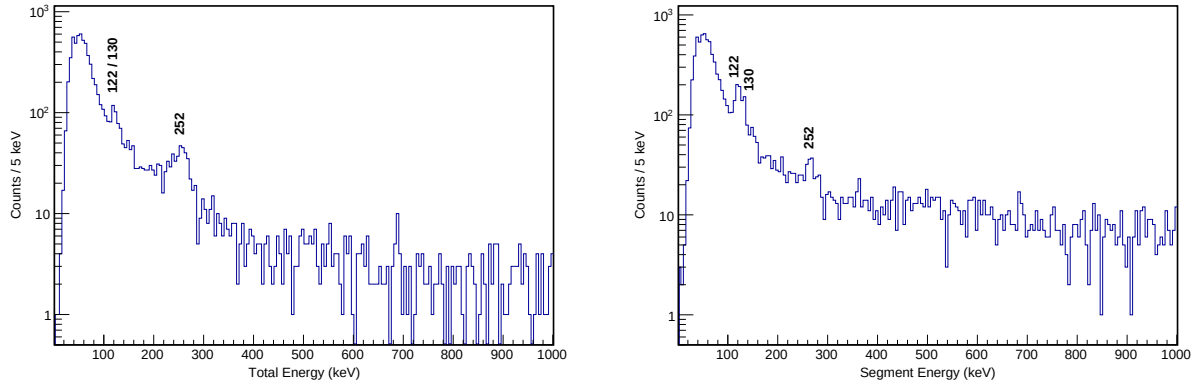

Figure 3.15: Example of an isomeric transition used for particle identification. Hydrogen-like $^{99}_{40}\mathrm{Zr}^{39+}$ was a charge-state contaminant of the fully stripped ion of interest $^{102}_{40}\mathrm{Zr}^{40+}$. The nuclide $^{99}\mathrm{Zr}$ has an excited state at 252 keV with a lifetime of 293 ns [24]. The excited state deexcites by emitting two γ rays with energies of 130 keV and 122 keV. The individual γ rays and summed energy were detected in the TAS spectrum (left panel) and sum-of-segments spectrum (right panel) for ions implanted into the DSSD using the particle identification gate for $^{102}\mathrm{Zr}$. The other counts in the spectra are from room background and Bremsstrahlung radiation, which is emitted as the ions slow down and stop in the DSSD.

Table 3.3: Energy deposition (MeV) in different detectors for two isotopes with approximately the same mass-to-charge ratio (A/q).

	$^{98}_{40}\mathrm{Zr}^{39+}$	$^{101}_{40}\mathrm{Zr}^{40+}$
PIN1	1735.2	1743.3
PIN2	2240.4	2237.7
DSSD	3444.8	3594.8

a similar mass-to-charge ratio as fully stripped $^{101}_{40}\mathrm{Zr}^{40+}$. This made $^{98}_{40}\mathrm{Zr}^{39+}$ a charge-state contaminant of the ion of interest $^{101}_{40}\mathrm{Zr}^{40+}$. Charge-state separation is usually accomplished by measuring the total kinetic energy of ions. Table 3.3 illustrates the benefits of a total kinetic energy measurement to separate $^{98}_{40}\mathrm{Zr}^{39+}$ from $^{101}_{40}\mathrm{Zr}^{40+}$. These two isotopes have similar energy losses in the two silicon PIN detectors. However, the difference in energy deposited in the DSSD is large enough to separate the two isotopes.

Many attempts were made at using total kinetic energy to separate charge states. All of these attempts were unsuccessful. The conclusion was made that charge-state separation

was unsuccessful because the dual-gain preamplifiers for the DSSD saturated during the implantation of an ion. However, because they were shaping preamplifiers, the output signal was properly shaped. Even though properly shaped, because of the saturation, the output signals were not dependent on the energy of the ion. The output signals from the dual-gain preamplifiers were attenuated (Sec. 3.1.2), and sent to DDAS. This attenuation was necessary to prevent the clipping of signals in DDAS. However, the signals entering DDAS were not dependent on the energy of the ion, making charge-state separation impossible. Other methods resorted to for reducing charge-state contamination will be described individually for each nuclide in later sections.

3.2.2 Correlations

Once the ions delivered to the experimental end station had been identified (Sec. 3.2.1), the next step was to correlate the subsequent β-delayed radiation to those ions. As mentioned in Sec. 3.1.2, the DSSD was used to detect high-energy ion implantations and subsequent low-energy β-decay electrons. In software, events were created using a 2 μs coincidence time window and classified as either an implantation or decay. The implantation of an ion and its subsequent β decay are two distinct types of events, are temporally separated (determined by the β-decay half-life), and also may be spatially separated (with respect to the DSSD pixel size). The goal of correlating decay events to implantation events is to create another type of event: a correlation event. A correlation event has the particle identification information associated with the implantation event and the β-delayed radiation information associated with the decay event. The only unique property of a correlation event is the correlation time, which is the difference in time between the decay event and the implantation event.

Events were classified as an implantation if there was a signal in both of the silicon PIN

detectors, there was a measurement of the time of flight and momentum of an ion, there was at least one strip that fired on both sides of the DSSD in the low-gain stage, and there was no signal in the veto detector. As mentioned in Sec. 3.1.2.2, the strips of the DSSD in the low-gain stage were gain matched with secondary beam. The pixel in which the implantation occurred was defined by the strip that received the maximum energy deposition on each side. The secondary beam was defocused to try to illuminate as much of the surface of the DSSD as possible. This was done in order to increase the amount of time between consecutive implantations per pixel.

The top panel of Fig. 3.16 shows the spatial distribution of implantation events in the DSSD. The spatial distribution is a two-dimensional histogram. The x axis is the strip number that received the maximum energy deposition on the back side, and the y axis is the strip number that received the maximum energy deposition on the front side. This spatial distribution is determined by the secondary beam profile. As shown in the top panel of Fig. 3.16, implantation events were not evenly distributed over the detector surface. There were more implantation events in central pixels compared to peripheral pixels. Furthermore, the central pixels experienced a higher implantation rate compared to peripheral pixels. This is shown in the bottom panel of Fig. 3.16. The average time between consecutive implantations is smaller for central pixels compared to peripheral pixels.

Simply dividing the total number of implantations by the amount of time and total number of pixels yields an average implantation rate of (1403857 implantation events) / (156659 seconds) / (256 pixels) $\approx$ 0.035 implantations/second for a single pixel. This would yield an average time between consecutive implantations of (0.035 implantations/second)$^{-1}$ $\approx$ 29 seconds/implantation for a single pixel. However, this calculation does not consider the spatial distribution of implantation events in the DSSD. Taking into account the spatial

distribution of implantation events in the DSSD produced the bottom panel of Fig. 3.16. The average time between consecutive implantations was approximately 12 seconds for central pixels and gradually increased when moving towards peripheral pixels.

Events were classified as a decay if neither silicon PIN detector had a signal, there were no signals in the low-gain stage of the DSSD, there was at least one strip that fired on both sides of the DSSD in the high-gain stage, and there was no signal in the veto detector. The pixel in which the decay occurred was defined in the same way as described for an implantation. As mentioned in Sec. 3.1.2.2, the strips of the DSSD in the high-gain stage were calibrated with sources of ^{228}Th, ^{241}Am, and ^{249}Cf, and the thresholds for the strips ranged from 150 keV to 200 keV.

The top panel of Fig. 3.17 shows the spatial distribution of decay events in the DSSD. As with the spatial distribution of implantation events, the spatial distribution is a two-dimensional histogram. The x axis is the strip number that received the maximum energy deposition on the back side, and the y axis is the strip number that received the maximum energy deposition on the front side. The spatial distribution of decay events is similar to the spatial distribution of implantation events (top panel of Fig. 3.16). The bottom panel of Fig. 3.17 shows the average number of decay events observed in the DSSD within a one second time interval. For central pixels, there is on average approximately 0.25 observed decays per second. The average number gradually decreases when moving from central pixels to peripheral pixels. Note that this is the average number of *observed* (that is, detected) decays. The β-decay electron detection efficiency of the DSSD was not 100%, so there were more decay events than what was observed and shown in the bottom panel of Fig. 3.17. It should also be noted that for each implantation, multiple β decays are expected coming from the decay of future generations (for example, the daughter and granddaughter).

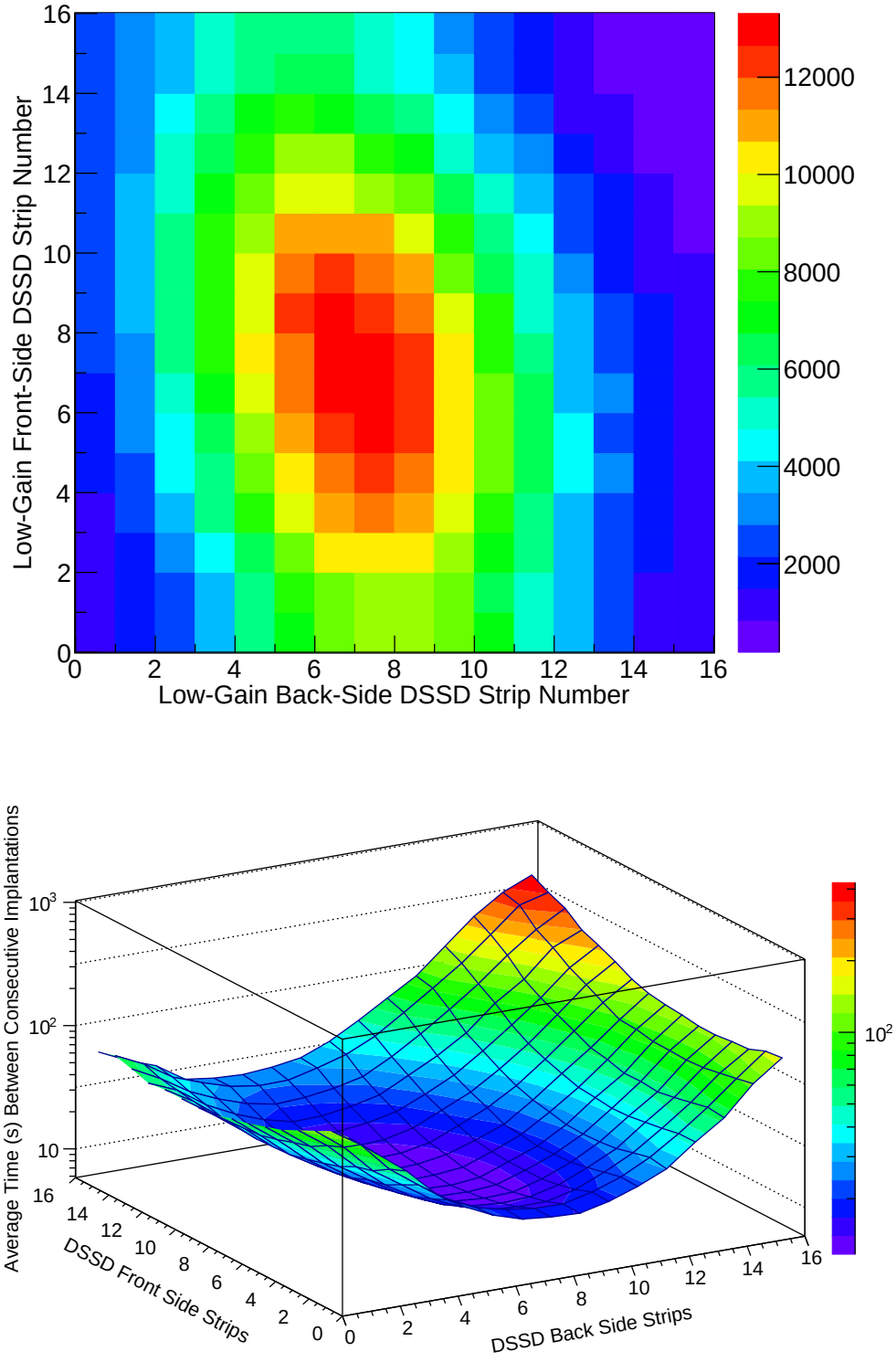

Figure 3.16: Top panel: Spatial distribution of implantation events in the DSSD. Bottom panel: Average time in seconds between consecutive implantations for each pixel of the DSSD. The average time for central pixels is approximately 12 seconds. The average time gradually increases when moving from central pixels to peripheral pixels.

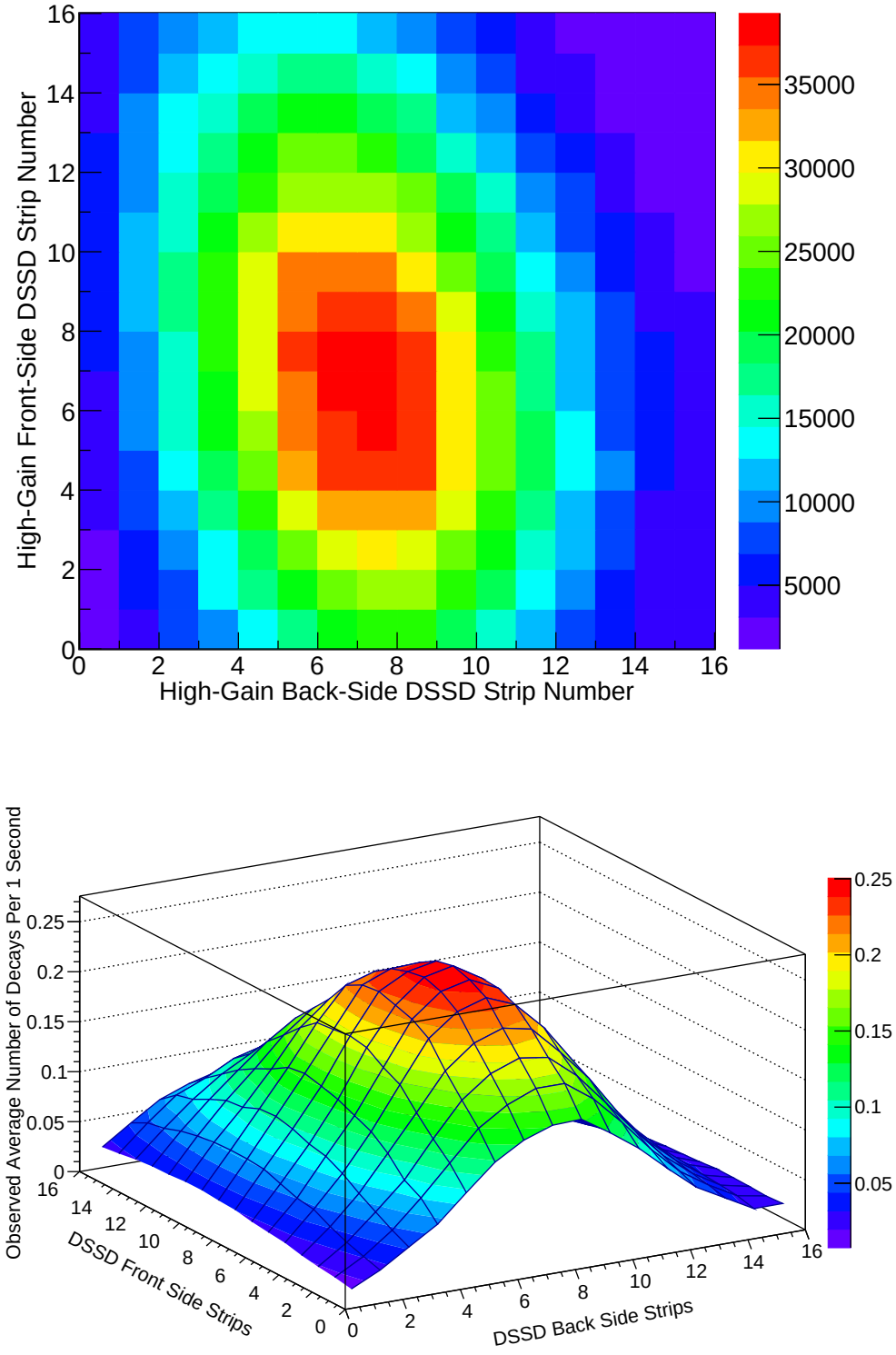

Figure 3.17: Top panel: Spatial distribution of decay events in the DSSD. Bottom panel: The average number of decay events observed in the DSSD within a one second time interval. For central pixels, there is on average approximately 0.25 observed decays per second. The average number gradually decreases when moving from central pixels to peripheral pixels.

Decays were correlated to an implantation according to the following logic. First, when a decay was identified, implantations that previously occurred were searched for in the correlation field, and whichever implantation was closest in time to the decay was selected as a candidate to be correlated to the decay. In the present work, a single-pixel correlation field was used, meaning the implantation and decay had to have occurred in the same pixel. Second, there had to have been a sufficient amount of time that passed between the candidate implantation and the previous implantation in the same pixel. This condition helps to remove ambiguity of the decay originating from the most recent implantation in the correlation field. Third, the decay had to have happened within a certain amount of time of the implantation known as the correlation time window. The correlation logic is summarized in Fig. 3.18. Figure 3.19 shows the spatial distribution of correlation events in the DSSD. The spatial distribution is defined in the same manner as for implantation events and decay events. The spatial distribution of correlation events is similar to the spatial distribution of implantation events (top panel of Fig. 3.16) and the spatial distribution of decay events (top panel of 3.17).

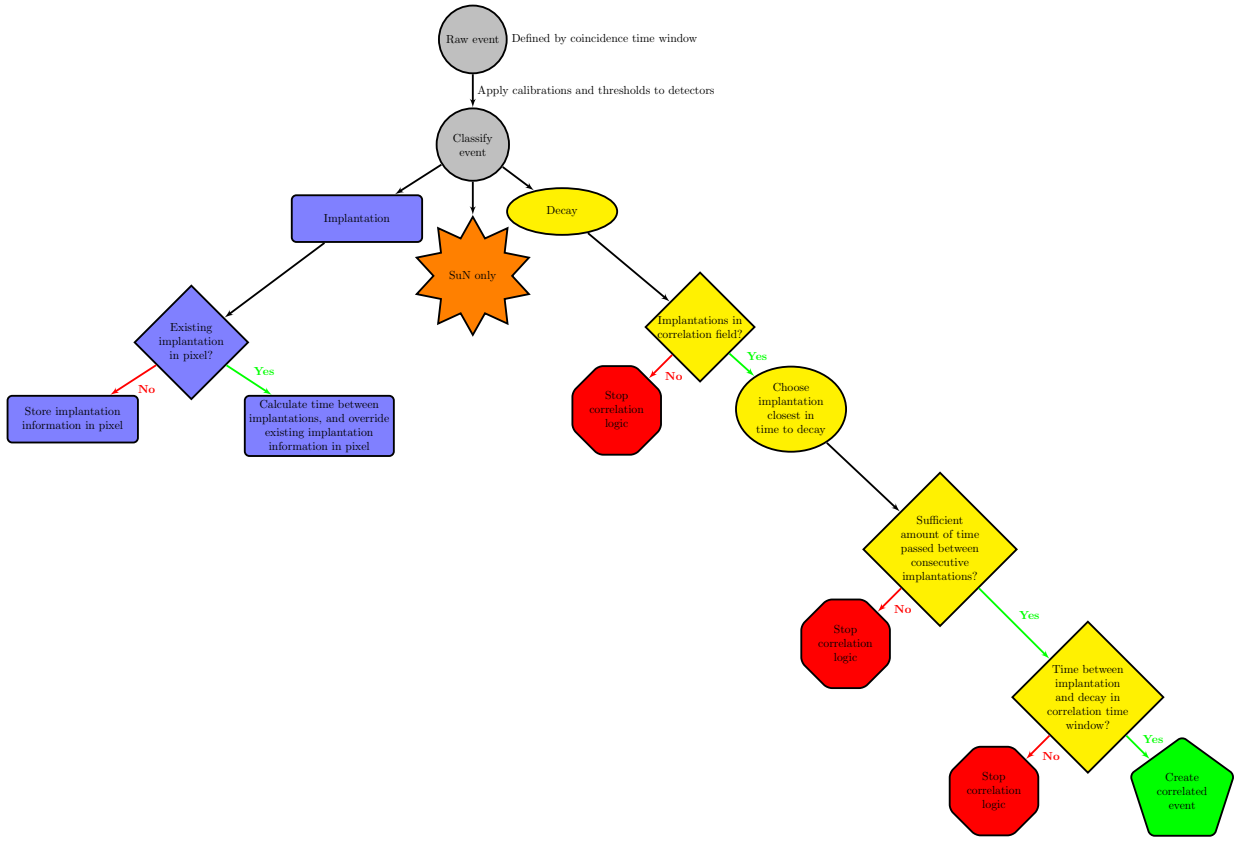

Figure 3.18: Correlation logic used in NSCL experiment e12001. The end result is a correlation event that has the particle identification information associated with the implantation event and the β-delayed radiation information associated with the decay event. A "SuN only" event mostly refers to room background radiation, but may also be from the γ decay of an implantation in an isomeric state that γ decays outside of the coincidence time window of the implantation event.

The correlation logic described in this section and summarized in Fig. 3.18 correlates all decay events to the most recent implantation event in the correlation field. This is not the only correlation logic that exists in the literature (see, for example, Sec. 2.2 of Ref. [151]). Another correlation method only correlates the first decay event to the most recent implantation event in the correlation field. Yet another method correlates all decay events to all previous implantation events in the correlation field. These three methods have different correlation efficiencies and amounts of contamination in β-delayed γ-ray spectra and decay curves. This contamination may come from random correlations as described in Sec. 3.2.2.1.

3.2.2.1 Random Correlations

Random correlations occur when a decay event is correlated to the incorrect implantation event. They may occur for any correlation logic. These random correlations are sometimes referred to as false correlations, spurious correlations, or accidental correlations. They arise from many different scenarios that can occur throughout an experiment.

One scenario involves the accumulated activity in the DSSD. For each implanted ion in the experiment, an average of 4-5 β decays were necessary to reach stability. This accumulated activity in the DSSD from the relatively long decay chains created a persistent background of decay events. For example, at the end of the experiment (when secondary beam was no longer delivered to the experimental end station and there were no ions being implanted into the DSSD), the rate of observed decays was 5 decays/seconds. The bottom panel of Fig. 3.17 shows the rate of observed decays when secondary beam was delivered to the experimental end station. All of these rates actually would have been larger because the β-decay electron detection efficiency of the DSSD was not 100%. Decays from this persistent background may have been incorrectly correlated to an implantation. Because the half-lives of the nuclides in

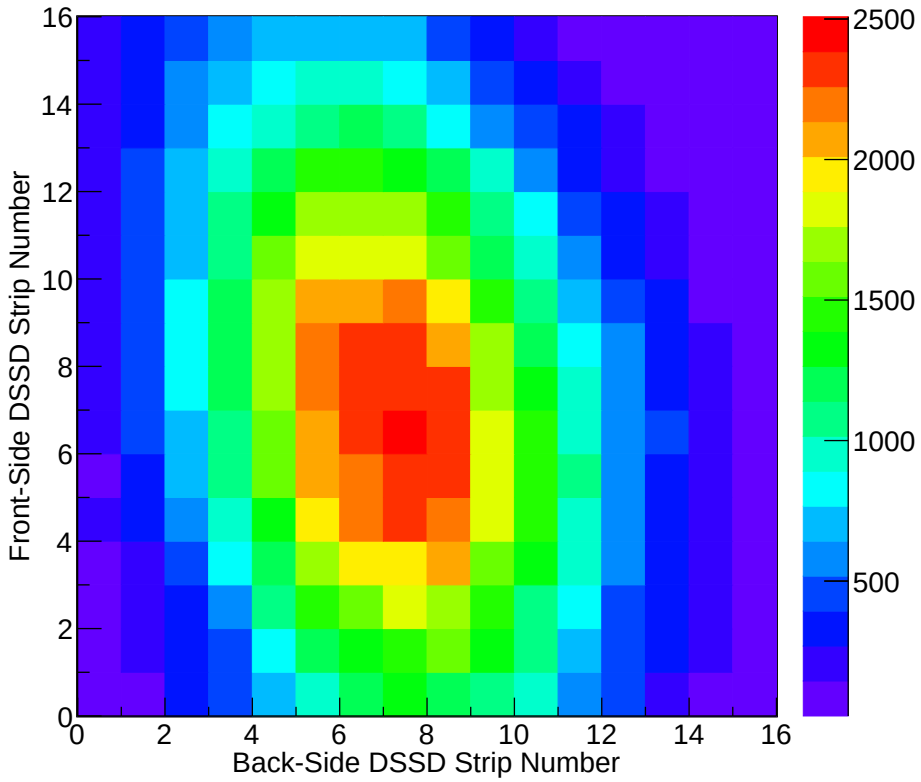

Figure 3.19: Spatial distribution of correlation events in the DSSD with a correlation time window of one second. Because a single pixel correlation field was used, the spatial distribution of correlated implantations and correlated decays is the same. This means there is only one spatial distribution of correlation events.

the experiment are on the order of seconds, the correlation time window was relatively large in order to correctly correlate a decay to an implantation and collect enough statistics in the experimental β-delayed γ-ray spectra for the TAS analysis. However, a relatively large correlation time window came at the expense of an increase in random correlations due to the persistent background of decays events.

Another scenario that may occur during an experiment is shown in Fig. 3.20. In this scenario, a later implantation is localized in the same spatial region as an earlier implantation, but before the earlier implantation undergoes β decay. If the earlier implantation then undergoes β decay, and this decay event is only correlated to the most recent implantation in the correlation field, then the decay of the earlier implantation is incorrectly correlated to the later implantation. This type of random correlation results in an incorrect, shorter decay time assigned to the later implantation. Any β-delayed radiation from the decay is also incorrectly assigned to the later implantation.

Another scenario that may occur during an experiment is shown in Fig. 3.21. In this scenario, an earlier implantation is localized to one pixel and the subsequent β-decay electron is localized to a different pixel. This is because the β-decay electron had a maximum energy deposition in that pixel. In between those two events, a later implantation is localized in the same pixel as the one where the β-decay electron from the earlier implantation will be localized. If the decay event is only correlated to the most recent implantation in the correlation field, then the decay of the earlier implantation is incorrectly correlated to the later implantation. This type of random correlation results in an incorrect, shorter decay time assigned to the later implantation. Any β-delayed radiation from the decay is also incorrectly assigned to the later implantation.

The analysis performed for ^{76}Ga in Sec. 2.4 consisted of two parts. One part was fitting

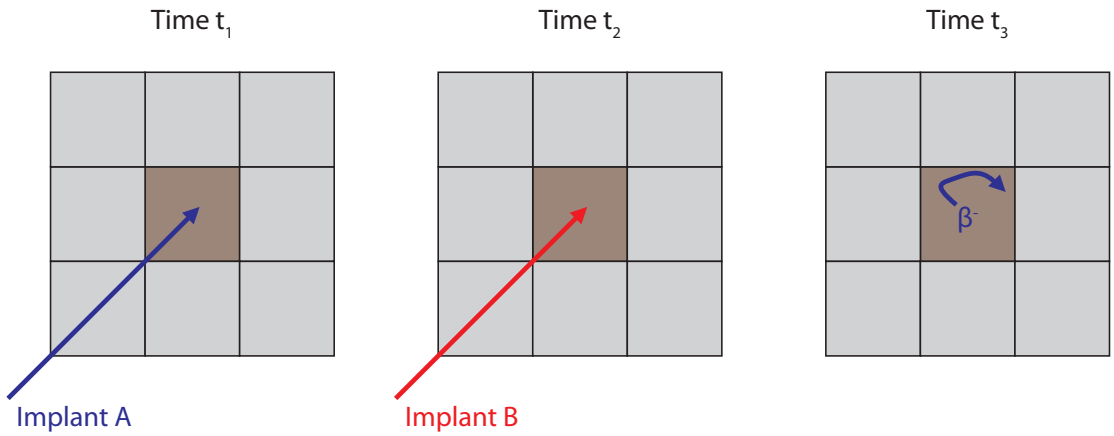

Figure 3.20: Sequence of events resulting in a random correlation. A subset of pixels in the DSSD is shown for different events at times t_1, t_2, and t_3 (with $t_1 < t_2 < t_3$). At time t_1, an ion is implanted (Implant A) in a pixel. At time t_2, another ion is implanted (Implant B) in the same pixel as Implant A. At time t_3, Implant A undergoes β decay. The decay event is localized to the same pixel as Implant A and Implant B. If decay events are only correlated to the most recent implantation event in the correlation field, then the decay is incorrectly correlated to Implant B. This results in a random correlation in which an incorrect, shorter decay time is assigned to Implant B. Any β-delayed radiation from the decay is also incorrectly assigned to Implant B.

the decay curve with the Bateman equations in order to extract the half-life. The other part was fitting TAS spectra with simulated components in order to extract the β-decay feeding intensity distribution. The same analysis will be performed for the nuclides in this chapter. Unlike the case of ^{76}Ga, the decay curves and TAS spectra of the nuclides in this chapter will have background from random correlations. Including random correlations as a component when fitting decay curves and TAS spectra is crucial for extracting accurate results.

Different methods exist in the literature for creating random correlations. These methods create correlations that are random in either space or time. For example, a recent result that created random correlations in space is found in Ref. [152] and a recent result that created random correlations in time is found in Ref. [153]. The analysis for nuclides in this chapter created correlations that were random in time. This method was developed in Ref.

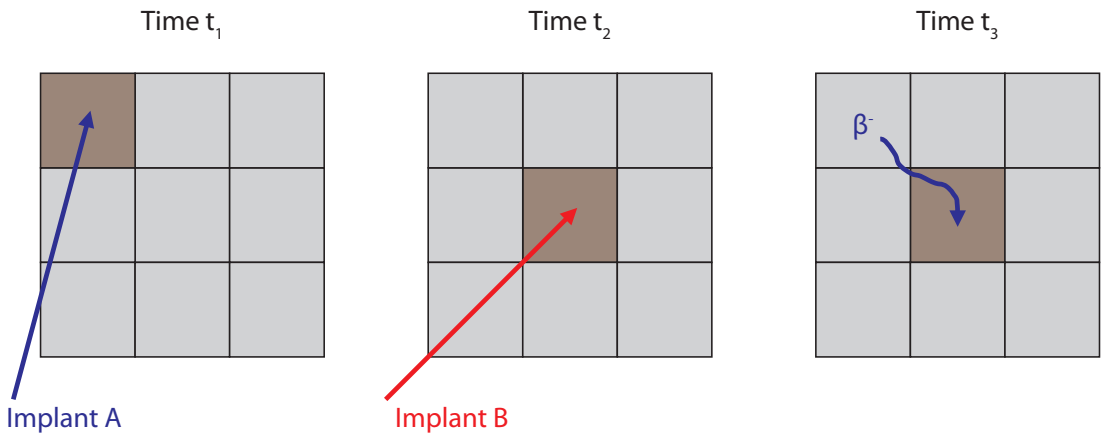

Figure 3.21: Sequence of events resulting in a random correlation. A subset of pixels in the DSSD is shown for different events at times t_1, t_2, and t_3 (with $t_1 < t_2 < t_3$). At time t_1, an ion is implanted (Implant A) in a pixel. At time t_2, another ion is implanted (Implant B) in a pixel that is different from Implant A. At time t_3, Implant A undergoes β decay. The maximum energy deposition of the decay event occurs in a pixel that is different from Implant A but the same as Implant B. If decay events are only correlated to the most recent implantation event in the correlation field, then the decay is incorrectly correlated to Implant B. This results in a random correlation in which an incorrect, shorter decay time is assigned to Implant B. Any β-delayed radiation from the decay is also incorrectly assigned to Implant B.

[151]. This method involves running the analysis backward in time. The random correlations remove a free parameter from the fit of the decay curve and provide a background component when fitting TAS spectra.

As mentioned in Sec. 3.2.2, in this dissertation decay events were only correlated to the most recent implantation in the correlation field. Because of this, the background from random correlations will be exponential (see, for example, Sec. 2.2 of Ref. [151]). If, on the other hand, decay events had been correlated to all previous implantation events in the correlation field, the background from random correlations would have been flat (see, for example, Sec. 2.2 of Ref. [151]). Compared to correlating all decay events to only the most recent implantation event in the correlation field, correlating all decay events to all previous implantation events in the correlation field will result in a larger correlation efficiency but will come at the expense of many random correlations. Because β-delayed γ-ray spectra with less contamination are in general preferred for a TAS analysis, the correlation logic used in this dissertation only considers the most recent implantation event in the correlation field.

3.2.3 Total Absorption Spectroscopy

Once correlations had been performed (Sec. 3.2.2), the next step was to fit the β-delayed, correlated γ-ray spectra to extract the β-decay feeding intensity distribution for the different ions. With a segmented total absorption spectrometer, multiple experimental spectra can be created to aid in extracting the β-decay feeding intensity distribution. A spectrum can be labeled with the subscript i (for example, one value of i could correspond to the TAS spectrum, and another value of i could correspond to the sum-of-segments spectrum). Each spectrum has j bins. Using a modified version of the notation developed in Ref. [141], the experimental spectra obtained with a segmented total absorption spectrometer are described

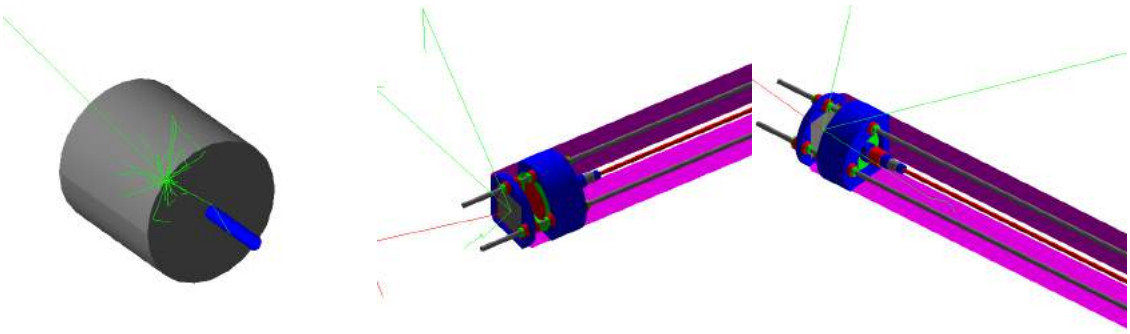

Figure 3.22: Visualization of the GEANT4 simulation for the SuN detector (left panel) and the implantation station at the center of SuN (middle and right panels). The green lines are γ-ray tracks and the red lines are β-decay electron tracks.

as

$$d_{ij} = \sum_k R_{ijk} f_k + \sum_l C_{ijl}, \tag{3.2}$$

where d_{ij} is the number of counts in bin j of experimental spectrum i, R_{ijk} is the detector response function with counts in bin j of spectrum i due to the population of level k in the daughter from β decay, f_k is the number of β decays that feed level k, and C_{ijl} is the number of counts in bin j of spectrum i due to contamination from source l.

3.2.3.1 GEANT4 Simulation

The detector response functions of SuN, R_{ijk} in Eq. 3.2, were modeled with GEANT4 [142] and included phenomena associated with the β-decay transition from the initial level of the parent to the final level of the daughter, and the possible subsequent electromagnetic deexcitation of the final level. These phenomena included the β-decay electron with a realistic kinetic energy distribution [76], and any γ-ray cascades to the ground state or isomeric state(s) of the daughter. A visualization of the GEANT4 simulation of SuN and the implantation station is shown in Fig. 3.22.

Table 3.4: Standard deviation (σ) of a Gaussian function fit to various experimental γ-ray peaks, along with the corresponding energy resolution.

Source	Decay	Energy (keV)	σ (keV)	Resolution (%)
^{241}Am	$^{241}\text{Am} \rightarrow {}^{237}\text{Np}$	59.5	5.3	21.0
^{249}Cf	$^{249}\text{Cf} \rightarrow {}^{245}\text{Cm}$	388.2	16.9	10.2
^{228}Th	$^{208}\text{Tl} \rightarrow {}^{208}\text{Pb}$	583.2	21.1	8.5

The GEANT4 simulation of SuN had an existing resolution function to determine the energy resolution of SuN's NaI(Tl) crystals that was developed for a different application of the SuN detector [25]. The resolution function was created with the existing experimental data at that time. The lowest-energy γ ray included in the resolution function was 511 keV (see Table 5.1 and Fig. 5.11 of Ref. [25]). The creator of the existing resolution function noted in Sec. 5.5 of Ref. [25] that this resolution function is not ideal for low-energy γ rays. Because the nuclides in this dissertation emit low-energy γ rays when they undergo β decay, additional data points for low-energy γ rays were added to the resolution function. These data points were experimentally determined by fitting the peak of individual γ rays from calibration sources. Table 3.4 lists the calibration source, γ-ray energy, and standard deviation of a Gaussian fit to the peak in the spectrum. These data points were added to the existing resolution function from Ref. [25]. Figure 3.23 shows the resolution function used in the GEANT4 simulations for NSCL experiment e12001.

As mentioned in Sec. 3.1.3.2, a sharp energy threshold was not applied to the segments of SuN. Unlike the sharp energy threshold applied in Ch. 2 or in Sec. 6.2 of Ref. [25], a gradual threshold was implemented in the GEANT4 simulation. The gradual threshold was necessary because the nuclides in this dissertation emit low-energy γ rays when they undergo β decay. Figure 3.24 shows a comparison of experimental and simulated sum-of-segments spectra for ^{60}Co. One GEANT4 simulation uses the resolution function from Ref. [25]. This

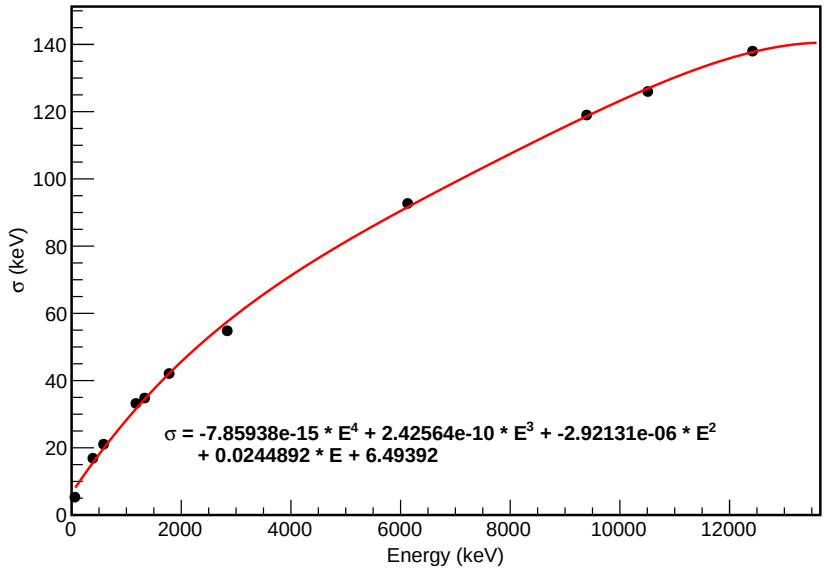

Figure 3.23: Standard deviation in the detected energy of SuN's NaI(Tl) crystals as a function of γ-ray energy. The points correspond to experimental data and the curve is the best fit function that was implemented in the GEANT4 simulation.

simulation does not include a gradual threshold for the segments of SuN. Another simulation uses the resolution function displayed in Fig. 3.23. This simulation does include a gradual threshold for the segments of SuN. For the simulation that does include a gradual threshold for the segments of SuN, there is excellent agreement with experiment at low energies (less than 100 keV).

To achieve the same detection efficiency, the detector response functions and experimental spectra had the same coincidence requirements and detector thresholds. The detector response functions were created for two distinct types of levels populated in the daughter: known levels at discrete energies and pseudo levels within a quasi-continuum. The boundary between these two types of levels is called the critical energy (sometimes referred to as the cutoff energy).

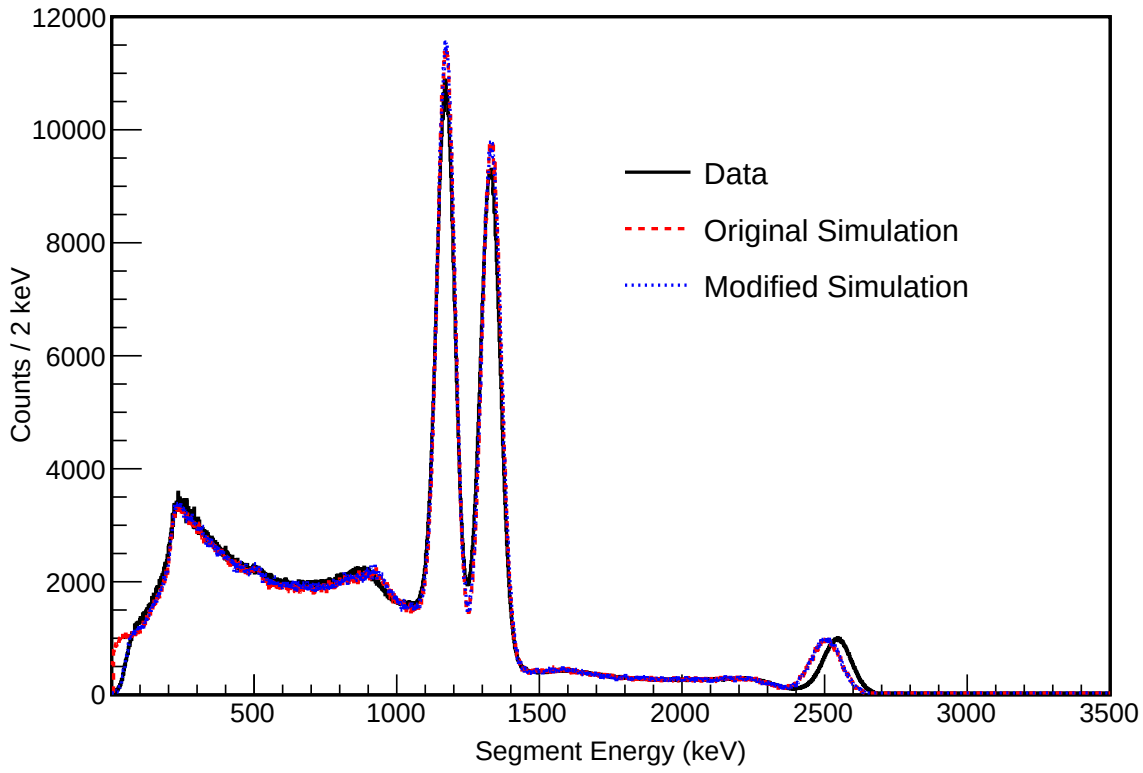

Figure 3.24: Comparison of experimental and simulated sum-of-segments spectra for ^{60}Co. Normalized room background has been subtracted from the experimental spectrum. The experimental spectrum is shown with a black, solid line. The simulation using the resolution function from Ref. [25] is shown with a red, dashed line. This simulation does not include a gradual threshold for the segments of SuN. The simulation using the resolution function displayed in Fig. 3.23 is shown with a blue, dotted line. This simulation does include a gradual threshold for the segments of SuN. The effect of the gradual threshold can be seen at low energies (less than 100 keV).

3.2.3.2 Known Levels

Known levels occur below the critical energy, where the level scheme is assumed to be complete in terms of energies, spins, parities, and branching ratios. The Reference Input Parameter Library (RIPL-3) [154] contains a value of the critical energy for nuclides. In this dissertation, the critical energy was determined by comparing the experimental TAS and sum-of-segments spectra with those obtained from simulation using the existing decay scheme as found in an Evaluated Nuclear Structure Data File (ENSDF) [155]. Information about known levels usually comes from high-resolution measurements obtained with high-purity germanium detectors, although segmented total absorption spectrometers may also be used to estimate some of this information [156].

The energies, spins, and parities of known levels and the relative γ-ray intensities for transitions between known levels were taken from ENSDF [155]. Transitions included the possibility of internal conversion according to internal conversion coefficients calculated using BrIcc [13]. In the case of β decay directly populating either the ground state or β-decaying isomeric state(s) of the daughter, the detector response function was produced only from collisional energy losses between β-decay electrons and the sensitive volume of SuN or the associated bremsstrahlung radiation.

Some known levels may have unknown or tentative spin and/or parity assignments. This information determines the probability of internal conversion and affects transitions from the quasi-continuum to known levels. In these cases, multiple level schemes were constructed that differed in the spin and/or parity assignments and used in the TAS analysis to assess uncertainties in the extracted β-decay feeding intensity distribution.

3.2.3.3 Pseudo Levels

Above the critical energy, a quasi-continuum was assumed to exist, which was divided into energy bins. At the center of each energy bin was placed a pseudo level, which acted as a representative for all nearby levels within the energy resolution of SuN. The spacing between pseudo levels was dependent on the energy resolution of SuN: Because the full width at half maximum increases as the energy increases (Fig. 3.23), the spacing between pseudo levels (equivalently, the size of each energy bin) increased as the energy increased. For example, the spacing between pseudo levels near 2000 keV was approximately 100 keV, whereas the spacing between pseudo levels near 3000 keV was approximately 150 keV.

The γ-ray cascades from pseudo levels were created with the statistical model as implemented in DICEBOX [157]. In the DICEBOX program, the user gives as input as much information as possible about the known levels (for example, energies, spins, parities, relative γ-ray intensities, and total internal conversion coefficients). The user also gives as input the critical energy. Above the critical energy, the program uses statistical properties to describe how levels are distributed and how they deexcite with γ rays. These statistical properties are the nuclear level density (NLD) and γ-ray strength functions (γSFs) for E1, M1, and E2 transitions. When running DICEBOX to generate γ-ray cascades from a pseudo level, the user gives as input the energy, spin, and parity of the pseudo level. Between the energy of the pseudo level and the critical energy, DICEBOX generates a set of levels using the nuclear level density. Transitions between levels in the quasi-continuum and transitions between a level in the quasi-continuum to a known level are governed by the γ-ray strength functions. When a transition reaches a known level, the transitions between known levels are determined by the input relative γ-ray intensities and total internal conversion coeffi-

cients. This procedure is repeated for all pseudo levels within the quasi-continuum. Other implementations of the statistical model to create γ-ray cascades can be found in DECAYGEN [158], DEGEN [159], CASCADE [160, 161, 162, 163], γDEX [164], and RAINIER [165].

The relevant features of DICEBOX in the creation of the γ-ray cascades were the choice of a nuclear level density (NLD), γ-ray strength functions (γSFs) for E1, M1, and E2 transitions, and the critical energy, E_{crit}. The NLD came from the Hartree-Fock-Bogoliubov plus combinatorial method [166], the E1 γSF was modeled as a modified Lorentzian with a constant nuclear temperature (0.5 MeV), and the M1 γSF and E2 γSF were modeled as standard Lorentzians. The resonance energy, width, and peak cross section for the E1 γSF were taken from experimental measurements compiled in RIPL-3 [154], and for the M1 γSF and E2 γSF were taken from systematics according to RIPL-3. Table 3.5 contains the relevant parameters used in DICEBOX for the different nuclides in the present work.

The spins and parities of pseudo levels were determined using β-decay selection rules for allowed Gamow-Teller transitions ($\Delta J = 0, \pm 1$; $\Delta\pi = +$; no 0^+ to 0^+). The assumption was made that first-forbidden Gamow-Teller transitions were not necessary because they are in general less probable than allowed Gamow-Teller transitions. For a given energy of a pseudo level, the different spins will decay differently via E1, M1, and E2 transitions within the quasi-continuum and from the quasi-continuum to a known level. Including the different spins was important because the summing efficiency of SuN depends on how the deexcitation of a pseudo level is partitioned in terms of number of γ rays and their individual energies [95]. To reduce the number of detector response functions used in the TAS analysis, an average detector response function was created from the different spins.

Table 3.5: The values used for different parameters in DICEBOX when creating pseudo levels above E_{crit} (critical energy) for the three daughter nuclides in the present work. The parameters associated with giant resonances that were needed for the γ-ray strength functions were E_r (resonance energy), Γ (width), and σ (peak cross section). The parameters for the E1 γ-ray strength function were from the nearest nuclide of the same type (even Z and even N, even Z and odd N, etc.) for which experimental measurements exist in RIPL-3. However, there were no odd Z and odd N measurements near $^{102}_{41}Nb_{61}$ and therefore the nearest measurement was used regardless of even/odd proton/neutron numbers. The nearest nuclides for $^{101}_{41}Nb_{60}$, $^{102}_{41}Nb_{61}$, and $^{109}_{44}Ru_{65}$ were $^{103}_{45}Rh_{58}$, $^{100}_{42}Mo_{58}$, and $^{117}_{50}Sn_{67}$, respectively. The final results of this work were not sensitive to small variations in these parameters.

		γ-ray strength function parameters								
		E1			M1			E2		
Nuclide	E_{crit}	E_r	Γ	σ	E_r	Γ	σ	E_r	Γ	σ
	[keV]	[MeV]	[MeV]	[mb]	[MeV]	[MeV]	[mb]	[MeV]	[MeV]	[mb]
$^{101}_{41}Nb_{60}$	2119	16.62	8.56	187.50	8.80	4.00	1.76	13.53	4.90	2.02
$^{102}_{41}Nb_{61}$	941	16.02	8.44	167.00	8.78	4.00	1.72	13.48	4.89	2.01
$^{109}_{44}Ru_{65}$	1268	15.64	5.02	257.50	8.58	4.00	1.49	13.19	4.80	2.20

3.2.3.4 Contamination

The potential sources of contamination, C_{ijl} in Eq. 3.2, included room background, electronic pulse pileup, random correlations of implantation and decay events, charge-state contamination, and the β decay of future descendants (for example, the daughter). Each potential source was investigated and included in the TAS analysis if necessary.

The experimental spectra used in the TAS analysis were obtained by correlating decay events to implantation events with spatial and temporal information. Decay events were naturally gated by a β-decay electron, producing β-gated spectra. As mentioned in Sec. 3.2.2, a 2 μs coincidence time window was used to create events, which reduced the probability of recording room background during a decay event. Therefore, contamination from room background was negligible.

Electronic pulse pileup will depend on the counting rate of each of SuN's PMTs during the experiment. Throughout the experiment, the average counting rate was approximately

900 Hz. For only decay events, the average counting rate was approximately 7 Hz for PMTs of the central segments, and approximately 1 Hz for PMTs of the outer segments. This low counting rate meant contamination from electronic pulse pileup was negligible.

Within the correlation procedure, not all decay events were correlated to the correct implantation event, resulting in random correlations. These random correlations were characterized by performing correlations backward in time as described in Sec. 3.2.2.1.

As mentioned in Sec. 3.2.1.2, there was charge-state contamination in the particle identification spectrum. Because measuring the total kinetic energy of each ion was not possible in the experiment (Sec. 3.2.1.2), separation of different charge states was not possible. Other methods to reduce charge-state contamination will be described individually for each nuclide.

Depending on the half-life of the daughter for a given nuclide, there may be contamination from the decay of the daughter within the correlation time window. Methods to estimate or eliminate contamination from the decay of the daughter will be described individually for each nuclide.

3.2.3.5 Fitting

Once the contamination was accounted for as best as possible, the detector response functions were used to simultaneously fit all the experimental spectra by minimizing the global χ^2 value

$$\chi^2_{\text{global}} = \sum_i \sum_j \left(\frac{d_{ij} - \sum_k R_{ijk} f_k - \sum_l C_{ijl}}{\sqrt{d_{ij}}} \right)^2 . \tag{3.3}$$

The quantities in Eq. 3.3 were defined in Eq. 3.2. In Eq. 3.3, d_{ij} was obtained from experiment, R_{ijk} was obtained from simulation, and, in this dissertation, C_{ijl} was obtained from experiment. Unlike the analysis performed in Sec. 2.3 in which GEANT4 was used to simu-

late the response of SuN to individual γ-ray cascades, the analysis performed in this chapter according to Eq. 3.3 used GEANT4 to simulate the response of SuN to levels populated in β decay. The experimental spectra included in the calculation of χ^2_{global} included a total of nine spectra with various gates or restrictions applied to them. The nine spectra were the TAS spectrum, sum-of-segments spectrum, multiplicity spectrum, and the sum-of-segments and multiplicity spectra gated on the TAS spectrum from 0-800 keV, 800-2500 keV, and 2500 keV to the end of the TAS spectrum. These three energy regions were appropriate based on the statistics in the gated spectra. All nine spectra were included in the calculation to further constrain the summing efficiency of SuN, make the TAS analysis more sensitive to the finer details of the decay scheme, and help find the true minimum in the χ^2_{global} space. In addition, after minimizing χ^2_{global}, the initial number of decaying nuclei was compared between experiment and simulation. This comparison is based on the following logic:

1. In the experiment, the number of correlated events for a particular ion is known. For example, considering all correlated events, this is the number of counts in the particle identification spectrum for a particular ion. Alternatively, this is the number of counts in the decay curve for a particular ion. Assuming all contamination has been removed from the particle identification spectrum or decay curve, then only a single decay event is correlated to an implantation event. With this assumption, the number of correlated events for a particular ion may also be referred to as the initial number of decaying nuclei (of that particular ion).

2. After fitting the experimental TAS spectra, the β-decay feeding intensity distribution is known. This distribution provides information about the population of each level in β decay needed to fit the experimental TAS spectra. Using this distribution and the

efficiency of SuN, the initial number of decaying nuclei can be determined in simulation.

3. Once the initial number of decaying nuclei has been determined in simulation, a comparison can be made with experiment.

In Eq. 3.3, the number of decays feeding each level was repeatedly adjusted until χ^2_{global} was minimized. The minimization was performed with MINUIT [167] from the ROOT data analysis toolkit [168]. The number of decays feeding each level was then normalized to unity to obtain the β-decay feeding intensity distribution

$$I_{\beta_i} = \frac{f_i}{\sum_k f_k}. \tag{3.4}$$

The β-decay feeding intensity distribution was then converted to a Gamow-Teller transition strength, $B(\text{GT})$, distribution using Eq. 1.24. The whole analysis procedure used to extract the β-decay feeding intensity distribution and Gamow-Teller transition strength distribution is illustrated in Fig. 3.25.

3.3 Results

3.3.1 Half-lives

In this section, half-lives are extracted for neutron-rich nuclides in the A = 100-110 mass region. These nuclides were delivered to the experimental end station during NSCL experiment e12001. Half-lives for many nuclides in this section were measured decades ago in experiments that performed chemical separation of fission fragments. Both the separation and identification of fragments in these past experiments were challenging and authors of-

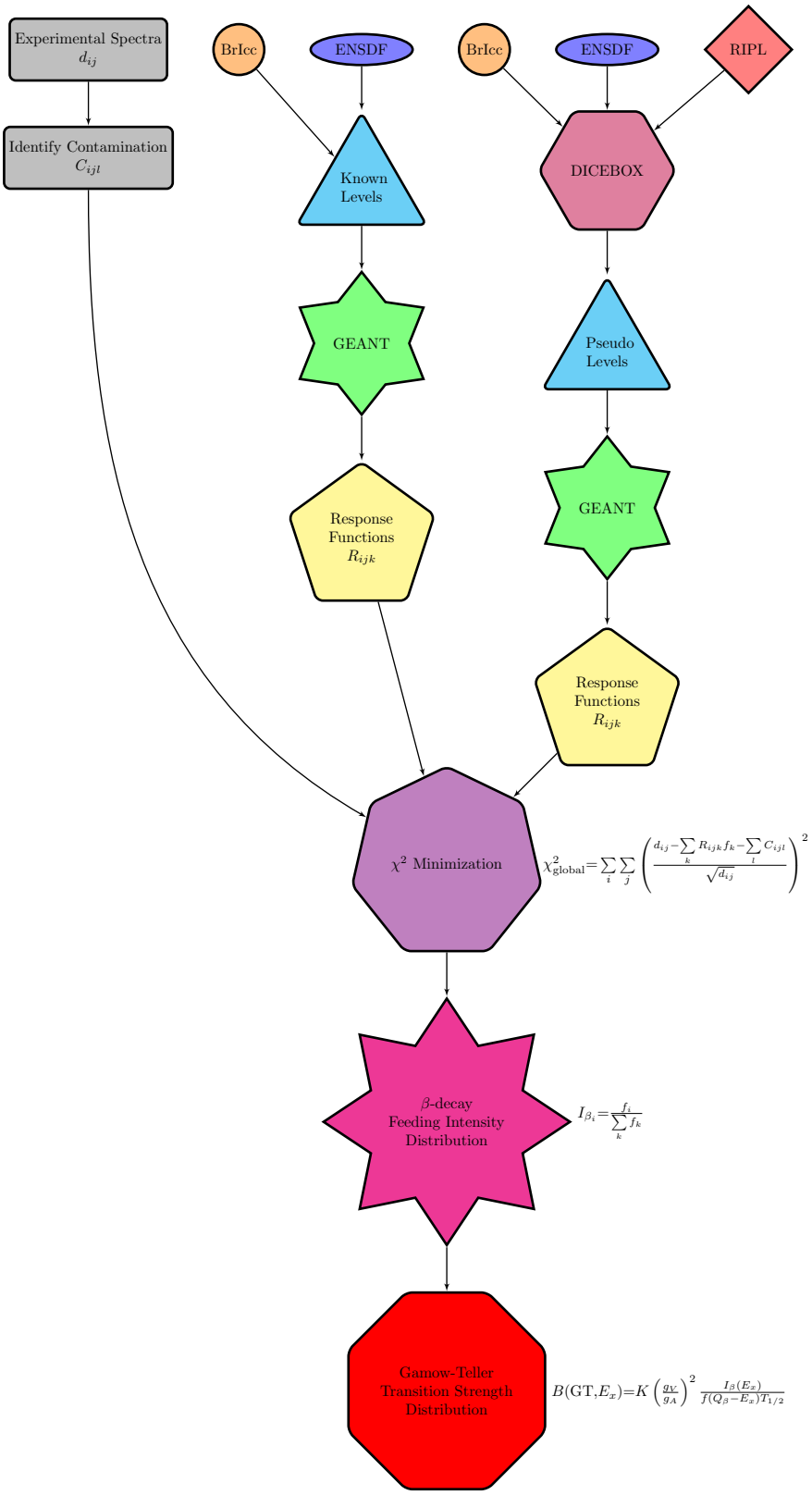

Figure 3.25: Analysis pipeline used to extract the β-decay feeding intensity distribution and Gamow-Teller transition strength distribution in NSCL experiment e12001.

ten reported possible contamination issues. For this reason, the present work provides new measurements of half-lives in the A = 100-110 mass region using a consistent technique.

A decay curve was created for each nuclide of interest by histogramming the time difference between the implantation of an ion and its subsequent β decay and was used to extract the half-life. Isolating events in the decay curve from the nuclide of interest was obtained by simultaneously gating on a sum peak in the TAS spectrum and a γ ray in the sum-of-segments spectrum. This technique is detailed for a specific nuclide in Sec. 3.3.1.2.

In addition to any random correlations (Sec. 3.2.2.1), in this technique there possibly are additional sources of background that must be considered. If the nuclide of interest to be isolated is the parent, these potential background sources include events from the decay of future descendants (for example, the daughter) and also from possible charge-state contaminants (Sec. 3.2.1.2). Consulting the decay schemes of the parent, future descendants, and charge-state contaminant enabled the selection of events that included an established level and γ ray from the decay of the nuclide of interest. In addition, sum peaks and γ rays of higher energies were favored in order to reduce the possibility of including events from incomplete summation in the TAS spectrum and events from Compton-scattered γ rays in the sum-of-segments spectrum.

If applicable to certain nuclides, the ground-state-to-ground-state Q values for β decay [16] were used to identify appropriate gating regions in the TAS spectrum. For example, the ground-state-to-ground-state Q value for the parent ^{104}Nb is 8531 keV, the daughter ^{104}Mo is 2153 keV, and the charge-state contaminant ^{101}Nb^{40+} is 4628 keV [16]. Therefore, counts in the TAS spectrum above approximately 4628 keV should only originate from the decay of ^{104}Nb.

Two decay curves were created for each gating combination, with the only difference be-

ing that one was created using forward-time correlations and the other using backward-time correlations. The distribution of backward-time correlations, representing random correlations between implantations and decays (Sec. 3.2.2.1), was fit with an exponential function, the results of which were used and held fixed as a background component while fitting the forward-time correlations with an appropriate form of the Bateman equations [169].

In this section, each β decay is discussed separately. In Figs. 3.26, 3.28, 3.29, 3.30, 3.31, 3.32, and 3.33, "Data" refers to forward-time correlations, "Random Correlations Data" refers to backward-time correlations, "Random Correlations Fit" refers to the exponential fit of backward-time correlations, and "Total Fit" refers to the fit of forward-time correlations with the Bateman equations and an exponential background with fixed parameters from the fit of backward-time correlations. Table 3.6 contains a description of the selection of events in the decay curve and a comparison of the half-life from the present work with previous measurements.

3.3.1.1 $^{99}_{39}\mathbf{Y}_{60} \rightarrow {}^{99}_{40}\mathbf{Zr}_{59}$

In Ref. [195], a large β-decay feeding intensity is assigned to a level in ^{99}Zr at 724.5 keV, with the most probable deexcitation pathways being either a single γ ray with energy 724.4 keV or two γ rays with energies of 602.7 keV and 121.7 keV. In the present work, there is a visible sum peak in the TAS spectrum at the energy of this level and all three γ rays are observed in the sum-of-segments spectrum gated on the sum peak. Combining the decay curves from gating on the sum peak and the 121.7-keV γ ray and gating on the sum peak and the 602.7-keV γ ray produced the total decay curve shown in Fig. 3.26 and resulted in a half-life of 1.27 $\pm$ 0.25 s.

The half-life of ^{99}Y has been previously measured in fission-based experiments [172,

Table 3.6: Half-lives from the present work along with previous measurements. The selection of events in the TAS spectrum ("Level(s)") and sum-of-segments spectrum ("γ ray(s)") to extract the half-life are listed for each nuclide. If a reference cited in the ENSDF file could not be obtained, the ENSDF file is cited along with the original reference. A previous measurement that does not contain any uncertainty will have no uncertainty in this table.

Nuclide	Level(s) (keV)	γ ray(s) (keV)	Present Work (s)	Previous Measurements (s)
^{99}Y	724.5 724.5	602.7 121.7	1.27(25)	1.36(11) [170], 1.40(7) [170], 1.486(7) [171], 1.47(2) [172], 1.51(8) [173], 1.45(22) [174], 1.48(2) [175], 1.1(3) [176, 24]
^{101}Zr	1840-2040	1740-2040	2.27(12)	2.0(3) [177, 178], 2.2(3) [177, 178], 2.5(1) [179], 3.3(6) [180], 2.4 [181]
^{102}Zr	599.48 599.48	535.13, 599.48 599.48	2.01(8)	2.9(2) [182], 2.1 [181]
^{102m}Nb	296.61	296.61	1.33(27)	1.3(2) [182]
^{103}Nb	102.6	102.6	1.34(7)	1.5(2) [182], 1.5(2) [183], 1.3(1) [184, 185]
^{104m}Nb	4640-7240 2000-2160 2600-2920	192.2 192.2 192.2	0.97(10)	0.8(2) [182], 0.91(2) [186, 187], 0.99(7) [188], 1.0(1) [175]
^{109}Tc	1158.7, 1267.8	1158.7, 1267.8	0.87(7)	1.14(3) [189], 1.04(11) [189], 0.82(10) [175], 0.86(3) [190], 0.93(3) [191, 192], 0.9(1) [193, 192], 1.4(4) [194]

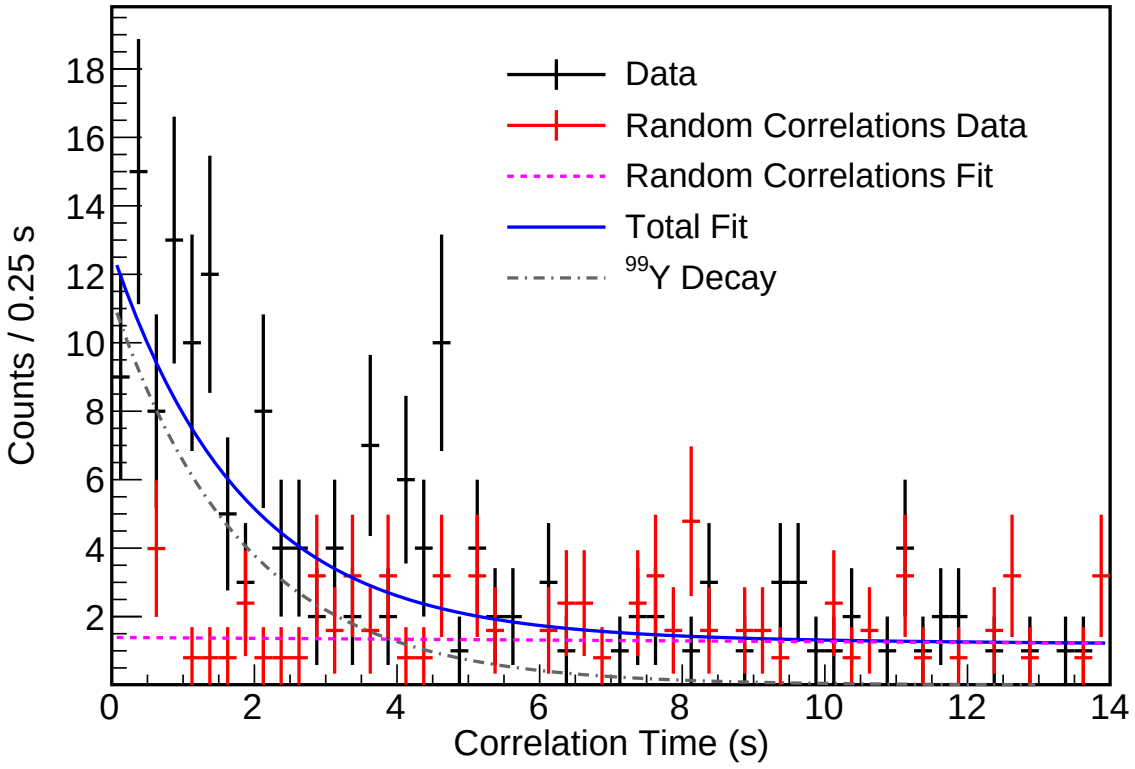

Figure 3.26: Decay curve for ^{99}Y. The selection of events in this decay curve is described in Table 3.6 and Sec. 3.3.1.1.

173, 174, 175, 176], experiments using the isotope separator on-line (ISOL) technique [171], and fragmentation-based experiments [170]. The half-life from the present work is in good agreement with previous measurements.

3.3.1.2 $^{101}_{40}\mathbf{Zr}_{61} \rightarrow {}^{101}_{41}\mathbf{Nb}_{60}$

The half-life of ^{101}Zr has been previously measured in fission-based experiments [177, 179, 180, 181]. Refs. [181, 179] both reported a large β-decay feeding intensity to levels in ^{101}Nb around 2 MeV. These measurements have been compiled in the decay scheme from ENSDF [178], which shows a group of nearby levels around 2 MeV (specifically, those levels between 1878.1 keV and 2030.65 keV, inclusive) that collectively have a relatively large β-decay

feeding intensity. In the present work, the TAS spectrum contains a prominent sum peak around 2 MeV [see Fig. 3.27(a)]. Examining the sum-of-segments spectrum while gating on this sum peak shows the high-energy γ rays (between roughly 1.8 MeV and 2 MeV within the energy resolution of SuN) that have a large probability to be emitted during the deexcitation of these levels that form the sum peak [see Fig. 3.27(b)]. Gating on the sum peak from these levels in the TAS spectrum and γ rays in the sum-of-segments spectrum produced the decay curve shown in Fig. 3.28 and resulted in a half-life of 2.27 $\pm$ 0.12 s, in good agreement with previous measurements.

3.3.1.3 $^{102}_{40}\mathbf{Zr}_{62} \rightarrow {}^{102}_{41}\mathbf{Nb}_{61}$

Ref. [2] observed a large β-decay feeding intensity to a level in ^{102}Nb at 599.48+x keV, where x is energy of the β-decaying isomeric state. In the present work, the TAS spectrum contains a prominent sum peak at 600 keV. The level at 599.48+x keV can deexcite to a level at 64.38+x keV, which in turn deexcites to the β-decaying isomeric state. The latter transition has a total internal conversion coefficient of 0.78 [2, 196, 13]. There are therefore counts to the left of the sum peak at 600 keV from internal conversion. Examining the sum-of-segments spectrum while gating on the sum peak at 600 keV and counts from internal conversion in the TAS spectrum shows the 535.13-keV and 599.48-keV γ rays that are emitted during the deexcitation of this level. Gates involving different combinations of this level and the two γ rays resulted in a half-life of 2.01 $\pm$ 0.08 s. The decay curve shown in Fig. 3.29 is gated on the sum peak at 600 keV in the TAS spectrum and γ ray with the same energy in the sum-of-segments spectrum.

The half-life of ^{102}Zr has been previously measured in fission-based experiments [182, 181]. One of those experiments only indirectly measured the half-life of ^{102}Zr by following

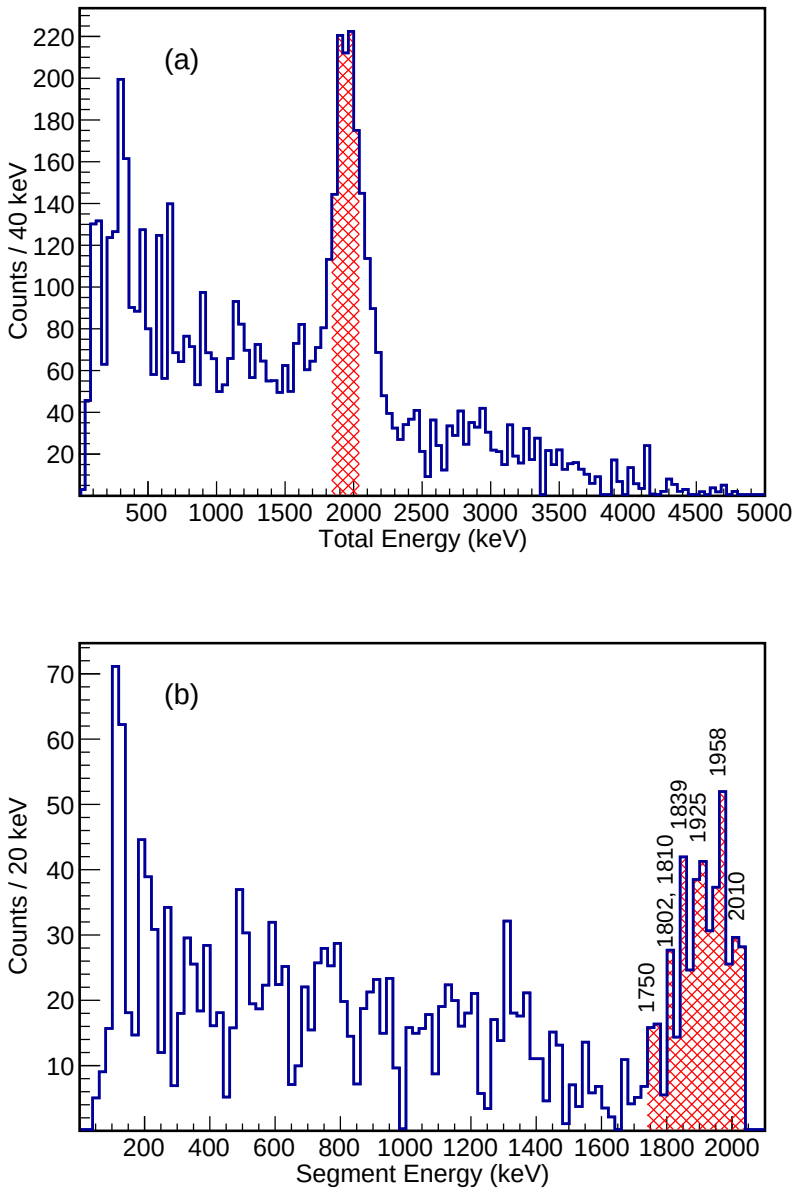

Figure 3.27: β-delayed γ-ray spectra for decay events correlated to ^{101}Zr implantations with a correlation time window of one second. The backward-time correlations (random background) have been subtracted from the forward-time correlations. The top panel, labeled (a), shows the TAS spectrum, and the red, cross hatches indicate the selection of events used to examine the individual γ rays in the sum-of-segments spectrum in the bottom panel. The bottom panel, labeled (b), shows the sum-of-segments spectrum only for certain events in the TAS spectrum as indicated in the top panel. Individual γ rays identified within the energy resolution of SuN are labeled. In (b), the red, cross hatches indicate the selection of events used to create the decay curve for ^{101}Zr, which is shown in Fig. 3.28.

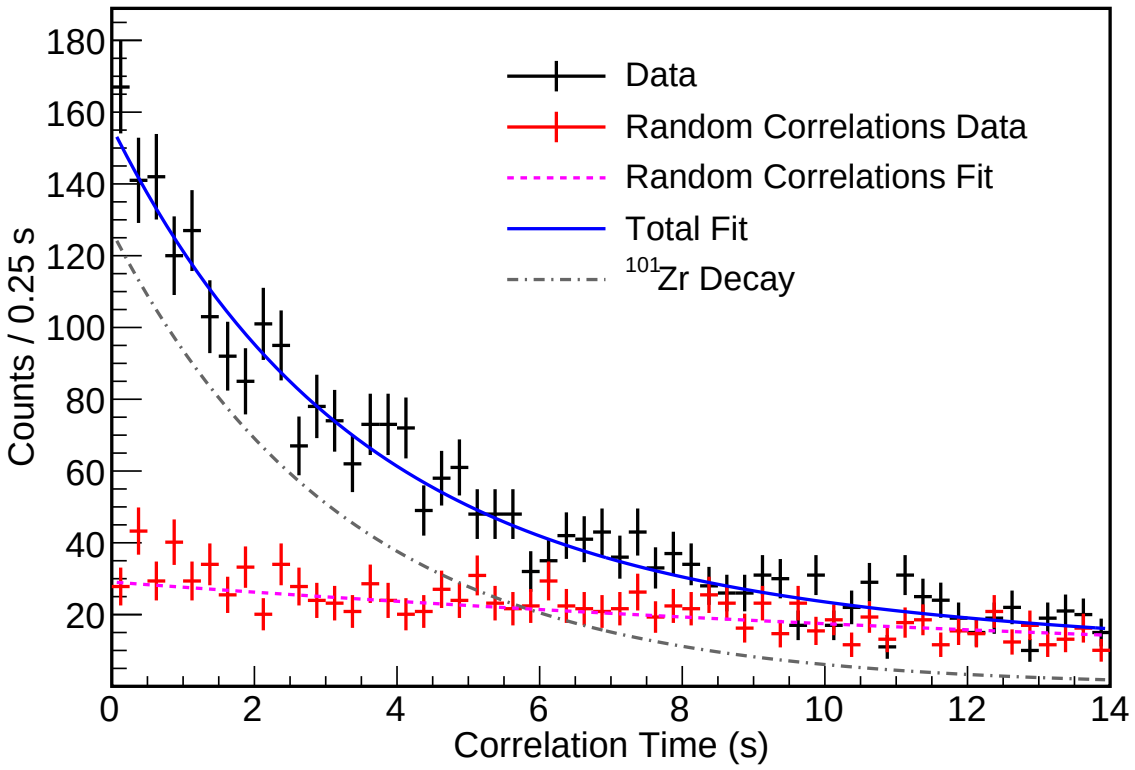

Figure 3.28: Decay curve for ^{101}Zr. The selection of events in this decay curve is described in Table 3.6 and shown in Fig. 3.27.

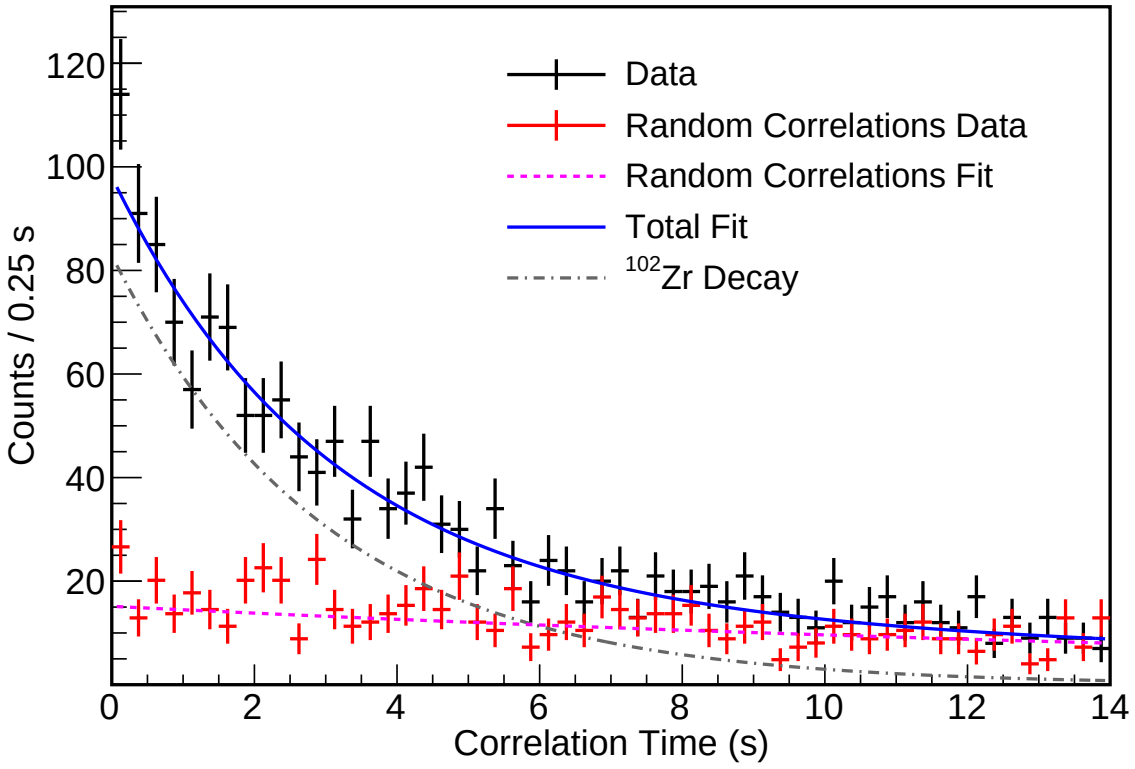

Figure 3.29: Decay curve for ^{102}Zr. The selection of events in this decay curve is described in Table 3.6 and Sec. 3.3.1.3.

the growth and decay of the daughter ^{102}Nb [182]. The half-life from the present work is in good agreement with one (Ref. [181]) of the two previous measurements.

3.3.1.4 $^{102m}_{41}\mathbf{Nb}_{61} \rightarrow {}^{102}_{42}\mathbf{Mo}_{60}$

The half-life of ^{102m}Nb has been previously measured in fission-based experiments [182]. For the decay of ^{102}Zr in the present work, there is an intense sum peak in the TAS spectrum at approximately 296 keV and a very intense peak with the same energy in the sum-of-segments spectrum. However, the decay schemes for the parent ^{102}Zr [196] and the charge-state contaminant ^{99}Zr^{39+} [24] do not list, around this energy, any levels that could be populated or γ rays that could be emitted during their respective β decays. Meanwhile,

a decay scheme exists for the ground state but not the β-decaying isomeric state of the daughter ^{102}Nb [196]. No evidence was found in the TAS spectrum for the decay of the ground state of the daughter, which agrees with Ref. [2] in terms of the β decay of ^{102}Zr populating levels in ^{102}Nb that are built on top of the β-decaying isomeric state. The origin of the peaks at approximately 296 keV in the TAS and sum-of-segments spectra was assigned to be from the β-decaying isomeric state populating the first excited state in ^{102}Mo at 296.61 keV. Gating on both this sum peak in the TAS spectrum and γ ray in the sum-of-segments spectrum produced the decay curve in Fig. 3.30 and resulted in a half-life of 1.33 $\pm$ 0.27 s, in good agreement with the previous measurement. In fitting the decay curve with the Bateman equations that described the growth and decay of ^{102m}Nb, the half-life of ^{102}Zr as determined in Sec. 3.3.1.3 was held constant.

3.3.1.5 $^{103}_{41}\mathbf{Nb}_{62} \rightarrow {}^{103}_{42}\mathbf{Mo}_{61}$

Refs. [183, 197] place the first excited state of ^{103}Mo populated in the β decay of ^{103}Nb at 102.6 keV. In the present work, the TAS spectrum and ungated sum-of-segments spectrum contain a prominent peak at this energy. Gating on both the sum peak from the first excited state and the γ ray produced the decay curve shown in Fig. 3.31, resulting in a half-life of 1.34 $\pm$ 0.07 s.

The half-life of ^{103}Nb has been previously measured in fission-based experiments [182, 183, 184]. The half-life from the present work is in good agreement with previous measurements.

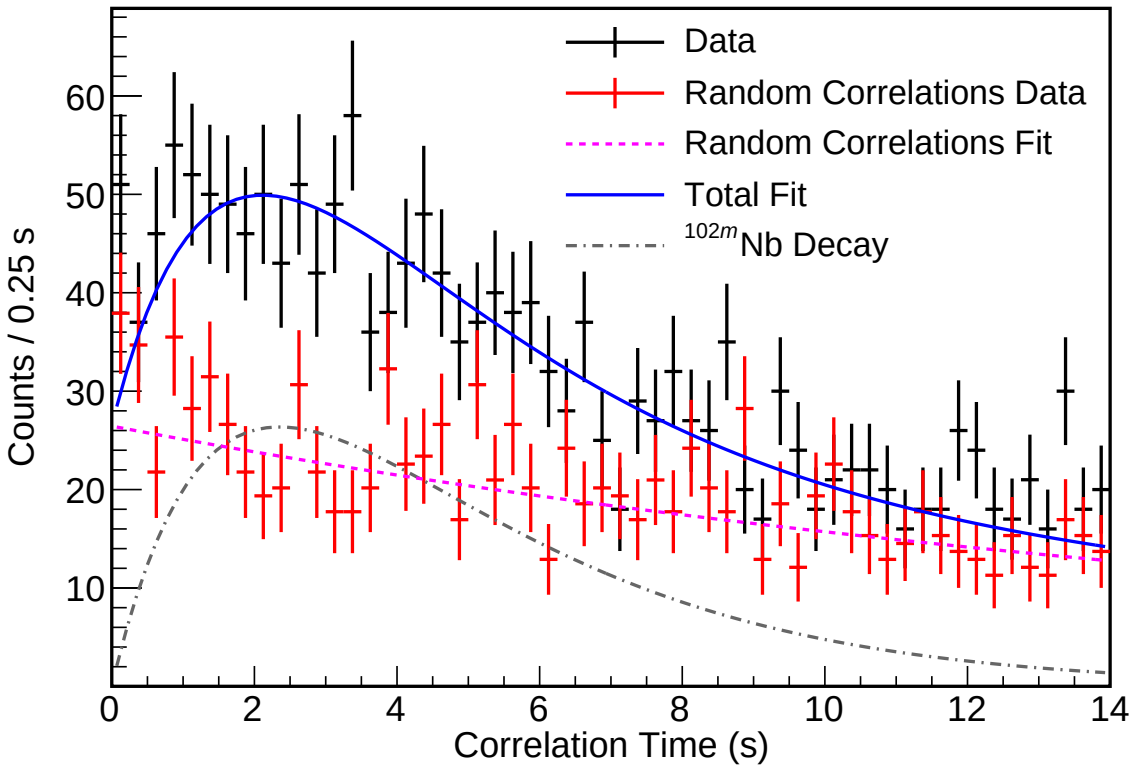

Figure 3.30: Decay curve for ^{102m}Nb. The selection of events in this decay curve is described in Table 3.6 and Sec. 3.3.1.4.

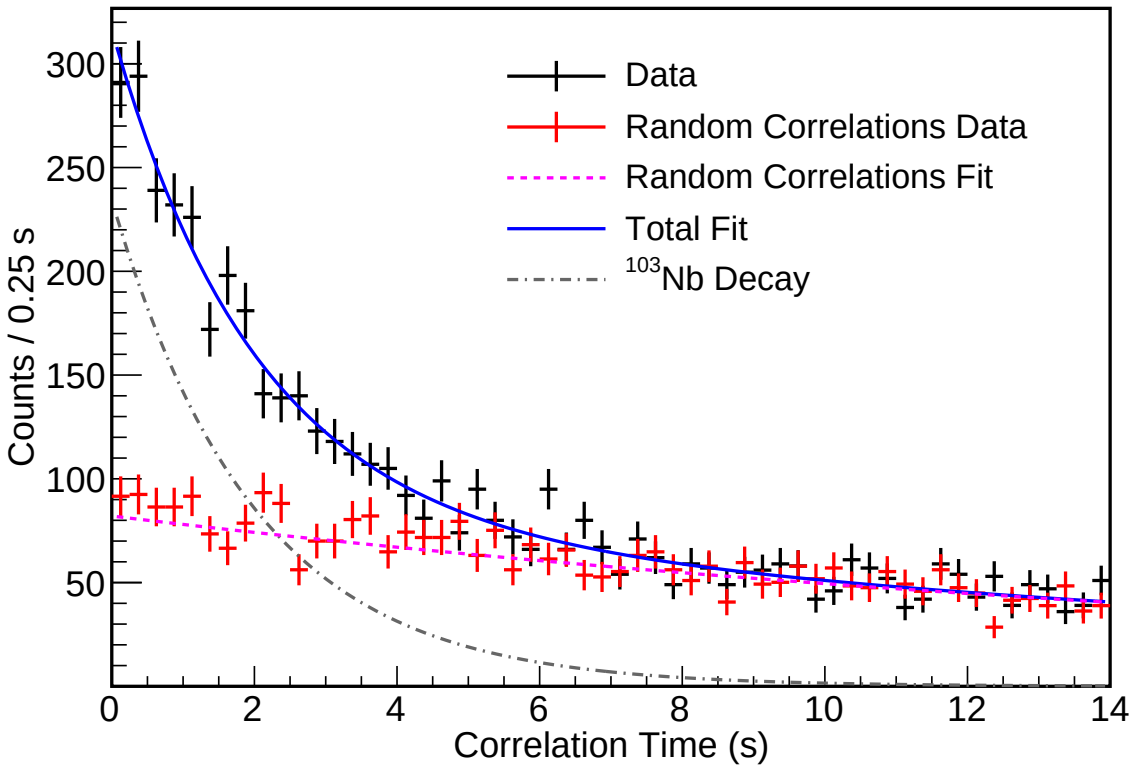

Figure 3.31: Decay curve for ^{103}Nb. The selection of events in this decay curve is described in Table 3.6 and Sec. 3.3.1.5.

3.3.1.6 $^{104m}_{41}\mathbf{Nb}_{63} \rightarrow {}^{104}_{42}\mathbf{Mo}_{62}$

The half-life of ^{104m}Nb has been previously measured in fission-based experiments [182, 186, 188, 175]. There are two β-decaying states in ^{104}Nb [182, 188]: a longer-lived ground state and shorter-lived isomeric state. The shorter-lived isomeric state predominately emits γ rays with energies of 368.4 keV, 477.5 keV, 519.2 keV, 555.3 keV, and 771.4 keV [188]. These γ rays are visible in the sum-of-segments spectrum. The decay curves gated on each of these γ rays were fit individually and the extracted half-lives were consistent with the half-life of the shorter-lived isomeric state [187]. Ref. [188] identified the 192.2 keV γ ray as originating from both the longer-lived ground state and shorter-lived isomeric state. A fit of the decay curve gated on only this γ ray produced a half-life consistent with the half-life of the shorter-lived isomeric state. No component for the longer-lived ground state was necessary for the fit of the decay curve. Ref. [188] identified a γ ray with an energy of 693.9 keV as originating from predominately the longer-lived ground state. In the present work, this γ ray has no significant peak in the sum-of-segments spectrum. With little evidence found for the longer-lived ground state in the decay curves and sum-of-segments spectrum, the conclusion was made that the fragmentation reaction in the experiment of the present work populated primarily the shorter-lived isomeric state, unlike all the previous fission-based experiments that produced both states of ^{104}Nb through fission.

The TAS spectrum is dominated by two sum peaks: the first sum peak is relatively narrow and symmetric, centered on approximately 2060 keV, and is attributed to the level at 2061.3 keV identified in Ref. [188] based on the γ rays observed in the sum-of-segments spectrum while gating on this sum peak; the second sum peak has a relatively wide right shoulder and is attributed to the collection of levels at 2656.6 keV, 2671.1 keV, 2684.5 keV,

2791.8 keV, and 2888.0 keV that were identified in Ref. [188] based on the γ rays observed in the sum-of-segments spectrum while gating on this sum peak.

The ground-state-to-ground-state Q value for the parent ^{104}Nb is 8531 keV, the daughter ^{104}Mo is 2153 keV, and the charge-state contaminant ^{101}Nb^{40+} is 4628 keV [16]. Therefore, counts in the TAS spectrum above approximately 4628 keV should only originate from the decay of ^{104}Nb.

The reported half-life is a result of fitting two decay curves. The first decay curve was created by gating on both of the dominant sum peaks in the TAS spectrum and the 192.2-keV γ ray in the sum-of-segments spectrum (see Fig. 3.32). The second decay curve was created by gating on the region of the TAS spectrum above 4628 keV and the 192.2-keV γ ray in the sum-of-segments spectrum. Taking the average of the half-lives from the two decay curves yielded a half-life of 0.97 $\pm$ 0.10 s. The half-life from the present work is in good agreement with previous measurements.

3.3.1.7 $^{109}_{43}\mathbf{Tc}_{66} \rightarrow {}^{109}_{44}\mathbf{Ru}_{65}$

In Ref [190], γ rays with energies 1158.7(5) keV and 1267.8(5) keV were observed from the β decay of ^{109}Tc. However, these γ rays were not placed in the decay scheme. In the present work, the TAS spectrum contains two sum peaks that correspond to these energies, meaning there are levels in ^{109}Ru with the same energies. Gating on both of these sum peaks in the TAS spectrum and both of these γ rays in the sum-of-segments spectrum produced the decay curve in Fig. 3.33 and resulted in a half-life of 0.87 $\pm$ 0.07 s.

The half-life of ^{109}Tc has been previously measured in fission-based experiments [175, 190, 191, 193, 194] and fragmentation-based experiments [189]. The half-life from the present work is in good agreement with previous measurements.

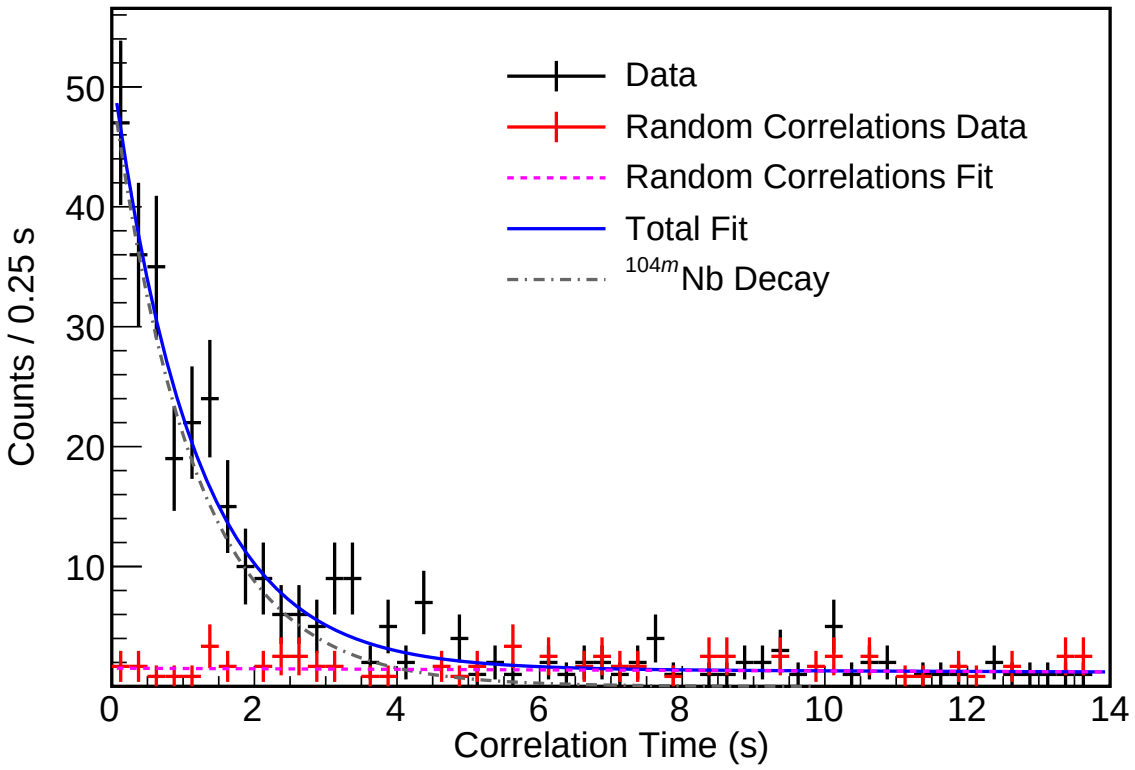

Figure 3.32: Decay curve for ^{104m}Nb. The selection of events in this decay curve is described in Table 3.6 and Sec. 3.3.1.6.

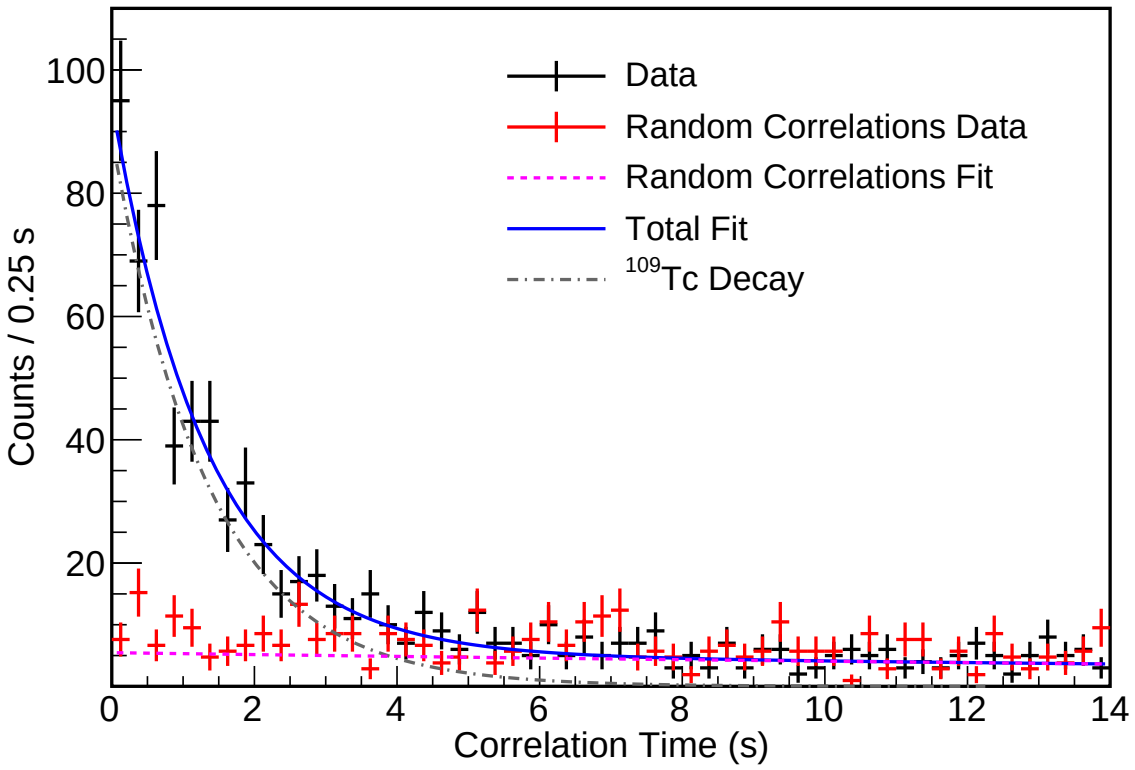

Figure 3.33: Decay curve for ^{109}Tc. The selection of events in this decay curve is described in Table 3.6 and Sec. 3.3.1.7.

3.3.2 Total Absorption Spectroscopy

In this section, the β-decay feeding intensity distributions and B(GT) distributions are extracted for ^{101}Zr, ^{102}Zr, and ^{109}Tc. In an attempt to learn about the shape of the ground state of the parent nucleus, the extracted distributions are compared to QRPA calculations by P. Sarriguren [87, 88]. In these QRPA calculations, the first step is to calculate the potential energy curve as a function of the quadrupole deformation parameter β_2 for a nuclide. A value of $\beta_2 = 0$ corresponds to a spherical shape (no quadrupole deformation). Negative values of β_2 correspond to oblate deformation (shaped like a discus), while positive values of β_2 correspond to prolate deformation (shaped like a rugby ball). In the second step, the quadrupole deformation parameters are found that minimize the potential energy curve. In the third step, those β_2 values that minimize the potential energy curve are used to calculate the B(GT) distribution. This calculation assumes similar shapes for the ground state of the parent nucleus and all the populated states in the daughter nucleus. The reason for this is because β-decay transitions connecting different shapes are disfavored (that is, there is a small overlap in the initial wave function of the parent nucleus and the final wave function of the daughter nucleus). In these calculations, the deformation breaks the degeneracy of the spherical single-particle wave functions. This results in the B(GT) distributions (and β-decay feeding intensity distributions) for deformed shapes (oblate and prolate) being much more fragmented than a spherical shape (see Sec. 3.3 of Ref. [102]).

The extracted distributions are compared to other QRPA calculations, which are commonly used to provide β-decay properties in r-process reaction network calculations. One set of QRPA calculations is by T. Marketin [198, 199] and the other is by P. Möller [200, 201]. The QRPA calculations that are compared to the experimental results in this dissertation

Table 3.7: QRPA calculations that are compared to the experimental results in this dissertation.

Calculation Name	Author	Reference
QRPA 1	P. Sarriguren	[87, 88]
QRPA 2	T. Marketin	[198, 199]
QRPA 3	P. Möller	[200, 201]

are summarized in Table 3.7.

One difference between the three QRPA calculations (see Table 3.7) is the way in which they solve the Schrödinger equation. QRPA 1 and QRPA 2 use a self-consistent approach, while QRPA 3 uses a phenomenological approach. In the self-consistent approach, the underlying mean field calculation must be consistent. That is, the residual interaction used in the QRPA calculation must be derived from the same force that determines the mean field. The Skyrme interaction [202] is used in QRPA 1, while a fully relativistic model is used in QRPA 2. In the phenomenological approach, the mean field and residual interaction are independently chosen. A phenomenological central potential (such as a folded-Yukawa potential) is used in QRPA 3. Another difference between the three QRPA calculations is that QRPA 1 and QRPA 3 can calculate β-decay properties for deformed nuclei, while QRPA 2 assumes only spherical nuclei.

3.3.2.1 $^{101}_{40}\mathbf{Zr}_{61} \rightarrow {}^{101}_{41}\mathbf{Nb}_{60}$

The half-life of the parent ^{101}Zr is 2.27(12) s (Sec. 3.3.1.2), the daughter ^{101}Nb is 7.1(3) s [178], and the charge-state contaminant $^{98}Zr^{39+}$ is 30.7(4) s [203]. Because the experimental spectra used in the TAS analysis were obtained with a correlation time window of one second, the amount of contamination from the decay of the charge-state contaminant was negligible. Contamination from the daughter was estimated with spectra obtained with a

later correlation time window (6 to 7 s). These spectra were scaled by the Bateman equations [169] to estimate their contribution in the correlation time window used in the TAS analysis (0 to 1 s). The ground-state-to-ground-state Q value for the β decay of the parent ^{101}Zr is 5726 keV, while the one-neutron separation energy of the daughter ^{101}Nb is 7165 keV [16], making β-delayed neutron emission energetically impossible.

Detector response functions were created for known levels populated in β decay below the critical energy (Table 3.5). They were created using information from the existing level scheme of the daughter from ENSDF [178]. All levels below the critical energy have unknown or tentative spin and parity assignments, and therefore four level schemes were constructed with different spin and parity assumptions. The different level schemes contributed to the uncertainty in the extracted β-decay feeding intensity distribution. There were a total of 36 detector response functions for known levels, starting at 0 keV and ending at 2119 keV.

Detector response functions were created for pseudo levels above the critical energy (Table 3.5). The spin and parity of the ground state of the parent ^{101}Zr is $(3/2^+)$ [178]. According to β-decay selection rules for allowed Gamow-Teller transitions, the states populated in the daughter are $1/2^+$, $3/2^+$, and $5/2^+$. Following these rules, γ-ray cascades from three pseudo levels were created with DICEBOX for each energy bin in the quasi-continuum. These three pseudo levels had corresponding detector response functions created with GEANT4, from which an average detector response function was created and used in the TAS analysis. There were a total of 17 average detector response functions for pseudo levels, starting at 2220 keV (where the total level density is approximately 0.23 / keV [166] and the energy resolution of SuN is approximately 115 keV) and ending at 4195 keV (where the total level density is approximately 5.57 / keV [166] and the energy resolution of SuN is approximately 173 keV).

The TAS spectrum, sum-of-segments spectrum, and multiplicity spectrum are shown in Fig. 3.34. One dominating feature of the TAS spectrum is the sum peak from a group of levels (specifically, those levels between 1878.1 keV and 2030.65 keV, inclusive) that collectively have a relatively large β-decay feeding intensity. Previous fission-based experiments also observed that these levels collectively have a relatively large β-decay feeding intensity. In one of those previous experiments, the authors state in Sec. 2 of Ref. [181] that they observed a relatively large β-decay feeding intensity to levels at 1928 keV, 1958 keV, and 2009 keV. However, no values were given for the β-decay feeding intensity to those levels. In another previous experiment, Ref. [179] created a decay scheme for ^{101}Zr. In that decay scheme [179], the collective β-decay feeding intensity assigned to the levels between 1878.1 keV and 2030.65 keV, inclusive, is 19.5%. Taking into account the uncertainty, the minimum and maximum collective β-decay feeding intensity is 14.1% and 24.9%, respectively. In the present work, the collective β-decay feeding intensity extracted for these levels is 23.6%, and the minimum and maximum collective β-decay feeding intensity is 22.2% and 25.0%, respectively. The present work and the decay scheme of Ref. [179] are in agreement for the collective β-decay feeding intensity assigned to this group of levels.

Another dominating feature of the TAS spectrum is the ground-state-to-ground-state transition. However, the ground-state-to-ground-state transition is hard to observe in the TAS spectrum. This is because the ground-state-to-ground-state transition does not emit any characteristic γ rays, and instead appears as a broad continuum. The ground-state-to-ground-state transition was included as one of the response functions in the fitting procedure. In the decay scheme of Ref. [179], the β-decay feeding intensity assigned to the ground-state-to-ground-state transition is 57(11)%. In the present work, the β-decay feeding intensity for the ground-state-to-ground-state transition is $51.2^{+2.8}_{-12.2}$%. The present work and the decay

scheme of Ref. [179] are in agreement for the β-decay feeding intensity assigned to the ground-state-to-ground-state transition.

In the sum-of-segments spectrum, noticeable features include peaks corresponding to γ rays with a relatively large absolute γ-ray intensity [178]. This includes a peak corresponding to the 119.3 keV γ ray, a peak corresponding to the 205.7 keV and 208.5 keV γ rays, and a broad peak corresponding to γ rays with energies between 1810.1 keV and 2009.5 keV.

The β-decay feeding intensity distribution of ^{101}Zr as a function of excitation energy in the daughter nucleus ^{101}Nb is reported in Table 3.8. The β-decay feeding intensity distribution in Table 3.8 is an average of the different level schemes assumed for the daughter (Sec. 3.2.3.2). The amount of β-decay feeding intensity to known levels is 91.4% and to pseudo levels is 8.6%. Three different sources of uncertainty contribute to the total uncertainty that is reported in Table 3.8. The first source of uncertainty comes from the statistics of the TAS spectrum. The inherent statistical uncertainty in the number of counts per bin in the TAS spectrum is directly related to the uncertainty in the extracted β-decay feeding intensity distribution. The weighted average of the uncertainty from statistics was 10%. The second source of uncertainty comes from variations in the level schemes of the daughter (Sec. 3.2.3.2). For each excitation energy, the minimum, average, and maximum intensity using the different level schemes was calculated. The difference between the average and the minimum (maximum) intensity contributes to the lower (upper) bound on the uncertainty. The weighted average of the uncertainty from multiple level schemes was 2%. The third source of uncertainty comes from the ground-state-to-ground-state transition and is discussed below.

Extracting the β-decay feeding intensity for the ground-state-to-ground-state transition relies on the collisional energy losses between β-decay electrons and the sensitive volume

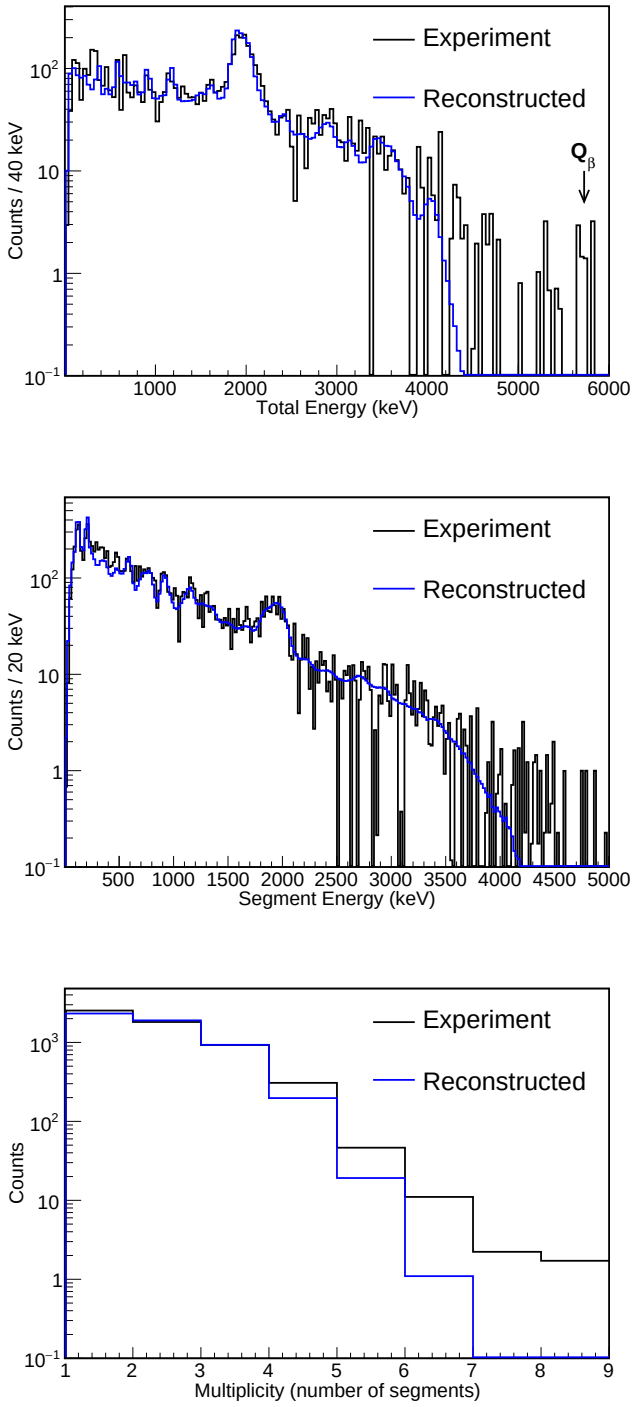

Figure 3.34: Comparison of experimental (black, solid line) and reconstructed (blue, solid line) spectra from the β decay of ^{101}Zr for the TAS spectrum (top panel), sum-of-segments spectrum (middle panel), and multiplicity spectrum (bottom panel). The experimental spectra were obtained by correlating decay events to ^{101}Zr implantations with a correlation time window of one second. Contamination from random correlations and the decay of the daughter has been subtracted from the experimental spectra. There is a label for the ground-state-to-ground-state Q value in the TAS spectrum for the β decay of ^{101}Zr at 5726 keV [16].

Table 3.8: The β-decay feeding intensity distribution of ^{101}Zr as a function of excitation energy in the daughter nucleus ^{101}Nb. Intensity values below 10^{-4} % are set to 0.

Energy (keV)	Intensity (%)	Error (–)	Error (+)	Energy (keV)	Intensity (%)	Error (–)	Error (+)
0	51.2	12.2	2.8	1844	0.0002	0.0002	0.0003
119	0.0002	0.0002	0.0003	1878	8.01	0.43	0.43
206	0.0001	0.0001	0.0001	1925	3.92	0.26	0.26
208	0	0	0	1929	0.0038	0.0038	0.0032
255	0.0000	0.0000	0.0001	1958	4.15	0.23	0.25
346	0.0011	0.0011	0.0024	2010	1.98	0.11	0.14
374	1.94	0.25	0.26	2031	5.51	0.31	0.31
532	0.0000	0.0000	0.0001	2096	0.010	0.010	0.015
593	2.95	0.50	0.51	2119	1.78	0.13	0.13
598	0.0000	0.0000	0.0001	2220	0.837	0.092	0.094
673	1.21	0.18	0.18	2320	0.016	0.015	0.035
703	0.0014	0.0014	0.0017	2420	1.20	0.18	0.18
722	0.68	0.15	0.15	2520	0.0013	0.0013	0.0021
778	0	0	0	2620	0.350	0.171	0.098
782	0.90	0.14	0.14	2720	0.0001	0.0001	0.0001
879	0.025	0.024	0.016	2820	0.34	0.12	0.24
900	0	0	0	2920	1.40	0.25	0.19
912	2.08	0.28	0.28	3020	0.012	0.012	0.015
922	0.013	0.009	0.015	3145	0.84	0.15	0.15
953	0	0	0	3295	0.0001	0.0001	0.0002
1061	0.0020	0.0020	0.0025	3445	1.27	0.27	0.28
1110	0	0	0	3595	1.28	0.27	0.27
1120	0.0015	0.0015	0.0029	3745	0.47	0.20	0.19
1126	0	0	0	3895	0.0001	0.0001	0.0001
1180	3.12	0.32	0.32	4045	0.53	0.16	0.16
1294	0.0012	0.0011	0.0020	4195	0.109	0.065	0.065
1620	1.89	0.20	0.20				

of SuN or the associated bremsstrahlung radiation. Because no characteristic γ rays are emitted, the sensitivity of SuN to this type of transition is reduced. An additional analysis procedure was performed to test the sensitivity of SuN to the ground-state-to-ground-state transition. This additional procedure was comparing the initial number of decaying nuclei between experiment and simulation (Sec. 3.2.3.5).

The left panel of Fig. 3.35 shows the reduced χ^2_{global} as a function of ground-state-to-ground-state transition probability. The β-decay feeding intensity was fixed for the ground-state-to-ground-state transition while the β-decay feeding intensity was allowed to vary for all other levels. In total, 100 fits were performed. In these fits, the β-decay feeding intensity was fixed for the ground-state-to-ground-state transition between 0-1%, 1-2%, ..., 98-99%, 99-100%. For each fit, the reduced χ^2_{global} was calculated. The β-decay feeding intensity distribution reported in Table 3.8 was extracted without any constraint on the ground-state-to-ground-state transition. The ground-state-to-ground-state transition probability in Table 3.8 is 51.2%, which corresponds to the minimum of the distribution in the left panel of Fig. 3.35.

Note that the same plot as Fig. 3.35 could be made with χ^2_{global} on the y axis instead of reduced χ^2_{global}. In that case, the statistical uncertainty in the ground-state-to-ground-state transition would not be the ground-state-to-ground-state transitions that are one χ^2_{global} unit from the minimum. Estimating the uncertainty using one χ^2_{global} unit from the minimum would only vary the β-decay feeding intensity for the ground-state-to-ground-state transition and hold constant the β-decay feeding intensity for all other levels. However, this would not make sense because the β-decay feeding intensity is bound by the constraint that the sum is unity (1.0 or 100%). Therefore, the feeding to all levels must be varied for each fit.

The right panel of Fig. 3.35 shows the initial number of decaying nuclei in experiment

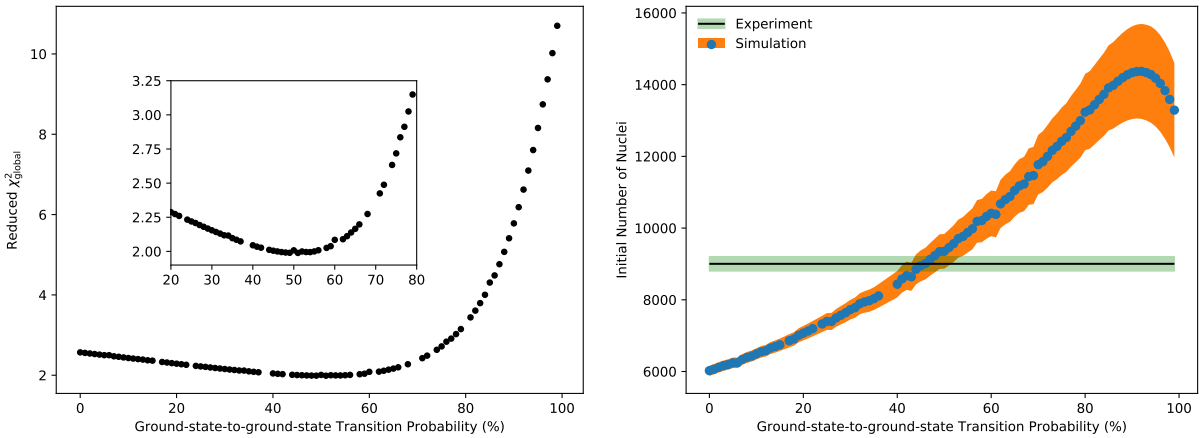

Figure 3.35: Left panel: Reduced χ^2_{global} as a function of ground-state-to-ground-state transition probability for the β decay of ^{101}Zr. The inset shows an enlarged view of the minimum. Right panel: Initial number of nuclei as a function of ground-state-to-ground-state transition probability for the β decay of ^{101}Zr.

and simulation as a function of ground-state-to-ground-state transition probability. The uncertainty in the initial number of decaying nuclei in experiment was statistical and was from the subtraction of random correlations and decays of the daughter. The uncertainty in the initial number of decaying nuclei in simulation was from the uncertainty in the summing efficiency of SuN. That is, the uncertainty in the extracted β-decay feeding intensity for each level was 10% [95].

In the right panel of Fig. 3.35, wherever the uncertainty bands intersect, the ground-state-to-ground-state transition probability yields a consistent initial number of decaying nuclei between experiment and simulation. The ground-state-to-ground-state transition probability corresponding to the minimum in the left panel of Fig. 3.35 is within the intersection of the uncertainty bands in the right panel of Fig. 3.35. The lower and upper bounds of the intersection were adopted for the uncertainty in the ground-state-to-ground-state transition.

Figure 3.36 shows a comparison of experimental and theoretical cumulative β-decay feeding intensity distributions and cumulative B(GT) distributions for the β decay of ^{101}Zr. The

upper left panel of Fig. 3.36 contains the cumulative β-decay feeding intensity distribution for the present work and QRPA 1 calculations (Table 3.7). The QRPA 1 calculations were performed assuming the shape of the ground state of ^{101}Zr is oblate (quadrupole deformation parameter of $\beta_2 = -0.207$) and prolate (quadrupole deformation parameter of $\beta_2 = 0.362$). Both shapes have similar half-lives ($T_{1/2}$ = 3.34 s for the oblate shape and $T_{1/2}$ = 3.73 s for the prolate shape), but different cumulative β-decay feeding intensity distributions. The half-life for the oblate shape and prolate shape is 47% larger and 64% larger, respectively, than the half-life extracted in the current work. The ground-state-to-ground-state transition in experiment is better reproduced by the prolate shape. Between approximately 500 keV and 2000 keV, the current work is in agreement with the oblate shape. After approximately 2300 keV, the current work is in agreement with both shapes. Both shapes have a relatively large increase in the cumulative β-decay feeding intensity distribution between approximately 1000 keV and 1200 keV that is not observed in the current work. The same situation occurs at approximately 3500 keV. Only the oblate shape has a relatively large increase in the cumulative β-decay feeding intensity distribution at levels near 2000 keV that is observed in experiment.

The lower left panel of Fig. 3.36 contains the cumulative B(GT) distribution for the present work and QRPA 1 (Table 3.7). The cumulative B(GT) distributions in this panel correspond to the cumulative β-decay feeding intensity distributions in the upper left panel. As with the cumulative β-decay feeding intensity distributions in the upper left panel, both shapes have similar half-lives and yet different cumulative B(GT) distributions. Between 0 keV and approximately 1800 keV, the current work is in better agreement with the prolate shape. Between approximately 1800 keV and 3500 keV, the current work is not in agreement with any shape. However, unlike the prolate shape, the oblate shape has an increase in

the cumulative B(GT) distribution in this energy region, which is observed in experiment. The cumulative B(GT) distribution in the current work ends approximately in between the cumulative B(GT) distributions for the different shapes. Only the oblate shape has a relatively large increase in the cumulative B(GT) distribution at levels near 2000 keV that is observed in experiment.

The QRPA 1 calculations correspond to pure shape configurations, either oblate or prolate. None of these pure shape configurations reproduce the experimental cumulative β-decay feeding intensity distribution or B(GT) distribution. This may indicate that some type of mixture between these two shapes is necessary to reproduce the result from the current work.

The upper right panel of Fig. 3.36 contains the cumulative β-decay feeding intensity distribution for the present work, QRPA 2, and QRPA 3 (Table 3.7). None of these QRPA calculations reproduce the ground-state-to-ground-state transition from the current work. Both of these QRPA calculations are characterized by a small cumulative β-decay feeding intensity at low energies, and then a sudden and relatively large increase in the cumulative β-decay feeding intensity distribution at higher energies. In QRPA 2, this occurs at approximately 2500 keV. In QRPA 3, this occurs at approximately 3500 keV. None of these calculations reproduce the structure in the cumulative β-decay feeding intensity distribution from the current work. The half-life from QRPA 2 is 63% smaller than the half-life extracted in the current work. Meanwhile, the half-life from QRPA 3 is larger than the half-life extracted in the current work by more than a factor of ten.

The lower right panel of Fig. 3.36 contains the cumulative B(GT) distribution for the present work and QRPA 3. The cumulative B(GT) distributions in this panel correspond to the cumulative β-decay feeding intensity distributions in the upper right panel. The cumulative B(GT) distribution from the current work and QRPA 3 are not in agreement for

any energy. Note that the quadrupole deformation parameter used in QRPA 3 is $\beta_2 = 0.376$. This is similar to the value used in QRPA 1 ($\beta_2 = 0.362$). In addition, the cumulative B(GT) distributions for these prolate shapes are qualitatively similar. For example, both calculations have a small cumulative B(GT) at low energies, and then a relatively large increase in the cumulative B(GT) at approximately 3500 keV. The total B(GT) within the ground-state-to-ground-state Q value is similar for both calculations. However, the half-lives for the prolate calculations (3.73 s and 37.48 s) are different. In addition, the cumulative β-decay feeding intensity distributions for the prolate shapes are markedly different.

3.3.2.2 $^{102}_{40}\mathbf{Zr}_{62} \rightarrow {}^{102}_{41}\mathbf{Nb}_{61}$

The half-life of the parent ^{102}Zr is 2.01(8) s (Sec. 3.3.1.3), the daughter ^{102m}Nb is 1.33(27) s (Sec. 3.3.1.4), and the charge-state contaminant ^{99}Zr^{39+} is 2.1(1) s [24]. Contamination from the daughter was estimated with spectra obtained with a later correlation time window (6 to 7 s). These spectra were scaled by the Bateman equations [169] to estimate their contribution in the correlation time window used in the TAS analysis (0 to 1 s). Charge-state contamination from ^{99}Zr^{39+} was minimized with conservative gates in the particle identification spectrum. The ground-state-to-ground-state Q value for the β decay of the parent ^{102}Zr is 4717 keV, while the one-neutron separation energy of the daughter ^{102}Nb is 5484 keV [16], making β-delayed neutron emission energetically impossible.

The half-life extracted from the decay curve gated simultaneously on the TAS and sum-of-segments spectra in Sec. 3.3.1.4 led to the conclusion that the β decay of ^{102}Zr populates levels in ^{102}Nb that are built on top of the β-decaying isomeric state. The same conclusion was found in Ref. [2], and therefore their energy assigned to the β-decaying isomeric state ("x" = 93 keV) was adopted in the present work.

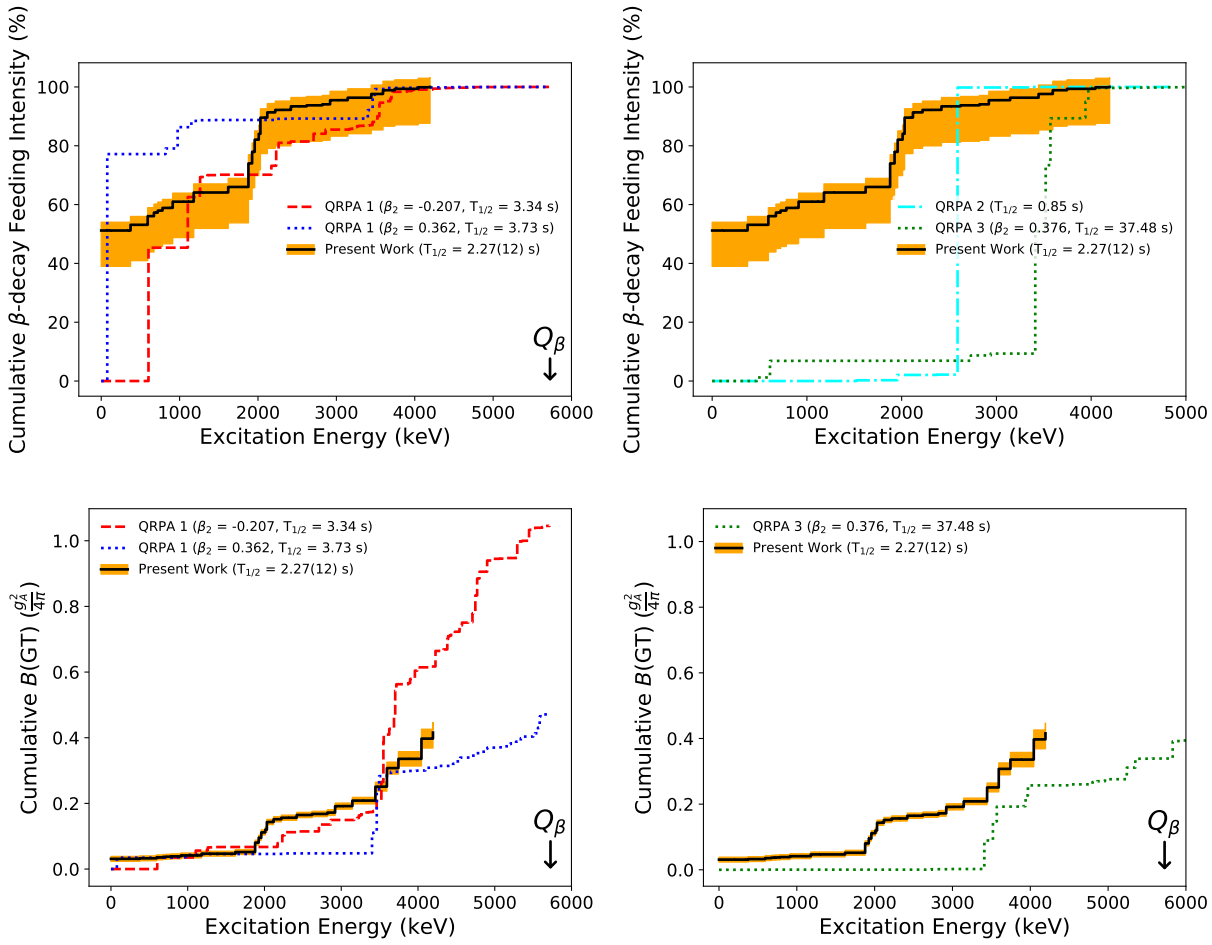

Figure 3.36: Comparison of experimental and theoretical cumulative β-decay feeding intensity distributions and cumulative B(GT) distributions for the β decay of ^{101}Zr. The upper panels show cumulative β-decay feeding intensity. The lower panels show cumulative B(GT). The left panels contain QRPA 1 calculations. In the left panels, the present work (black, solid line, with uncertainty in orange shading) is compared to QRPA 1 calculations assuming the shape of the ground state of the parent is oblate (red, dashed line) and prolate (blue, dotted line). The right panels contain QRPA calculations commonly used in r-process reaction network calculations. In the right panels, the present work (black, solid line, with uncertainty in orange shading) is compared to QRPA 2 (cyan, dash-dotted line) and QRPA 3 (green, dotted line). The lower right panel does not contain a QRPA 2 calculation. Some panels may contain an arrow indicating the ground-state-to-ground-state Q value for the β decay of ^{101}Zr at 5726 keV [16]. The experimental and theoretical half-lives $T_{1/2}$ are provided in parentheses. If the quadrupole deformation parameter β_2 was provided with a theoretical calculation, that is provided in the parentheses.

Detector response functions were created for known levels populated in β decay below the critical energy (Table 3.5). They were created using information from the existing level scheme of the daughter from ENSDF [196]. There were a total of 12 detector response functions for known levels, starting at 0+x keV and ending at 941+x keV.

The level at 20+x keV has a single transition to the level at 0+x keV. This transition has a large total internal conversion coefficient [2, 196]. Any radiation emitted during this transition, regardless of whether or not internal conversion occurred, is below the detection threshold of SuN. As a consequence, the detector response functions for the levels at 0+x keV and 20+x keV were nearly identical. Therefore, a single detector response function was used for both levels in the TAS analysis at 0+x keV.

Detector response functions were created for pseudo levels above the critical energy (Table 3.5). The spin and parity of the ground state of the parent ^{102}Zr is 0^+ [196]. According to β-decay selection rules for allowed Gamow-Teller transitions, the states populated in the daughter are 1^+. Following these rules, γ-ray cascades from one pseudo level was created with DICEBOX for each energy bin in the quasi-continuum. Each pseudo level had a corresponding detector response function created with GEANT4. There were a total of 28 detector response functions for pseudo levels, starting at 1000+x keV (where the total level density is approximately 0.08 / keV [166] and the energy resolution of SuN is approximately 71 keV) and ending at 3000+x keV (where the total level density is approximately 3.50 / keV [166] and the energy resolution of SuN is approximately 143 keV).

The TAS spectrum, sum-of-segments spectrum, and multiplicity spectrum are shown in Fig. 3.37. The sum peak corresponding to the level at 599.48+x keV is one of the dominating features in the TAS spectrum. A previous experiment studying the β decay of ^{102}Zr assigned a β-decay feeding intensity of 25(2)% to this level [2, 196]. In the present work, the β-decay

feeding intensity extracted for this level is $23.1^{+1.5}_{-1.5}$%. The present work and the decay scheme of Ref. [2, 196] are in agreement for the β-decay feeding intensity assigned to this level.

The ground-state-to-ground-state transition is another dominating feature of the TAS spectrum. Because the ground-state-to-ground-state transition does not emit any characteristic γ rays, observing this transition in the TAS spectrum is difficult. In the decay scheme of Ref. [2, 196], an upper limit of 59(3)% was assigned to the ground-state-to-ground-state transition. In the present work, the β-decay feeding intensity for the ground-state-to-ground-state transition is 45.0^{+7}_{-9}%. This value is consistent with the upper limit placed by the authors of the decay scheme in Ref. [2]. An upper limit could only be placed on the ground-state-to-ground-state transition in Ref. [2] because the decay scheme ended at 940.5+x keV. With a ground-state-to-ground-state Q value for the β decay of ^{102}Zr at 4717 keV [16], the authors of Ref. [2] noted that there was probably some β-decay feeding intensity to higher-lying levels that was missed due to their limited detection sensitivity.

Peaks corresponding to γ rays with a relatively large absolute γ-ray intensity [178] can be seen in the sum-of-segments spectrum. This includes a peak corresponding to the 64.46 keV γ ray, a peak corresponding to the 152.4 keV and 156.14 keV γ rays, a peak corresponding to the 535.13 keV γ ray, and a peak corresponding to the 599.48 keV γ ray. The strongest transitions observed in Ref. [2] had energies of 64 keV, 535 keV, and 599 keV.

The β-decay feeding intensity distribution of ^{102}Zr as a function of excitation energy in the daughter nucleus ^{102}Nb is reported in Table 3.9. The β-decay feeding intensity distribution in Table 3.9 is the result of the single level scheme assumed for the daughter. The amount of β-decay feeding intensity to known levels is 74.6% and to pseudo levels is 25.4%. Two different sources of uncertainty contribute to the total uncertainty that is

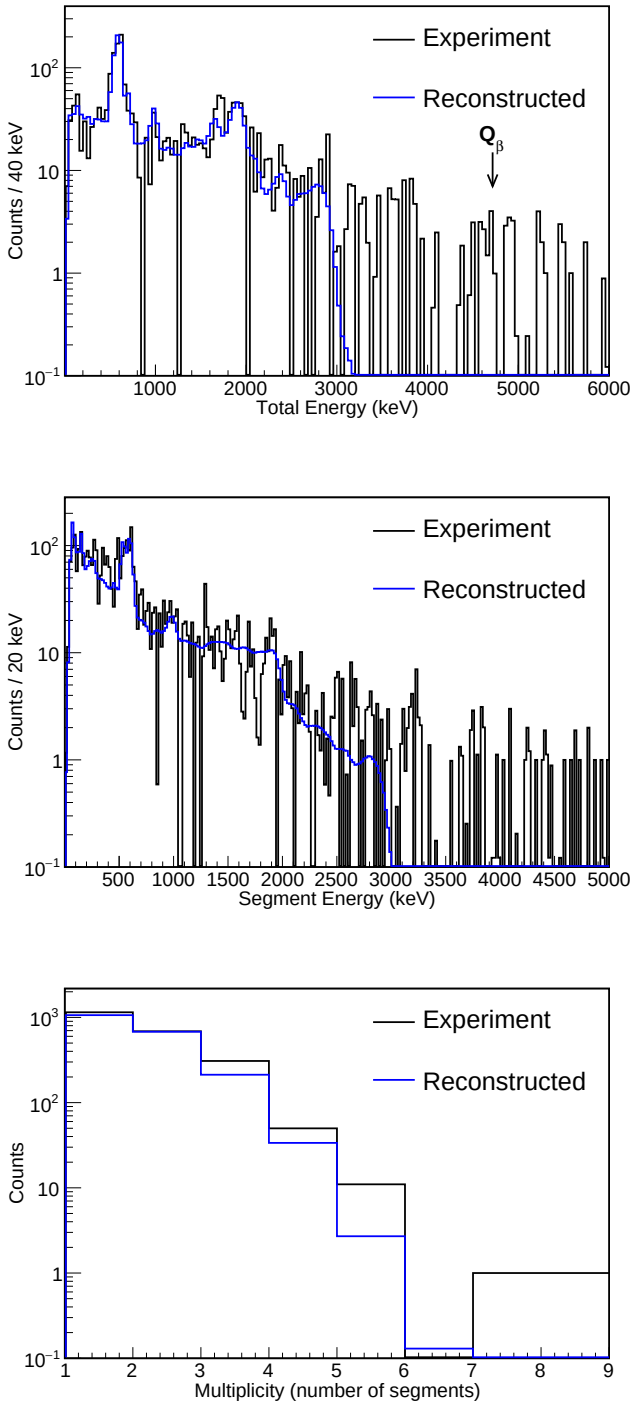

Figure 3.37: Comparison of experimental (black, solid line) and reconstructed (blue, solid line) spectra from the β decay of ^{102}Zr for the TAS spectrum (top panel), sum-of-segments spectrum (middle panel), and multiplicity spectrum (bottom panel). The experimental spectra were obtained by correlating decay events to ^{102}Zr implantations with a correlation time window of one second. Contamination from random correlations and the decay of the daughter has been subtracted from the experimental spectra. There is a label for the ground-state-to-ground-state Q value in the TAS spectrum for the β decay of ^{102}Zr at 4717 keV [16].

reported in Table 3.9. These sources were discussed for the case of ^{101}Zr in Sec. 3.3.2.1. The weighted average of the uncertainty from statistics was 13%. There was only one level scheme assumed for ^{102}Nb, so there was no uncertainty from multiple level schemes. The uncertainty from the ground-state-to-ground-state transition (or, in this case, transition from the ground state to the β-decaying isomeric state) is discussed below.

The analysis procedure for determining the uncertainty in the ground-state-to-ground-state transition was already discussed for the case of ^{101}Zr in Sec. 3.3.2.1. The left panel of Fig. 3.38 shows the reduced χ^2_{global} as a function of ground-state-to-ground-state transition probability (or, in this case, transition from the ground state to the β-decaying isomeric state). The β-decay feeding intensity distribution reported in Table 3.9 was extracted without any constraint on the ground-state-to-ground-state transition. The ground-state-to-ground-state transition probability in Table 3.9 is 45.0%, which corresponds to the minimum of the distribution in the left panel of Fig. 3.38.

The right panel of Fig. 3.38 shows the initial number of decaying nuclei in experiment and simulation as a function of ground-state-to-ground-state transition probability. The ground-state-to-ground-state transition probability of 45.0% (Table 3.9 and the minimum of the distribution in the left panel of Fig. 3.38) does not intersect with the uncertainty band from experiment. Instead, the intersection of the uncertainty bands is centered on 60%. Therefore, the fit in which the ground-state-to-ground-state transition probability was held fixed between 60% and 61% is reported in Table 3.10. The lower and upper bounds of the intersection of the uncertainty bands were adopted for the uncertainty in the ground-state-to-ground-state transition reported in Table 3.10. This uncertainty was also adopted for the uncertainty in the ground-state-to-ground-state transition reported in Table 3.9. There have been other cases in which uncertainty in the ground-state-to-ground-transition probability

Table 3.9: The β-decay feeding intensity distribution of ^{102}Zr as a function of excitation energy in the daughter nucleus ^{102}Nb. Intensity values below 10^{-4} % are set to 0. As explained in Sec. 3.3.2.2, each level was assumed to be built on top of the β-decaying isomeric state. That is, a value of "x" = 93 keV as determined by Ref. [2] should be added to each level. As explained in Sec. 3.3.2.2, the detector response function for the level at 20+x keV was not used in the TAS analysis.

Energy (keV)	Intensity (%)	Error (–)	Error (+)	Energy (keV)	Intensity (%)	Error (–)	Error (+)
0	45.0	9.0	7.0	1480	1.18	0.28	0.28
20	0	0	0	1540	0	0	0
64	0.0003	0.0001	0.0001	1600	0	0	0
94	0	0	0	1660	2.82	0.39	0.39
156	0.74	0.13	0.13	1720	1.29	0.13	0.13
161	0	0	0	1780	0.0011	0.0001	0.0001
246	0	0	0	1840	0.828	0.094	0.094
258	0	0	0	1900	4.04	0.51	0.51
431	0.93	0.18	0.18	1960	4.17	0.62	0.62
599	23.1	1.5	1.5	2020	0	0	0
705	4.82	0.61	0.61	2100	1.57	0.36	0.36
941	0	0	0	2200	0.0333	0.0080	0.0080
1000	3.27	0.72	0.72	2300	0.087	0.021	0.021
1060	0	0	0	2400	1.36	0.33	0.33
1120	0.212	0.054	0.054	2500	0	0	0
1180	0.51	0.13	0.13	2600	0.59	0.14	0.14
1240	0	0	0	2700	0.59	0.13	0.13
1300	0	0	0	2800	0.98	0.35	0.35
1360	1.02	0.30	0.30	2900	0.89	0.22	0.22
1420	0	0	0	3000	0.0005	0.0004	0.0004

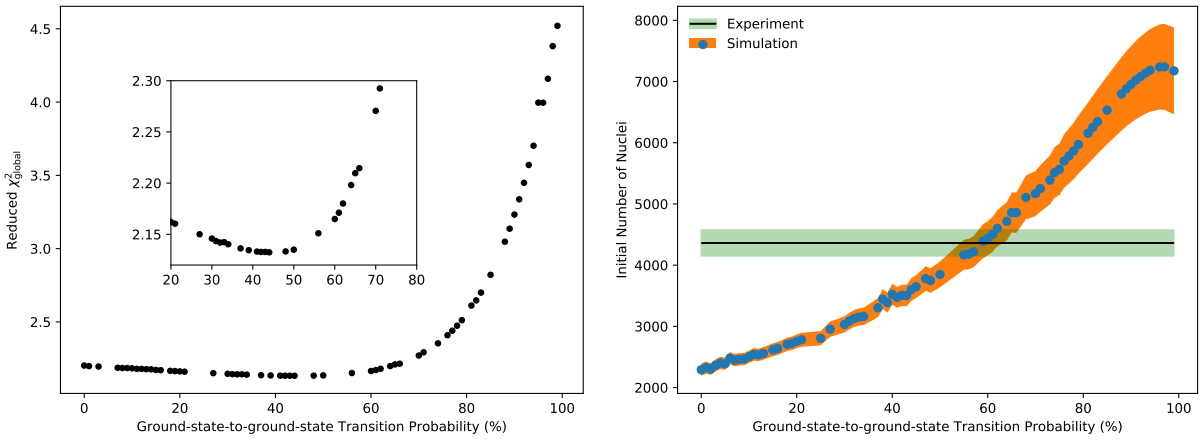

Figure 3.38: Left panel: Reduced χ^2_{global} as a function of ground-state-to-ground-state transition probability for the β decay of ^{102}Zr. The inset shows an enlarged view of the minimum. Right panel: Initial number of nuclei as a function of ground-state-to-ground-state transition probability for the β decay of ^{102}Zr.

in a TAS measurement has resulted in two reported β-decay feeding intensity distributions. For example, this was the case for ^{105}Tc in Ref. [79].

Figure 3.39 shows a comparison of experimental and theoretical cumulative β-decay feeding intensity distributions and cumulative B(GT) distributions for the β decay of ^{102}Zr. The upper left panel of Fig. 3.39 contains the cumulative β-decay feeding intensity distribution for the present work and QRPA 1 calculations (Table 3.7). The QRPA 1 calculations were performed assuming the shape of the ground state of ^{102}Zr is oblate (quadrupole deformation parameter of $\beta_2 = -0.193$) and prolate (quadrupole deformation parameter of $\beta_2 = 0.373$). These shapes have different half-lives ($T_{1/2} = 1.43$ s for the oblate shape and $T_{1/2} = 4.01$ s for the prolate shape), and different cumulative β-decay feeding intensity distributions. The half-life for the oblate shape and prolate shape is 29% smaller and 100% larger, respectively, than the half-life extracted in the current work. The transition between the ground state of ^{102}Zr and the β-decaying isomeric state of ^{102}Nb that is extracted in the current work is in between that of the oblate shape and prolate shape. Between approximately 800 keV and

Table 3.10: The β-decay feeding intensity distribution of ^{102}Zr as a function of excitation energy in the daughter nucleus ^{102}Nb. Intensity values below 10^{-4} % are set to 0. As explained in Sec. 3.3.2.2, each level was assumed to be built on top of the β-decaying isomeric state. That is, a value of "x" = 93 keV as determined by Ref. [2] should be added to each level. As explained in Sec. 3.3.2.2, the detector response function for the level at 20+x keV was not used in the TAS analysis. As explained in Sec. 3.3.2.2, the values reported in this table are from the fit in which the ground-state-to-ground-state transition was held fixed between 60 and 61%.

Energy (keV)	Intensity (%)	Error (–)	Error (+)	Energy (keV)	Intensity (%)	Error (–)	Error (+)
0	60.0	9.0	7.0	1480	0.50	0.12	0.12
20	0	0	0	1540	0	0	0
64	0	0	0	1600	0	0	0
94	0	0	0	1660	2.52	0.35	0.35
156	0	0	0	1720	0.533	0.056	0.056
161	0	0	0	1780	0	0	0
246	0	0	0	1840	1.07	0.12	0.12
258	0	0	0	1900	2.93	0.37	0.37
431	0.170	0.033	0.033	1960	3.15	0.47	0.47
599	17.1	1.1	1.1	2020	0	0	0
705	4.11	0.52	0.52	2100	1.15	0.26	0.26
941	0	0	0	2200	0.070	0.017	0.017
1000	2.19	0.48	0.48	2300	0	0	0
1060	0	0	0	2400	1.06	0.25	0.25
1120	0.271	0.070	0.070	2500	0	0	0
1180	0.040	0.011	0.011	2600	0.364	0.088	0.088
1240	0	0	0	2700	0.60	0.13	0.13
1300	0	0	0	2800	0.66	0.23	0.23
1360	0.79	0.24	0.24	2900	0.72	0.18	0.18
1420	0	0	0	3000	0	0	0

1500 keV, the current work is in agreement with the prolate shape. After approximately 1700 keV, the current work is in agreement with both shapes. Both shapes have a sudden and relatively large increase in the cumulative β-decay feeding intensity distribution between approximately 1800 keV and 2000 keV that is not observed in the current work. The oblate shape has a relatively large increase in the cumulative β-decay feeding intensity distribution at 599+x keV that is observed in the current work. Meanwhile, the prolate shape has no increase in the cumulative β-decay feeding intensity distribution at this energy.

The lower left panel of Fig. 3.39 contains the cumulative B(GT) distribution for the present work and QRPA 1 (Table 3.7). The cumulative B(GT) distributions in this panel correspond to the cumulative β-decay feeding intensity distributions in the upper left panel. As with the cumulative β-decay feeding intensity distributions in the upper left panel, both shapes have different half-lives and different cumulative B(GT) distributions. Between 0 keV and approximately 700 keV, the current work is in agreement with both shapes. After approximately 1000 keV, the current work is in between both shapes. The total B(GT) at approximately 3000 keV for the current work is slightly closer to the oblate shape. However, no shape satisfactorily describes the experimental result.

As already mentioned in Sec. 3.3.2.1, the QRPA 1 calculations correspond to pure shape configurations, either oblate or prolate. None of these pure shape configurations reproduce the experimental cumulative β-decay feeding intensity distribution or B(GT) distribution. This may indicate that some type of mixture between these two shapes is necessary to reproduce the result from the current work.

The upper right panel of Fig. 3.39 contains the cumulative β-decay feeding intensity distribution for the present work, QRPA 2, and QRPA 3 (Table 3.7). The transition between the ground state of ^{102}Zr and the β-decaying isomeric state of ^{102}Nb that is extracted in the

current work is not reproduced by either calculation. Only QRPA 3 has a relatively large β-decay feeding intensity to a level with very low energy (less than 100 keV). Both of these QRPA calculations are characterized by a small cumulative β-decay feeding intensity at low energies, and then a sudden and relatively large increase in the cumulative β-decay feeding intensity distribution at higher energies. Almost 100% of the β-decay feeding intensity goes to a level at approximately 1300 keV in QRPA 2. Levels between approximately 1500 keV and 2000 keV collectively receive most of the β-decay feeding intensity in QRPA 3. None of these calculations reproduce the relatively large increase in the cumulative β-decay feeding intensity distribution at 599+x keV that is observed in the current work. The half-life for QRPA 2 and QRPA 3 is 74% smaller and 361% larger, respectively, than the half-life extracted in the current work.

The lower right panel of Fig. 3.39 contains the cumulative B(GT) distribution for the present work and QRPA 3. The cumulative B(GT) distributions in this panel correspond to the cumulative β-decay feeding intensity distributions in the upper right panel. The cumulative B(GT) distribution from the current work and the QRPA calculation are not in agreement for any energy. In this QRPA calculation, the quadrupole deformation parameter is $\beta_2 = 0.376$. The QRPA 1 calculation uses a similar value for the prolate shape of $\beta_2 = 0.373$. The cumulative B(GT) distributions for these prolate shapes are qualitatively similar between 0 keV and 4000 keV. The total B(GT) from 0 keV to 4000 keV is similar for both calculations. In addition, the cumulative B(GT) distributions from both calculations are always less than experiment. However, the half-lives for the prolate calculations (4.01 s and 9.27 s) are different.

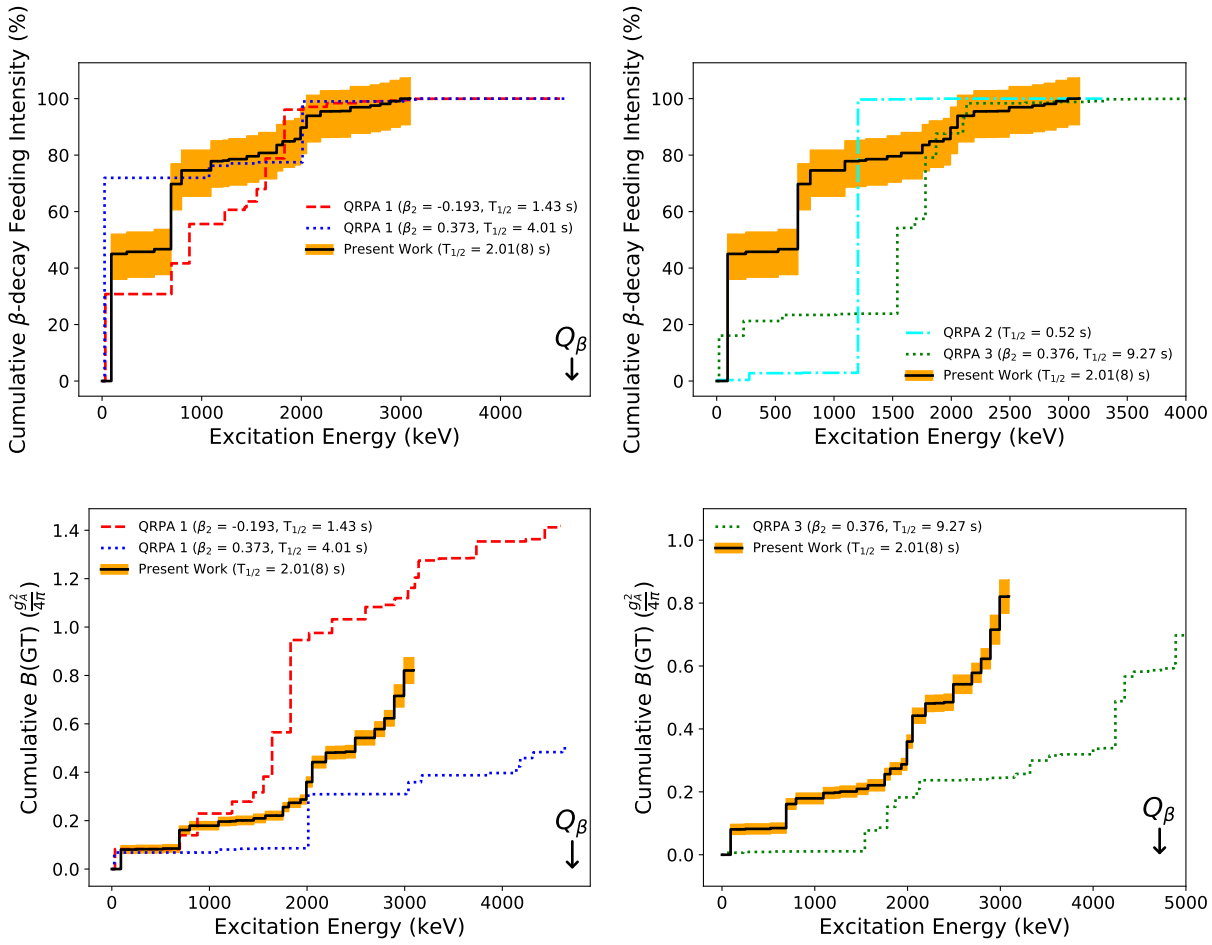

Figure 3.39: Comparison of experimental and theoretical cumulative β-decay feeding intensity distributions and cumulative B(GT) distributions for the β decay of ^{102}Zr. The upper panels show cumulative β-decay feeding intensity. The lower panels show cumulative B(GT). The left panels contain QRPA 1 calculations. In the left panels, the present work (black, solid line, with uncertainty in orange shading) is compared to QRPA 1 calculations assuming the shape of the ground state of the parent is oblate (red, dashed line) and prolate (blue, dotted line). The right panels contain QRPA calculations commonly used in r-process reaction network calculations. In the right panels, the present work (black, solid line, with uncertainty in orange shading) is compared to QRPA 2 (cyan, dash-dotted line) and QRPA 3 (green, dotted line). The lower right panel does not contain a QRPA 2 calculation. Some panels may contain an arrow indicating the ground-state-to-ground-state Q value for the β decay of ^{102}Zr at 4717 keV [16]. The experimental and theoretical half-lives $T_{1/2}$ are provided in parentheses. If the quadrupole deformation parameter β_2 was provided with a theoretical calculation, that is provided in the parentheses.

3.3.2.3 $^{109}_{43}\mathbf{Tc}_{66} \rightarrow {}^{109}_{44}\mathbf{Ru}_{65}$

In addition to ^{109}Tc, other technetium isotopes have been studied with the TAS technique. The β decay of ^{100}Tc was studied with the TAS technique to provide experimental data in the A = 100 isobaric chain in order to constrain nuclear structure models used in double β decay calculations of ^{100}Mo [204]. The β decays of ^{102,104,105,106,107}Tc were studied with the TAS technique in order to assess their impact on the production of decay heat [78, 79] and antineutrino energy spectra [84] from nuclear reactors.

The half-life of the parent ^{109}Tc is 0.87(7) s (Sec. 3.3.1.7), the daughter ^{109}Ru is 34.4(2) s [192], and the charge-state contaminant ^{106}Tc^{42+} is 35.6(6) s [205]. Because the experimental spectra used in the TAS analysis were obtained with a correlation time window of one second, the amount of contamination from the decay of the daughter and charge-state contaminant was negligible. The ground-state-to-ground-state Q value for the β decay of the parent ^{109}Tc is 6456 keV, while the one-neutron separation energy of the daughter ^{109}Ru is 5148 keV [16], making β-delayed neutron emission energetically possible. However, previous experiments obtained β-delayed neutron emission probabilities of 0.08(2)% [175] and $\leq$ 1% [189]. Additionally, there was no evidence in the TAS spectrum of a sum peak around 7 MeV, which would have resulted from thermal neutron capture on the ^{23}Na or ^{127}I of SuN. Therefore, β-delayed neutron emission was not incorporated into the TAS analysis.

Detector response functions were created for known levels populated in β decay below the critical energy (Table 3.5). They were created using information from the existing level scheme of the daughter from ENSDF [192] and also a recent high-resolution study of the β-decay of ^{109}Tc [206]. All levels below the critical energy have tentative spin and parity assignments, and therefore four level schemes were constructed with different spin and parity

assumptions. The different level schemes contributed to the uncertainty in the extracted β-decay feeding intensity distribution. There were a total of 21 detector response functions for known levels, starting at 0 keV and ending at 1268 keV.

Detector response functions were created for pseudo levels above the critical energy (Table 3.5). The spin and parity of the ground state of the parent ^{109}Tc is $(5/2^+)$ [192]. According to β-decay selection rules for allowed Gamow-Teller transitions, the states populated in the daughter are $3/2^+$, $5/2^+$, and $7/2^+$. Following these rules, γ-ray cascades from three pseudo levels were created with DICEBOX for each energy bin in the quasi-continuum. These three pseudo levels had corresponding detector response functions created with GEANT4, from which an average detector response function was created and used in the TAS analysis. There were a total of 33 average detector response functions for pseudo levels, starting at 1350 keV (where the total level density is approximately 0.07 / keV [166] and the energy resolution of SuN is approximately 82 keV) and ending at 5110 keV (where the total level density is approximately 25 / keV [166] and the energy resolution of SuN is approximately 194 keV).

The TAS spectrum, sum-of-segments spectrum, and multiplicity spectrum are shown in Fig. 3.40. There are many small sum peaks in the TAS spectrum. The transition in the daughter ^{109}Ru from the first excited state at 68.75 keV to the ground state has a total internal conversion coefficient of 4.97 [192, 13]. This total internal conversion coefficient is relatively large because the nucleus ^{109}Ru has a relatively high atomic number, the transition energy is relatively small, and the multipolarity (E2) is relatively large. Many levels populated in β decay pass through the first excited state, which means that many γ-ray cascades will not emit a 68.75 keV γ ray but instead a 68.75 keV conversion electron. This conversion electron will not deposit energy in SuN. There are other transitions in ^{109}Ru with

non-negligible total internal conversion coefficients. Therefore, counts for some of the sum peaks will be displaced by a certain energy, resulting in broadened sum peaks. Two larger sum peaks are noticeable at 1159.0 keV and 1267.8 keV.

The decay scheme of Ref. [192] assigned a β-decay feeding intensity of 35(6)% for the ground-state-to-ground-state transition based on a measurement by Ref. [207]. Meanwhile, the decay scheme of Ref. [190] did not assign a β-decay feeding intensity for the ground-state-to-ground-state transition. In the current work, the β-decay feeding intensity for the ground-state-to-ground-state transition is $5.7^{+5.8}_{-5.7}$%.

In the sum-of-segments spectrum, noticeable features include peaks corresponding to γ rays with a relatively large absolute γ-ray intensity [178]. For example, there is a peak corresponding to the 195.0 keV γ ray.

The β-decay feeding intensity distribution of ^{109}Tc as a function of excitation energy in the daughter nucleus ^{109}Ru is reported in Table 3.11. The β-decay feeding intensity distribution in Table 3.11 is an average of the different level schemes assumed for the daughter (Sec. 3.2.3.2). The amount of β-decay feeding intensity to known levels is 67.4% and to pseudo levels is 32.6%. Three different sources of uncertainty contribute to the total uncertainty that is reported in Table 3.11. These sources were discussed for the case of ^{101}Zr in Sec. 3.3.2.1. The weighted average of the uncertainty from statistics was 11%. The weighted average of the uncertainty from multiple level schemes was 30%. The uncertainty from the ground-state-to-ground-state transition is discussed below.

The analysis procedure for determining the uncertainty in the ground-state-to-ground-state transition was already discussed for the case of ^{101}Zr in Sec. 3.3.2.1. The left panel of Fig. 3.41 shows the reduced χ^2_{global} as a function of ground-state-to-ground-state transition probability. The β-decay feeding intensity distribution reported in Table 3.11 was extracted

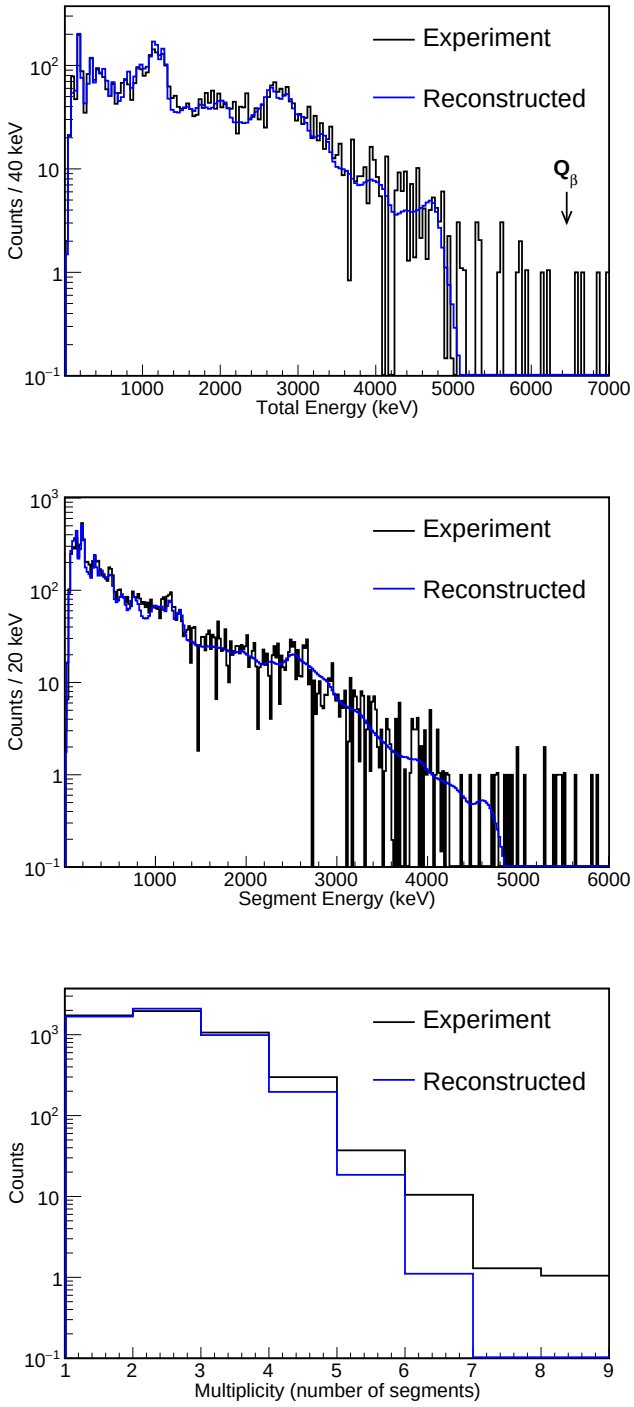

Figure 3.40: Comparison of experimental (black, solid line) and reconstructed (blue, solid line) spectra from the β decay of ^{109}Tc for the TAS spectrum (top panel), sum-of-segments spectrum (middle panel), and multiplicity spectrum (bottom panel). The experimental spectra were obtained by correlating decay events to ^{109}Tc implantations with a correlation time window of one second. Contamination from random correlations has been subtracted from the experimental spectra. There is a label for the ground-state-to-ground-state Q value in the TAS spectrum for the β decay of ^{109}Tc at 6456 keV [16].

Table 3.11: The β-decay feeding intensity distribution of ^{109}Tc as a function of excitation energy in the daughter nucleus ^{109}Ru. Intensity values below 10^{-4} % are set to 0.

Energy (keV)	Intensity (%)	Error (–)	Error (+)	Energy (keV)	Intensity (%)	Error (–)	Error (+)
0	5.7	5.7	5.8	1830	1.0	0.9	1.2
69	0.35	0.33	0.19	1910	0.50	0.50	0.88
96	0.05	0.05	0.11	1990	2.3	1.1	1.2
132	0.0001	0.0001	0.0002	2080	1.6	1.5	1.5
138	0	0	0	2180	0.5	0.5	1.4
185	3.34	0.32	0.39	2280	0.52	0.52	0.80
191	0	0	0	2380	0.57	0.57	0.97
195	5.26	0.68	0.48	2480	1.24	0.43	0.41
197	0	0	0	2580	0.010	0.010	0.029
230	0.0001	0.0001	0.0002	2680	5.9	2.2	1.1
256	0.0001	0.0001	0.0002	2780	2.3	2.3	3.1
332	3.98	0.50	0.49	2880	2.5	2.2	3.5
405	0.0002	0.0002	0.0005	2980	1.6	1.6	4.0
408	1.55	0.23	0.24	3080	2.6	2.6	1.4
498	0.0001	0.0001	0.0003	3205	0.7	0.7	1.5
515	6.28	0.88	0.88	3355	2.1	1.4	1.0
628	1.73	0.43	0.33	3505	0.39	0.37	0.82
811	4.00	0.51	0.50	3655	0.24	0.24	0.28
995	8.07	0.82	0.82	3805	0.032	0.032	0.094
1159	16.2	1.2	1.2	3955	0.76	0.36	0.77
1268	10.90	0.83	0.80	4105	0.34	0.34	0.27
1350	0.18	0.18	0.52	4255	0.015	0.015	0.045
1430	0.24	0.24	0.31	4405	0.32	0.25	0.50
1510	0.08	0.08	0.24	4570	0.40	0.40	0.33
1590	1.16	1.06	0.44	4750	0.97	0.58	0.73
1670	0.15	0.15	0.38	4930	0.13	0.13	0.12
1750	1.28	1.02	0.63	5110	0	0	0

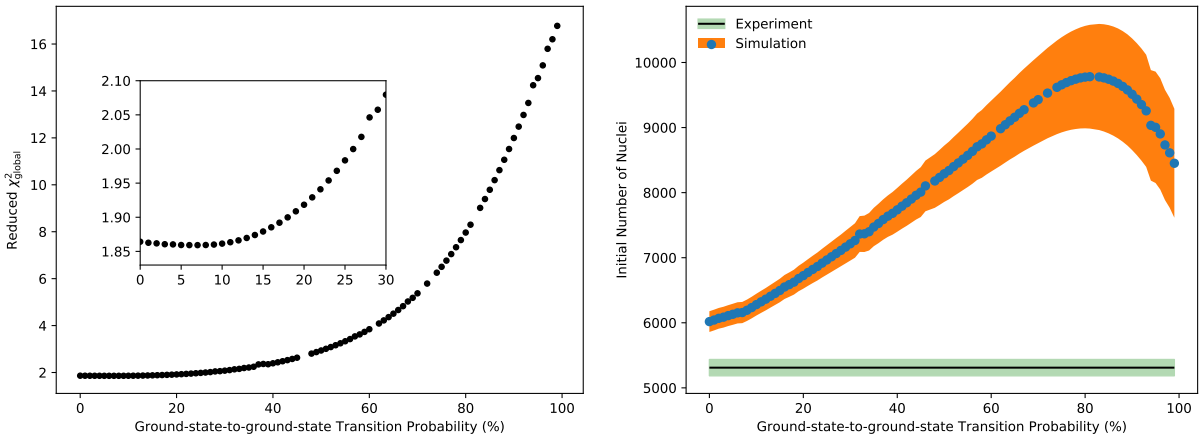

Figure 3.41: Left panel: Reduced χ^2_{global} as a function of ground-state-to-ground-state transition probability for the β decay of ^{109}Tc. The inset shows an enlarged view of the minimum. Right panel: Initial number of nuclei as a function of ground-state-to-ground-state transition probability for the β decay of ^{109}Tc.

without any constraint on the ground-state-to-ground-state transition. The ground-state-to-ground-state transition probability in Table 3.11 is 5.7%, which corresponds to the minimum of the distribution in the left panel of Fig. 3.41.

The right panel of Fig. 3.41 shows the initial number of decaying nuclei in experiment and simulation as a function of ground-state-to-ground-state transition probability. There is no intersection in the uncertainty bands. Therefore, an uncertainty was assigned to the ground-state-to-ground-state transition that covered the minimum in the left panel of Fig. 3.41.

Figure 3.42 shows a comparison of experimental and theoretical cumulative β-decay feeding intensity distributions and cumulative B(GT) distributions for the β decay of ^{109}Tc. The upper left panel of Fig. 3.42 contains the cumulative β-decay feeding intensity distribution for the present work and QRPA 1 calculations (Table 3.7). The QRPA 1 calculations were performed assuming the shape of the ground state of ^{109}Tc is oblate (quadrupole deformation parameter of $\beta_2 = -0.214$) and prolate (quadrupole deformation parameter of $\beta_2 = 0.320$).

These shapes have different half-lives ($T_{1/2}$ = 0.99 s for the oblate shape and $T_{1/2}$ = 3.04 s for the prolate shape), and different cumulative β-decay feeding intensity distributions. The half-life from the current work is in good agreement with that of the oblate shape, but is less than the half-life of the prolate shape. Both calculations are in agreement with zero β-decay feeding intensity for the ground-state-to-ground-state transition. Only the oblate shape has any significant β-decay feeding intensity below 2000 keV. Below approximately 1200 keV, the present work and the oblate shape are qualitatively similar. The prolate shape has a sudden and relatively large increase in the cumulative β-decay feeding intensity distribution at approximately 2500 keV, which is not observed in the present work. The current work is not in agreement with the prolate shape until approximately 2500 keV. After approximately 2500 keV, the present work is in agreement with both shapes.

The lower left panel of Fig. 3.42 contains the cumulative B(GT) distribution for the present work and QRPA 1 (Table 3.7). The cumulative B(GT) distributions in this panel correspond to the cumulative β-decay feeding intensity distributions in the upper left panel. As with the cumulative β-decay feeding intensity distributions in the upper left panel, both shapes have different half-lives and different cumulative B(GT) distributions. Only the oblate shape has any significant B(GT) below 2000 keV. Between approximately 2800 keV and 3400 keV, the present work is in agreement with both shapes. Between approximately 3400 keV and 4800 keV, the present work is in between both shapes. By the energy of the last pseudo level, the total B(GT) for the present work is in agreement with the oblate shape.

The cumulative β-decay feeding intensity distribution for the oblate shape better describes the current work. In addition, the half-lives for the present work and the oblate shape are in agreement. The total B(GT) for the present work and the oblate shape are in agreement below the one-neutron separation energy of the daughter. All these facts suggest

a dominant oblate deformation for ^{109}Tc. In Ref. [208], β- and γ-coincidence spectroscopy of the nearby technetium isotope ^{111}Tc provided evidence of oblate deformation for that nucleus. Therefore, the current work is in agreement with Ref. [208] in terms of a nearby technetium isotope in the same mass region having a similar deformation.

The upper right panel of Fig. 3.42 contains the cumulative β-decay feeding intensity distribution for the present work, QRPA 2, and QRPA 3 (Table 3.7). The QRPA 3 calculations were performed assuming the shape of the ground state of ^{109}Tc is oblate (quadrupole deformation parameter of $\beta_2 = -0.2481$) and prolate (quadrupole deformation parameter of $\beta_2 = 0.309$). All calculations are in agreement with zero β-decay feeding intensity for the ground-state-to-ground-state transition. All calculations have a sudden and relatively large increase in the cumulative β-decay feeding intensity distribution. For the oblate shape in QRPA 3, this occurs at approximately 300 keV. For the prolate shape in QRPA 3, this occurs at approximately 3000 keV. For QRPA 2, this occurs at approximately 3800 keV. However, the cumulative β-decay feeding intensity distribution for the present work shows more fragmentation and a gradual increase throughout the entire energy range. Below approximately 3000 keV, the present work is not in agreement with any calculation. Only after approximately 3000 keV does the present work agree with any of the calculations. The half-life from QRPA 2 is 99% larger than the half-life extracted in the current work. For QRPA 3, the half-life for the oblate shape and prolate shape is 63% smaller and 417% larger, respectively, than the half-life extracted in the current work.

The lower right panel of Fig. 3.42 contains the cumulative B(GT) distribution for the present work and QRPA 3. The cumulative B(GT) distributions in this panel correspond to the cumulative β-decay feeding intensity distributions in the upper right panel. The cumulative B(GT) distribution from the current work and the QRPA calculations are rarely

in agreement for any energy. Between 0 keV and the one-neutron separation energy of the daughter, the present work is in between both shapes. At the one-neutron separation energy of the daughter, the total B(GT) for the present work is in agreement with the oblate shape.

There are many similarities in the calculations from QRPA 1 and QRPA 3 (Table 3.7). The quadrupole deformation parameters of the oblate shapes ($\beta_2 = -0.214$ and $\beta_2 = -0.2481$) are similar. The quadrupole deformation parameters of the prolate shapes ($\beta_2 = 0.320$ and $\beta_2 = 0.309$) are similar. The half-lives of the oblate shapes ($T_{1/2} = 0.99$ s and $T_{1/2} = 0.32$ s) are similar. The half-lives of the prolate shapes ($T_{1/2} = 3.04$ s and $T_{1/2} = 4.50$ s) are similar. The half-lives of the oblate shapes are less than those of the prolate shapes.

The oblate shapes have a relatively large increase in the cumulative β-decay feeding intensity distribution at low energies. The increase occurs at similar energies for the oblate shapes. In QRPA 1, the increase occurs at approximately 400 keV. In QRPA 3, the increase occurs at approximately 300 keV. The increase is larger in the QRPA 3 calculation. The prolate shapes have a small cumulative β-decay feeding intensity at low energies, and then a sudden and relatively large increase in the cumulative β-decay feeding intensity distribution at higher energies. The increase occurs at similar energies for the prolate shapes. In QRPA 1, the increase occurs at approximately 2500 keV. In QRPA 3, the increase occurs at approximately 3000 keV. The cumulative B(GT) distributions for the prolate shapes are less than the current work.

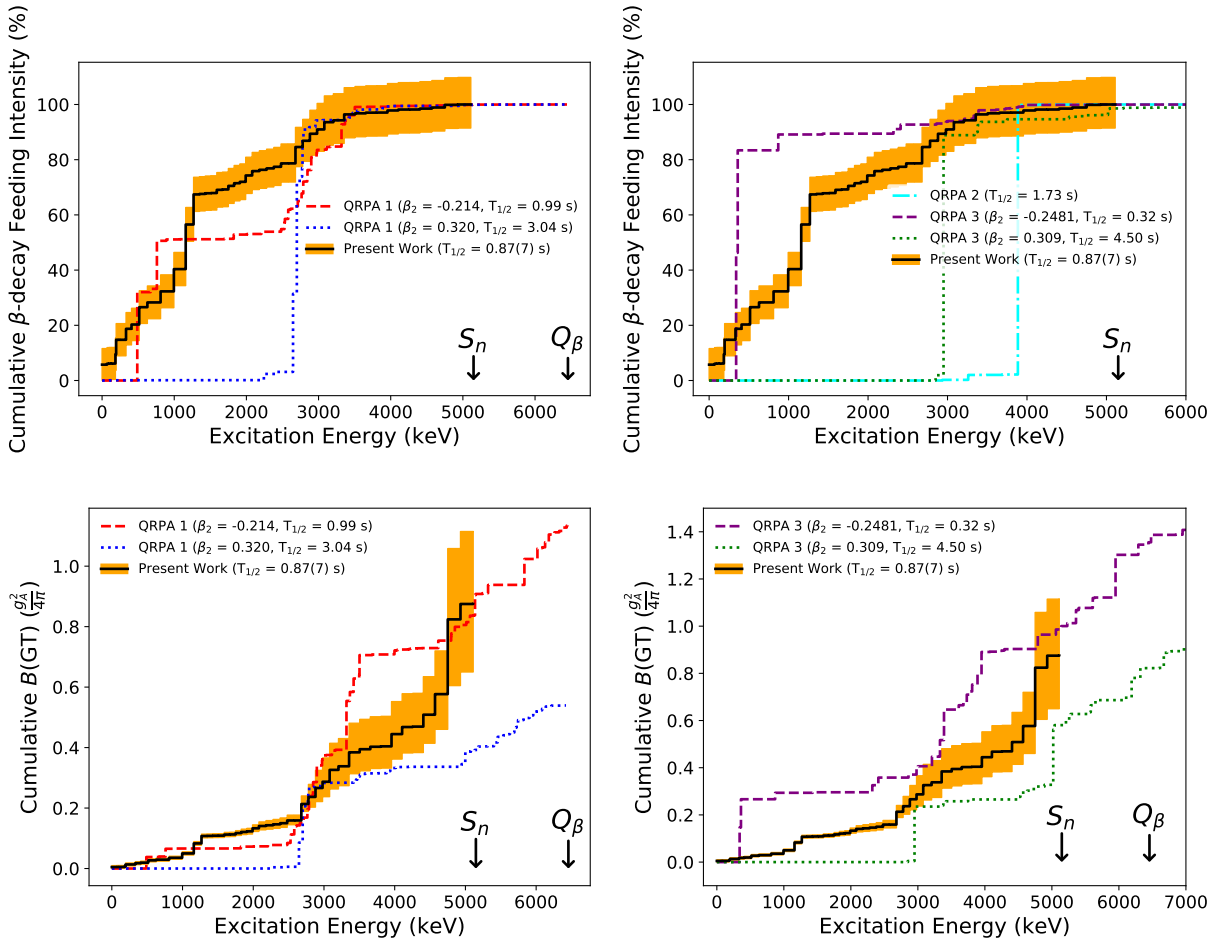

Figure 3.42: Comparison of experimental and theoretical cumulative β-decay feeding intensity distributions and cumulative B(GT) distributions for the β decay of ^{109}Tc. The upper panels show cumulative β-decay feeding intensity. The lower panels show cumulative B(GT). The left panels contain QRPA 1 calculations. In the left panels, the present work (black, solid line, with uncertainty in orange shading) is compared to QRPA 1 calculations assuming the shape of the ground state of the parent is oblate (red, dashed line) and prolate (blue, dotted line). The right panels contain QRPA calculations commonly used in r-process reaction network calculations. In the right panels, the present work (black, solid line, with uncertainty in orange shading) is compared to QRPA 2 (cyan, dash-dotted line) and QRPA 3 (green, dotted line and purple, dashed line). The lower right panel does not contain a QRPA 2 calculation. Some panels may contain an arrow indicating the ground-state-to-ground-state Q value for the β decay of ^{109}Tc at 6456 keV [16]. All panels contain an arrow indicating the one-neutron separation energy S_n of the daughter ^{109}Ru at 5148 keV [16]. The experimental and theoretical half-lives $T_{1/2}$ are provided in parentheses. If the quadrupole deformation parameter β_2 was provided with a theoretical calculation, that is provided in the parentheses.

Chapter 4

Summary and Outlook

The astrophysical r process is responsible for approximately half of the solar system abundance pattern beyond the iron peak. Although the general mechanism of the r process was outlined more than six decades ago, theoretical models are unable to reproduce the r-process contribution to the solar system abundances.

This inability is due to uncertainty in both the astrophysical environment(s) and the underlying nuclear physics. Reducing these nuclear physics uncertainties was the goal of this dissertation. Of all the nuclear physics properties that play an important role in the r process, this dissertation focused on experimental measurements related to β decay.

To achieve that goal, a new experimental program was initiated at the National Superconducting Cyclotron Laboratory (NSCL) to study β-decay properties of nuclides relevant to the astrophysical r process. This experimental program used the Summing NaI(Tl) (SuN) detector and the total absorption spectroscopy (TAS) technique.

All β-decay experiments in this dissertation were performed at the Coupled Cyclotron Facility at the NSCL. The commissioning experiment with a thermalized beam was performed with the β decay of ^{76}Ga. The extracted half-life agrees with previously published values. However, the extracted beta-decay feeding intensity distribution disagrees with the existing decay scheme at the National Nuclear Data Center. Because ^{76}Ga is only one unit away from stability, this experiment highlighted the fact that the Pandemonium effect may

appear anywhere on the chart of the nuclides. The extracted β-decay feeding intensity distribution and B(GT) distribution were compared to theoretical models that are used to calculate nuclear matrix elements relevant to the neutrinoless double-β decay.

The commissioning experiment with a fast beam was performed with neutron-rich nuclides in the A = 100-110 mass region. This experiment was also the first-ever application of the TAS technique with a fast beam produced via projectile fragmentation. In this experiment, the β-decay half-lives were extracted for ^{99}Y, ^{101}Zr, ^{102}Zr, ^{102m}Nb, ^{103}Nb, ^{104m}Nb, and ^{109}Tc. Additionally, the β-decay feeding intensity distributions and B(GT) distributions were extracted for ^{101}Zr, ^{102}Zr, and ^{109}Tc. These distributions can be used to constrain theoretical models used to calculate β-decay properties of nuclides relevant to the r process. Theoretical models commonly used to provide β-decay properties in r-process network calculations are the QRPA calculations by P. Moller and T. Marketin. The calculations by these authors were not able to reproduce the extracted β-decay feeding intensity distributions and B(GT) distributions. The extracted distributions were compared to another set of QRPA calculations in an attempt to learn about the shape of the ground state of the parent nucleus. These QRPA calculations were performed by P. Sarriguren. For ^{101}Zr and ^{102}Zr, calculations assuming a pure shape configuration (oblate or prolate) were not able to reproduce the extracted distributions. These results may indicate that some type of mixture between oblate and prolate is necessary to reproduce the extracted distributions. For ^{109}Tc, a comparison of the extracted distribution with QRPA calculations suggests a dominant oblate configuration.

The experiment described in Ch. 3 demonstrates the feasibility of employing the TAS technique with a fast beam. This opens the door to extracting β-decay feeding intensity distributions and B(GT) distributions for nuclei far from stability, where the secondary beam

intensity may only be 10-100 particles per second. These extracted distributions will further constrain theoretical models used to calculate β-decay properties of nuclides relevant to the r process. These experimental constraints will provide more confidence in the extrapolation of the theoretical models when calculating β-decay properties of nuclei on the r-process path, where there is currently no experimental data. Once the Facility for Rare Isotope Beams (FRIB) comes online, using the TAS technique with a fast beam could be used to study the β-decay properties of neutron-rich rare-earth nuclides [110]. As with the nuclides studied in Ch. 3, studying the neutron-rich rare-earth nuclides would have both a nuclear structure and nuclear astrophysics motivation [110]. The nuclear structure motivation would be to try to learn about the shape of the ground state of the parent nucleus, as different shapes have different B(GT) distributions [110]. The nuclear astrophysics motivation would be that these nuclides contribute to the formation of the rare-earth peak in the r-process solar system abundance pattern (Sec. 1.3.1 and Fig. 1.2). Accurate β-decay properties of these nuclides are needed in r-process reaction network calculations to help understand the formation of the rare-earth peak.

The experiment described in Ch. 3 marks the first time the TAS technique has been coupled with a fast beam. As this was the first-ever experiment of its kind, much was learned during the execution of the experiment and analysis of the data. This experiment studied nuclides in the A = 100-110 mass region. Since then, more TAS experiments with SuN and a fast beam have been performed. However, these experiments studied nuclides in a lighter mass region (A = 60-70). In this lighter mass region, charge-state contamination is not an experimental concern. Performing another TAS experiment with a fast beam in a heavier mass region will require the following considerations and improvements to the experimental setup. Some of these considerations apply to all future TAS experiments, regardless of mass

region.

For the experiment described in Ch. 3, the I2 scintillator was damaged (see Fig. 3.13). A fully operational I2 scintillator is crucial for particle identification. Therefore, future experiments must ensure that the I2 scintillator is fully operational prior to the start of the experiment.

The nuclides studied in the experiment described in Ch. 3 emit low-energy γ rays when they undergo β decay. After that experiment was performed, a triple PMT coincidence was enabled in DDAS for all of segments of SuN. This triple PMT coincidence permitted lower trigger thresholds for each PMT of SuN and increased the detection efficiency of low-energy γ rays. Future experiments must ensure that this important feature is enabled.

For the experiment described in Ch. 3, there was charge-state contamination in the particle identification spectrum (see Sec. 3.2.1.2). Charge-state contamination will need to be handled in future experiments that study nuclides in a relatively heavy mass region. Separation of different charge states was not possible using total kinetic energy in the experiment described in Ch. 3 (see Sec. 3.2.1.2). If future experiments will use total kinetic energy to perform charge-state separation, some form of modification to the experimental setup will be necessary. For example, using preamplifiers for the DSSD that do not saturate during implantation events.

For the experiment described in Ch. 3, contamination from random correlations was significant. After subtraction of the random correlations from the experimental spectra, relatively few statistics remained in the experimental spectra. Identifying peaks in the TAS spectrum and sum-of-segments spectrum was challenging due to the few statistics and the statistical fluctuations after the subtraction. To reduce the amount of random correlations, future experiments should take into account the beam rate compared to the β-decay half-

lives.

Some nuclides in this dissertation may benefit from being studied with a different experimental setup. An alternative experimental setup that would not involve random correlations is a tape station, such as the newly commissioned SuN Tape transport of Active Nuclei (SuNTAN). In this setup, a radioactive nucleus is implanted onto the moving tape system of SuNTAN. Removing background from the decay of the daughter is accomplished by cycling in a clean piece of tape to the implantation point at the center of SuN. How often the tape is cycled depends on the half-life of the implanted ion and daughter. For example, such an experimental setup may be beneficial for studying the β decay of ^{101}Zr. The half-life of the parent ^{101}Zr is approximately 2.3 seconds and the half-life of the daughter ^{101}Nb is approximately 7.1 seconds. As this technique does not require correlations, there is no background from random correlations. However, using a fast beam (with many different nuclides) is not possible with this technique. Only a thermalized beam (containing a single nuclide) can be used with this technique. Therefore, it would be beneficial if the NSCL beam thermalization area tried to develop thermalized beams in this heavier mass region.

APPENDIX

Appendix A

e12001 Experimental Setup

The experiment described in Ch. 3 marks the first time the TAS technique has been coupled with a fast beam. As this was the first-ever experiment of its kind, a considerable amount of time went into setting up for the experiment. This appendix contains detailed figures and diagrams of the experimental setup that may be helpful for future experiments. Note that the text on the figures may be hard or impossible to read in the print version of this dissertation. Therefore, these figures are meant to be viewed in the electronic version of this dissertation, in which the reader may magnify the figures to see all the details.

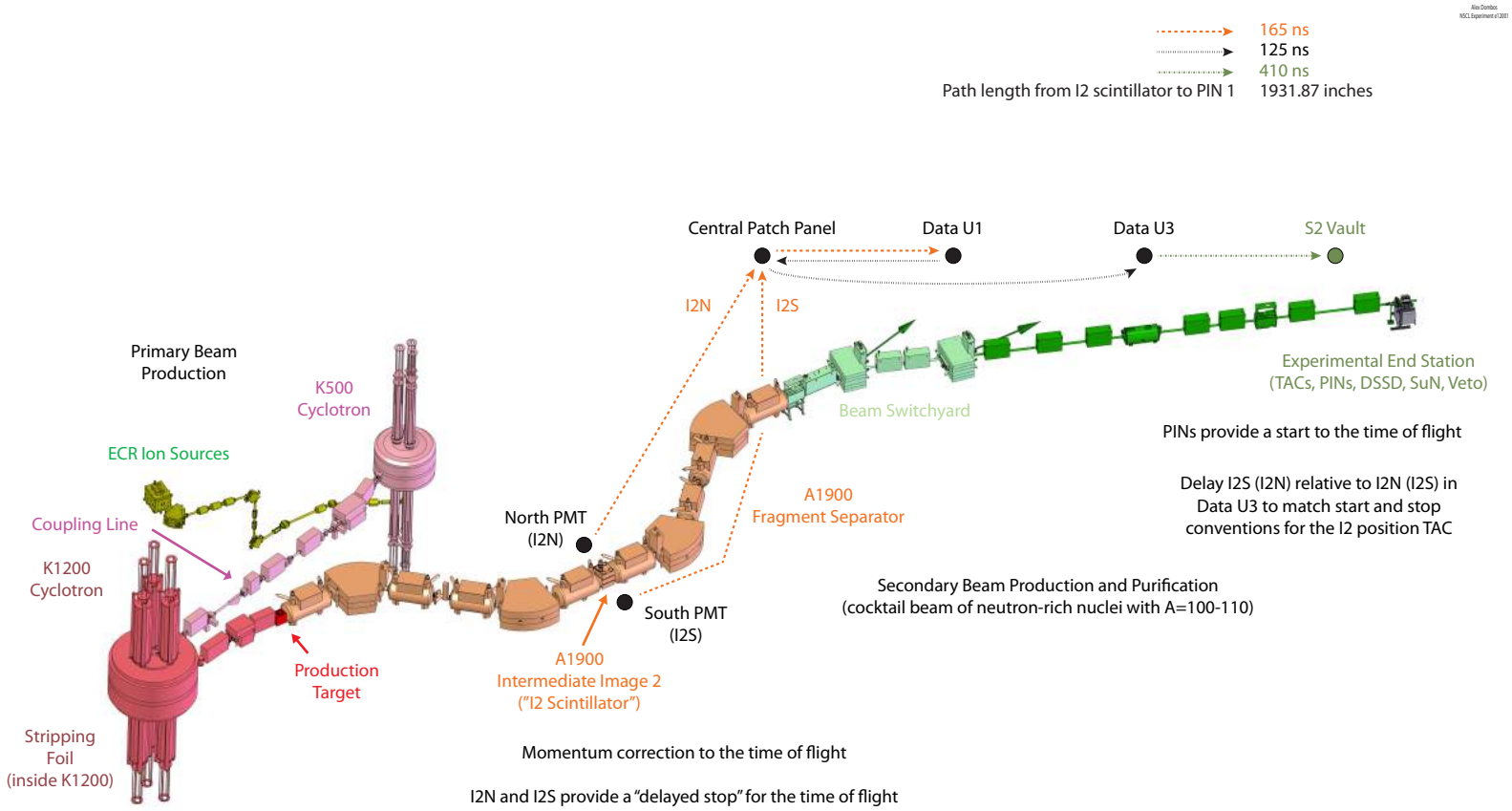

Figure A.1: Schematic layout of the Coupled Cyclotron Facility at the NSCL. Shown are the K500 cyclotron, K1200 cyclotron, A1900 fragment separator, and the experimental end station in the S2 vault.

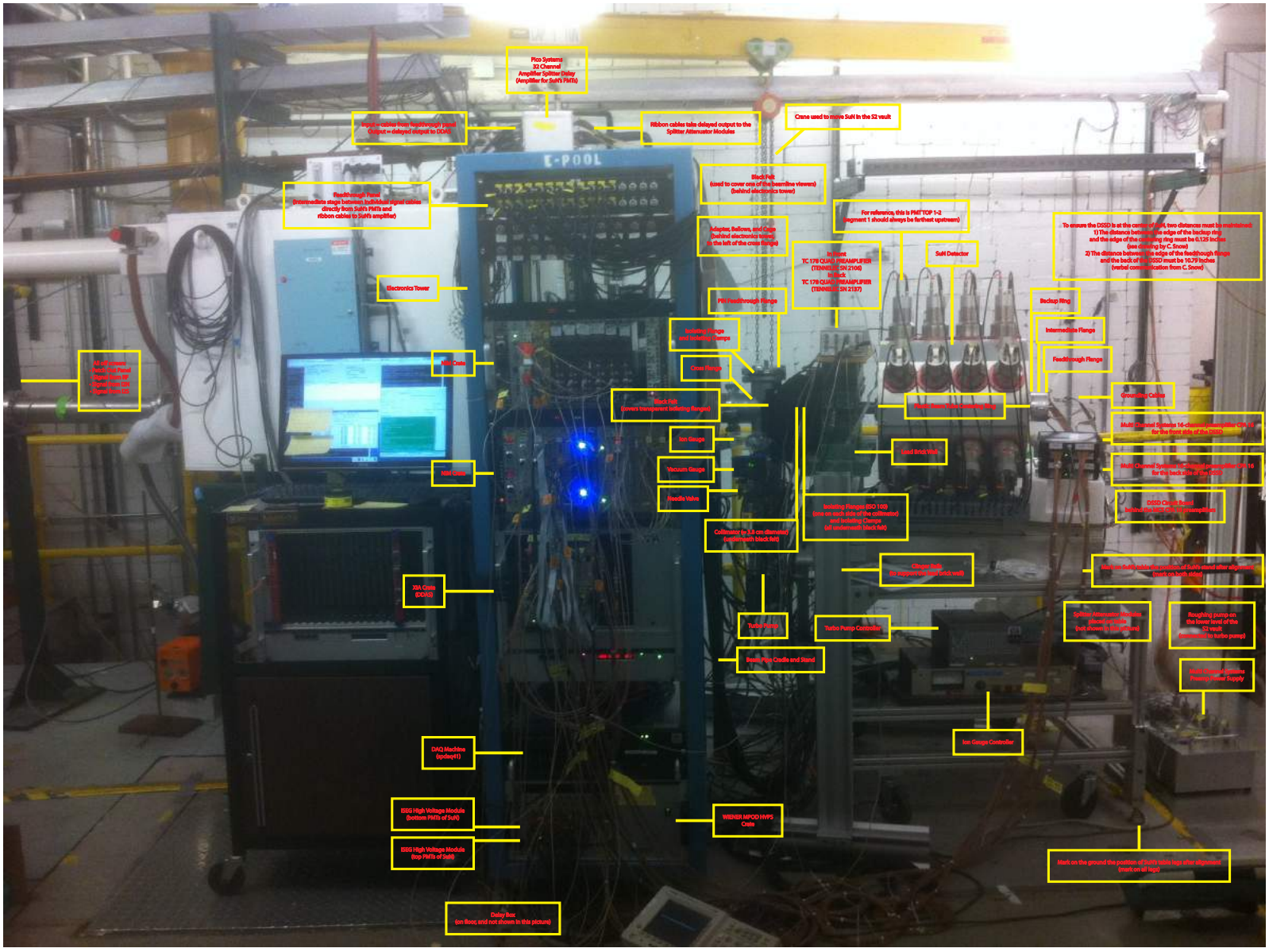

Figure A.2: Experimental end station in the S2 vault for NSCL experiment e12001. The secondary beam from the A1900 fragment separator enters from the left side of the picture.

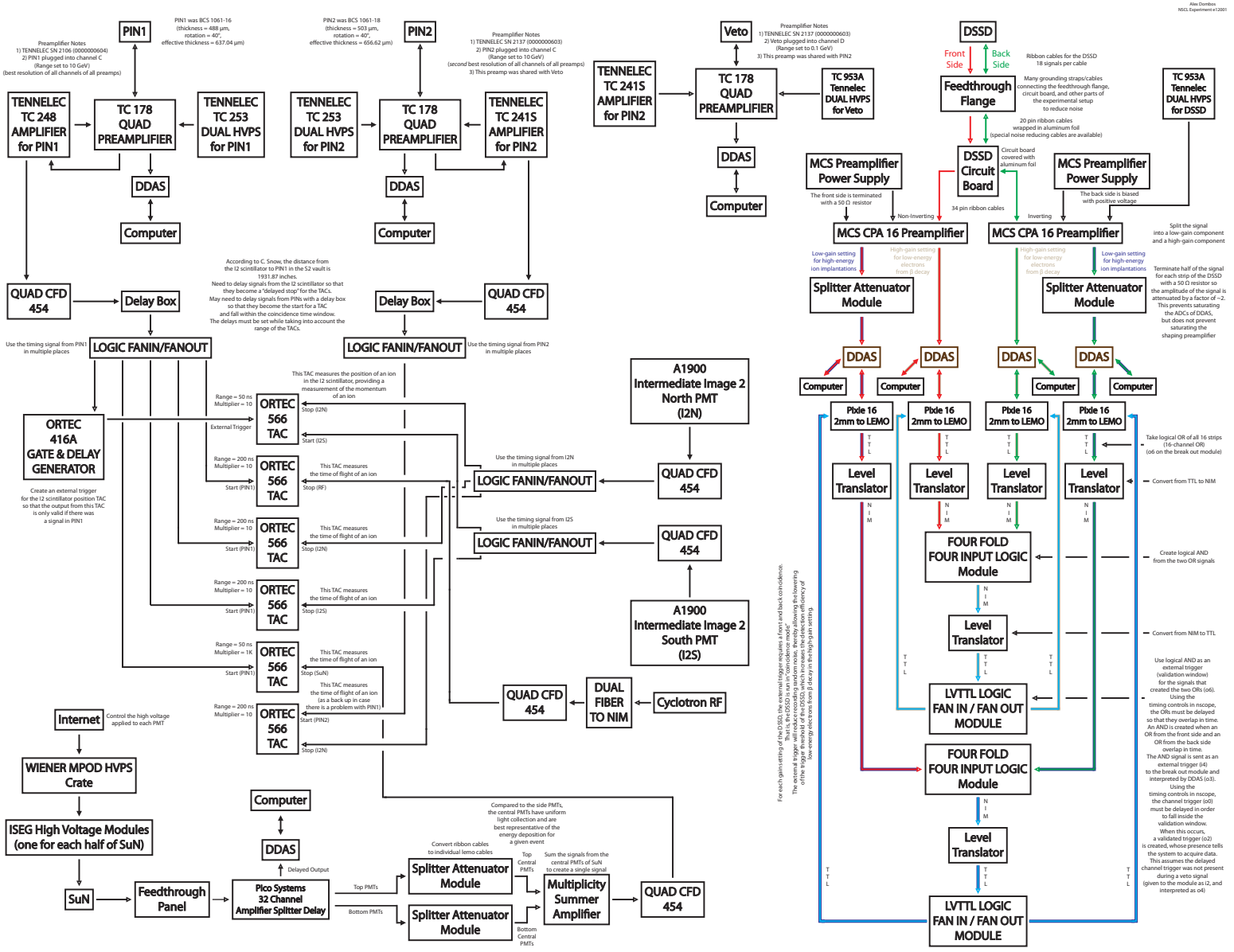

Figure A.3: Overview of the electronics setup for NSCL experiment e12001. All detectors are shown along with trigger conditions. This figure may be viewed together with Fig. A.4.

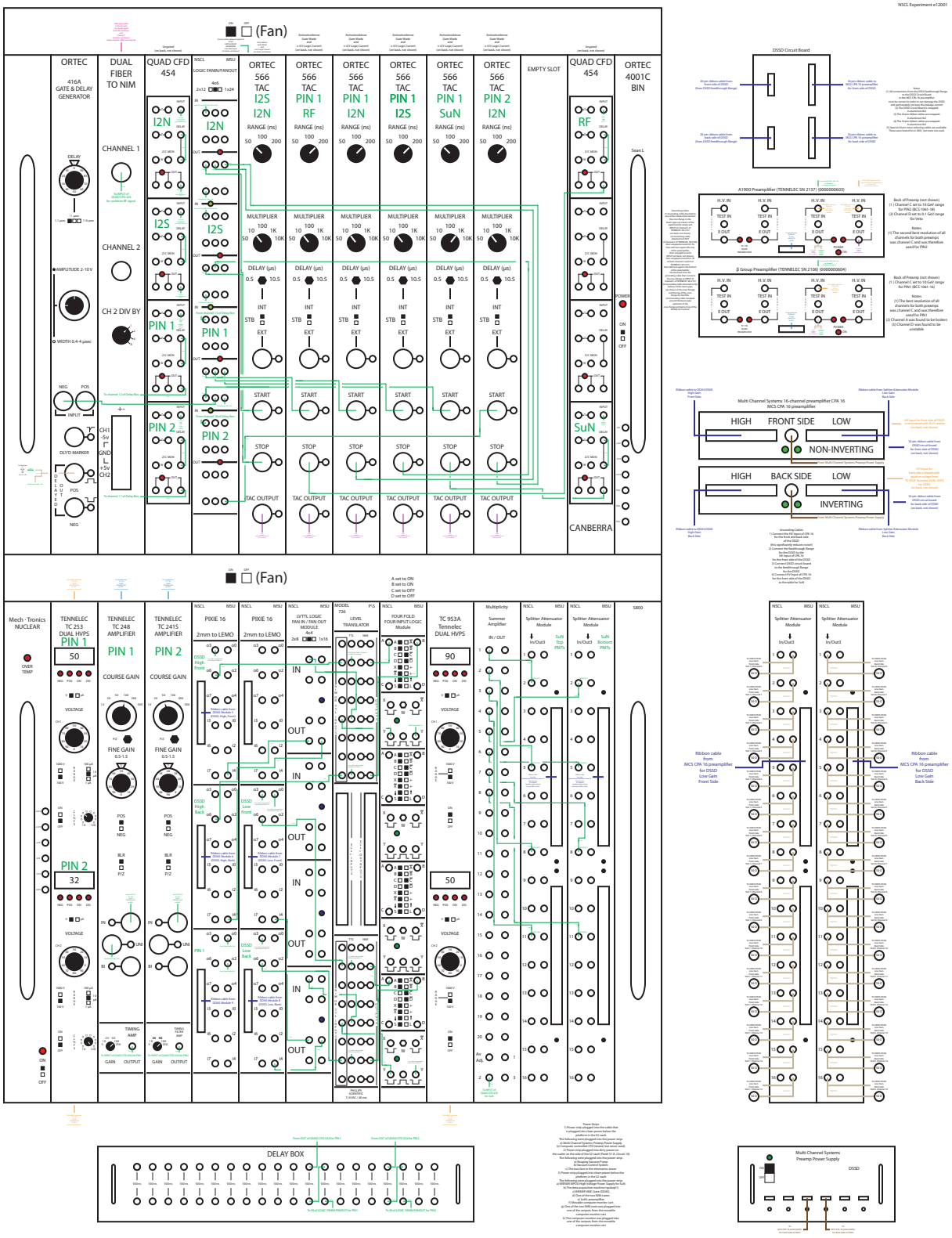

Figure A.4: Overview of the NIM crates and other equipment for NSCL experiment e12001. This figure may be viewed together with Fig. A.3.

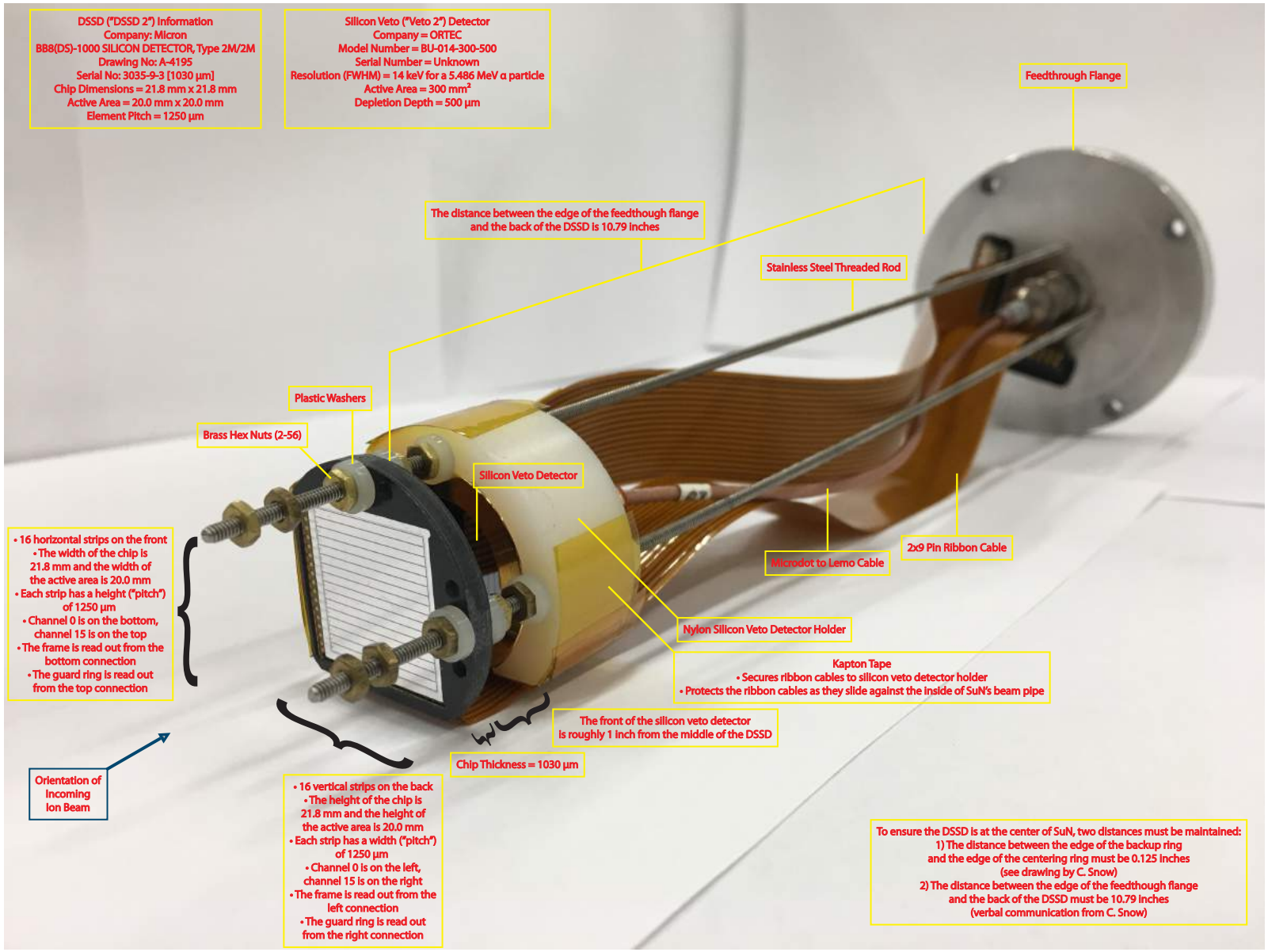

Figure A.5: The implantation station used for NSCL experiment e12001. Shown are the double-sided silicon-strip detector (DSSD) and the silicon surface barrier detector (veto).

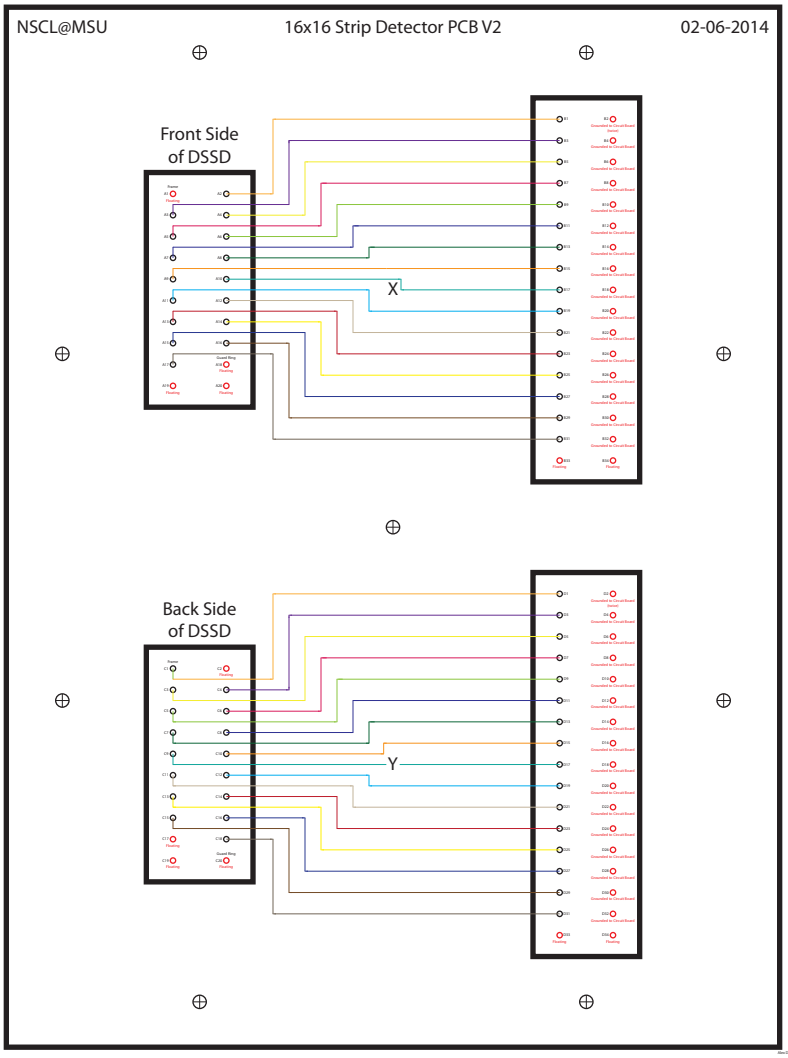

Figure A.6: Diagram of the circuit board that was an intermediate stage between the DSSD and the dual-gain preamplifiers.

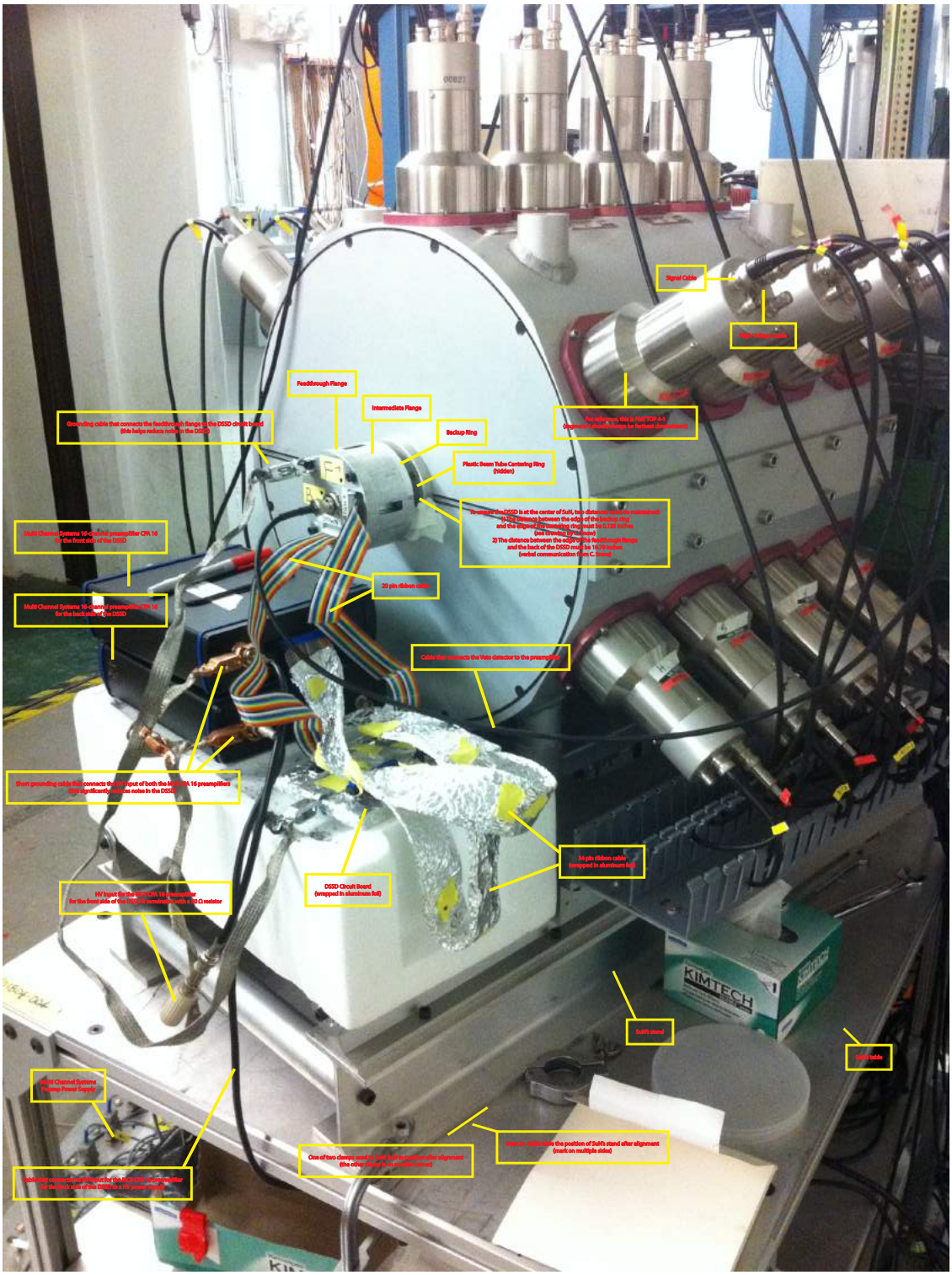

Figure A.7: The SuN detector during NSCL experiment e12001. Also shown are cables for the implantation station inside of SuN, and the circuit board and dual-gain preamplifiers for the DSSD.

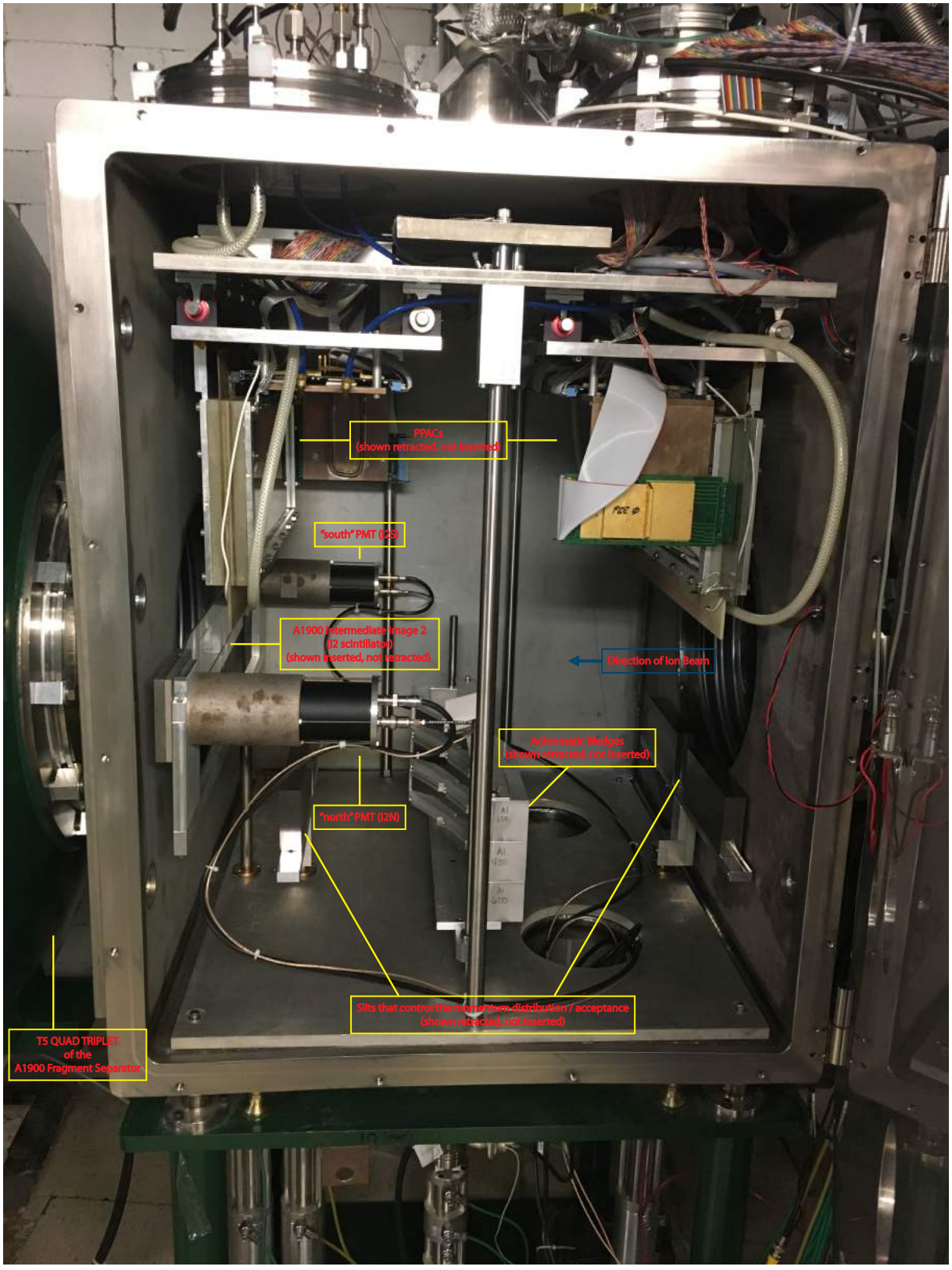

Figure A.8: The chamber in the A1900 fragment separator that contains the Image 2 scintillator. Shown are the Image 2 scintillator, achromatic wedges, and the slits that control the momentum acceptance.

BIBLIOGRAPHY

BIBLIOGRAPHY

[1] W. D. Loveland, D. J. Morrissey, and G. T. Seaborg, *Modern Nuclear Chemistry*, 1st ed. (Wiley-Interscience, 2005).

[2] S. Rinta-Antila, T. Eronen, V.-V. Elomaa, U. Hager, J. Hakala, A. Jokinen, P. Karvonen, H. Penttilä, J. Rissanen, T. Sonoda, A. Saastamoinen, and J. Äystö, The European Physical Journal A **31**, 1 (2007).

[3] P. Möller, A. J. Sierk, T. Ichikawa, and H. Sagawa, Atomic Data and Nuclear Data Tables **109-110**, 1 (2016).

[4] K. Lodders, The Astrophysical Journal **591**, 1220 (2003).

[5] M. Arnould and S. Goriely, Physics Reports **384**, 1 (2003).

[6] C. Sneden, J. J. Cowan, and R. Gallino, Annual Review of Astronomy and Astrophysics **46**, 241 (2008).

[7] M. Arnould, S. Goriely, and K. Takahashi, Physics Reports **450**, 97 (2007).

[8] C. Sneden, I. Roederer, J. Cowan, and J. E. Lawler, 11th Symposium on Nuclei in the Cosmos (NIC XI) **100**, 1 (2011).

[9] D. J. Price and S. Rosswog, "Producing ultra-strong magnetic fields in neutron star mergers," `http://users.monash.edu.au/~dprice/research/nsmag/`, accessed: 2018-06-01.

[10] D. J. Price and S. Rosswog, Science **312**, 719 (2006).

[11] T. Sprouse and M. R. Mumpower, "PRISM (Portable Routines for Integrated nucleoSynthesis Modeling," in preparation.

[12] M. R. Mumpower, R. Surman, G. C. McLaughlin, and A. Aprahamian, Progress in Particle and Nuclear Physics **86**, 86 (2016).

[13] T. Kibédi, T. W. Burrows, M. B. Trzhaskovskaya, P. M. Davidson, and C. W. Nestor, Nuclear Instruments and Methods in Physics Research Section A: Accelerators, Spectrometers, Detectors and Associated Equipment **589**, 202 (2008).

[14] National Nuclear Data Center, "BrIcc v2.3S Conversion Coefficient Calculator," `http://bricc.anu.edu.au/`, accessed: 2018-06-01.

[15] K. P. Rykaczewski, Physics **3** (2010), 10.1103/Physics.3.94.

[16] Meng Wang, G. Audi, F. G. Kondev, W. J. Huang, S. Naimi, and Xing Xu, Chinese Physics C **41**, 030003 (2017).

[17] M. Wang, G. Audi, A. Wapstra, F. Kondev, M. MacCormick, X. Xu, and B. Pfeiffer, Chinese Physics C **36**, 1603 (2012).

[18] B. Singh, Nuclear Data Sheets **74**, 63 (1995).

[19] K. Takahashi, T. Kuroyanagi, H. Yuta, K. Kotajima, K. Nagatani, and H. Morinaga, Journal of the Physical Society of Japan **16**, 1664 (1961).

[20] D. C. Camp and B. P. Foster, Nuclear Physics A **177**, 401 (1971).

[21] B. Grapengiesser, E. Lund, and G. Rudstam, Journal of Inorganic and Nuclear Chemistry **36**, 2409 (1974).

[22] H. W. Taylor, D. A. Craig, B. Singh, and D. A. Viggars, The International Journal of Applied Radiation and Isotopes **36**, 89 (1985).

[23] A. C. Dombos, D.-L. Fang, A. Spyrou, S. J. Quinn, A. Simon, B. A. Brown, K. Cooper, A. E. Gehring, S. N. Liddick, D. J. Morrissey, F. Naqvi, C. S. Sumithrarachchi, and R. G. T. Zegers, Phys. Rev. C **93**, 064317 (2016).

[24] E. Browne and J. K. Tuli, Nuclear Data Sheets **145**, 25 (2017).

[25] S. J. Quinn, *Capture Cross Sections for the Astrophysical p process*, Ph.D. thesis, Michigan State University (2015).

[26] E. Caurier, G. Martínez-Pinedo, F. Nowacki, A. Poves, and A. P. Zuker, Rev. Mod. Phys. **77**, 427 (2005).

[27] M. G. Mayer, Phys. Rev. **74**, 235 (1948).

[28] M. G. Mayer, Phys. Rev. **75**, 1969 (1949).

[29] M. G. Mayer, Phys. Rev. **78**, 16 (1950).

[30] M. G. Mayer, Phys. Rev. **78**, 22 (1950).

[31] O. Haxel, J. H. D. Jensen, and H. E. Suess, Phys. Rev. **75**, 1766 (1949).

[32] M. Asplund, N. Grevesse, A. J. Sauval, and P. Scott, Annual Review of Astronomy and Astrophysics **47**, 481 (2009).

[33] K. J. R. Rosman and P. D. P. Taylor, Journal of Physical and Chemical Reference Data **27**, 1275 (1998).

[34] E. M. Burbidge, G. R. Burbidge, W. A. Fowler, and F. Hoyle, Rev. Mod. Phys. **29**, 547 (1957).

[35] F. Käppeler, H. Beer, and K. Wisshak, Reports on Progress in Physics **52**, 945 (1989).

[36] F. Käppeler, R. Gallino, S. Bisterzo, and W. Aoki, Rev. Mod. Phys. **83**, 157 (2011).

[37] J. J. Cowan and W. K. Rose, The Astrophysical Journal **212**, 149 (1977).

[38] A. Simon, A. Spyrou, T. Rauscher, C. Fröhlich, S. J. Quinn, A. Battaglia, A. Best, B. Bucher, M. Couder, P. A. DeYoung, X. Fang, J. Görres, A. Kontos, Q. Li, L.-Y. Lin, A. Long, S. Lyons, A. Roberts, D. Robertson, K. Smith, M. K. Smith, E. Stech, B. Stefanek, W. P. Tan, X. D. Tang, and M. Wiescher, Phys. Rev. C **87**, 055802 (2013).

[39] S. J. Quinn, A. Spyrou, A. Simon, A. Battaglia, M. Couder, P. A. DeYoung, A. C. Dombos, X. Fang, J. Görres, A. Kontos, Q. Li, S. Lyons, B. S. Meyer, G. F. Peaslee, D. Robertson, K. Smith, M. K. Smith, E. Stech, W. P. Tan, X. D. Tang, and M. Wiescher, Phys. Rev. C **88**, 011603 (2013).

[40] A. Spyrou, S. J. Quinn, A. Simon, T. Rauscher, A. Battaglia, A. Best, B. Bucher, M. Couder, P. A. DeYoung, A. C. Dombos, X. Fang, J. Görres, A. Kontos, Q. Li, L. Y. Lin, A. Long, S. Lyons, B. S. Meyer, A. Roberts, D. Robertson, K. Smith, M. K. Smith, E. Stech, B. Stefanek, W. P. Tan, X. D. Tang, and M. Wiescher, Phys. Rev. C **88**, 045802 (2013).

[41] S. J. Quinn, A. Spyrou, E. Bravo, T. Rauscher, A. Simon, A. Battaglia, M. Bowers, B. Bucher, C. Casarella, M. Couder, P. A. DeYoung, A. C. Dombos, J. Görres, A. Kontos, Q. Li, A. Long, M. Moran, N. Paul, J. Pereira, D. Robertson, K. Smith, M. K. Smith, E. Stech, R. Talwar, W. P. Tan, and M. Wiescher, Phys. Rev. C **89**, 054611 (2014).

[42] F. Naqvi, S. J. Quinn, A. Spyrou, A. Battaglia, M. Couder, P. A. DeYoung, A. C. Dombos, X. Fang, J. Görres, A. Kontos, Q. Li, S. Lyons, D. Robertson, A. Simon, K. Smith, M. K. Smith, E. Stech, W. P. Tan, and M. Wiescher, Phys. Rev. C **92**, 025804 (2015).

[43] A. Simon, M. Beard, A. Spyrou, S. J. Quinn, B. Bucher, M. Couder, P. A. DeYoung, A. C. Dombos, J. Görres, A. Kontos, A. Long, M. T. Moran, N. Paul, J. Pereira, D. Robertson, K. Smith, E. Stech, R. Talwar, W. P. Tan, and M. Wiescher, Phys. Rev. C **92**, 025806 (2015).

[44] S. J. Quinn, A. Spyrou, A. Simon, A. Battaglia, M. Bowers, B. Bucher, C. Casarella, M. Couder, P. A. DeYoung, A. C. Dombos, J. Görres, A. Kontos, Q. Li, A. Long, M. Moran, N. Paul, J. Pereira, D. Robertson, K. Smith, M. K. Smith, E. Stech, R. Talwar, W. P. Tan, and M. Wiescher, Phys. Rev. C **92**, 045805 (2015).

[45] M. R. Mumpower, G. C. McLaughlin, and R. Surman, Phys. Rev. C **85**, 045801 (2012).

[46] S. Goriely, A&A **342**, 881 (1999).

[47] A. Frebel and J. E. Norris, Annual Review of Astronomy and Astrophysics **53**, 631 (2015).

[48] H. R. Jacobson and A. Frebel, Journal of Physics G: Nuclear and Particle Physics **41**, 044001 (2014).

[49] A. Frebel, Astronomische Nachrichten **331**, 474.

[50] T. C. Beers and N. Christlieb, Annual Review of Astronomy and Astrophysics **43**, 531 (2005).

[51] P. S. Barklem, N. Christlieb, T. C. Beers, V. Hill, M. S. Bessell, J. Holmberg, B. Marsteller, S. Rossi, F.-J. Zickgraf, and D. Reimers, A&A **439**, 129 (2005).

[52] C. Siqueira Mello, V. Hill, B. Barbuy, M. Spite, F. Spite, T. C. Beers, E. Caffau, P. Bonifacio, R. Cayrel, P. François, H. Schatz, and S. Wanajo, A&A **565**, A93 (2014).

[53] G. J. Wasserburg, M. Busso, and R. Gallino, The Astrophysical Journal Letters **466**, L109 (1996).

[54] Y.-Z. Qian and G. J. Wasserburg, Physics Reports **333-334**, 77 (2000).

[55] F. Montes, T. C. Beers, J. Cowan, T. Elliot, K. Farouqi, R. Gallino, M. Heil, K.-L. Kratz, B. Pfeiffer, M. Pignatari, and H. Schatz, The Astrophysical Journal **671**, 1685.

[56] A. Arcones and F. Montes, The Astrophysical Journal **731**, 5 (2011).

[57] F.-K. Thielemann, A. Arcones, R. Käppeli, M. Liebendörfer, T. Rauscher, C. Winteler, C. Fröhlich, I. Dillmann, T. Fischer, G. Martinez-Pinedo, K. Langanke, K. Farouqi, K.-L. Kratz, I. Panov, and I. K. Korneev, Progress in Particle and Nuclear Physics **66**, 346 (2011), particle and Nuclear Astrophysics.

[58] S. Wanajo, T. Kajino, G. J. Mathews, and K. Otsuki, The Astrophysical Journal **554**, 578 (2001).

[59] J. Beun, G. C. McLaughlin, R. Surman, and W. R. Hix, Phys. Rev. D **73**, 093007 (2006).

[60] S. Wanajo, The Astrophysical Journal Letters **770**, L22 (2013).

[61] J. M. Lattimer and D. N. Schramm, The Astrophysical Journal **192**, L145 (1974).

[62] F.-K. Thielemann, M. Eichler, I. V. Panov, and B. Wehmeyer, Annual Review of Nuclear and Particle Science **67**, 253 (2017).

[63] A. Bauswein, S. Goriely, and H.-T. Janka, The Astrophysical Journal **773**, 78 (2013).

[64] J. M. Lattimer, F. Mackie, D. G. Ravenhall, and D. N. Schramm, The Astrophysical Journal **213**, 225 (1977).

[65] O. Korobkin, S. Rosswog, A. Arcones, and C. Winteler, Monthly Notices of the Royal Astronomical Society **426**, 1940 (2012).

[66] Argast, D., Samland, M., Thielemann, F.-K., and Qian, Y.-Z., A&A **416**, 997 (2004).

[67] M. Dominik, K. Belczynski, C. Fryer, D. E. Holz, E. Berti, T. Bulik, I. Mandel, and R. O'Shaughnessy, The Astrophysical Journal **759**, 52 (2012).

[68] S. Shen, R. J. Cooke, E. Ramirez-Ruiz, P. Madau, L. Mayer, and J. Guedes, The Astrophysical Journal **807**, 115 (2015).

[69] Y. Ishimaru, S. Wanajo, and N. Prantzos, The Astrophysical Journal Letters **804**, L35 (2015).

[70] A. P. Ji, A. Frebel, A. Chiti, and J. D. Simon, Nature **531**, 610 (2016).

[71] D. A. Coulter, R. J. Foley, C. D. Kilpatrick, M. R. Drout, A. L. Piro, B. J. Shappee, M. R. Siebert, J. D. Simon, N. Ulloa, D. Kasen, B. F. Madore, A. Murguia-Berthier, Y.-C. Pan, J. X. Prochaska, E. Ramirez-Ruiz, A. Rest, and C. Rojas-Bravo, Science **358**, 1556 (2017).

[72] B. D. Metzger, Living Reviews in Relativity **20**, 3 (2017).

[73] B. P. Abbott *et al.* (LIGO Scientific Collaboration and Virgo Collaboration), Phys. Rev. Lett. **119**, 161101 (2017).

[74] D. Kasen, N. R. Badnell, and J. Barnes, The Astrophysical Journal **774**, 25 (2013).

[75] D. Kasen, B. Metzger, J. Barnes, E. Quataert, and E. Ramirez-Ruiz, Nature **551**, 80 (2017).

[76] P. Venkataramaiah, K. Gopala, A. Basavaraju, S. S. Suryanarayana, and H. Sanjeeviah, Journal of Physics G: Nuclear Physics **11**, 359 (1985).

[77] G. K. Schenter and P. Vogel, Nuclear Science and Engineering **83**, 393 (1983).

[78] A. Algora, D. Jordan, J. L. Taín, B. Rubio, J. Agramunt, A. B. Perez-Cerdan, F. Molina, L. Caballero, E. Nácher, A. Krasznahorkay, M. D. Hunyadi, J. Gulyás, A. Vitéz, M. Csatlós, L. Csige, J. Äysto, H. Penttilä, I. D. Moore, T. Eronen, A. Jokinen, A. Nieminen, J. Hakala, P. Karvonen, A. Kankainen, A. Saastamoinen, J. Rissanen, T. Kessler, C. Weber, J. Ronkainen, S. Rahaman, V. Elomaa, S. Rinta-Antila, U. Hager, T. Sonoda, K. Burkard, W. Hüller, L. Batist, W. Gelletly, A. L. Nichols, T. Yoshida, A. A. Sonzogni, and K. Peräjärvi, Phys. Rev. Lett. **105**, 202501 (2010).

[79] D. Jordan, A. Algora, J. L. Taín, B. Rubio, J. Agramunt, A. B. Perez-Cerdan, F. Molina, L. Caballero, E. Nácher, A. Krasznahorkay, M. D. Hunyadi, J. Gulyás, A. Vitéz, M. Csatlós, L. Csige, J. Äysto, H. Penttilä, I. D. Moore, T. Eronen, A. Jokinen, A. Nieminen, J. Hakala, P. Karvonen, A. Kankainen, A. Saastamoinen, J. Rissanen, T. Kessler, C. Weber, J. Ronkainen, S. Rahaman, V. Elomaa, U. Hager, S. Rinta-Antila, T. Sonoda, K. Burkard, W. Hüller, L. Batist, W. Gelletly, A. L. Nichols, T. Yoshida, A. A. Sonzogni, K. Peräjärvi, A. Petrovici, K. W. Schmid, and A. Faessler, Phys. Rev. C **87**, 044318 (2013).

[80] E. Valencia, J. L. Tain, A. Algora, J. Agramunt, E. Estevez, M. D. Jordan, B. Rubio, S. Rice, P. Regan, W. Gelletly, Zs. Podolyák, M. Bowry, P. Mason, G. F. Farrelly, A.-A. Zakari-Issoufou, M. Fallot, A. Porta, V. M. Bui, J. Rissanen, T. Eronen, I. Moore, H. Penttilä, J. Äystö, V.-V. Elomaa, J. Hakala, A. Jokinen, V. S. Kolhinen, M. Reponen, V. Sonnenschein, D. Cano-Ott, A. R. Garcia, T. Martínez, E. Mendoza, R. Caballero-Folch, B. Gomez-Hornillos, V. Gorlichev, F. G. Kondev, A. A. Sonzogni, and L. Batist, Phys. Rev. C **95**, 024320 (2017).

[81] B. C. Rasco, K. P. Rykaczewski, A. Fijałkowska, M. Karny, M. Wolińska-Cichocka, R. K. Grzywacz, C. J. Gross, D. W. Stracener, E. F. Zganjar, J. C. Blackmon, N. T. Brewer, K. C. Goetz, J. W. Johnson, C. U. Jost, J. H. Hamilton, K. Miernik, M. Madurga, D. Miller, S. Padgett, S. V. Paulauskas, A. V. Ramayya, and E. H. Spejewski, Phys. Rev. C **95**, 054328 (2017).

[82] S. Rice, A. Algora, J. L. Tain, E. Valencia, J. Agramunt, B. Rubio, W. Gelletly, P. H. Regan, A.-A. Zakari-Issoufou, M. Fallot, A. Porta, J. Rissanen, T. Eronen, J. Äystö, L. Batist, M. Bowry, V. M. Bui, R. Caballero-Folch, D. Cano-Ott, V.-V. Elomaa, E. Estevez, G. F. Farrelly, A. R. Garcia, B. Gomez-Hornillos, V. Gorlychev, J. Hakala, M. D. Jordan, A. Jokinen, V. S. Kolhinen, F. G. Kondev, T. Martínez, P. Mason, E. Mendoza, I. Moore, H. Penttilä, Zs. Podolyák, M. Reponen, V. Sonnenschein, A. A. Sonzogni, and P. Sarriguren, Phys. Rev. C **96**, 014320 (2017).

[83] A. Fijałkowska, M. Karny, K. P. Rykaczewski, B. C. Rasco, R. Grzywacz, C. J. Gross, M. Wolińska-Cichocka, K. C. Goetz, D. W. Stracener, W. Bielewski, R. Goans, J. H. Hamilton, J. W. Johnson, C. Jost, M. Madurga, K. Miernik, D. Miller, S. W. Padgett, S. V. Paulauskas, A. V. Ramayya, and E. F. Zganjar, Phys. Rev. Lett. **119**, 052503 (2017).

[84] M. Fallot, S. Cormon, M. Estienne, A. Algora, V. M. Bui, A. Cucoanes, M. Elnimr, L. Giot, D. Jordan, J. Martino, A. Onillon, A. Porta, G. Pronost, A. Remoto, J. L. Taín, F. Yermia, and A.-A. Zakari-Issoufou, Phys. Rev. Lett. **109**, 202504 (2012).

[85] A.-A. Zakari-Issoufou, M. Fallot, A. Porta, A. Algora, J. L. Tain, E. Valencia, S. Rice, V. M. Bui, S. Cormon, M. Estienne, J. Agramunt, J. Äystö, M. Bowry, J. A. Briz, R. Caballero-Folch, D. Cano-Ott, A. Cucoanes, V.-V. Elomaa, T. Eronen, E. Estévez, G. F. Farrelly, A. R. Garcia, W. Gelletly, M. B. Gomez-Hornillos, V. Gorlychev, J. Hakala, A. Jokinen, M. D. Jordan, A. Kankainen, P. Karvonen, V. S. Kolhinen, F. G. Kondev, T. Martinez, E. Mendoza, F. Molina, I. Moore, A. B. Perez-Cerdán, Zs. Podolyák, H. Penttilä, P. H. Regan, M. Reponen, J. Rissanen, B. Rubio, T. Shiba, A. A. Sonzogni, and C. Weber (IGISOL collaboration), Phys. Rev. Lett. **115**, 102503 (2015).

[86] B. C. Rasco, M. Wolińska-Cichocka, A. Fijałkowska, K. P. Rykaczewski, M. Karny, R. K. Grzywacz, K. C. Goetz, C. J. Gross, D. W. Stracener, E. F. Zganjar, J. C. Batchelder, J. C. Blackmon, N. T. Brewer, S. Go, B. Heffron, T. King, J. T. Matta, K. Miernik, C. D. Nesaraja, S. V. Paulauskas, M. M. Rajabali, E. H. Wang, J. A. Winger, Y. Xiao, and C. J. Zachary, Phys. Rev. Lett. **117**, 092501 (2016).

[87] P. Sarriguren and J. Pereira, Phys. Rev. C **81**, 064314 (2010).

[88] P. Sarriguren, A. Algora, and J. Pereira, Phys. Rev. C **89**, 034311 (2014).

[89] J. C. Hardy and I. S. Towner, Phys. Rev. C **79**, 055502 (2009).

[90] J. C. Hardy and I. S. Towner, Nuclear Physics News **16**, 11 (2006).

[91] B. Rubio and W. Gelletly, "Beta Decay of Exotic Nuclei," in *The Euroschool Lectures on Physics with Exotic Beams, Vol. III*, edited by J. S. Al-Khalili and E. Roeckl (Springer Berlin Heidelberg, Berlin, Heidelberg, 2009) pp. 99–151.

[92] Y. Fujita, B. Rubio, and W. Gelletly, Progress in Particle and Nuclear Physics **66**, 549 (2011).

[93] J. C. Hardy, L. C. Carraz, B. Jonson, and P. G. Hansen, Physics Letters B **71**, 307 (1977).

[94] E. Browne and J. K. Tuli, Nuclear Data Sheets **114**, 1849 (2013).

[95] A. Simon, S. J. Quinn, A. Spyrou, A. Battaglia, I. Beskin, A. Best, B. Bucher, M. Couder, P. A. DeYoung, X. Fang, J. Görres, A. Kontos, Q. Li, S. N. Liddick, A. Long, S. Lyons, K. Padmanabhan, J. Peace, A. Roberts, D. Robertson, K. Smith, M. K. Smith, E. Stech, B. Stefanek, W. P. Tan, X. D. Tang, and M. Wiescher, Nuclear Instruments and Methods in Physics Research Section A: Accelerators, Spectrometers, Detectors and Associated Equipment **703**, 16 (2013).

[96] C. J. Prokop, S. N. Liddick, B. L. Abromeit, A. T. Chemey, N. R. Larson, S. Suchyta, and J. R. Tompkins, Nuclear Instruments and Methods in Physics Research Section A: Accelerators, Spectrometers, Detectors and Associated Equipment **741**, 163 (2014).

[97] P. Urkedal, X. Z. Zhang, and I. Hamamoto, Phys. Rev. C **64**, 054304 (2001).

[98] I. Hamamoto and X. Z. Zhang, Zeitschrift für Physik A Hadrons and Nuclei **353**, 145 (1995).

[99] F. Frisk, I. Hamamoto, and X. Z. Zhang, Phys. Rev. C **52**, 2468 (1995).

[100] P. Sarriguren, E. Moya de Guerra, A. Escuderos, and A. C. Carrizo, Nuclear Physics A **635**, 55 (1998).

[101] P. Sarriguren, E. Moya de Guerra, and A. Escuderos, Nuclear Physics A **658**, 13 (1999).

[102] P. Sarriguren, E. Moya de Guerra, and A. Escuderos, Nuclear Physics A **691**, 631 (2001).

[103] P. Sarriguren, E. Moya de Guerra, and A. Escuderos, Phys. Rev. C **64**, 064306 (2001).

[104] P. Sarriguren, O. Moreno, R. Álvarez-Rodríguez, and E. Moya de Guerra, Phys. Rev. C **72**, 054317 (2005).

[105] O. Moreno, P. Sarriguren, R. Álvarez-Rodríguez, and E. Moya de Guerra, Phys. Rev. C **73**, 054302 (2006).

[106] O. Moreno, R. Álvarez-Rodríguez, P. Sarriguren, E. Moya de Guerra, J. M. Udías, and J. R. Vignote, Phys. Rev. C **74**, 054308 (2006).

[107] P. Sarriguren, Phys. Rev. C **79**, 044315 (2009).

[108] J. M. Boillos and P. Sarriguren, Phys. Rev. C **91**, 034311 (2015).

[109] P. Sarriguren, Phys. Rev. C **91**, 044304 (2015).

[110] P. Sarriguren, Phys. Rev. C **95**, 014304 (2017).

[111] E. Poirier, F. Maréchal, Ph. Dessagne, A. Algora, M. J. G. Borge, D. Cano-Ott, J. C. Caspar, S. Courtin, J. Devin, L. M. Fraile, W. Gelletly, G. Heitz, A. Jungclaus, G. Le Scornet, Ch. Miehé, E. Nácher, B. Rubio, P. Sarriguren, J. L. Tain, O. Tengblad, and C. Weber (the ISOLDE Collaboration), Phys. Rev. C **69**, 034307 (2004).

[112] E. Nácher, A. Algora, B. Rubio, J. L. Taín, D. Cano-Ott, S. Courtin, Ph. Dessagne, F. Maréchal, Ch. Miehé, E. Poirier, M. J. G. Borge, D. Escrig, A. Jungclaus, P. Sarriguren, O. Tengblad, W. Gelletly, L. M. Fraile, and G. Le Scornet, Phys. Rev. Lett. **92**, 232501 (2004).

[113] A. B. Pérez-Cerdán, B. Rubio, W. Gelletly, A. Algora, J. Agramunt, E. Nácher, J. L. Taín, P. Sarriguren, L. M. Fraile, M. J. G. Borge, L. Caballero, Ph. Dessagne, A. Jungclaus, G. Heitz, F. Marechal, E. Poirier, M. D. Salsac, and O. Tengblad, Phys. Rev. C **88**, 014324 (2013).

[114] M. E. Estévez Aguado, A. Algora, J. Agramunt, B. Rubio, J. L. Taín, D. Jordán, L. M. Fraile, W. Gelletly, A. Frank, M. Csatlós, L. Csige, Zs. Dombrádi, A. Krasznahorkay, E. Nácher, P. Sarriguren, M. J. G. Borge, J. A. Briz, O. Tengblad, F. Molina, O. Moreno, M. Kowalska, V. N. Fedosseev, B. A. Marsh, D. V. Fedorov, P. L. Molkanov, A. N. Andreyev, M. D. Seliverstov, K. Burkard, and W. Hüller, Phys. Rev. C **92**, 044321 (2015).

[115] J. A. Briz, E. Nácher, M. J. G. Borge, A. Algora, B. Rubio, Ph. Dessagne, A. Maira, D. Cano-Ott, S. Courtin, D. Escrig, L. M. Fraile, W. Gelletly, A. Jungclaus, G. Le Scornet, F. Maréchal, Ch. Miehé, E. Poirier, A. Poves, P. Sarriguren, J. L. Taín, and O. Tengblad, Phys. Rev. C **92**, 054326 (2015).

[116] A. Spyrou, S. N. Liddick, A. C. Larsen, M. Guttormsen, K. Cooper, A. C. Dombos, D. J. Morrissey, F. Naqvi, G. Perdikakis, S. J. Quinn, T. Renstrøm, J. A. Rodriguez, A. Simon, C. S. Sumithrarachchi, and R. G. T. Zegers, Phys. Rev. Lett. **113**, 232502 (2014).

[117] M. Guttormsen, T. Ramsøy, and J. Rekstad, Nuclear Instruments and Methods in Physics Research Section A: Accelerators, Spectrometers, Detectors and Associated Equipment **255**, 518 (1987).

[118] A. Schiller, L. Bergholt, M. Guttormsen, E. Melby, J. Rekstad, and S. Siem, Nuclear Instruments and Methods in Physics Research Section A: Accelerators, Spectrometers, Detectors and Associated Equipment **447**, 498 (2000).

[119] F. T. Avignone, S. R. Elliott, and J. Engel, Rev. Mod. Phys. **80**, 481 (2008).

[120] J. D. Vergados, H. Ejiri, and F. Šimkovic, Reports on Progress in Physics **75**, 106301 (2012).

[121] B. J. Mount, M. Redshaw, and E. G. Myers, Phys. Rev. C **81**, 032501 (2010).

[122] H. V. Klapdor-Kleingrothaus, A. Dietz, L. Baudis, G. Heusser, I. V. Krivosheina, B. Majorovits, H. Paes, H. Strecker, V. Alexeev, A. Balysh, A. Bakalyarov, S. T. Belyaev, V. I. Lebedev, and S. Zhukov, The European Physical Journal A - Hadrons and Nuclei **12**, 147 (2001).

[123] C. E. Aalseth, F. T. Avignone, R. L. Brodzinski, S. Cebrian, E. Garcia, D. Gonzalez, W. K. Hensley, I. G. Irastorza, I. V. Kirpichnikov, A. A. Klimenko, H. S. Miley, A. Morales, J. Morales, A. Ortiz de Solorzano, S. B. Osetrov, V. S. Pogosov, J. Puimedon, J. H. Reeves, M. L. Sarsa, A. A. Smolnikov, A. S. Starostin, A. G. Tamanyan, A. A. Vasenko, S. I. Vasiliev, and J. A. Villar (IGEX Collaboration), Phys. Rev. D **65**, 092007 (2002).

[124] C. E. Aalseth, F. T. Avignone, R. L. Brodzinski, S. Cebrian, E. Garcia, D. Gonzales, W. K. Hensley, I. G. Irastorza, I. V. Kirpichnikov, A. A. Klimenko, H. S. Miley, A. Morales, J. Morales, A. Ortiz de Solorzano, S. B. Osetrov, V. S. Pogosov, J. Puimedon, J. H. Reeves, M. L. Sarsa, A. A. Smolnikov, A. S. Starostin, A. G. Tamanyan, A. A. Vasenko, S. I. Vasiliev, and J. A. Villar, Phys. Rev. D **70**, 078302 (2004).

[125] M. Agostini, M. Allardt, E. Andreotti, A. M. Bakalyarov, M. Balata, I. Barabanov, M. Barnabé Heider, N. Barros, L. Baudis, C. Bauer, N. Becerici-Schmidt, E. Bellotti, S. Belogurov, S. T. Belyaev, G. Benato, A. Bettini, L. Bezrukov, T. Bode, V. Brudanin, R. Brugnera, D. Budjáš, A. Caldwell, C. Cattadori, A. Chernogorov, F. Cossavella, E. V. Demidova, A. Domula, V. Egorov, R. Falkenstein, A. Ferella, K. Freund, N. Frodyma, A. Gangapshev, A. Garfagnini, C. Gotti, P. Grabmayr, V. Gurentsov, K. Gusev, K. K. Guthikonda, W. Hampel, A. Hegai, M. Heisel, S. Hemmer, G. Heusser, W. Hofmann, M. Hult, L. V. Inzhechik, L. Ioannucci, J. Janicskó Csáthy, J. Jochum, M. Junker, T. Kihm, I. V. Kirpichnikov, A. Kirsch, A. Klimenko, K. T. Knöpfle, O. Kochetov, V. N. Kornoukhov, V. V. Kuzminov, M. Laubenstein, A. Lazzaro, V. I. Lebedev, B. Lehnert, H. Y. Liao, M. Lindner, I. Lippi, X. Liu, A. Lubashevskiy, B. Lubsandorzhiev, G. Lutter, C. Macolino, A. A. Machado, B. Majorovits, W. Maneschg, M. Misiaszek, I. Nemchenok, S. Nisi, C. O'Shaughnessy, L. Pandola, K. Pelczar, G. Pessina, A. Pullia, S. Riboldi, N. Rumyantseva, C. Sada, M. Salathe, C. Schmitt, J. Schreiner, O. Schulz, B. Schwingenheuer, S. Schönert, E. Shevchik, M. Shirchenko, H. Simgen, A. Smolnikov, L. Stanco, H. Strecker, M. Tarka, C. A. Ur, A. A. Vasenko, O. Volynets, K. von Sturm, V. Wagner, M. Walter, A. Wegmann, T. Wester, M. Wojcik, E. Yanovich, P. Zavarise, I. Zhitnikov, S. V. Zhukov, D. Zinatulina, K. Zuber, and G. Zuzel (GERDA Collaboration), Phys. Rev. Lett. **111**, 122503 (2013).

[126] C. A. Ur, Nuclear Physics B - Proceedings Supplements **217**, 38 (2011), Proceedings of the Neutrino Oscillation Workshop (NOW 2010).

[127] N. Abgrall, E. Aguayo, F. T. Avignone III, *et al.*, Advances in High Energy Physics **2014** (2014), 10.1155/2014/365432.

[128] J. Suhonen and O. Civitarese, Physics Reports **300**, 123 (1998).

[129] J. Kotila and F. Iachello, Phys. Rev. C **85**, 034316 (2012).

[130] S. Stoica and M. Mirea, Phys. Rev. C **88**, 037303 (2013).

[131] J. Kotila, J. Barea, and F. Iachello, Phys. Rev. C **91**, 064310 (2015).

[132] P. Vogel, Journal of Physics G: Nuclear and Particle Physics **39**, 124002 (2012).

[133] A. Giuliani and A. Poves, Advances in High Energy Physics **2012** (2012), 10.1155/2012/857016.

[134] R. A. Sen'kov and M. Horoi, Phys. Rev. C **90**, 051301 (2014).

[135] D.-L. Fang, A. Faessler, V. Rodin, and F. Šimkovic, Phys. Rev. C **83**, 034320 (2011).

[136] J. Barea, J. Kotila, and F. Iachello, Phys. Rev. C **91**, 034304 (2015).

[137] B. A. Brown, D.-L. Fang, and M. Horoi, Phys. Rev. C **92**, 041301(R) (2015).

[138] D. J. Morrissey, B. M. Sherrill, M. Steiner, A. Stolz, and I. Wiedenhoever, Nuclear Instruments and Methods in Physics Research Section B: Beam Interactions with Materials and Atoms **204**, 90 (2003), 14th International Conference on Electromagnetic Isotope Separators and Techniques Related to their Applications.

[139] K. L. Cooper, *Commissioning and Characterization of the NSCL's Large Volume Linear Gas Cell*, Ph.D. thesis, Michigan State University (2016).

[140] K. Cooper, C. S. Sumithrarachchi, D. J. Morrissey, A. Levand, J. A. Rodriguez, G. Savard, S. Schwarz, and B. Zabransky, Nuclear Instruments and Methods in Physics Research Section A: Accelerators, Spectrometers, Detectors and Associated Equipment **763**, 543 (2014).

[141] D. Cano-Ott, J. L. Tain, A. Gadea, B. Rubio, L. Batist, M. Karny, and E. Roeckl, Nuclear Instruments and Methods in Physics Research Section A: Accelerators, Spectrometers, Detectors and Associated Equipment **430**, 333 (1999).

[142] S. Agostinelli, J. Allison, K. Amako, J. Apostolakis, H. Araujo, P. Arce, M. Asai, D. Axen, S. Banerjee, G. Barrand, F. Behner, L. Bellagamba, J. Boudreau, L. Broglia, A. Brunengo, H. Burkhardt, S. Chauvie, J. Chuma, R. Chytracek, G. Cooperman, G. Cosmo, P. Degtyarenko, A. Dell'Acqua, G. Depaola, D. Dietrich, R. Enami, A. Feliciello, C. Ferguson, H. Fesefeldt, G. Folger, F. Foppiano, A. Forti, S. Garelli, S. Giani, R. Giannitrapani, D. Gibin, J. J. G. Cadenas, I. González, G. G. Abril, G. Greeniaus, W. Greiner, V. Grichine, A. Grossheim, S. Guatelli, P. Gumplinger, R. Hamatsu,

K. Hashimoto, H. Hasui, A. Heikkinen, A. Howard, V. Ivanchenko, A. Johnson, F. W. Jones, J. Kallenbach, N. Kanaya, M. Kawabata, Y. Kawabata, M. Kawaguti, S. Kelner, P. Kent, A. Kimura, T. Kodama, R. Kokoulin, M. Kossov, H. Kurashige, E. Lamanna, T. Lampén, V. Lara, V. Lefebure, F. Lei, M. Liendl, W. Lockman, F. Longo, S. Magni, M. Maire, E. Medernach, K. Minamimoto, P. M. de Freitas, Y. Morita, K. Murakami, M. Nagamatu, R. Nartallo, P. Nieminen, T. Nishimura, K. Ohtsubo, M. Okamura, S. O'Neale, Y. Oohata, K. Paech, J. Perl, A. Pfeiffer, M. G. Pia, F. Ranjard, A. Rybin, S. Sadilov, E. D. Salvo, G. Santin, T. Sasaki, N. Savvas, Y. Sawada, S. Scherer, S. Sei, V. Sirotenko, D. Smith, N. Starkov, H. Stoecker, J. Sulkimo, M. Takahata, S. Tanaka, E. Tcherniaev, E. S. Tehrani, M. Tropeano, P. Truscott, H. Uno, L. Urban, P. Urban, M. Verderi, A. Walkden, W. Wander, H. Weber, J. P. Wellisch, T. Wenaus, D. C. Williams, D. Wright, T. Yamada, H. Yoshida, and D. Zschiesche, Nuclear Instruments and Methods in Physics Research Section A: Accelerators, Spectrometers, Detectors and Associated Equipment **506**, 250 (2003).

[143] B. A. Brown and W. D. M. Rae, Nuclear Data Sheets **120**, 115 (2014).

[144] M. Honma, T. Otsuka, T. Mizusaki, and M. Hjorth-Jensen, Phys. Rev. C **80**, 064323 (2009).

[145] B. A. Brown, private communication.

[146] E. Mané, B. Cheal, J. Billowes, M. L. Bissell, K. Blaum, F. C. Charlwood, K. T. Flanagan, D. H. Forest, C. Geppert, M. Kowalska, A. Krieger, J. Krämer, I. D. Moore, R. Neugart, G. Neyens, W. Nörtershäuser, M. M. Rajabali, R. Sánchez, M. Schug, H. H. Stroke, P. Vingerhoets, D. T. Yordanov, and M. Žáková, Phys. Rev. C **84**, 024303 (2011).

[147] D.-L. Fang and B. A. Brown, in preparation.

[148] N. Gove and M. Martin, Atomic Data and Nuclear Data Tables **10**, 205 (1971).

[149] J. I. Prisciandaro, A. C. Morton, and P. F. Mantica, Nuclear Instruments and Methods in Physics Research Section A: Accelerators, Spectrometers, Detectors and Associated Equipment **505**, 140 (2003), proceedings of the tenth Symposium on Radiation Measurements and Applications.

[150] "Micron Semiconductor Ltd." available online at `http://www.micronsemiconductor.co.uk/`.

[151] T. Kurtukian-Nieto, J. Benlliure, and K.-H. Schmidt, Nuclear Instruments and Methods in Physics Research Section A: Accelerators, Spectrometers, Detectors and Associated Equipment **589**, 472 (2008).

[152] A. Spyrou, A. C. Larsen, S. N. Liddick, F. Naqvi, B. P. Crider, A. C. Dombos, M. Guttormsen, D. L. Bleuel, A. Couture, L. Crespo Campo, R. Lewis, S. Mosby, M. R. Mumpower, G. Perdikakis, C. J. Prokop, S. J. Quinn, T. Renstrøm, S. Siem, and R. Surman, Journal of Physics G: Nuclear and Particle Physics **44**, 044002 (2017).

[153] A. I. Morales, A. Algora, B. Rubio, K. Kaneko, S. Nishimura, P. Aguilera, S. E. A. Orrigo, F. Molina, G. de Angelis, F. Recchia, G. Kiss, V. H. Phong, J. Wu, D. Nishimura, H. Oikawa, T. Goigoux, J. Giovinazzo, P. Ascher, J. Agramunt, D. S. Ahn, H. Baba, B. Blank, C. Borcea, A. Boso, P. Davies, F. Diel, Z. Dombrádi, P. Doornenbal, J. Eberth, G. de France, Y. Fujita, N. Fukuda, E. Ganioglu, W. Gelletly, M. Gerbaux, S. Grévy, V. Guadilla, N. Inabe, T. Isobe, I. Kojouharov, W. Korten, T. Kubo, S. Kubono, T. Kurtukián Nieto, N. Kurz, J. Lee, S. Lenzi, J. Liu, T. Lokotko, D. Lubos, C. Magron, A. Montaner-Pizá, D. R. Napoli, H. Sakurai, H. Schaffner, Y. Shimizu, C. Sidong, P.-A. Söderström, T. Sumikama, H. Suzuki, H. Takeda, Y. Takei, M. Tanaka, and S. Yagi, Phys. Rev. C **95**, 064327 (2017).

[154] R. Capote, M. Herman, P. Obložinský, P. G. Young, S. Goriely, T. Belgya, A. V. Ignatyuk, A. J. Koning, S. Hilaire, V. A. Plujko, M. Avrigeanu, O. Bersillon, M. B. Chadwick, T. Fukahori, Zhigang Ge, Yinlu Han, S. Kailas, J. Kopecky, V. M. Maslov, G. Reffo, M. Sin, E. Sh. Soukhovitskii, and P. Talou, Nuclear Data Sheets **110**, 3107 (2009), special Issue on Nuclear Reaction Data.

[155] J. Tuli, Nuclear Instruments and Methods in Physics Research Section A: Accelerators, Spectrometers, Detectors and Associated Equipment **369**, 506 (1996).

[156] B. C. Rasco, A. Fijałkowska, M. Karny, K. P. Rykaczewski, M. Wolińska-Cichocka, K. C. Goetz, R. K. Grzywacz, C. J. Gross, K. Miernik, and S. V. Paulauskas, Journal of the Physical Society of Japan Conference Proceedings **6**, 030018 (2015).

[157] F. Bečvář, Nuclear Instruments and Methods in Physics Research Section A: Accelerators, Spectrometers, Detectors and Associated Equipment **417**, 434 (1998).

[158] J. L. Tain and D. Cano-Ott, Nuclear Instruments and Methods in Physics Research Section A: Accelerators, Spectrometers, Detectors and Associated Equipment **571**, 719 (2007).

[159] D. Jordan, A. Algora, and J. L. Tain, Nuclear Instruments and Methods in Physics Research Section A: Accelerators, Spectrometers, Detectors and Associated Equipment **828**, 52 (2016).

[160] D. Pandit, S. Bhattacharya, D. Mondal, P. Roy, K. Banerjee, S. Mukhopadhyay, S. Pal, A. De, B. Dey, and S. R. Banerjee, Phys. Rev. C **97**, 041301 (2018).

[161] S. Bhattacharya, D. Pandit, S. Mukhopadhyay, S. Pal, and S. R. Banerjee, Phys. Rev. C **78**, 064601 (2008).

[162] S. Bhattacharya, D. Pandit, B. Dey, D. Mondal, S. Mukhopadhyay, S. Pal, A. De, and S. R. Banerjee, Phys. Rev. C **90**, 054319 (2014).

[163] F. Pühlhofer, Nuclear Physics A **280**, 267 (1977).

[164] G. Schramm, R. Massarczyk, A. R. Junghans, T. Belgya, R. Beyer, E. Birgersson, E. Grosse, M. Kempe, Z. Kis, K. Kosev, M. Krtička, A. Matic, K. D. Schilling, R. Schwengner, L. Szentmiklósi, A. Wagner, and J. L. Weil, Phys. Rev. C **85**, 014311 (2012).

[165] L. E. Kirsch and L. A. Bernstein, Nuclear Instruments and Methods in Physics Research Section A: Accelerators, Spectrometers, Detectors and Associated Equipment **892**, 30 (2018).

[166] S. Goriely, S. Hilaire, and A. J. Koning, Phys. Rev. C **78**, 064307 (2008).

[167] F. James, "MINUIT Function Minimization and Error Analysis: Reference Manual Version 94.1," (1994).

[168] R. Brun and F. Rademakers, Nuclear Instruments and Methods in Physics Research Section A: Accelerators, Spectrometers, Detectors and Associated Equipment **389**, 81 (1997), new Computing Techniques in Physics Research V.

[169] H. Bateman, Proceedings of the Cambridge Philosophical Society **15**, 423 (1910).

[170] M. Quinn, A. Aprahamian, J. Pereira, R. Surman, O. Arndt, T. Baumann, A. Becerril, T. Elliot, A. Estrade, D. Galaviz, T. Ginter, M. Hausmann, S. Hennrich, R. Kessler, K.-L. Kratz, G. Lorusso, P. F. Mantica, M. Matos, F. Montes, B. Pfeiffer, M. Portillo, H. Schatz, F. Schertz, L. Schnorrenberger, E. Smith, A. Stolz, W. B. Walters, and A. Wöhr, Phys. Rev. C **85**, 035807 (2012).

[171] G. Rudstam, K. Aleklett, and L. Sihver, Atomic Data and Nuclear Data Tables **53**, 1 (1993).

[172] P. L. Reeder and R. A. Warner, Phys. Rev. C **28**, 1740 (1983).

[173] H. A. Selič, G. Sadler, T. A. Khan, W.-D. Lauppe, H. Lawin, K. Sistemich, E. Monnand, J. Blachot, J. P. Bocquet, and F. Schussler, Zeitschrift für Physik A Atoms and Nuclei **289**, 197 (1979).

[174] M. Asghar, J. P. Gautheron, G. Bailleul, J. P. Bocquet, J. Greif, H. Schrader, G. Siegert, C. Ristori, J. Crancon, and G. I. Crawford, Nuclear Physics A **247**, 359 (1975).

[175] T. Mehren, B. Pfeiffer, S. Schoedder, K.-L. Kratz, M. Huhta, P. Dendooven, A. Honkanen, G. Lhersonneau, M. Oinonen, J.-M. Parmonen, H. Penttilä, A. Popov, V. Rubchenya, and J. Äystö, Phys. Rev. Lett. **77**, 458 (1996).

[176] H.-D. Schüssler and G. Herrmann, Radiochim. Acta **18**, 123 (1972).

[177] N. Trautmann, N. Kaffrell, H. W. Behlich, H. Folger, G. Herrmann, D. Hübscher, and H. Ahrens, Radiochim. Acta **18**, 86 (1972).

[178] J. Blachot, Nuclear Data Sheets **83**, 1 (1998).

[179] H. Ohm, M. Liang, U. Paffrath, B. De Sutter, K. Sistemich, A. -M. Schmitt, N. Kaffrell, N. Trautmann, T. Seo, K. Shizuma, G. Molnár, K. Kawade, and R. A. Meyer, Zeitschrift für Physik A Hadrons and Nuclei **340**, 5 (1991).

[180] J. Eidens, E. Roeckl, and P. Armbruster, Nuclear Physics A **141**, 289 (1970).

[181] M. Graefenstedt, U. Keyser, F. Münnich, F. Schreiber, H. R. Faust, and H. Weikard, Zeitschrift für Physik A Atomic Nuclei **327**, 383 (1987).

[182] H. Ahrens, N. Kaffrell, N. Trautmann, and G. Herrmann, Phys. Rev. C **14**, 211 (1976).

[183] K. Shizuma, H. Ahrens, J. P. Bocquet, N. Kaffrell, B. D. Kern, H. Lawin, R. A. Meyer, K. Sistemich, G. Tittel, and N. Trautmann, Zeitschrift für Physik A Atoms and Nuclei **315**, 65 (1984).

[184] U. Paffrath, H.-J. Wadenpohl, H. Ohm, and K. Sistemich, *The Level Scheme of* ${}^{103}_{41}Nb_{62}$, Tech. Rep. JUL-Spez-442, p. 28 (1988).

[185] D. De Frenne, Nuclear Data Sheets **110**, 2081 (2009).

[186] G. Battistuzzi, K. Kawade, B. D. Kern, T. A. Khan, W. D. Lauppe, H. Lawin, H. A. Selič, K. Sistemich, and A. Wolf, *Studies at the Fission Product Separator JOSEF*, Tech. Rep. NEANDC(E)-212U, Vol V, p. 35 (1980).

[187] J. Blachot, Nuclear Data Sheets **108**, 2035 (2007).

[188] B. D. Kern, K. Sistemich, W.-D. Lauppe, and H. Lawin, Zeitschrift für Physik A Atoms and Nuclei **306**, 161 (1982).

[189] J. Pereira, S. Hennrich, A. Aprahamian, O. Arndt, A. Becerril, T. Elliot, A. Estrade, D. Galaviz, R. Kessler, K.-L. Kratz, G. Lorusso, P. F. Mantica, M. Matos, P. Möller, F. Montes, B. Pfeiffer, H. Schatz, F. Schertz, L. Schnorrenberger, E. Smith, A. Stolz, M. Quinn, W. B. Walters, and A. Wöhr, Phys. Rev. C **79**, 035806 (2009).

[190] H. Penttilä, *Studies of Very Neutron-Rich Odd-Mass Nuclei with 109 ≤ A ≤ 119*, Ph.D. thesis, University of Jyväskylä (1992).

[191] J. B. Wilhelmy, *High-Resolution Gamma and X-Ray Spectroscopy on Unseparated Fission Products*, Ph.D. thesis, University of California, Berkeley (1969).

[192] S. Kumar, J. Chen, and F. G. Kondev, Nuclear Data Sheets **137**, 1 (2016).

[193] T. Altzitzoglou, J. Rogowski, M. Skålberg, J. Alstad, G. Herrmann, N. Kaffrell, G. Skarnemark, W. Talbert, and N. Trautmann, Radiochim. Acta **51**, 145 (1990).

[194] N. Trautmann, N. Kaffrell, H. Ahrens, and P. F. Dittner, Phys. Rev. C **13**, 872 (1976).

[195] G. Lhersonneau and S. Brant, Phys. Rev. C **72**, 034308 (2005).

[196] D. De Frenne, Nuclear Data Sheets **110**, 1745 (2009).

[197] M. Liang, H. Ohm, I. Ragnarsson, and K. Sistemich, Zeitschrift für Physik A Hadrons and Nuclei **346**, 101 (1993).

[198] T. Marketin, D. Vretenar, and P. Ring, Phys. Rev. C **75**, 024304 (2007).

[199] T. Marketin, L. Huther, and G. Martínez-Pinedo, Phys. Rev. C **93**, 025805 (2016).

[200] P. Möller and J. Randrup, Nuclear Physics A **514**, 1 (1990).

[201] J. Krumlinde and P. Möller, Nuclear Physics A **417**, 419 (1984).

[202] E. Chabanat, P. Bonche, P. Haensel, J. Meyer, and R. Schaeffer, Nuclear Physics A **635**, 231 (1998).

[203] B. Singh and Z. Hu, Nuclear Data Sheets **98**, 335 (2003).

[204] V. Guadilla, A. Algora, J. L. Tain, J. Agramunt, D. Jordan, A. Montaner-Pizá, S. E. A. Orrigo, B. Rubio, E. Valencia, J. Suhonen, O. Civitarese, J. Äystö, J. A. Briz, A. Cucoanes, T. Eronen, M. Estienne, M. Fallot, L. M. Fraile, E. Ganioğlu, W. Gelletly, D. Gorelov, J. Hakala, A. Jokinen, A. Kankainen, V. Kolhinen, J. Koponen, M. Lebois, T. Martinez, M. Monserrate, I. Moore, E. Nácher, H. Penttilä, I. Pohjalainen, A. Porta, J. Reinikainen, M. Reponen, S. Rinta-Antila, K. Rytkönen, T. Shiba, V. Sonnenschein, A. A. Sonzogni, V. Vedia, A. Voss, J. N. Wilson, and A.-A. Zakari-Issoufou, Phys. Rev. C **96**, 014319 (2017).

[205] D. D. Frenne and A. Negret, Nuclear Data Sheets **109**, 943 (2008).

[206] M. K. Smith, *Chasing Triaxiality: Probing Structure in the $A \sim 110$ Region via Lifetime Measurements of 109Ru and 109Tc with Fast Timing*, Ph.D. thesis, University of Notre Dame (2017).

[207] J. Kurpeta, W. Urban, A. Płochocki, J. Rissanen, J. A. Pinston, V.-V. Elomaa, T. Eronen, J. Hakala, A. Jokinen, A. Kankainen, I. D. Moore, H. Penttilä, A. Saastamoinen, C. Weber, and J. Äystö, Phys. Rev. C **86**, 044306 (2012).

[208] J. Kurpeta, W. Urban, A. Płochocki, J. Rissanen, J. A. Pinston, V.-V. Elomaa, T. Eronen, J. Hakala, A. Jokinen, A. Kankainen, P. Karvonen, I. D. Moore, H. Penttilä, A. Saastamoinen, C. Weber, and J. Äystö, Phys. Rev. C **84**, 044304 (2011)